



**HAL**  
open science

## Compound coatings of Ca-phosphates and/ titanate on metallic implants for medical applications

Ibrahim Hadeer Ibrahim Mohamed

► **To cite this version:**

Ibrahim Hadeer Ibrahim Mohamed. Compound coatings of Ca-phosphates and/ titanate on metallic implants for medical applications. Other [cond-mat.other]. Université de Strasbourg; Ĝāmi'at al-Qāhirat (Le Caire), 2013. English. NNT: 2013STRAE035 . tel-00991949

**HAL Id: tel-00991949**

**<https://theses.hal.science/tel-00991949>**

Submitted on 16 May 2014

**HAL** is a multi-disciplinary open access archive for the deposit and dissemination of scientific research documents, whether they are published or not. The documents may come from teaching and research institutions in France or abroad, or from public or private research centers.

L'archive ouverte pluridisciplinaire **HAL**, est destinée au dépôt et à la diffusion de documents scientifiques de niveau recherche, publiés ou non, émanant des établissements d'enseignement et de recherche français ou étrangers, des laboratoires publics ou privés.



**Thèse**  
présentée pour obtenir le grade de  
**Docteur de l'Université de Strasbourg**  
et  
**Docteur de l'Université Ain Shams University du Caire, Egypte**

SPECIALITE : Physique de la matière condensée  
Ecole Doctorale UdS 182 - Physique et chimie physique

Par

***Hadeer Ibrahim Mohamed Ibrahim***

---

**Compound coatings of Ca-phosphates and/ titanate on metallic implants for medical applications**

**Revêtement de phosphate de calcium sur dioxyde de titane pour des implants métalliques pour des applications médicales**

---

*Directrice de thèse* Adele Carradò, Maître de Conférences HDR  
Université de Strasbourg, Strasbourg, France

*Directeur de thèse* Mahmoud El-Sayed El-Sayed, Professeur  
Université Ain Shams, Le Caire, Egypte

*Rapporteur* Emmanuel Pauthe, Professeur  
Université de Cergy-Pontoise, France

*Rapporteur* Osiris Wanis Guirguis, Professeur  
Université du Cairo University

*Examineur* Wafa Abdel-Fattah, Professeur,  
National Reaserch of Cairo, Le Caire, Egypte

*Examineur* Genevieve Pourroy, Directeur de Recherche  
Université de Strasbourg, Strasbourg, France

Soutenue au Caire le 10 septembre 2013.



# **Compound coatings of Ca-phosphates and/ titanate on metallic implants for medical applications**

THESIS SUBMITTED TO  
THE FACULTY OF SCIENCE AIN SHAMS UNIVERSITY IN  
COLLABORATION TO UNIVERSITÉ de STRASBOURG  
UNIVERSITY FOR THE DEGREE OF  
DOCTOR OF PHILOSOPHY IN BIOPHYSICS

BY

**Hadeer Ibrahim Mohamed Ibrahim**

B.Sc. in Biophysics 2001

M.Sc. in Biophysics 2007

(2013)

**SUPERVISED BY:**

**Prof. Dr. El-Sayed Mahmoud El-Sayed**

Professor of Biophysics, Faculty of Science-Ain Shams University, Cairo, Egypt

**Dr. Adele Carradò**

Maître de Conférences Habilité à Diriger des Recherches  
Université de Strasbourg, France

### Acknowledgements

Ultimate thanks and praise to Allah.

I would like to express my deepest gratitude to Prof. Dr. Abdel Sattar Mohamed Sallam, Professor of Biophysics, Faculty of Science, Ain Shams University (ASU), for his valuable supervision, guidance and continuous encouragement.

My sincere gratitude and thankfulness go to Prof. Dr. El Sayed Mahmoud El Sayed, Professor of Biophysics, Faculty of Science, Ain Shams University (ASU), for his supervision stimulating discussion and great patients throughout the preparation of this thesis.

I would like to express my deepest gratitude to Prof. Mona Salah El-din Hassan, Professor of Biophysics, Faculty of Science, Ain Shams university (ASU), for her valuable supervision, stimulating discussion and great patience throughout the preparation of this thesis.

I would like to express my particular appreciation, indebtedness to Prof. Dr. Wafaa Ismail Abdel-Fattah, Professor of Bio-ceramics and ceramic/polymer composites at National Research Centre Biomaterials department (NRC, Dokki, Giza), for her noble supervision, driving inspiration, continuous advice and effective scientific and practical support. I'm greatly indebted to her and it was a great honour to work under her supervision.

Thanks go also to NRC and to Institut de Physique et Chimie des Matériaux de Strasbourg (IPCMS, France), for allowing the laboratories for experimental parts. By gaining access to their expertise and the laboratory facilities, my research capabilities have been enriched.

*Le travail présenté dans ce mémoire a été effectué au laboratoire IPCMS et Université de Strasbourg (UDS), au laboratoire NRC et ASU.*

*Je remercie mon superviseur français Dr. Adele Carradò, Maître de Conférences-HDR de l'IPCMS et UDS son aide apportée pendant les mesures, pour ses conseils et son support continue.*

*Mes remerciements vont aussi à Ms. Jacques Faerber, Dris Ihiawakrim, Guy Schmerber and Mlle Celine Kiefer pour l'aide technique qu'ils m'ont fournie pour la réalisation de mes expériences au laboratoire IPCMS et pour leurs cordialités.*

*Egalement merci à Monsieur le Professeur Marc Drillon, directeur de l'IPCMS, de m'avoir accueillie dans son laboratoire pour mes premières années de thèse, ainsi qu'à l'ensemble du personnel et thésards du laboratoire IPCMS. Je tiens aussi à adresser mes vifs remerciements à Madame le Professeur Geneviève Pourroy de l'IPCMS pour sa gentillesse et disponibilité qu'elle m'a témoigné lors de ma présence à Strasbourg.*

*Je remercie tout particulièrement le Dr. Thierry Roland de l'Institut Charles Sadron et Institut National des Sciences Appliquées. Je tiens à lui exprimer toute ma reconnaissance pour l'aide qu'il m'a fournie pendant la réalisation de mes expériences en microscopie confocale.*

Special thanks are to L'Oreal – UNESCO International Prize for Financial support allowing the prize for young scientists years 2010 and 2011 to continue scientific research for two years. Also thanks are due to EGIDE – Campus France IMHOTEP project for scientific cooperation between France/Egypt Academy for Scientific Research & Technology for two rounds of four years allowing cooperation between NRC and IPCMS, and supporting the laboratories for experimental parts and exchange of Professors.

My appreciation and gratitude go to my husband, Biophysist Mohamed Salah El-din Gad, my parent and all members of my dear family and special thanks to my son Yousof.

# Table of contents

	Page
List of abbreviations .....	xi
List of equations.....	xv
Resumé du manuscrit en français.....	2
General Introduction .....	14
<b>Chapter 1: State of the art</b> .....	<b>18</b>
1. Biomaterials .....	19
1.1. Biocompatibility and bioactivity.....	20
1.2. Metallic biomaterials .....	21
1.2.1. Titanium and its alloys.....	22
1.2.2. Medical application of Ti and its alloys.....	24
1.2.3. Bone and joint replacements.....	25
1.2.4. Dental implants.....	25
1.2.5. Maxillofacial and craniofacial treatments .....	25
2. Corrosion resistance.....	25
3. Surface treatment .....	27
3.1. Mechanical pretreatment of metals: Blasting.....	27
3.2. Electrochemical pretreatment of metal: Anodization .....	28
3.3. Chemical pretreatment of metal: Acid etching .....	28
3.4. Coating.....	29
3.4.1 Calcium phosphates.....	30
3.4.2. Biomimetic coating and simulated body fluid.....	31
3.4.3. Titanium nitride.....	33
<b>Chapter 2: Ca-P coating by autocatalytic method understanding and optimization of the process</b> .....	<b>34</b>
<b>PART I. Substrate pretreatment</b> .....	<b>36</b>
1. State of art: Surface state modification .....	36

## Table of contents

---

1.1. Surface roughness .....	36
1.2. Pretreatment in alkaline NaOH .....	37
1.3. Heat treatment .....	37
PART II. Coating deposition by autocatalytic baths on pretreated substrates .....	39
1. State of the art .....	39
1.1. Role of palladium ions .....	40
1.2. Role of silver ions (catalyser and antibacterial ions) .....	40
PART III. Experimental part .....	41
1. Materials and methods .....	41
Substrates .....	41
1.1. Step 1: Substrate pretreatment .....	42
1.1.1. Experimental procedure A: chemical route .....	43
1.1.2. Experimental procedure B: physical route .....	44
1.2. Step 2: Coating deposition: Acidic, alkaline and oxidant baths .....	45
1.3. Samples' notation .....	46
1.4. Step 3: Biocompatibility step .....	46
1.4.1. Preparation of SBF .....	47
2. Characterisations of the biolayer .....	47
<b>Chapter 3: Results and Discussions .....</b>	<b>49</b>
PART I. Pretreated metallic substrates .....	50
1. Morphological analysis of alkaline (NaOH) pretreated substrates .....	50
2. Topological analysis of alkaline (NaOH) pretreated substrates .....	54
3. Structural analysis of pretreated samples .....	56
Conclusion of Part I .....	58
Part II: Sample treated by acidic bath .....	59
1. Structural analysis of samples after treatment with acidic bath .....	59
1.1. Group I .....	59
1.2. Group II .....	63

## Table of contents

---

1.3. Group III .....	65
2. Morphological analysis of samples after treatment with acidic bath .....	67
2.1. Surface morphology of Group I .....	67
2.2. Surface morphology of Group II.....	69
2.3. Surface morphology of Group III .....	70
3. Biochemical analyses of SBF of Groups I, II and III.....	72
3.1. Group I.....	72
3.2. Group II.....	73
3.3. Group III .....	73
Conclusion of Part II.....	74
Part III. Alkaline bath .....	76
1. Structural analysis of samples after treatment with alkali bath.....	76
1.1 Structural analysis of Group I.....	76
1.2 Structural analysis of Group II.....	80
1.3 Structural analysis of Group III .....	81
2. Morphological analysis of samples after treatment with alkaline bath.....	83
2.1. Surface morphology of Group I.....	83
2.2. Surface morphology of Group II.....	86
2.3. Surface morphology of Group III .....	86
3. Biochemical analyses of SBF of Groups I, II and III.....	89
Conclusion of Part III.....	91
Part IV. Oxidant bath .....	92
1. Structural analysis of samples after treatment with oxidant bath .....	92
1.1. Structural analysis of Group I .....	92
1.2. Structural analysis of Group II.....	95
1.3. Structural analysis of Group III .....	97
2. Morphological analysis of samples after treatment with oxidant bath.....	98
2.1. Surface morphology of Group I.....	98

## Table of contents

---

2.2. Surface morphology of Group II.....	101
2.3. Surface morphology of Group III .....	101
3. Biochemical analyses of Groups I, II and III .....	103
Conclusion of Part IV .....	105
Conclusion .....	107
References.....	110
Arabic summary.....	125
Annex 1: Pulsed Laser Deposition.....	125
Annex 2: Calcium-phosphate phases .....	128
Amorphous Calcium Phosphate (ACP) .....	129
Dicalcium Phosphate Dehydrate (DCPD) and Anhydrous (DCPA).....	129
Tricalcium Phosphate (TCP).....	130
Octacalcium Phosphate (OCP) .....	130
Canaphite .....	131
Hydroxyapatite (HA) .....	131
Solubility of calcium phosphate compounds .....	132
Annex 3: Simulated body fluids.....	134
Annex 4: Analyses and Characterizations.....	137
Structural characterizations.....	138
Morphological characterizations.....	140
Biochemical analysis of SBF .....	141

<b>List of tables</b>	<b>page</b>
Tableau 1. Compositions des bains autocatalytiques.....	7
Tableau 2. Compositions (mM) des SBF1 et SBF1.5 en comparaison avec le plasma sanguin humain [Kokubo & Takadama, 2006]. ....	7
Table 1. Biomaterials classes with their advantages and disadvantages [Sáenz et al.,1999] .....	19
Table 2. Types of tissue response to different foreign materials [Hench and Best, 2004].....	20
Table 3. Some characteristics of several metallic implant materials [Long and Rack, 1998]. ....	22
Table 4. Chemical composition of different grades of Ti and its alloy (ASTM, F67-89, 1992; ASTM, F136-84, 1992).....	23
Table 5. Titanium and its alloys for biomedical applications registered in according to international Standards ASTM, ISO, or JIS.....	23
Table 6. Mechanical properties of Ti and its alloys [Long and Rack, 1998]. ....	24
Table 7. Average surface roughness using several methods.....	28
Table 8. Several methods for Ca-P coatings[Yang et al., 2005] .....	30
Table 9. Existing calcium orthophosphates and their major properties [Dorozhkin, 2009]. ....	31
Table 10. The development of simulated body fluid to imitate the extracellular fluid compared to human blood plasma. ....	32
Table 11. Composition of Kroll etching solution. ....	44
Table 12. PLD experimental conditions of TiN films.....	45
Table 13. Inorganic composition of chemical baths. ....	45
Table 14. Samples' notation. ....	46
Table 15. Ionic concentration (mM) of SBF1 and SBF1.5 in comparison with human blood plasma [Kokubo and Takadama, 2006].....	46
Table 16. Substrate, buffer layer and catalyst used in each group .....	50
Table 17. Sample notation of pretreated substrates. (Duration of SBF is in day: d).....	50
Table 18. Complete series of sample (Group I, II and II) treated with acidic autocatalytic bath. ....	60
Table 19. Complete series of sample (Group I, II and II) treated with alkaline autocatalytic bath) ....	77
Table 20. Complete series of sample (Group I, II and II) treated with oxidant autocatalytic bath. ....	93
Table 21. Comparative composition of inorganic phases of adult human calcified tissues [Dorozhkin & Epple, 2002].....	132
Table 22. The development of simulated fluid to imitate the extracellular fluid of the human blood plasma. ....	135
Table 23. Analysis of Ca <sup>2+</sup> concentration .....	141
Table 24. Preparation of Control and unknown samples. ....	142
Table 25. Analysis of P concentration. ....	142
Table 26. Prepration of control and unknown samples.....	142

<b>List of figures</b>	<b>Page</b>
Figure 1. Schéma des deux méthodes employées dans ce travail de thèse. ....	4
Figure 2. Schéma représentatif du travail expérimental.....	6
Figure 3. Micrographie MEB de la structure de la couche tampon de titanate de sodium composée d'agglomérats sphériques (a), grossissement de la structure hautement nanoreticulé (b) and épaisseur de la couche de titanate de sodium (c). ....	8
Figure 4. Clichés MEB de couches de phosphate de calcium obtenues par immersion dans le bain SBF1 (a et d) puis dans le bain SBF1.5 (b et c) pour des couches de titanate de sodium obtenues après 1 h ou 3 h de recuit. Les analyses FT-IR associées sont présentées en (c) et (d).....	9
Figure 5. Micrographie MEB de la structure couche intermédiaire de TiN après le bain acide et différentes immersion en SBF.....	10
Figure 6. Clichés MEB des couches de phosphate de calcium obtenues dans un bain alcalin (avec PdCl <sub>2</sub> ou AgCl) et par immersion dans le bain SBF1 puis SBF1.5 et leurs analyses EDS associées. ...	11
Figure 7. Micrographie MEB des dépôts obtenus par un bain oxydant (avec PdCl <sub>2</sub> ou AgCl) et après immersion dans SBF1 puis dans SBF1.5 et leurs analyses EDS associées. ....	12
Figure 8. Sketch of employed methods in the present work. ....	16
Figure 9. Several metallic implants sites [Manivasagam et al., 2010].....	21
Figure 10. Schematic presentation of initiation and mechanism of corrosion of a dental implant [Gittens et al., 2011].....	26
Figure 11. Flow sheet of experimental design .....	35
Figure 12. Structural change of titanium surface after NaOH (alkaline) treatment and heat treatment [Kokubo and Yamaguchi, 2010].....	38
Figure 13. Surface structure changes of Ti metal after alkaline and thermal treatment then soaked in SBF [Kokubo and Yamaguchi, 2010].....	39
Figure 14. Schematic diagram of the specimens' classifications.....	42
Figure 15. Schematic diagram of the experimental work. ....	43
Figure 16. Schematic principle of PLD system. ....	44
Figure 17. FESEM images of TAV polished and cleaned; after chemical etching and NaOH treated and their corresponding EDS-X analyses. Sample's notation is given in <b>Table 17</b> . ....	51
Figure 18. FESEM images of TAV <sub>400</sub> and TAV <sub>4000</sub> with two heating rate (10 and 3°C/minute) and their corresponding EDS-X analyses. Sample's notation is given in <b>Table 17</b> .....	52
Figure 19. FESEM images of (a) TAV <sub>400</sub> -1h after immersion 4 d in SBF1, (b) TAV <sub>400</sub> -1h-SBF1 after immersion another 2 d in SBF1.5, (d) TAV <sub>400</sub> -3h after immersion 4 d in SBF1, (e) TAV <sub>400</sub> -3h-SBF1 after immersion additional 2 d in SBF1.5, (g,h) TAV <sub>4000</sub> immersed in SBF for 7 d, (j,k), Ti <sub>4000</sub> immersed in SBF for 14 d and (c,f,i,l) their corresponding EDS-X analyses.....	53
Figure 20. Confocal 3D images of roughness TAV polished and cleaned (a and b), after chemical etching (c,d) and after alkaline treatment (e, f).....	55
Figure 21. Confocal 3D images of roughness TAV <sub>400</sub> subjected to a heating rate 10°C/minute (a), and its immersion in SBF1 and SBF1.5 (b,c), TAV <sub>400</sub> subjected to heating rate 3°C/minute (d), its immersion in SBF1 and SBF 1.5 (e,f); TAV <sub>4000</sub> subjected to a heating rate of 3°C/minute (g), its immersion in SBF (h), Ti <sub>4000</sub> subjected to a heating rate 3°C/minute (i) and its immersion in SBF (j). ....	56
Figure 22. FT-IR Spectra of (a) TAV <sub>400</sub> subjected to heating rate 10°C/minute, (b) 3°C/minute after immersing in SBF1 followed by SBF1.5 for 4 and 2 d and (c) TAV <sub>4000</sub> after immersing in SBF1 for 7 and 14 d. ....	57

Figure 23. FT-IR spectra after immersing 2 h in acidic bath followed by immersion in SBF (a) TAV <sub>400</sub> subjected to 1h heat treatment. (b) TAV <sub>400</sub> , (c) TAV <sub>4000</sub> and (d) Ti <sub>4000</sub> were subjected to 3 h heat treatment. ....	61
Figure 24. TF-XRD patterns for (a) TAV <sub>4000</sub> and (b) Ti <sub>4000</sub> after treatment in acidic bath for 2 h (red) and after immersion in SBF for 14 d (blue). ....	62
Figure 25. TEM images on the scratched coating Ti <sub>4000</sub> -Ac <sub>Pd</sub> (a) and after SBF for 14 d (d), the corresponding SAED patterns (b,e) and their corresponding EDS-X analyses (c,f). ....	63
Figure 26. TF-XRD patterns for TAV <sub>4000</sub> after treatment in acidic bath with AgCl for 2 h (red) and after immersion in SBF for 7 d (blue). ....	64
Figure 27. TEM images of Ca-P coatings (a) after 2 h in acidic bath with AgCl and d) after SBF1 for 7 d, (b,e) diffraction pattern and (c,f) corresponding EDS-X analyses. ....	64
Figure 28. FT-IR spectra of TiN (a) after 1 h, (d) after 2 h in acidic bath followed to immersion in SBF1 and SBF1.5. ....	65
Figure 29. TF-XRD patterns for TiN after treatment in acidic bath (a) with PdCl <sub>2</sub> for 1 h (red), (b) with PdCl <sub>2</sub> for 2 h (red) followed by immersing in SBF 1 for 4 d (black), then another 2 d in SBF1.5 (blue) and (c) with AgCl for 2 h (red) followed by immersion for 14 d in SBF1 (blue). ....	66
Figure 30. TEM image of scratch layer after 2h in Ac bath with AgCl (a) and its corresponding EDS-X analysis. ....	67
Figure 31. FESEM images of different substrates after immersion for 2 h in acidic bath: (a,b) TAV <sub>400</sub> -1h, (d,e) TAV <sub>400</sub> -3h, (g,h) TAV <sub>4000</sub> , (j, k) Ti <sub>4000</sub> and (c,f,i,l) their corresponding EDS-X analyses. ....	67
Figure 32. FESEM images of Group I after immersion for 2 h in acidic bath followed by immersion in SBF1 for 4 d followed by another 2 d in SBF1.5 and their corresponding EDS-X analyses. ....	68
Figure 33. FESEM images of TAV <sub>4000</sub> (a,b) after immersion in acidic bath for 2 h, (d,e) after immersion TAV <sub>4000</sub> -Ac <sub>Ag</sub> in SBF for 7 d and (c,f) corresponding EDS-X analyses. ....	70
Figure 34. FESEM images of TiN after immersion in acidic bath (a,b) with PdCl <sub>2</sub> for 1 h, (d,e) with PdCl <sub>2</sub> for 2 h, (g,h) with AgCl for 2 h and (f,i) corresponding EDS-X analyses. ....	71
Figure 35. FESEM images of TiN-Ac after immersion in SBF(a) SBF1 for 4 d, (b) SBF1.5 for another 2 d, (d) SBF1 for 4 d, (e) SBF1.5 for another 2 d, (g) SBF1 for 7 d, (h) SBF for 14 d and (c,f,i) corresponding EDS-X analyses. ....	72
Figure 36. Concentrations of Ca <sup>2+</sup> and P ions(a) TAV <sub>400</sub> in SBF1 (4 d) followed by another 2 d in SBF1.5, (b) TAV <sub>4000</sub> and Ti <sub>4000</sub> in SBF for 7 and 14 d. ....	73
Figure 37. Concentrations of Ca <sup>2+</sup> and P ions in SBF after immersion of TAV <sub>4000</sub> immersed in acidic bath with AgCl after 3 and 7 d. ....	73
Figure 38. Concentrations of Ca <sup>2+</sup> and P ions (a) TiN after treatment with acidic bath for 1 and 2 h with PdCl <sub>2</sub> in SBF1 (4 d) followed by another 2 d in SBF1.5, (b) TiN after treatment with acidic bath for 2 h with AgCl in SBF for 7 and 14 d. ....	74
Figure 39. FT-IR spectra after immersing 2 h in alkaline bath followed by immersion in SBF (a) TAV <sub>400</sub> subjected to heating rate 10°C/minute, (b) TAV <sub>400</sub> , (c) TAV <sub>4000</sub> and (d) Ti <sub>4000</sub> subjected to heating rate 3°C/minute. ....	78
Figure 40. TF-XRD patterns for (a) TAV <sub>4000</sub> and (b) Ti <sub>4000</sub> after treatment in alkaline bath for 2h (red) and after immersion in SBF for 14 d (blue). ....	79
Figure 41. TEM images of calcium phosphate coatings (a) TAV <sub>4000</sub> after 2h in alkaline bath, (d)TAV <sub>4000</sub> -Al <sub>Pd</sub> , (g) Ti <sub>4000</sub> -Al <sub>Pd</sub> after SBF for 14 d, (b,e,h) corresponding SAED and (c,f,i) and their corresponding EDS-X analyses. ....	79
Figure 42. TF-XRD patterns for TAV <sub>4000</sub> after treatment in alkaline bath with AgCl for 2 h (red) and after immersion in SBF for 7 d (blue). ....	81
Figure 43. TEM images of calcium phosphate coatings a) after 2 h in alkaline bath with AgCl and d) after SBF for 7 d, (b,e) diffraction pattern and (c,f) their corresponding EDS-X analyses. ....	81

Figure 44. FT-IR spectra of TiN after treatment in alkaline bath and after immersion in SBF1 for 4 d then another 2 d in SBF1.5. .... 82

Figure 45. XRD patterns for TiN after treatment in alkaline bath (a) with PdCl<sub>2</sub> and (b) with AgCl (Red) then followed by immersion in SBF (black and blue). .... 82

Figure 46. (a) TEM image of calcium phosphate coatings after 2 h in alkaline bath with AgCl, (b) corresponding SAED and (c) corresponding EDS-X analysis..... 83

Figure 47. FESEM images of different substrates after immersion for 2 h in alkaline bath: (a,b) TAV<sub>400</sub>-1h, (d,e) TAV<sub>400</sub>-3h, (g,h) TAV<sub>4000</sub>, (j,k) Ti<sub>4000</sub> and (c,f,i,l) their corresponding EDS-X analyses..... 84

Figure 48. FESEM images of Group I after immersion for 2 h in alkaline bath followed by immersion in SBF: (a,b) TAV<sub>400</sub>-1h-Al<sub>Pd</sub> immersed in SBF1 for 4 d followed by another 2 d in SBF1.5, (d,e) TAV<sub>400</sub>-3h-Al<sub>Pd</sub> immersed in SBF1 for 4 d followed by another 2 d in SBF1.5, (g,h) TAV<sub>4000</sub>-Al<sub>Pd</sub> immersed in SBF for 7 and 14 d, (j,k) Ti<sub>4000</sub>-Al<sub>Pd</sub> immersed in SBF for 7 and 14 d and (c, f, i, l) their corresponding EDS-X analysis. .... 85

Figure 49. FESEM images of TAV<sub>4000</sub> (a,b) after immersion in alkaline bath for 2 h, (d,e) after immersion TAV<sub>4000</sub>-Al<sub>Ag</sub> in SBF for 7 d and (c,f) corresponding EDS-X analyses. .... 86

Figure 50. FESEM images of TiN after immersion in alkaline bath (a,b,c) with PdCl<sub>2</sub> for 1 h, (e,f,g) with AgCl for 2 h and (d, h) corresponding EDS-X analyses..... 87

Figure 51. FESEM images of TiN-Al after immersion in (a, b) SBF1 for 4 d, (d,e,f) SBF1.5 for another 2 d, (h,i,j) SBF1 for 7 d, (l,m) SBF for 14 d and (c,g,k,n) corresponding EDS-X analyses. ... 88

Figure 52. Concentrations of Ca<sup>2+</sup> and P ions (a) TAV<sub>400</sub> in SBF1 (4 d) followed by another 2 d in SBF1.5, (b)TAV<sub>4000</sub> and Ti<sub>4000</sub> in SBF for 7 and 14 d. Group I ..... 89

Figure 53. Concentration of Ca<sup>2+</sup> and P ions in SBF after immersion of TAV<sub>4000</sub> immersed in alkaline bath with AgCl after 3 and 7 d. Group II. .... 90

Figure 54. Concentrations of Ca<sup>2+</sup> and P ions(a) TiN after treatment with alkaline bath for 1 and 2 h with PdCl<sub>2</sub> in SBF1 (4 d) followed by another 2 d in SBF1.5, (b)TiN after treatment with alkaline bath for 2 h with AgCl in SBF for 7 and 14 d. Group III ..... 90

Figure 55. FT-IR spectra after immersing 2 h in oxidant bath followed by immersion in SBF (a) TAV<sub>400</sub> subjected to heating rate 10°C/minute, (b) TAV<sub>400</sub> subjected to heating rate 3°C/minute, (c) TAV<sub>4000</sub> subjected to heating rate 3°C/minute and (d) Ti<sub>4000</sub> subjected to heating rate 3°C/minute..... 94

Figure 56. TF-XRD patterns for (a) TAV<sub>4000</sub> and (b) Ti<sub>4000</sub> after treatment in oxidant bath for 2 h (red) and after immersion in SBF for 14 d (blue). .... 95

Figure 57. TEM image of calcium phosphate coatings (a) Ti<sub>4000</sub> after 2 h in oxidant bath, (b) corresponding SAED and (c) corresponding EDS-X analysis..... 95

Figure 58. TF-XRD patterns for TAV<sub>4000</sub> after treatment in oxidant bath with AgCl for 2h (red) and after immersion in SBF for 7 d (blue). .... 96

Figure 59. a) TEM image of calcium phosphate coatings after 2 h in oxidant bath with AgCl, b) corresponding SAED and (c) corresponding EDS-X analysis..... 96

Figure 60. FT-IR spectra of TiN after immersion in oxidant bath with PdCl<sub>2</sub> followed with immersion in SBF1 for 4 d then another 2 d in SBF1.5..... 97

Figure 61. XRD patterns for TiN after treatment in oxidant bath (a) with PdCl<sub>2</sub> and (b) with AgCl (red) then followed with immersion in SBF (black and blue). .... 98

Figure 62. FESEM images of different substrates after immersion for 2 h in oxidant bath: (a,b) TAV<sub>400</sub>-1h, (d,e) TAV<sub>400</sub>-3h, (g,h) TAV<sub>4000</sub>, (j,k) Ti<sub>4000</sub> and (c,f,i,l) their corresponding EDS-X analyses..... 99

Figure 63. FESEM images of Group I after immersion for 2 h in oxidant bath followed by immersion in SBF: (a,b) TAV<sub>400</sub>-1h-Ox<sub>Pd</sub> immersed in SBF1 for 4 d followed by another 2 d in SBF1.5, (d,e) TAV<sub>400</sub>-3h-Ox<sub>Pd</sub> immersed in SBF1 for 4 d followed by another 2 d in SBF1.5, (g,h) TAV<sub>4000</sub>-Ox<sub>Pd</sub>

## Table of contents

---

immersed in SBF for 7 and 14 d, (j,k) Ti <sub>4000</sub> -Ox <sub>Pd</sub> immersed in SBF for 7 and 14 d and (c,f i,l) their corresponding EDS-X analyses. ....	100
Figure 64. FESEM images of TAV <sub>4000</sub> (a,b) after immersion in oxidant bath for 2 h, (d,e) after immersion TAV <sub>4000</sub> -Ox <sub>Ag</sub> in SBF for 7 d and (c,f) corresponding EDS-X analyses.....	101
Figure 65. FESEM images of TiN after immersion in oxidant bath (a,b) with PdCl <sub>2</sub> for 1 h, (d,e,f) with AgCl for 2 h and (c,g) corresponding EDS-X analyses. ....	102
Figure 66. FESEM images of TiN-Ox after immersion in (a,b) SBF1 for 4 d, (d,e) SBF1.5 for another 2 d, (g) SBF1 for 7 d, (h) SBF for 14 d and (c,f,i) corresponding EDS-X analyses. ....	102
Figure 67. Concentrations of Ca <sup>2+</sup> and P ions (a) TAV <sub>400</sub> in SBF1 (4 d) followed by another 2 d in SBF1.5, (b) TAV <sub>4000</sub> and Ti <sub>4000</sub> in SBF for 7 and 14 d. ....	103
Figure 68. Concentrations of Ca <sup>2+</sup> and P ions in SBF after immersion of TAV <sub>4000</sub> immersed in oxidant bath with AgCl after 3 and 7 d. ....	104
Figure 69. Concentrations of Ca <sup>2+</sup> and P ions (a) TiN after treatment with oxidant bath for 1 and 2 h with PdCl <sub>2</sub> in SBF1 (4 d) followed by another 2 d in SBF1.5, (b) TiN after treatment with oxidant bath for 2 h with AgCl in SBF for 7 and 14 d. ....	104
Figure 70. Schematic diagram of PLD, Copyright: <a href="https://rt.grc.nasa.gov/main/rlc/pulsed-laser-deposition-laboratory">https://rt.grc.nasa.gov/main/rlc/pulsed-laser-deposition-laboratory</a> and <a href="http://www.nlo.hw.ac.uk/research.html">http://www.nlo.hw.ac.uk/research.html</a> .....	126
Figure 71. Solubility isotherms of Ca-P phases at 37 °C and I = 0.1 M. Copyright 1992 International & American Association for Dental Research. Critical Reviews in Oral Biology and Medicine, 3(1/2). 61-82 (1992).....	133

### List of abbreviations

ACP:	Amorphous calcium phosphate
AgCl:	Silver chloride
Ag <sup>+</sup> :	Silver ion
Al:	Aluminium
Al <sub>2</sub> O <sub>3</sub> :	Aluminium oxide
ASTM:	American Society for Testing and Materials
C <sub>4</sub> H <sub>6</sub> O <sub>4</sub> :	Succinic acid
Ca <sup>2+</sup> :	Calcium ion
CaCl <sub>2</sub> :	Calcium chloride
Ca-P:	Calcium phosphate
CDHA:	Calcium-deficient hydroxyapatite
Cl <sup>-</sup> :	Chloride ion
CO <sub>3</sub> <sup>2-</sup> :	Carbonate group
Co–Cr:	Cobalt chromium alloy
Co–Cr–Mo:	Cobalt-chrome-molybdenum
CP-Ti:	Commercially pure titanium
c–SBF:	Corrected SBF
DCPA:	Dicalcium phosphate anhydrous
DCPD:	Dicalcium phosphate dihydrate
dd:	double distilled
E. Coli:	Escherichia coli
EDS:	Electron dispersive spectrometry
FA:	Fluorapatite
Fe:	Iron
FESEM:	Field emission scanning electron microscopy
FT–IR:	Fourier Transform Infrared
GPa:	Gigapascal

## Table of contents

---

HA:	Hydroxyapatite
H <sub>2</sub> O <sub>2</sub> :	Oxygen peroxide
H <sub>2</sub> SO <sub>4</sub> :	Sulphuric acid
HCl:	Hydrochloric acid
HCO <sub>3</sub> <sup>-</sup> :	Hydrogen carbonate
HF:	Hydrofluoric acid
HNO <sub>3</sub> :	Nitric acid
HPO <sub>4</sub> <sup>2-</sup> :	Hydrogen phosphate
ICP:	Inductively coupled plasma
ISO:	International Organization for Standardization
JIS:	Japanese International Standards
K <sup>+</sup> :	Potassium ion
KOH:	Potassium hydroxide
M:	Mole
MCPA:	Monocalcium phosphate anhydrous
MCPM:	Monocalcium phosphate monohydrate
Mg <sup>2+</sup> :	Magnesium ion
µm:	micro-meter
MPa:	Mega Pascal
Mn:	Manganese
m-SBF:	Modified SBF
Na <sup>+</sup> :	Sodium ion
NaCl:	Sodium chloride
NaOH:	Sodium hydroxide
NaF:	Sodium fluoride
NaH <sub>2</sub> PO <sub>2</sub> .H <sub>2</sub> O:	Sodium hypophosphite
NaP <sub>2</sub> O <sub>7</sub> 10H <sub>2</sub> O:	Sodium pyrophosphate
Nb:	Niobium

## Table of contents

---

Ni:	Nickel
n-SBF:	Newly improved SBF
OH <sup>-</sup> :	Hydroxyl group
P:	Phosphorus
PO <sub>4</sub> <sup>3-</sup> :	Phosphate group
P <sub>2</sub> O <sub>7</sub> <sup>4-</sup> :	Pyrophosphate group
P – OH:	Phosphorus and oxygen hydroxyl bond
PdCl <sub>2</sub> :	Palladium chloride
PLD:	Pulsed Laser Deposition
Pt :	Platinum
OCP:	Octacalcium phosphate
Ra:	Mean roughness
Rq:	Root mean square roughness
r-SBF:	Revised SBF
rpm:	Revolutions per minute
SBF:	Simulated Body Fluid
Si:	Silicon
SiC:	Silicon carbide
Ta:	Tantalum
TCP:	Tricalcium phosphate
α-TCP:	α-Tricalcium phosphate
β-TCP:	β-Tricalcium phosphate
TEM:	Transmission Electron Microscope
Ti:	Titanium
Ti-6Al-4V:	High-grade titanium aluminium vanadium alloy
TiN:	Titanium nitride
TiO <sub>2</sub> :	Titanium oxide
Ti-OH:	Hydrated titania

## Table of contents

---

TMZF:	Alloys based on the Ti-12Mo-6Zr-2Fe
TNTZ:	Alloys based on the Ti-Nb-Ta-Zr
TNZT:	Alloys based on the Ti-35Nb-5Ta-7Zr
TNZTO:	Alloys based on the Ti-35Nb-5Ta-7Zr-0.4O
TTCP:	Tetracalcium phosphate
TRIS:	Tris-hydroxymethylaminomethane [(CH <sub>2</sub> OH) <sub>3</sub> CNH <sub>2</sub> ]
V:	Vanadium
W:	Tungsten
XRD:	X-ray diffraction
UTS:	Ultimate strength
YS:	Yield strength
Zr:	Zirconium

<b>List of equations</b>	<b>Page</b>
Anodic dissolution: $M \rightarrow M^{n+} + n(\text{electrons})$ Eq.1.....	26
Cathodic reduction: $O_2 + 2H_2O + 4e \rightarrow 4OH^-$ Eq.2.....	26
Corrosion product: $M^+ + OH^- \rightarrow M(OH)$ Eq.3.....	26
$TiO_2 + OH^- \longrightarrow HTiO_3^-$ Eq. 4.....	37
$Ti + 3OH^- \longrightarrow Ti(OH)_3^+ + 4e^-$ Eq. 5.....	37
$Ti(OH)_3^+ + e^- \longrightarrow TiO_2 \cdot H_2O + \frac{1}{2}H_2 \uparrow$ Eq. 6.....	37
$Ti(OH)_3^+ + OH^- \longrightarrow Ti(OH)_4$ Eq. 7.....	37
$TiO_2 \cdot nH_2O + OH^- \longrightarrow HTiO_3 \cdot nH_2O$ Eq. 8.....	37
$V_s = \frac{S_a}{10}$ Eq. 9.....	47
$HPO_4^{2-} + H_2O \rightleftharpoons H_3O^+ + PO_4^{3-}$ Eq. 10.....	76
$P2O7^{4-} + H_2O \rightarrow 2HPO_4^{2-}$ Eq. 11.....	80
$6CaHPO_4 + 4Ca^{2+} + 8OH^- \longrightarrow Ca_{10}(PO_4)_6(OH)_2 + 6H_2O$ Eq. 12.....	89
$2 H_2O_2 \rightarrow 2 H_2O + O_2$ Eq. 13.....	105
$h(\theta) = \frac{MK^2}{2\pi\rho_s Z_s^2} (1+k^2 \tan^2 \theta)^{3/2}$ Eq. 14.....	127
$h(\theta) = \frac{M}{2\pi\rho_s Z_s^2} \cos^3 \theta$ Eq. 15.....	127
$Ca_9(PO_4)_6 + 7H_2O \longrightarrow Ca_8H_2(PO_4)_6 \cdot 5H_2O + Ca^{2+} + 2OH^-$ Eq. 16.....	129
$6CaHPO_4 + 4Ca^{2+} + 8OH^- \longrightarrow Ca_{10}(PO_4)_6(OH)_2 + 6H_2O$ Eq. 17.....	129
$10CaHPO_4 \cdot 2H_2O \longrightarrow Ca_8H_2(PO_4)_6 \cdot 5H_2O + 2Ca^{2+} + 4H_2PO_4^- + 15H_2O$ Eq. 18.....	129
$Ca_8H_2(PO_4)_6 \cdot 5H_2O + 2Ca^{2+} \longrightarrow Ca_{10}(PO_4)_6(OH)_2 + 4H^+$ Eq. 19.....	130
$d_{hkl} = \frac{\lambda}{2\sin \theta}$ Eq. 20.....	138

# **Resumé du manuscrit en français**

Les prothèses et les implants artificiels ont été développés pour préserver l'intégrité et le confort de vie des personnes souffrant de déficiences fonctionnelles graves. Des dispositifs d'assistance corporelle capables de suppléer les fonctions des structures lésées ont été fabriqués dans ce but. Les matériaux utilisés sont souvent des métaux, largement utilisés en substitution des tissus durs ou des phosphates de calcium (Ca-P) très utilisés en chirurgie osseuse depuis les années 60, malgré des caractéristiques mécaniques défavorables, en particulier celles de l'hydroxyapatite (HA).

La plupart des implants orthopédiques sont métalliques en raison de leurs bonnes propriétés mécaniques. C'est pourquoi, le *titane* (Ti) et *ses alliages* caractérisés par une remarquable biocompatibilité, sont largement utilisés comme structures pour des implants orthopédiques ou dentaires [Liu et al., 2004]. Cependant, la condition essentielle pour tous les matériaux artificiels implantés, est de démontrer leur biocompatibilité, mais aussi leur bioactivité une fois implantés. Les matériaux métalliques ne sont que bioinertes ou au mieux biotolérés et différents types de traitements de surface sont nécessaires afin d'améliorer leur bioactivité. Néanmoins, celle-ci n'est pas aussi performante que celle des céramiques en phosphate de calcium. L'ostéointégration à l'interface « titane-os » ne peut pas se réaliser à cause de la bioinertie du métal et au lieu d'une interface os-tissu, il se forme une interface « os-collagène ».

L'alliage de titane Ti-6Al-4V est couramment utilisé en médecine est pour ses bonnes propriétés mécaniques, sa résistance à la corrosion, aux contraintes mécaniques et à l'usure, ainsi que sa relative inertie vis-à-vis des tissus vivants. Malgré cela, quelques réserves persistent liées à la libération d'ions aluminium et vanadium sous certaines conditions de température et pH. Ces ions peuvent s'accumuler dans les tissus [Surowska and Bienias, 2010], et créer des problèmes de stabilité sur une longue période de temps [Symietz et al., 2010].

Pour combiner les bonnes propriétés mécaniques des matériaux métalliques et obtenir des surfaces bioactives, des revêtements de phosphate de calcium ont été développés. Le but est d'améliorer la biocompatibilité et la bioactivité du système et créer une barrière contre l'éventuelle libération d'ions toxiques du substrat métallique [Rosu et al., 2012].

Les revêtements de surface ostéoconducteurs sur des prothèses métalliques sont apparus vers la fin des années 80. En particulier, le dépôt d'HA - sur la surface métallique- obtenu par « torche plasma » a été étudié par *de Groot* [de Groot, 1987] et a permis d'améliorer le comportement biologique de la surface métallique. Par la suite, différentes techniques physiques et chimiques de dépôt ont été développées tels que la torche à plasma, la pulvérisation cathodique, le trempage, la tournette, l'électrophorèse, l'ablation laser, la voie biomimétique, .... Parmi ces méthodes, la technique de recouvrement par *ablation laser pulsé* (PLD) est utilisée pour l'obtention de dépôts phosphocalciques à partir des années 90 [Cotell, 1993]. Son avantage principal est la conservation de la stœchiométrie de la cible vers le dépôt. Par contre, l'inconvénient de cette technique est la difficulté d'obtenir des dépôts sur des surfaces complexes.

Des films de phosphate de calcium ont été obtenus par *méthode biomimétique*. Cette dernière est un procédé physico-chimique dans lequel un substrat métallique est trempé dans une solution qui simule les conditions physiologiques, (simulated body fluid ou, SBF), pour une période de temps suffisante pour former une couche de phosphate de calcium [Kokubo et al., 2003; Kim et al., 1997].

C'est dans ce contexte que s'inscrivent les travaux réalisés au cours de cette thèse. Notre démarche s'éloigne cependant du dépôt de matériaux céramiques par voie physique comme la « torche à plasma ». En effet, les matériaux apatitiques sont déposés en bain *autocatalytique* contenant du

chlorure de palladium ( $\text{PdCl}_2$ ) ou d'argent ( $\text{AgCl}$ ) comme catalyseurs. Le dépôt a lieu essentiellement au cours d'une réaction d'oxydoréduction.

Notre démarche a été de développer une nouvelle voie de synthèse. Après un polissage mécanique et décapage chimique du substrat de Titane ou Ti-6Al-4V, deux types de couches intermédiaires ont été obtenus (**Fig. 1**). Dans la première méthode, une couche intermédiaire en *titanate de sodium* a été obtenue par un prétraitement alcalin sur le substrat en Ti ou Ti-6Al-4V. Elle a été ensuite soumise à un traitement thermique afin de créer une couche alvéolaire nanométrique. Celle-ci facilite la croissance d'une couche de phosphate de calcium par voie *autocatalytique* d'une manière similaire au procédé de formation de l'os naturel [Mohammed et al., 2012].

La deuxième méthode consiste en la réalisation d'une couche intermédiaire de 100 à 500 nm en alliage métallique (TiN, préparé par voie physique par PLD) sur le substrat de Ti-CP 3. Le dépôt par PLD est préféré pour déposer le TiN car la couche produite est très homogène, et présente une rugosité de surface plus faible. Cependant le coût du traitement PLD est élevé. D'autre part, le dépôt de TiN présente des propriétés mécaniques avantageuses. En particulier, le TiN pourrait permettre d'améliorer les propriétés mécaniques de l'implant telles qu'une forte résistance à la fatigue, une dureté, un module de Young, et une rigidité très élevés, ainsi qu'un faible coefficient d'usure mécanique, proches des valeurs caractéristiques des os humains [Pelletier et al., 2011]. La couche de TiN possède de bonnes propriétés bioactives et permet de prévenir une infection bactérienne.

La première solution a été la plus largement étudiée, tandis que la deuxième a été réalisée sur la fin de la thèse et les résultats présentés sont préliminaires.

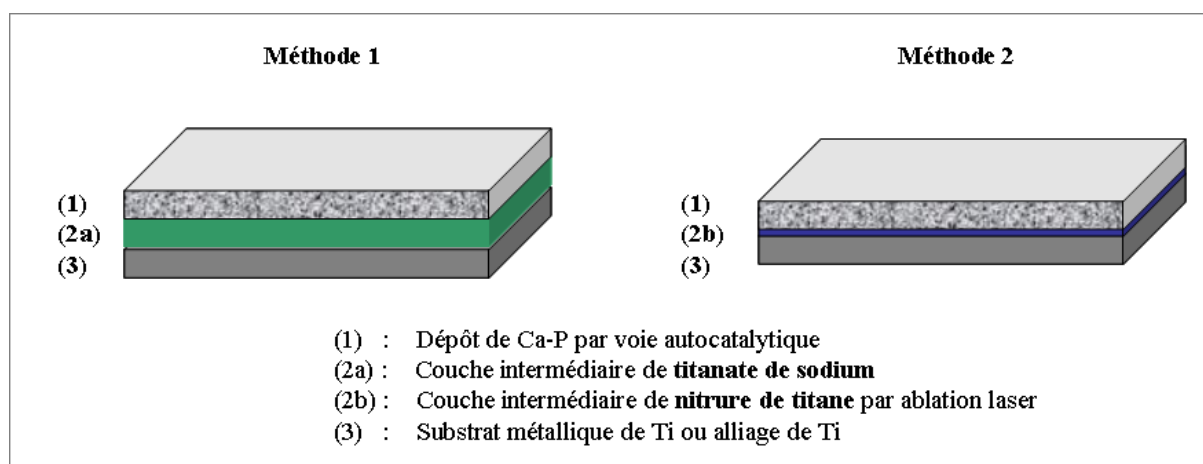


Figure 1. Schéma des deux méthodes employées dans ce travail de thèse.

Cette thèse est organisée autour de trois parties.

Elle débute par **une introduction générale** qui permet de comprendre la démarche de ce travail, une étude bibliographique des travaux réalisés dans ce domaine, ainsi qu'une description des matériaux céramiques - en particulier la famille des phosphates de calcium - et métalliques utilisés tel que le titane et ses alliages. Ensuite, plusieurs méthodes de dépôt et de modifications de surface sont proposées pour améliorer l'utilisation à long terme des implants métalliques. Et enfin, les procédés biomimétiques et autocatalytiques permettant d'obtenir un revêtement de phosphate de calcium sur le titane et son alliage Ti-6Al-4V sont décrits. **Les travaux sont divisés en deux grandes parties. Enfin**, une conclusion générale reprend les discussions et les conclusions de ce travail.

### A) Première partie : La couche de phosphate de calcium

La première partie consiste à préparer des échantillons multicouches comprenant le substrat métallique, revêtu d'une couche intermédiaire et ensuite d'une couche de phosphate de calcium (**Fig. 1**). Trois bains autocatalytiques différents sont utilisés: un bain oxydant, un bain acide ou un bain alcalin. Les trois bains ont été portés à une température comprise entre 60 et 80°C, avec un pH de 5,3 pour le bain acide, 7 pour le bain oxydant et 9,2 pour le bain alcalin. Ces bains dépendent principalement de la réaction d'oxydoréduction dans laquelle le chlorure de palladium (PdCl<sub>2</sub>) ou le chlorure d'argent (AgCl) sont utilisés comme catalyseurs. Ce dernier est aussi un agent antibactérien [Jing et al., 2010; Rastogi et al., 2011]. Le schéma décrivant les expériences qui ont servi d'appuis à ce travail est présenté dans la Fig. 2.

Trois substrats (Ti CP-3, Ti CP-1 ou Ti-6Al-4V) recouverts de deux couches tampons de nature (titanate de sodium et nitrure de titane) et de rugosité différentes polissage mécanique à l'aide de papiers abrasifs de P400 et P4000) ont été étudiés :

#### 1) Le titanate de sodium comme couche tampon

La *couche tampon* en titanate de sodium, a été chimiquement préparée en plusieurs étapes : une attaque chimique sur le substrat de titane en utilisant un réactif de Kroll modifié suivi par un traitement alcalin (NaOH) ; puis un traitement thermique à une température de 630°C avec une rampe de température de 3°C/minute ou 10°C/minute, et un maintien pendant 3 h ou 1 h à 630°C respectivement. Les matériaux sont ensuite laissés à refroidir jusqu'à température ambiante (environ 20°C) dans le four.

#### 2) Le nitrure de titane comme couche tampon

La *deuxième couche tampon* en nitrure de titane a été déposée par ablation laser (PLD) sur le substrat métallique après polissage mécanique et chimique. Une couche de nitrure de titane 300 nm (TiN) a été déposée sur le substrat de titane par PLD pour améliorer les propriétés d'adhésion et antimicrobienne du matériau. Les dépôts ont été effectués par des pulsations générées par laser YAG Quantel ( $\lambda = 355$  nm). La source laser a été placée hors de la chambre d'irradiation. La taille du spot d'irradiation était d'environ 2 mm<sup>2</sup> et la fluence incidente était de 1.5 J/cm<sup>2</sup>. Le substrat a été monté sur un support spécial qui peut être mis en rotation et/ou en translation pendant l'application des irradiations laser multi-pulsations pour éviter le perçage et pour soumettre constamment une nouvelle zone à l'exposition laser. Durant l'exposition, le substrat a été maintenu à une température d'environ 600°C.

A partir de ces deux substrats prétraités, une couche de phosphate de calcium a été déposée en utilisant des bains autocatalytiques (acides, alcalins et oxydants, **Tableau 1**). Ces bains ont des compositions, pH et températures semblables et diffèrent par les catalyseurs utilisés (chlorure de palladium ou d'argent).

La stabilité du phosphate de calcium formé par voie autocatalytique a été étudiée en immergeant les échantillons dans une solution SBF (Simulated Body Fluid) pour des périodes de temps variées. Des analyses morphologiques par microscopie électronique à balayage couplé à l'analyse en dispersion d'énergie (MEB – EDS-X), microscopie électronique à transmission (MET) et microscopie confocale, et des analyses structurales par spectroscopie infrarouge à transformée de Fourier (FT-IR) et diffraction des rayons X (DRX) ont été effectuées avant et après chaque bain SBF à différentes concentrations ioniques (**Tableau 2**). Les quantités de calcium et de phosphore présents dans la solution SBF ont été mesurées au cours du temps par spectrométrie démission optique par plasma à couplage inductif (ICP/OES). Le schéma suivant résume les étapes expérimentales conduites dans cette partie expérimentale de la thèse.

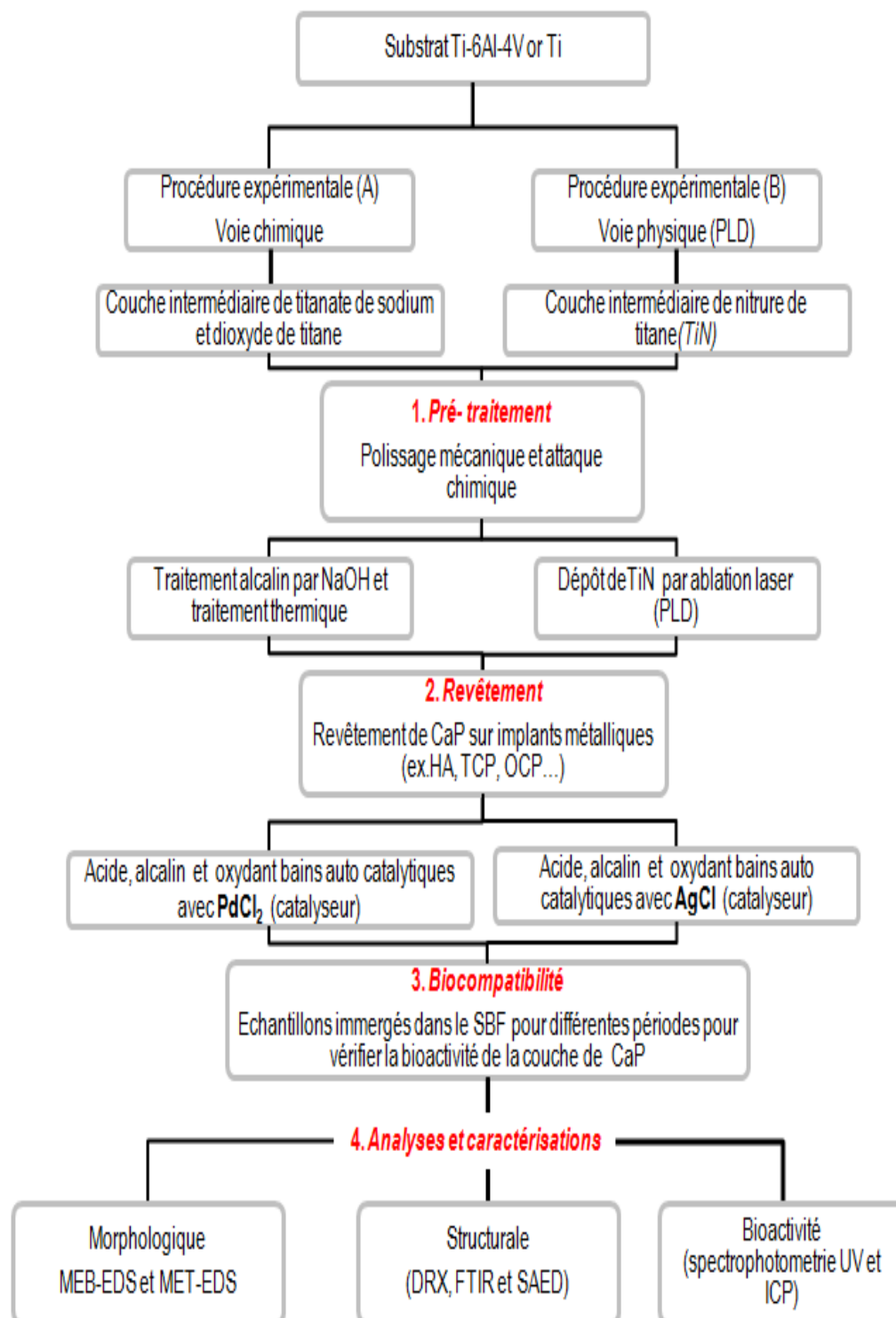


Figure 2. Schéma représentatif du travail expérimental.

Ces trois bains précédemment étudiés par Reis [Leonor and Reis, 2003; Oliveira et al., 2005] pour des polymères, ont été adaptés et améliorés pour être utilisés sur des alliages métalliques ou des métaux. Nous avons réalisé pour la première fois cette méthode sur des substrats métalliques, Ti CP-3 et Ti-6Al-4V. Le schéma représentatif du travail expérimental réalisé est présenté en **Fig. 2**.

Tableau 1. Compositions des bains autocatalytiques.

Bain	Réactifs		Concentrations [g/L]	pH	Temp. du bain. [°C]
Acide	Chlorure de calcium	CaCl <sub>2</sub>	21.0	NaOH: 5.3 ± 0.1	80 ± 2
	Fluorure de sodium	NaF	5.0		
	Acide succinique	C <sub>4</sub> H <sub>6</sub> O <sub>4</sub>	7.0		
	Hypophosphite de sodium	NaH <sub>2</sub> PO <sub>2</sub> ·H <sub>2</sub> O	24.0		
	Chlorure de palladium ou argent	PdCl <sub>2</sub> or AgCl	0.885		
Alcaline	Chlorure de calcium	CaCl <sub>2</sub>	25.0	NaOH: 9.2 ± 0.1	60±2
	Pyrophosphate de sodium	NaP <sub>2</sub> O <sub>7</sub> ·10 H <sub>2</sub> O	50		
	Hypophosphite de sodium	NaH <sub>2</sub> PO <sub>2</sub> H <sub>2</sub> O	21.0		
	Chlorure de palladium ou argent	PdCl <sub>2</sub> or AgCl	0.885		
Oxydant	Chlorure de calcium	CaCl <sub>2</sub>	5.6	NaOH: 7.0 ± 0.1	60 ± 2
	Pyrophosphate de sodium	NaP <sub>2</sub> O <sub>7</sub> ·10 H <sub>2</sub> O	6.7		
	Peroxyde d'hydrogène	H <sub>2</sub> O <sub>2</sub>	34		
	Chlorure de palladium ou argent	PdCl <sub>2</sub> or AgCl	0.9		

Tableau 2. Compositions (mM) des SBF1 et SBF1.5 en comparaison avec le plasma sanguin humain [Kokubo & Takadama, 2006].

	Ionic concentration (mM)							
	Na <sup>+</sup>	K <sup>+</sup>	Mg <sup>2+</sup>	Ca <sup>2+</sup>	Cl <sup>-</sup>	HCO <sub>3</sub> <sup>-</sup>	HPO <sub>4</sub> <sup>2-</sup>	SO <sub>4</sub> <sup>2-</sup>
Plasma sanguin	142.0	5.0	1.5	2.5	103.0	27.0	1.0	0.5
SBF1	142.0	5.0	1.5	2.5	147.8	4.2	1.0	0.5
SBF1.5	213.0	7.5	2.3	3.8	221.7	6.3	1.5	0.8

Dans cette partie, les principes de fonctionnement des techniques expérimentales utilisées pour caractériser les revêtements avant et après les tests de bioactivité, (analyse morphologique, analyse structurale, et analyse biochimique) sont décrits d'un point de vue théorique et pratique.

## B) Deuxième partie : caractérisation des revêtements de phosphate de calcium

La deuxième partie porte sur la caractérisation et l'étude des revêtements des Ca-P obtenus par les trois bains (acides, alcalins et oxydant) sur différentes surfaces métalliques. Les dépôts ont été étudiés d'un point de vue structural par DRX et FT-IR, et morphologique par MEB-EDS-X et MET. La stabilité des couches de Ca-P a été mesurée dans le fluide corporel (SBF) pour des périodes différentes utilisant des analyses biochimiques telles que des kits de produits chimiques avec spectrophotomètre ou par plasma à couplage inductif (ICP).

1) Nous avons observé que **la couche intermédiaire de titanate de sodium** présente une structure hétérogène composée d'agglomérats sphériques d'un diamètre de 1 à 2 microns (**Fig. 3(a)**) déposés sur une structure poreuse nanométrique, hautement nano-réticulée et alvéolaire avec une porosité inférieure à 200 nm (**Fig. 3(b)**). Ces pores forment des alvéoles s'apparentant à la structure naturelle d'un os spongieux. Ces alvéoles comprennent des parois relativement fines et plates (**Fig. 3**).

Les trois bains autocatalytiques permettent un dépôt de Ca-P sur la couche intermédiaire de titanate de sodium [Mohammed et al., 2012]. Le traitement chimique et thermique permet la formation d'une couche examinée en microscopie électronique à balayage sous un angle de 50° pour montrer la couche d'une épaisseur d'environ 1.8 µm (**Fig. 3(c)**). Celle-ci contient des ions Na<sup>+</sup> et Ti<sup>4+</sup> ions, et sa composition correspond à couche de titanate de sodium de formule chimique Na<sub>2</sub>Ti<sub>5</sub>O<sub>11</sub>. Ce traitement

permet la nucléation et la croissance d'hydroxyapatite sur le titane prétraité par la solution d'hydroxyde de sodium.

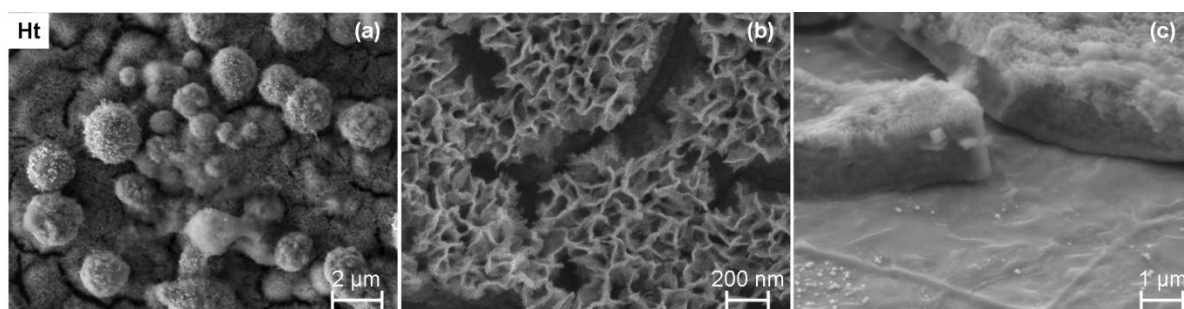


Figure 3. Micrographie MEB de la structure de la couche tampon de titanate de sodium composée d'agglomérats sphériques (a), grossissement de la structure hautement nanoreticulée (b) and épaisseur de la couche de titanate de sodium (c).

L'absence de délaminage de la couche de phosphate de calcium a été observé en microscopie électronique à balayage (*Chapitre 3, Part I*). Particulièrement, il a été observé que le traitement NaOH, suivi par un traitement thermique (1 et 3 h) a permis de former une couche de Ca-P et CaCO<sub>3</sub> compacte après immersion dans l'SBF (**Fig. 4(c,f)**).

De plus, la croissance de Ca-P après 4 jours passés dans le bain SBF1 a été observée seulement pour les échantillons qui avaient subi un traitement thermique de 3 h (**Fig. 4(d,f)**), tandis que la formation de Ca-P est apparue seulement après une immersion supplémentaire dans le bain SBF1.5 pour les échantillons traités thermiquement pendant 1 h (**Fig. 4(b,c)**). Finalement, les résultats suggèrent qu'un recuit du titanate de sodium pendant 3 h (**Fig. 4(a,b,c)**) améliore la croissance d'une couche stable de Ca-P et CaCO<sub>3</sub> comparé à un recuit de 1 h (**Fig. 4(d,e,f)**).

Sur la couche intermédiaire de titane de sodium, les baignades acides (avec PdCl<sub>2</sub> ou AgCl) ont réussi à couvrir l'ensemble du substrat de titane avec une couche de Ca-P (*Chapitre 3, Part II*). Les revêtements obtenus avec les deux catalyseurs sont stables après un trempage dans SBF pendant différentes périodes de temps (**Tableau 1**). On peut conclure que l'état de surface de l'échantillon (TAV<sub>400</sub> vs TAV<sub>4000</sub>) influence la couche formée par le bain acide :

(i) les couches de Ca-P formées ne sont pas stables après SBF pour les échantillons à plus forte rugosité (TAV<sub>400</sub>-1h-AcPd et TAV<sub>400</sub>-3h-AcPd). La détection de minuscules quantités de Ca et P par analyses EDS a confirmé la dégradation des dépôts après immersion dans la solution de SBF;

(ii) L'analyse des substrats TAV<sub>4000</sub> et Ti<sub>4000</sub> prétraités a montré que les couches de Ca-P croissent pendant le procédé autocatalytique (particulièrement dans le cas de Ti<sub>4000</sub>). Ce dépôt formé après 2 h dans le bain acide sur Ti<sub>4000</sub> est de l'OCP. Enfin, après immersion dans le SBF, ces films sont stables.

2) Nous avons pris une nouvelle direction en remplaçant le catalyseur PdCl<sub>2</sub> par l'AgCl dans tous les bains autocatalytiques et nous avons réalisé une comparaison entre les dépôts formés. Après 2 h d'immersion dans le bain acide contenant AgCl, une distribution homogène de Ca-P a été établie par des observations en MEB-EDS-X. Ces particules de Ca-P ont stimulé la formation d'une couche homogène de HA après l'immersion dans le SBF pendant 1 semaine. Ce dépôt a complètement couvert le substrat TAV. L'observation et la quantification de la stabilité de cette bio couche ont été aussi menées.

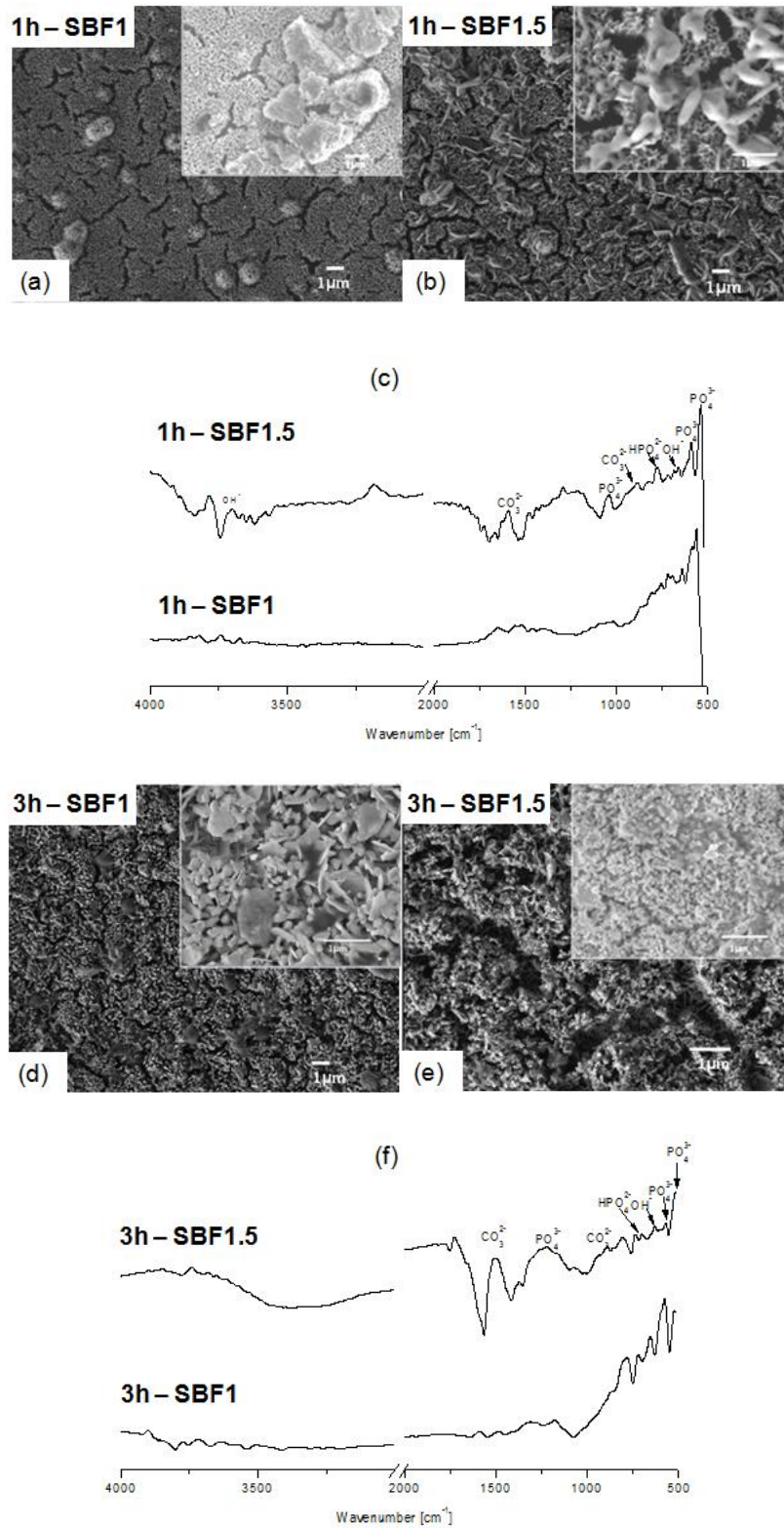


Figure 4. Clichés MEB de couches de phosphate de calcium obtenues par immersion dans le bain SBF1 (a et d) puis dans le bain SBF1.5 (b et c) pour des couches de titanate de sodium obtenues après 1 h ou 3 h de recuit. Les analyses FT-IR associées sont présentées en (c) et (d).

3) Malheureusement, la couche intermédiaire de TiN après le bain acide (utilisant les deux catalyseurs, **Fig. 5**) n'a pas favorisé la promotion de dépôt de Ca-P : le TiN semble même interdire ou peut-être retarder la croissance de Ca-P après deux semaines de trempage dans la solution de SBF.

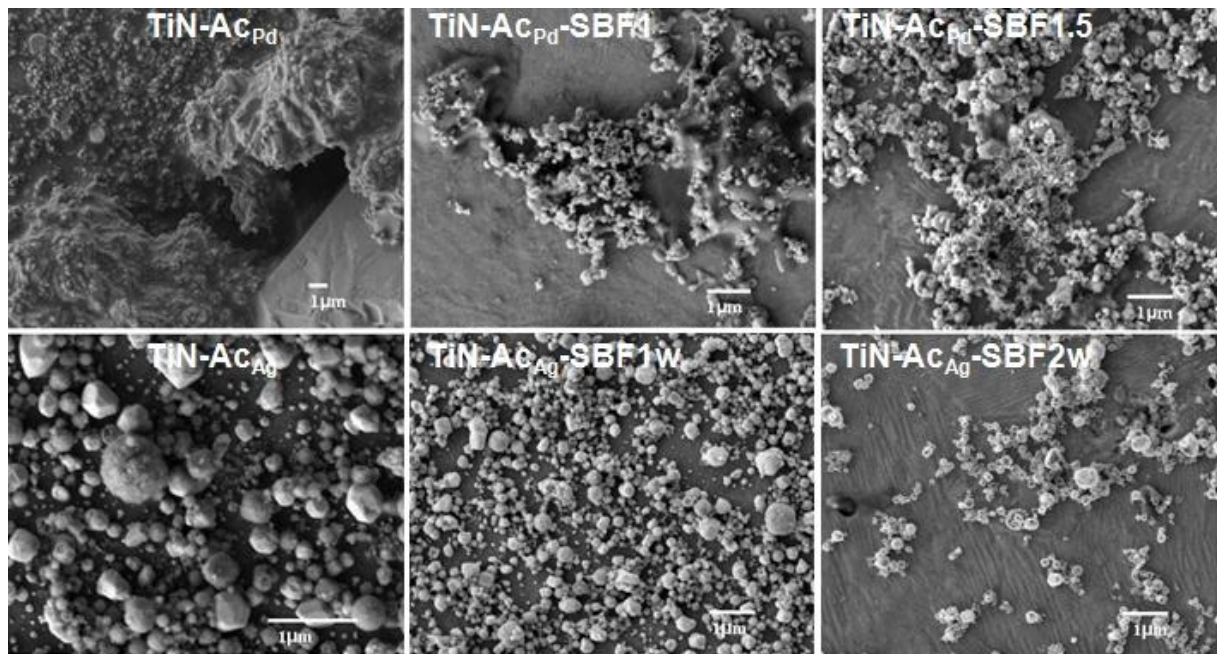


Figure 5. Micrographie MEB de la structure couche intermédiaire de TiN après le bain acide et différentes immersion en SBF.

Au contraire, le *bain alcalin* avec (avec  $\text{PdCl}_2$  ou  $\text{AgCl}$ ) ne recouvre pas uniformément toute la surface. Nous avons noté des dépôts d'agrégats de Ca-P répartis sur la surface. Il semble que ces agrégats accélèrent la formation d'apatite après l'immersion dans le SBF. Plus en détail, nous pouvons constater que la rugosité superficielle et le traitement thermique influencent la formation de la biocouche quand nous avons utilisé le bain alcalin :

(i) la couche de Ca-P formé sur l'échantillon  $\text{TAV}_{400-3\text{h-AcPd}}$ , après 2 h dans le bain alcalin est plus solide que sur l'échantillon  $\text{TAV}_{400-1\text{h-AcPd}}$ . Après 4 et 6 jours dans la solution de SBF, une augmentation de la présence des groupements  $\text{PO}_4^{3-}$  a été montré par FT-IR (*Chapitre 3, Part III*) ; Ceci n'a pas été observé par MEB. Cependant, par analyse d'EDS-X une quantité très faible de Ca et P a été mesurée. Finalement, on peut conclure que le bain alcalin n'a pas conduit à la formation de précipités de Ca-P sur les substrats ayant une très forte rugosité.

(ii) En diminuant la rugosité ( $\text{TAV}_{4000}$  et  $\text{Ti}_{4000}$ , **Fig. 6**), nous avons constaté que la phase brushite commence à se former sur le substrat après 2 h dans le bain alcalin. Celle-ci est transformée en HA après une immersion de 2 semaines dans le SBF. Ce résultat est confirmé en utilisant la FT-IR, la SAED-TEM et l'EDS-X. Ces résultats ont aussi été confirmés par l'analyse biochimique du SBF qui a montré une brusque absorption d'ions  $\text{Ca}^{2+}$  et P (*Chapitre 3, Part III*). En conséquence, le bain alcalin (avec  $\text{PdCl}_2$ ) a permis de déposer une couche de Ca-P.

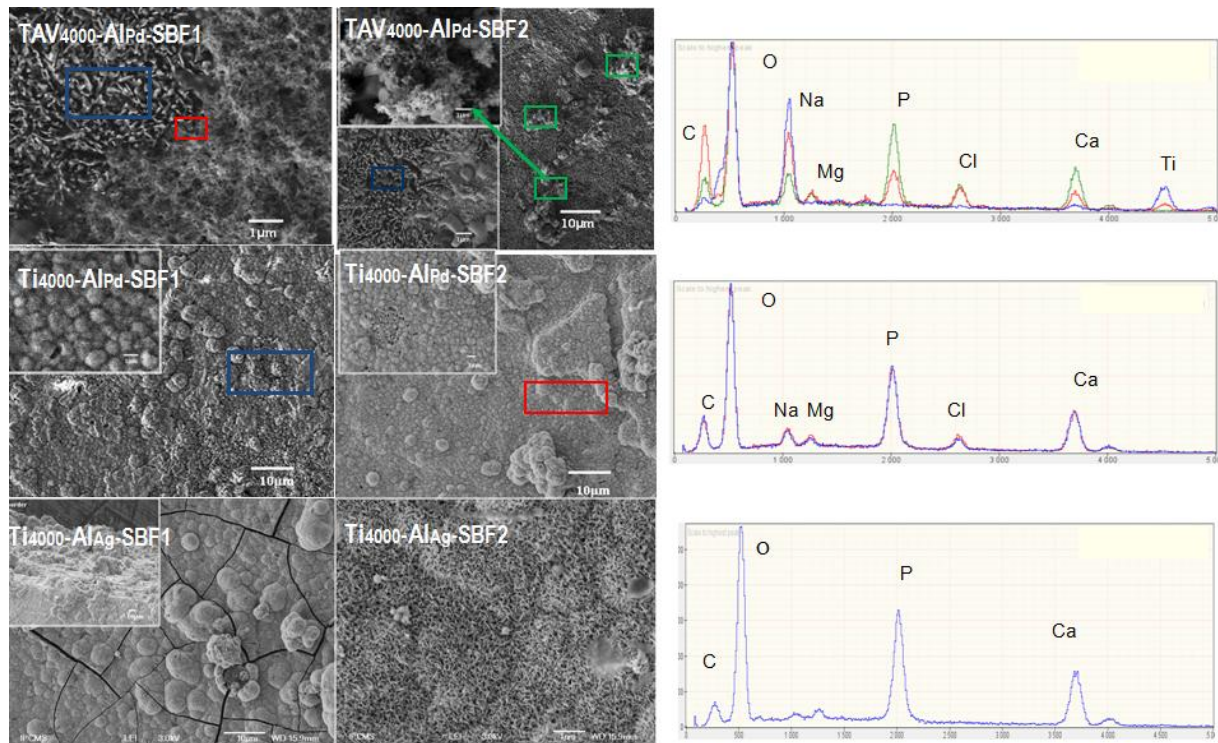


Figure 6. Clichés MEB des couches de phosphate de calcium obtenues dans un bain alcalin (avec  $PdCl_2$  ou  $AgCl$ ) et par immersion dans le bain SBF1 puis SBF1.5 et leurs analyses EDS associées.

En utilisant le bain autocatalytique modifié avec  $AgCl$ , la distribution de Ca-P est homogène après 2 h d'immersion sur les échantillons  $TAV_{4000}$ . En outre, les échantillons de rugosité plus importante ( $TAV_{400}$ ) sont recouverts par une couche épaisse et homogène d'HA après immersion dans le SBF pendant 1 semaine.

- Le dépôt d'agglomérats de Ca-P après les bains alcalins et pour les deux catalyseurs est facilité par la présence de la couche intermédiaire de TiN. La quantité d'agglomérats a augmenté dans le cas du  $PdCl_2$ , après 4 jours dans SBF1 suivi par 2 autres jours dans SBF1.5 ; tandis qu'avec  $AgCl$ , les précipitations formées sont superficielles et se dissolvent après 1 semaine dans le SBF. Finalement, pendant la deuxième semaine de séjour dans le SBF, la couche de Ca-P commence à se reconstruire.

Le troisième et dernier bain, le *bain oxydant*, permet la formation d'une couche de Ca-P; mais cette couche est un revêtement superficiel (pas de liaisons chimiques). Il est complètement dissous après une semaine dans le SBF (*Chapitre, Part IV, Fig. 7*). Nous vérifions l'effet du bain oxydant sur le titanate de sodium avec un traitement thermique à une température de  $630^\circ C$  et une rampe de température de  $3^\circ C/minute$  ou  $10^\circ C/minute$ . Nous observons que :

(i) pour une très haute rugosité ( $TAV_{400}$ ), la surface recouverte par le Ca-P est plus importante pour la rampe de  $10^\circ C/minute$ , tandis qu'après le trempage dans le SBF, le dépôt se dissout ;

(ii) pour les substrats  $TAV_{4000}$  ou  $Ti_{4000}$ , ce bain permet de recouvrir la surface du substrat de Ca-P mais par des plaquettes « superficielles », qui sont facilement dissoutes après 1 semaine dans le SBF. Les mêmes résultats ont été obtenus en utilisant le catalyseur  $AgCl$ .

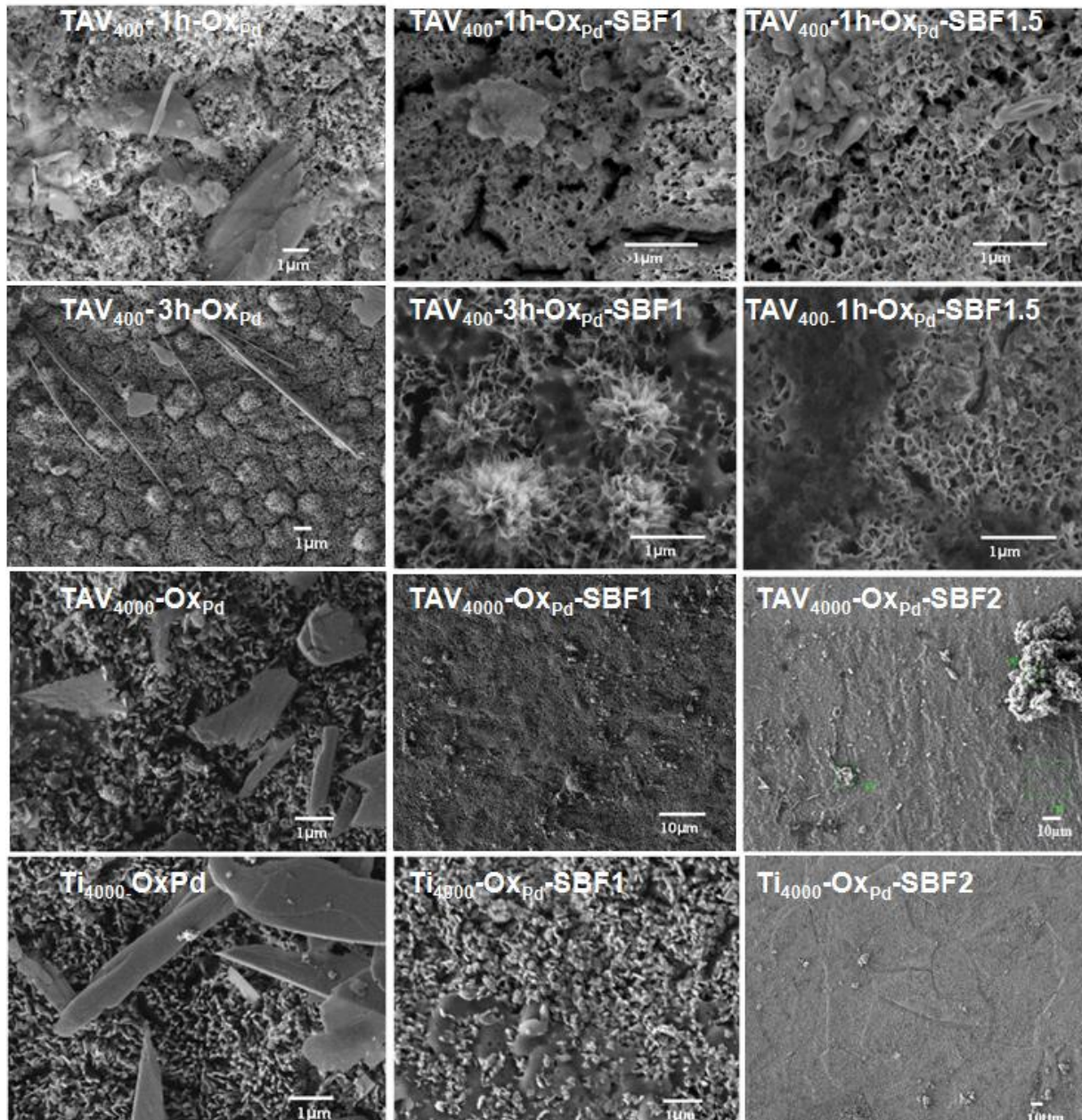


Figure 7. Micrographie MEB des dépôts obtenus par un bain oxydant (avec PdCl<sub>2</sub> ou AgCl) et après immersion dans SBF1 puis dans SBF1.5 et leurs analyses EDS associées.

En conclusion de cette thèse, cette voie d'élaboration de couches de phosphate de calcium a pour but de fournir un nouveau matériau améliorant la compatibilité des métaux ou des alliages avec l'os et de faciliter la préparation de matériaux d'implants nécessitant une bonne compatibilité avec l'os. De plus, cette méthode est une solution peu coûteuse, fiable, et utilisable à l'échelle industrielle. La couche de phosphate de calcium aussi bien que le titanate de sodium obtenus dans cette étude peuvent permettre d'être imprégnés par des agents actifs comme un ou plusieurs agents antibactériens (par exemple les ions argent Ag<sup>+</sup> [Chen et al., 2006], le Furanone [Baveja et al., 2004] contre le *Staphylococcus epidermidis* et le *Staphylococcus aureus* et/ou une ou plusieurs hormones de croissance (TGF-β1) et l'hormone parathyroïde (PTH) et la prostaglandine E2 (PGE2) [Anselme, 2000].

### References

- Anselme, K. (2000): Osteoblast adhesion on biomaterials, *Biomaterials* **21**(7): 667-681.
- Baveja, J.K.; Willcox, M.D.; Hume, E.B.; Kumar, N.; Odell, R. & Poole-Warren, L.A. (2004): Furanones as potential antibacterial coatings on biomaterials, *Biomaterials* **25** (20): 5003-5012.
- Chen, W.; Liu, Y.; Courtney, H.S.; Bettenga, M.; Agrawal, C.M.; Bumgardner, J.D. & Ong, J.L. (2006): In vitro antibacterial and biological properties of magnetron co-sputtered silver-containing hydroxyapatite coating, *Biomaterials* **27**(32): 5512-5517.
- Cotell, C.M. (1993): Pulsed laser deposition and processing of biocompatible hydroxylapatite thin films, *Applied Surface Science* **69**: 140-148
- De Groot, K.; Geesink, R.; Klein, C.P. & Serekian, P. (1987): Plasma sprayed coatings of hydroxylapatite. *Journal Biomedical Material Research* **21**(12):1375-81.
- Jing, Z.; Wang, C.; Wang, G.; Li, W. & Lu, D. (2010): Preparation and antibacterial activities of undoped and palladium doped titania nanoparticles. *Journal Sol-Gel Science Technology* **56**:121-127.
- Kim, H. M.; Miyaji, F.; Kokubo, T. & Nakamura, T. (1997a): Effect of heat treatment on apatite-forming ability of Ti metal induced by alkali treatment. *J. Material Science Material in Medicine* **8**: 341-347.
- Kokubo, T.; Kim, H. M. & Kawashita, M. (2003): Novel bioactive materials with different mechanical properties. *Biomaterials* **24**: 2161–85.
- Kokubo, T. & Takadama, H. (2006): How useful is SBF in predicting in vivo bone bioactivity? *Biomaterials* **27** (15): 2907-2915.
- Leonor, I.B. & Reis, R.L. (2003): An innovative autocatalytic deposition route to produce calcium-phosphate coatings on polymeric biomaterials. *Journal of Materials Science: Materials in Medicine* **14**: 435-441.
- Mohammed, H. I.; Abdel-Fattah, W. I.; El-Sayed, M.; Talaat, M. S.; Sallam, A. S. M.; Faerber, J.; Pourroy, G.; Roland, T. & Carradò, A. (2012): Influence of heat treatment on Ti6Al4V for biomimetic biolayer. *Bioinspired, Biomimetic and Nanobiomaterials* **1**(3), 173–182.
- Pelletier, H.; Carradò, A.; Faerber, J. & Mihailescu, I.N. (2011): Microstructure and mechanical characteristics of hydroxyapatite coatings on Ti/TiN/Si substrates synthesized by pulsed laser deposition. *Applied Physics A* **102**(3): 629-640.
- Rosu, R.A.; Serban, V.A.; Bucur, A.L. & Dragos, U. (2012): Deposition of titanium nitride and hydroxyapatite-based biocompatible composite by reactive plasma spraying. *Applied Surface Science* **258**: 3871– 3876.
- Surowska, B. & Bienias, J. (2010): Composite layers on titanium and Ti6Al4V alloy for medical applications. *J Achiev Mater. Manuf. Eng.* **43** (1), 162–169.
- Symietz, C.; Lehmann, E.; Gildenhaar, R.; Krüger, J; Berger, G. (2010): Femtosecond laser induced fixation of calcium alkali phosphate ceramics on titanium alloy bone implant material. *Acta Biomaterialia* **6** (8): 3318–3324.

# General Introduction

The prosthesis and the artificial implants were developed to preserve integrity and the comfort of human being suffering from strong functional deficiencies. The objective of their development is to allow the manufacturing of devices for bodily assistance able to compensate the functions of the offended structures. The metallic artificial implants are widely used as substitution of hard fabrics. Nevertheless, the essential requirement for any artificial implanted materials, especially metallic ones, is to demonstrate not only their biocompatibility but also their bioactivity with the host.

Since 1960, calcium phosphates (Ca-P) and especially the *hydroxyapatite* (HA) are strongly used in bone surgeries. Nevertheless, the mechanical characteristics of the ceramics, such as HA, are not excellent. Most of the orthopaedic implants are metallic. So *titanium* (Ti) and its *alloys* are suitable metallic implants, widely used as orthopaedic or dental implants due to their superior mechanical properties and excellent biocompatibility [Liu et al., 2004]. Nevertheless, the metallic materials can be bioinert or biocompatible and different kinds of surface treatments were necessary to improve their bioactivity. However, their bioactivities are not as good as those of calcium phosphate ceramics and during implantation they can only form osteointegration at the interface of titanium and bone tissue, instead of bone bonding.

One of the common titanium alloys used in medicine is Ti-6Al-4V for its suitable mechanical properties, its corrosion and wear resistance, mechanical stress and its relative inertia concerning living tissues. Despite that, there are some reservations: first the release of Al and V ions under certain conditions may accumulate inside the tissues [Surowska and Bienias, 2010], second their slowly integration of Ti or Ti-6Al-4V with the surrounding bone tissue without achievement of long-term stability [Symietz et al., 2010].

To maintain the high mechanical characteristics of metallic materials in addition to achieve fast and long term bioactive surfaces, implant surfaces should be coated with a developed calcium phosphate for its superior biocompatibility and bioactive acting as a barrier against ion release [Rosu et al., 2012].

The osteoconductive coatings on metallic prostheses appeared in the late 80's. In particular, the HA coating - on the metallic surface- obtained by "plasma spray" was studied by Groot [De Groot et al., 1987] and allowed to improve the biological behaviour of the metallic surface. Several physical and chemical methods were reported in many literatures to modify titanium implants surfaces such as the plasma spray, magnetron sputtering, the dip-coating, the sol-gel, the soaking, the electrophoresis, the pulsed laser deposition (PLD), and the biomimetic method. Among these coating methods, the PLD is used for depositing calcium phosphate films since 90's. Its main advantage is the well-controlled stoichiometry of the target in the coating. On the other hand, the drawback of this technique is the difficulty obtaining deposits on complex surfaces.

Calcium phosphate films have been obtained by biomimetic method. This latter is a physicochemical method in which a substrate is soaked in a solution that simulates the physiologic conditions, such as simulated body fluid (SBF), for periods of time enough to form a layer of calcium phosphate on the substrate [Kokubo et al., 2003; Kim et al., 1997].

In the present work, a coating method is presented as an alternative to the Plasma Spraying one. Our approach differs from the classical methods for coating HA on metal substrate. Indeed, the calcium phosphate layer is produced by autocatalytic baths using different palladium chloride (PdCl<sub>2</sub>) or silver chloride (AgCl) as catalysts. This new deposition route is based on a redox reaction.

Our approach was to develop a new chemical synthesis way. After a mechanical polishing and chemical treatment (e.g. using Kroll reagent) on the titanium or Ti-6Al-4V substrate, two different kinds of interlayer were obtained (**Fig. 8**). With the first method, an intermediate layer of sodium titanate was built up by alkaline pretreatment on the Ti or Ti-6Al-4V substrate and then thermally treated in order to obtain a nanometric network layer. It allows forming a calcium phosphate layer on the metallic implant by the autocatalytic method in a way similar to the process of natural bone formation [Mohammed et al., 2012a]. The second method consists of coating a titanium nitride buffer layer (TiN, physically prepared by PLD) having good tribological properties [Pelletier et al., 2011].

The first solution was widely studied, whereas the second was realized at the end of the thesis and the presented results are preliminary.

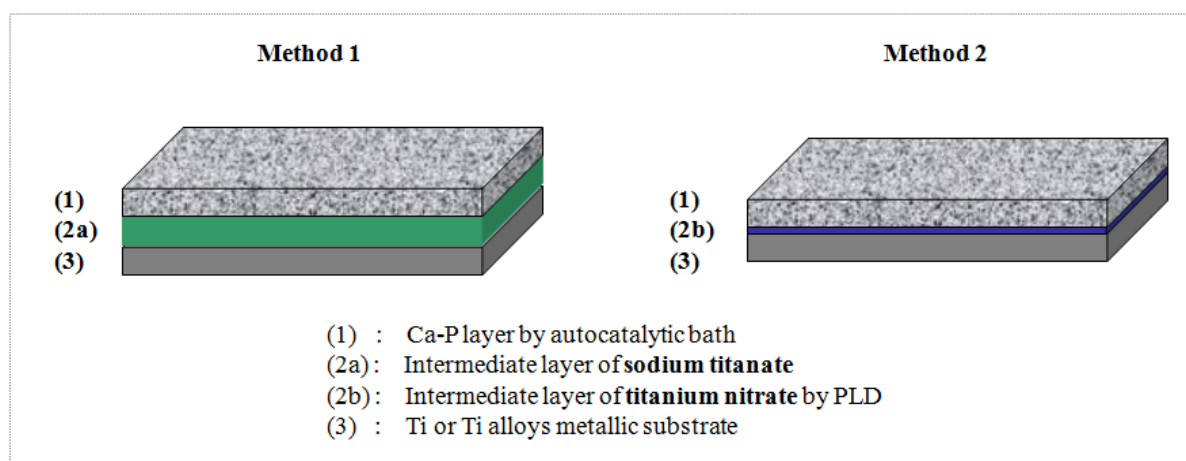


Figure 8. Sketch of employed methods in the present work.

The present work is organized in three parts.

It starts with a general introduction - that allows understanding our approach, the state of the art in this domain, as well as a description of the ceramic material – especially the calcium phosphate groups -, the metallic biomaterials, in particular the titanium and its alloys are introduced. Afterwards, several methods of surface modifications to enhance the long-term usage of metallic implant are presented. At last, the biomimetic and autocatalytic processes are described to obtain a calcium phosphate coating on titanium alloys.

Then the investigations are divided into two parts

**The first one** shows the experimental procedures for the preparation of the Ti or Ti-6Al-4V substrates, coated by an intermediate layer (**Fig. 8**), using three autocatalytic baths: oxidant, acidic and alkaline. The baths' temperatures were between 60 and 80°C, with a pH 5.3 for the acidic, 7 for the oxidant and 9.2 for the alkaline baths. These baths depend mainly on the redox reaction where the palladium chloride (PdCl<sub>2</sub>) or the silver chloride (AgCl) have been employed as catalysts. The latter is also an antibacterial agent [Jing et al., 2010; Rastogi et al, 2011].

These three baths previously studied by Leonor and Reis (2003) and Oliveira et al. (2005) for polymers, were adapted in our case and improved to be used on metallic alloys or metals. We realized for the first time this method on metallic substrates, Ti or Ti-6Al-4V. Moreover, details about different experimental techniques used for characterization of coatings before and after bioactivity

tests (structural analysis, morphological analysis and biochemical analysis) are introduced from a theoretical point of view.

**The second part** illustrates the characterisation and the study of the Ca-P coating obtained after pretreatment steps (alkaline and heat treatment) followed by the acidic, alkaline and oxidant baths on different substrates. The coatings were studied structurally by X-ray diffraction (XRD) and Fourier Transform Infrared (FT-IR) and morphologically by using a Scanning Electron Microscope with an Energy Dispersive X-Ray Spectrometer (SEM-EDS-X) and Transmission Electron Microscope (TEM). The stability of Ca-P layers was tested in a Simulated Body Fluid (SBF) for different periods using the biochemical analysis such as chemical kits with spectrophotometer or by inductively coupled plasma (ICP).

**Finally**, conclusions obtained from the results achieved, in this work, are given as well as recommendations for future research. The future research includes expanding the current study to investigate the effect of chemical baths on other metallic substrates.

# **Chapter 1**

## **State of the art**

## 1. Biomaterials

Bone defects that occur due to accidents, diseases, trauma or abnormal development require a skeletal reconstruction, which requires grafts of natural or synthetic materials to replace lost bone or to enhance new bone formation. The autologous bone graft is the best option available for bone reconstruction. However, the small size and limited number of donor sites, beside the cost of double surgery and pain involved, limit the extensive use of auto-grafts. Alternatives like allografts and xenografts carry risks of an immune rejection, a bacterial contamination and transmittable diseases [John et al., 2002]. A development in the field of biomaterials is, therefore, necessary. Subsequently, diseased or damaged tissue of the human body can be replaced by a variety of materials such as metals, polymers or ceramics depending on the mechanical, chemical and biological properties of the tissue to be substituted [Zollfrank et al., 2005]. The National Institutes of Health Consensus Development Conference (USA) defines a Biomaterial as-any substance (other than drugs) or combination of substances, synthetic or natural in origin, which can be used for any period of time, as a whole or as a part of a system which treats, augments or replaces any tissue, organ, or function of the body [Clinical Applications of Biomaterials, 1982; Boretos and Eden, 1984].

Biomaterials can be broadly categorized under the four divisions: metals, polymers, ceramics, and composites. Each material has its own advantages and disadvantages as shown in **Table 1**.

*Table 1. Biomaterials classes with their advantages and disadvantages [Sáenz et al.,1999]*

Materials	Advantages	Disadvantages	Examples
Metals	High strength; fatigue resistance; wear resistance; simple to fabricate	High modulus; corrosion; metal ion toxicity (e.g., Al, V, Cr, Ni...)	Stainless steel; Co–Cr alloys; Ti and its alloys
Ceramics	Bioactive materials; sometimes biodegradable or inert	Low strength in tension, low fracture toughness	Calcium phosphates; Zirconia; Alumina
Polymers	Easy to make; tailorable properties; surface modification ; immobilize cells ; biodegradable	Water and proteins absorption; surface contamination; wear and breakdown	Nylon; silicone; rubber; polyester; chitosan; silk fibroin

Every year a large numbers of orthopaedic and dental implant devices are being placed surgically. Metallic biomaterials, which are one of the largest groups of biomaterials, have been used almost exclusively for load-bearing implants, such as hip and knee prostheses and fracture fixation wires, pins, screws, and plates. The stainless steel (e.g. 316L), the cobalt-chromium molybdenum alloy, the pure titanium and titanium alloys dominate the biomedical metals material. Especially the titanium and its alloys due to their low density, good mechanical properties, are successfully used for various implants and medical devices. Beside their good mechanical properties, titanium biocompatibility is due to the presence of the surface oxide film which grows spontaneously on the surface upon exposure to air. The chemical stability and structure of the titanium oxide film allows a chemical inertness, corrosion resistance and repassivation ability. In general, there are several reasons hindering long-term stability of the metallic implant with surrounding bone tissue:

- 1) The biological inactivity (inertness) which causes a lackness of the structural biofunctions as the bone-conductivity which leads to integrate slowly with surrounding bone tissue;

2) The corrosion of metallic implants can adversely affect the biocompatibility and mechanical properties. As a basis, the used metallic implant must not cause any adverse biological reaction in the body and, simultaneously, they have to be stable;

3) The stress shielding<sup>1</sup> exists in load-bearing implants. This stress results from the metal which is much stiffer compared to the bone. The implanted (e.g. titanium) metal in the human body can carry a disproportional amount of load to the surrounding bone is stress-shielded leading to a resorption of the bone and consequently the uncoupling of the implants.

A parameter that plays a major role in both the quality and rate of osteointegration of metallic implants is the surface roughness. Highly roughened implants between 1-10 µm have been shown to favour the mechanical anchorage and the primary fixation to the bone [Junker et al., 2009; Shalabi et al., 2006]. At the same time, the topographies in the nanometre range are preferred to promote protein adsorption, osteoblastic cell adhesion and the rate of bone tissue healing in the peri-implant region.

Biomaterials have special needs in order to convene the biocompatibility and the bioactivity criteria. Recently, many studies were carried out about the development of composite coatings to achieve bioactivity and improve long-term interface strength, by combining the high mechanical characteristics of the metallic materials, used in order to manufacture implants (strength, hardness) with the high bioactivity properties of the ceramic materials, especially based on calcium phosphate(s), due to their structural similarity to the human bone.

### ***1.1. Biocompatibility and bioactivity***

The most widely used definition of *biocompatibility* comes from the "Consensus Conference on Definitions in Biomaterials". Biocompatibility is the ability of a material to perform with an appropriate host response in a specific application" [Williams, 1987]. There are several tests to observe the normal foreign body reaction. The implant is considered "biocompatible" if approximately after one month of operation the implant walled off in a tough, thin, vascular capsule, and the reaction site become quiescent.

As early as 1971 Hench defined *bioactivity* as a material characteristic that "allows it to form a bond with a living tissue". In 2002, the definition was changed to "the ability of a material to stimulate healing response and trick the cellular system into responding as if it were a natural tissue". By this, the implant will not only replace living tissue or organs not functioning correctly, but also will repair and assist the bone growth over the implant as well. Briefly, bioactivity is an osteointegration induction.

The body tissues respond differently depending on the type of foreign material as given in **Table 2**.

*Table 2. Types of tissue response to different foreign materials [Hench and Best, 2004].*

Type of foreign material	Tissue response
Toxic	Surrounding tissue dies
Non-toxic/ biologically inactive	Fibrous tissue of variable thickness develops
Non-toxic/ biologically active	Interfacial bond forms
Non-toxic/ resorbable	Surrounding developed tissue replaces material

---

<sup>1</sup> Stress shielding refers to the reduction in bone density as a result of normal stress from the bone by an implant.

Nowadays, the restoration materials can be relatively *bioinert* (i.e. titanium and its alloys), *bioactive* (i.e. bioglass, hydroxyapatite – HA) or *resorbable* (i.e. tricalcium phosphate – TCP) according to the respective tissue response.

The priority of a material for usage as an implant depends on its properties which should satisfy the needs suitable for the site of implantation.

### 1.2. Metallic biomaterials

Metallic biomaterials are used as internal fixation, as old as early 1900s, due to their excellent, mechanical properties and corrosion resistance. The type of metals used in biomedical surgeries depends on specific implant applications. Metals and alloys are used as substitutes for hard tissue replacement such as hip joint replacement and knee joints; for fracture healing aids as bone plates and screws, spinal fixation devices and dental implants.

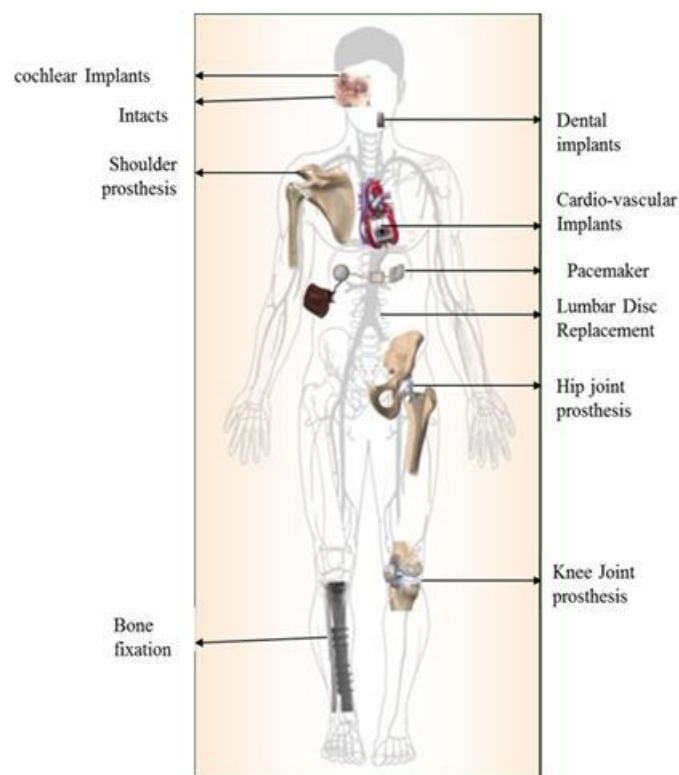


Figure 9. Several metallic implants sites [Manivasagam et al., 2010].

Specific metallic alloys are used for some devices such as vascular stents, catheter guide wires, orthodontic arch wires and cochlear implants, as shown in **Fig. 9**. Further, stainless steels, cobalt (Co) alloys, titanium (Ti) and its alloys, as shown in **Table 3**, are mainly used in the fabrication of metallic biomaterials and artificial implants subjected to loads, since they possess great mechanical properties, suitable for load-bearing applications [Niinomi, 2008].

Alloys were fabricated to modify and design new needed functions compared to the pure basic materials. The most popular and initially used alloy as biomaterials was cobalt-chrome (Co–Cr) and cobalt-chrome-molybdenum (Co–Cr–Mo), for implants which required high wear resistance such as artificial joints. However, when implanted into the body, as the metal-on-metal joint, the release of metallic ions due to corrosion has an adverse effect on the surrounding body tissue and eventually leads to failure of the implant.

Table 3. Some characteristics of several metallic implant materials [Long and Rack, 1998].

	Stainless steel	Cobalt–base alloys	Ti and Ti–base alloys
Designation	ASTM F-138 (" 316L DVM")	ASTM F-75; ASTM F-799; ASTM F-1537 (Cast and wrought)	ASTM F-67 (ISO5832/II); ASTM F-136(ISO5832/II); ASTM F-1295 (Cast and wrought)
Principal alloying elements (wt %)	Fe (bal.), Cr (17-20), Ni(12-14), Mo(2-4)	Co(bal.), Cr (19-30), Mo(0-10), Ni(0-37)	Ti(bal.), Al(6), V (4), Nb (7)
Advantages	Cost; availability processing	Wear resistance; corrosion resistance; fatigue strength	Biocompatibility; corrosion resistance; Fatigue strength
Disadvantages	Long term behaviour; high modulus	High modulus; biocompatibility	Power wear resistance; low shear strength
Primary utilizations	Temporary devices (fracture plates, screw, hip nails)	Dentistry castings; prostheses stems; load-bearing components	Long-term; permanent devices (nails, pacemakers)
Elastic modulus (GPa)	190	210-253	Ti: 110 Ti-6Al-4V: 116
Yield strength (GPa)	221-1213	448-1606	Ti: 485 Ti-6Al-4V: 896-1034
Tensile strength (MPa)	586-1351	655-1896	Ti: 760 Ti-6Al-4V: 965-1103
Fatigue limit (MPa)	241-820	207-950	Ti: 300 Ti-6Al-4V: 620

### 1.2.1. Titanium and its alloys

Titanium is one of the transition elements in group IV and period 4 of Mendeleev's periodic table. It has an atomic number of 22 and an atomic weight of 47.9 u. Being a transition element, Ti has an incompletely filled d shell in its electronic structure [Ogden, 1961]. This enables it to form solid solutions with most substitutional elements having a size factor within  $\pm 20\%$ . In the elemental form, Ti has a high melting point (1668°C) and possesses a hexagonal close packed crystal structure  $\alpha$  (hcp) up to a temperature of 882.5°C. Ti transforms into a body centred cubic structure  $\beta$  (bcc) above this temperature [Collings, 1984].

Titanium can be alloyed with various elements to improve its mechanical properties, such as strength, high temperature performance, creep resistance, ability, response to ageing heat treatments, and formability. Such alloying includes titanium-nickel (Ti-Ni), titanium-aluminium (Ti-Al), titanium-niobium (Ti-Nb), titanium-aluminium-niobium (Ti-6Al-7Nb) alloys and titanium-aluminium-vanadium alloys (Ti-6Al-4V) (Table 4).

Titanium alloys are classified into  $\alpha$ , near-  $\alpha$ ,  $\alpha + \beta$ , metastable  $\beta$ , or stable  $\beta$  depending on their room temperature microstructure [Polmear, 1981]. In this regard, alloying elements for titanium fall into three categories:

- $\alpha$  -stabilizers (Al, O, N, C);
- $\beta$  -stabilizers (Mo, V, Nb, Ta (isomorphous); Fe, W, Cr, Si, Co, Mn, H eutectoid);
- Neutrals (Zr).

The  $\alpha$  and near-  $\alpha$  titanium alloys exhibit superior corrosion resistance but have limited low temperature strength. In contrast, the  $\alpha + \beta$  alloys exhibit higher strength due to the presence of both the  $\alpha$  and  $\beta$  phases. The properties of the materials depend on their composition, the relative proportions of  $\alpha$  and  $\beta$  phases, the thermal treatment, and the thermo-mechanical processing conditions. The  $\beta$  alloys also offer the unique characteristic of a low elastic modulus and a superior corrosion resistance [Bania, 1993].

Ti alloys have the best biocompatibility compared to other metals, therefore, the research and development of Ti biomaterials is being pursued energetically in the field of metallic biomaterials. In **Table 4**, four grades of pure titanium (from Ti CP-1 to Ti CP-4) are presented: they are differentiated on the basis of the amount of impurities present such as oxygen (O), nitrogen (N) and iron (Fe). The amount of O in particular affects their ductility and the strength. Among the titanium alloys, Ti-6Al-4V, whose chemical composition is given in **Table 5**, is the most widely used for implant applications.

*Table 4. Chemical composition of different grades of Ti and its alloy (ASTM, F67-89, 1992; ASTM, F136-84, 1992).*

Elements	Ti CP-4 Grade 1 (wt %)	Ti CP-3 Grade 2 (wt %)	Ti CP-2 Grade 3 (wt %)	Ti CP-1 Grade 4 (wt %)	Ti-6Al-4V (wt %)
N	0.05	0.05	0.03	0.05	0.05
C	0.10	0.10	0.10	0.10	0.08
H	0.015	0.015	0.015	0.015	0.012
Fe	0.50	0.30	0.30	0.50	0.25
O	0.40	0.35	0.25	0.40	0.13
Al	–	–	–	–	5.50-6.50
V	–	–	–	–	3.50-4.50
Ti	Balance	Balance	Balance	Balance	Balance

*Table 5. Titanium and its alloys for biomedical applications registered in according to international Standards ASTM, ISO, or JIS.*

Titanium and its alloys	ASTM standard	ISO standard	JIS standard	Type of alloy
Ti CP-1	ASTM F 67	ISO 5832-2	JIS T 7401-1	$\alpha$
Ti CP-2	ASTM F 67	ISO 5832-2	JIS T 7401-1	$\alpha$
Ti CP-3	ASTM F 67	ISO 5832-2	JIS T 7401-1	$\alpha$
Ti CP-4	ASTM F 67	ISO 5832-2	JIS T 7401-1	$\alpha$
Ti-6Al-4V ELI	ASTM F 136	ISO 5832-3	-	$\alpha + \beta$
Ti-6Al-4V	ASTM F 1472	ISO 5832-3	JIS T 7401-2	$\alpha + \beta$
Ti-3Al-2.5V	ASTM F-2146	–	–	$\alpha + \beta$
Ti-5Al-2.5Fe	–	ISO 5832-10	–	$\alpha + \beta$
Ti-6Al-7Nb	ASTM F 1295	ISO 5832-11	JIS T 7401-3	$\alpha + \beta$
Ti-6Al-2Nb-1Ta	–	–	JIS T 7401-4	$\alpha + \beta$
Ti-15Zr-4Nb-2Ta-0.2Pd	–	–	JIS T 7401-5	$\alpha + \beta$
Ti-13Nb-13Zr	ASTM F 1713	–	–	$\beta$
Ti-12Mo-6Zr-2Fe	ASTM F 1813	–	–	$\beta$
Ti-15Mo	ASTM F 2066	–	–	$\beta$
Ti-15Mo-5Zr-3Al	–	-	JIS T7401-6	$\beta$

The use of titanium as an implant material dates back to the 1930s. It is primarily due to its lightness and good mechano-chemical properties. Afterward, new titanium alloy compositions, specifically tailored for biomedical applications, are developed. These first generations of orthopaedic alloys – including Ti-6Al-7Nb and Ti-5Al-2.5Fe with properties similar to Ti-6Al-4V – were developed to avoid the use of the alloying element vanadium (V) with its potential cytotoxicity and negative reaction with body tissues. Further, the biocompatibility enhancement and lower modulus have been achieved through the introduction of second generation titanium orthopaedic alloys including Ti-12Mo-6Zr-2Fe (TMZF), Ti-15Mo-5Zr-3Al, Ti-15Mo-3Nb-3O (21SRx), Ti-15Zr-4Nb-2Ta-0.2Pd

and Ti–15Sn–4Nb–2Ta–0.2Pd alloys, as well as the ‘completely biocompatible’ Ti-13Nb-13Zr alloy (**Table 6**). Finally, minimum elastic moduli have been achieved by ‘TNTZ’ alloys based on the Ti-Nb-Ta-Zr system, specifically by the development of the ‘biocompatible’ Ti-35Nb-5Ta-7Zr alloy [Long and Rack, 1998].

The mechanical properties of Ti and its alloys are summarized in **Table 6** [Long and Rack, 1998]. The strength levels for orthopaedic alloys are generally acceptable with adequate ductility, as defined by either the percent elongation or the percent reduction of area in a standard tensile test, being retained at room temperature. However, the elastic modulus of bone and the Ti are 10–40 GPa and 110 GPa, respectively. Since the Ti is much stiffer than bone [Geesink and Manly, 1993], the implant of solid Ti, therefore, can carry a disproportionate amount of load. This mechanical mismatch between the implant and the surrounding bone often leads to an inhomogeneous stress transfer [Dujovne et al., 1993; Engh and Bobyn, 1988]. The surrounding bone is then stress-shielded and experiences abnormally low levels of stress, which can lead to resorption of bone and in consequent the detaching of the implants [Lenthe et al., 1997; Wan et al., 1999].

*Table 6. Mechanical properties of Ti and its alloys [Long and Rack, 1998].*

Alloy designation	Microstructure	Elastic Modulus E (GPa)	Yield strength YS (MPa)	Ultimate strength UTS (MPa)
CP Ti	A	105	692	785
Ti-6Al-4V	$\alpha/\beta$	110	850-900	960-970
Ti-6Al-7Nb	$\alpha/\beta$	105	921	1024
Ti-5Al-2.5Fe	$\alpha/\beta$	110	914	1033
Ti-12Mo-6Zr-2Fe (TMZF)	Metastable $\beta$	74-85	1000-1060	1060-1100
Ti-15Mo-5Zr-3Al	Metastable $\beta$	82	771	812
Ti-Zr	Cast $\alpha/\beta$	N/A	N/A	900
Ti-13Nb-13Zr	$\alpha/\beta$	79	900	1030
Ti-35Nb-5Ta-7Zr (TNZT)	Metastable $\beta$	55	530	590
Ti-35Nb-5Ta-7Zr-0.4O (TNZTO)	Metastable $\beta$	66	976	1010
Bone	Viscoelastic composite	10-40	---	90-140

### **1.2.2. Medical application of Ti and its alloys**

Titanium and its alloys are generally regarded to have good biocompatibility but they are relatively inert. Titanium readily adsorbs proteins from biological fluids and its surface can also support cell growth and differentiation. After the materials are implanted into a human body, neutrophils and macrophages are first noted on the implants, followed by the formation of foreign body giant cells from activated macrophages. It is generally accepted that osteoprogenitor cells migrate to the implant site and differentiate into osteoblasts that make bone. After the materials have been implanted into the body, the first stage in the reaction (after interaction with water and ions) is non-specific protein adsorption. Afterwards, neutrophils and macrophages interrogate the implant. The macrophage interaction and cytokines released by the macrophages are believed to attract fibroblasts and drive the foreign body encapsulation process. In order to make titanium bond biologically to bones, surface modification methods have been proposed to improve the bone conductivity or bioactivity of titanium [Liu et al., 2004].

The reason for the use of titanium and its alloys as biomaterial stems from their lower modulus, their superior biocompatibility and their better corrosion resistance when compared to the more conventional stainless and cobalt-based alloys. These attractive properties are the driving force for the early introduction of  $\alpha$  (CP Ti) and  $\alpha + \beta$  (Ti-6Al-4V) alloys as well as the more recent development

of modern Ti-based alloys and orthopaedic metastable  $\beta$  titanium alloys [Long and Rack, 1998]. The applications of titanium and its alloys can be classified according to their biomedical functionalities.

### *1.2.3. Bone and joint replacements*

About one million patients worldwide are treated annually for total replacement of arthritic hips and knee joints. The prostheses come in many shapes and sizes. Due to its desirable properties, Ti and its alloys are widely used as hard tissue replacements in pins, bone plates, expandable rib cages, spinal fusion cages and finger or toe replacements.

One of the most common applications is artificial hip joints that consist of an articulating bearing (femoral head and cup) and stem. The articulating bearings must be positioned in such a way that they can reproduce the natural movement inside the hip joints whereas secure positioning of the femoral head in relation to the other components of the joint is achieved using the stem. The hip stem is anchored permanently to the intramedullary canal of the femur. The cup, which is the articulating partner of the femoral head, several designs, including cement less joints, use roughened bioactive surfaces (including hydroxyapatite) to stimulate osteointegration, limit resorption and thus increase the implant lifetime for especially younger recipients.

Ti and its alloys are also often used in knee joint replacements, which consist of a femoral component, tibial component, and patella [Xuanyong et al., 2004]. They are applied for shoulder and elbow joints and to protect the vertebrae following complicated and invasive back surgeries.

### *1.2.4. Dental implants*

Ti and its alloys are common in dental implants, due to its ability to fuse together with living bone tissue. This property makes it a huge benefit in the world of dentistry. Titanium dental implants have become the most widely accepted and successfully used type of implant due to its propensity to osteointegrate.

Most of the dental implants are placed according to the "osteointegration" concept that allows dental implants to fuse with bones. Surface modification technologies, such as grit blast, chemical etching, and plasma spraying are often utilised to improve the osteointegration ability of titanium dental implants [Xuanyong et al., 2004].

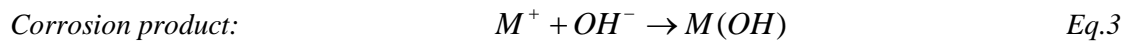
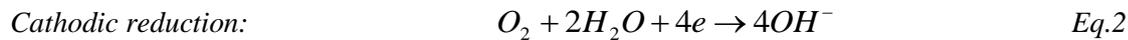
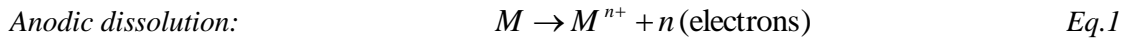
### *1.2.5. Maxillofacial and craniofacial treatments*

Surgeries to repair facial damage using patients own tissue cannot always achieve the desired results. Artificial parts may be required to restore the ability to speak or eat as well as for cosmetic appearance, to replace facial features lost through accidental damage or diseases. Osteointegrated titanium implants meeting all the requirements of biocompatibility and strength have made possible unprecedented advances in surgery, for the successful treatment of patients with large defects and hitherto highly problematic conditions.

## **2. Corrosion resistance**

Corrosion is the deterioration of a material as a result of chemical and/or electrochemical reactions with its surrounding environment. Implant materials used inside a human body are generally exposed to a harsh aqueous environment containing various anions ( $\text{Cl}^-$ ,  $\text{HCO}_3^-$ ,  $\text{HPO}_4^{2-}$ ), cations ( $\text{Na}^+$ ,  $\text{K}^+$ ,  $\text{Ca}^{2+}$ ,  $\text{Mg}^{2+}$ ), organic substances, and dissolved oxygen [Buddy et al., 2004]. There different types of corrosion that may take place on implant metallic materials are pitting, crevice, galvanic, intergranular, stress-corrosion cracking, corrosion fatigue, and fretting corrosion [Manivasagam et al.,

2010]. The mechanism of corrosion of metallic implant materials is based on the following fundamental equations [Buddy et al., 2004].



As shown in **Fig. 10**, the metallic components of the alloy are initially oxidized to their ionic forms and release a free electron. The dissolved oxygen presents in the aqueous environment then react with the water molecules and free electron to form hydroxyl ions ( $OH^-$ ). These hydroxyl anions then react with the metallic cations and form a corrosion product.

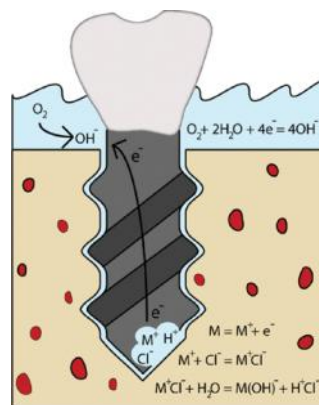


Figure 10. Schematic presentation of initiation and mechanism of corrosion of a dental implant [Gittens et al., 2011].

The first requirement for any material to be placed in the human body is its biocompatibility, necessary to prevent any adverse reaction like allergy, inflammation and toxicity. So biomaterial must withstand the body environment and should not degrade to a point that it cannot function as intended [Niinomi, 1998]. The excellent corrosion resistance of titanium alloys results from the formation of very stable, continuous, highly adherent, and protective oxide films on metal surfaces which allow them to be widely used in biomedical applications. Stoichiometric titanium dioxide ( $TiO_2$ ), in its two important crystalline modifications, rutile and anatase [Wu et al, 2006], possesses high refractive indices, high dielectric constants, high chemical stability, and biocompatibility as well as low friction coefficients. Rutile-type titanium dioxides,  $TiO_2$  and  $TiO_x$ , generally have blood compatibility [Nan, et al., 1994]. This oxide film plays an important role as an inhibitor for the release of metallic ions. Furthermore, the composition of the surface oxide film changes according to reactions between the surfaces of metallic materials and living tissues. Even a low concentration of dissolved oxygen, inorganic ions, proteins, and cells may accelerate the metal ion release. In addition, the dissolution of surface oxide film due to active oxygen species has also been reported [Kasemo and Lausmaa, 1986].

The primary aim of the surface treatments (surface modifications) is to enhance the protective passive film by changing its composition, structure and thickness, and/or by reducing the weak points such as non-metallic inclusions.

### 3. Surface treatment

In the field of biomaterials, surface treatments are known to induce chemical modifications of the implant, associated with the modifications of surface topography. The rate and quality of osteointegration in titanium implants are related to their surface properties such as surface composition, hydrophilicity and roughness which play an important role in implant-tissue interaction and osteointegration. There are several papers reporting that surface roughness of the implant affects the rate of osteointegration and biomechanical fixation [Cochran et al., 1998; Wennerberg et al., 1998].

Surface roughness can be divided into three levels depending on the scale of the features: macro-, micro- and nano-sized topologies.

The **macro level** is defined for topographical features as being in the range of millimetres to some tens of microns. This scale is directly related to the implant geometry, with threaded screw and macroporous surface treatments which give surface roughness of more than 10  $\mu\text{m}$ . Numerous reports have shown that both the early fixation and long-term mechanical stability of the prosthesis can be improved by a high roughness profile compared to smooth surfaces [Buser et al., 1991; Gotfredsen et al., 1995; Wennerberg et al., 1995]. The high roughness resulted in mechanical interlocking between the implant surface and bone on growth. However, a major risk with high surface roughness may be an increase in peri-implantitis as well as an increase in ionic leakage.

The **micro level** is defined for topographic profile of implants as being in the range of 1–10 $\mu\text{m}$ . This range of roughness maximizes the interlocking between mineralized bone and the surface of the implant. A theoretical approach suggested that the ideal surface should be covered with hemispherical pits approximately 1.5  $\mu\text{m}$  in depth and 4  $\mu\text{m}$  in diameter [Hansson and Norton, 1999]. So the moderate roughness of 1–2  $\mu\text{m}$  may limit these two parameters resulting from high roughness [Albrektsson and Wennerberg, 2005].

The **nano level** topographic range plays an important role in the adsorption of proteins, adhesion of osteoblastic cells and thus the rate of osteointegration [Brett et al., 2004]. However, it is quite difficult to produce surface roughness in this nano-range with chemical treatments. In addition, the optimal surface nano topography for the selective adsorption of proteins leading to the adhesion of osteoblastic cells and rapid bone apposition is unknown.

Numerous studies have shown that a surface roughness in the micro level range resulted in greater bone-to-implant contact and higher resistance to torque removal than other types of surface topography [Wennerberg et al., 1995 and 1998]. These reports have demonstrated that titanium implants with roughened surfaces have greater contact with bone than those with smoother surfaces [Wennerberg et al., 1998; Cochran et al., 1998].

Surface treatment is the process whereby the implant surface is cleaned and/or chemically, polished or grinded mechanically or electrochemically to roughen the implant surface to promote better adhesion between the bone and the implant. Briefly, coatings with apatitic materials on metal surface are also presented in the next paragraphs.

#### ***3.1. Mechanical pretreatment of metals: Blasting***

Metal surface can be blasted with hard ceramic particles such as *alumina, titanium oxide and calcium phosphate*. The ceramic particles are projected through a nozzle at a high velocity by means of

compressed air or by using a spinner. Depending on the size of the ceramic particles, different surface roughnesses can be produced on titanium implants. The blasting material has to be chemically stable, biocompatible and should not impede the osteointegration of the titanium implants. For example *titanium oxide* is also used for blasting titanium implants, with an average size of 25  $\mu\text{m}$  producing a moderately rough surface on dental implants in the range of 1–2  $\mu\text{m}$ . An experimental study using micro implants in humans showed a significant improvement for bone-to-implant contact for the  $\text{TiO}_2$  blasted implants in comparison with machined surfaces [Ivanoff et al., 2001]. Also Wennerberg et al. [Wennerberg et al., 1995] demonstrated, with a rabbit model, that grit blasting with  $\text{TiO}_2$  or  $\text{Al}_2\text{O}_3$  particles gave similar values of bone implant contact, but drastically increased the biomechanical fixation of the implants when compared to smooth titanium. Various methods have been developed in order to create a rough surface and improve the osteointegration of titanium implants, **Table 7**.

Table 7. Average surface roughness using several methods.

Type of polishing	Surface roughness [ $R_a$ ] ( $\mu\text{m}$ )	References
Diamond polished	0.16	[Anselme et al., 2000]
*P4000	0.3	[Anselme et al., 2000]
*P1200	0.43	[Anselme et al., 2000]
*P80	0.6	[Anselme et al., 2000]
**S500 $\mu\text{m}$	2.19	[Anselme et al., 2000]
**S3mm	3.4	[Anselme et al., 2000]
Sand blast and acid-etched	1.15	[Le Guehennec et al., 2007]

\*Silicon carbide paper was performed mechanically or manually

\*\* Sandblasting by alumina particles

### 3.2. Electrochemical pretreatment of metal: Anodization

Micro- or nano-porous surfaces may also be produced by potentiostatic or galvanostatic anodization of titanium in strong acids (e.g.  $\text{H}_2\text{SO}_4$ ,  $\text{H}_3\text{PO}_4$ ,  $\text{HNO}_3$  and HF), at high current density (e.g. 200  $\text{A}/\text{m}^2$ ) or potential (e.g. 100 V). The result of the anodization is to thicken the oxide layer to more than 1  $\mu\text{m}$  on titanium. When strong acids are used in an electrolyte solution, the oxide layer will be dissolved along current convection lines and thickened in other regions. The dissolution of the oxide layer along the current convection lines creates micro or nano-pores on the titanium surface [Sul et al., 2005; Xiropaidis et al., 2005; Huang et al., 2005]. Anodization produces modifications in the microstructure and the crystallinity of the titanium oxide layer [Sul et al., 2002]. This process is rather complex and depends on various parameters such as current density, concentration of acids, composition and electrolyte temperature. Anodized surfaces result in a strong reinforcement of the bone response with higher values of biomechanical and histomorphometric tests in comparison to machined ones [Sul et al., 2002].

### 3.3. Chemical pretreatment of metal: Acid etching

Another method for roughening titanium implant is the etching method by using strong acids such as HCl,  $\text{H}_2\text{SO}_4$ ,  $\text{HNO}_3$  and HF. Immersion of titanium implants for several minutes in a mixture of concentrated HCl and  $\text{H}_2\text{SO}_4$  heated above 100°C (dual acid-etching) is employed to produce a micro-rough surface. This type of surface promotes rapid osteointegration while maintaining long-term success over 3 years [Cho and Park, 2003]. It has been found that dual acid etched surfaces enhance the osteoconductive process through the attachment of fibrin and osteogenic cells, resulting in bone formation directly on the surface of the implant [Park and Davies, 2000].

### 3.4. Coating

Although metal implants play a bioactive role and fuse with living bone tissue, many research efforts in the field of biomaterials are focused on forming bioactive coatings on metallic substrates to combine the mechanical properties of the substrate and the bioactivity of the coatings. Titanium and Ti-6Al-4V integrate with the surrounding bone tissue but slowly, without achieving long-term stability [Symietz et al., 2010]. They can be improved by depositing materials with superior biocompatible and bioactive functions, which act as a barrier to ion releasing phenomena [Ige et al, 2009] and can be rapidly integrated and may perform their role for a long time without mechanical loosening. In order to obtain “the perfect implants” that are constantly subjected to load bearing, high mechanical characteristics of the metallic materials and high bioactivity properties of the ceramic coat have to be combined, especially based on calcium phosphate (Ca-P) layer design [Rosu et al., 2012].

*Calcium phosphate (Ca-P)* and particularly *hydroxyapatite (HA)* are widely used as a bioactive ceramic since they form a chemical bonding to bone. Hydroxyapatite (HA:  $\text{Ca}_{10}(\text{PO}_4)_6(\text{OH})_2$ ), the major mineral component of bones and teeth, is one of the most applicable materials for coating. Even so, because of the poor mechanical properties of bulk HA ceramics, they cannot be used as implant devices to replace large bone defects or for load-bearing applications as described by Hench and Wilson (1993). The use of HA coatings on titanium alloys leads to a structure that has good mechanical strength and good osteointegration properties at the surface and in the manufacturing of prosthetic devices. The system HA/Ti is used to improve the surface properties of the device and to induce osteointegration process [Daculsi and Bouler, 2003]. Furthermore, it has been demonstrated that the bond between HA and bone is better than that between titanium and bone [Radin and Ducheine, 1992; Filiaggi et al, 1993].

A considerable effort of researches has been devoted to develop techniques for HA thin coating on titanium [Long and Rack, 1998] by *physical and chemical deposition techniques*. The most common *physical methods* (**Table 8**) are: plasma spray [Carradò, 2010], magnetron sputtering [Yang et al., 2005] and pulsed laser deposition [Symietz et al., 2010] and while the most common *chemical routes* are dipping [Li et al, 1996], electro-codeposition [Han et al., 2001], sol-gel-derived coating [Carradò and Viart, 2010], biomimetic process (SBF) [Tanahashi and Matsuda, 1997; Adawy and Abdel-Fattah, 2013; Abdel-Fattah et al., 2011; El-Fayoumi et al., 2010; Abdel-Fattah et al., 2009; Adawy et al., 2009; Abdel-Fattah et al., 2008]

Among *physical deposition techniques*, pulsed laser deposition (PLD) is a very powerful process, which is employed successfully in biomedical, functional and protective films. PLD process allows the control of the interface layer between the substrate material and the thin film, which in turn can be used to substantially improve the film adhesion to substrate. More details are given in **Annex 1**.

Among *chemical routes*, *alkali-heat treatment* of titanium followed by biomimetic process seemed to be one of the most popular and effective methods [Kim et al., 1997]. Treatment with alkaline solution produces a titanate layer containing alkaline ions as sodium and titanium surface [Wen et al., 1998; Kim et al., 1996], which has the ability to induce the deposition of calcium phosphate ceramics *in vitro* or *in vivo* and thus are considered bioactive. At the same time, some reports indicated that *acid-alkaline treatment of titanium implants* [Takeuchi et al, 2003] might be more effective for the deposition of a homogeneous bone-like apatite layer on the surface of titanium when immersed in simulated body fluid (SBF) [Kokubo et al, 1996; Jonasova et al, 2004]. The *biomimetic process* imitates the mode in which bone-like hydroxyapatite crystals are formed in situ in a simulated body environment [Kokubo, 1996]. Thus, the coating is more readily degraded by osteopath [Liu et al,

2003] overcoming many of the drawbacks associated with other deposition techniques, such as the processes utilizing high temperature treatment.

Table 8. Several methods for Ca-P coatings [Yang et al., 2005].

Technique	Thickness (μm)	Advantages	Disadvantages
Thermal spraying	30-200	1) High deposition rates 2) Low cost	1) High temperatures induce decomposition 2) Rapid cooling produces amorphous coatings
Sputtering coating	0.5-3	1) Uniform coating thickness on flat substrates 2) Dense coating	1) Line of sight technique 2) Expensive time consuming 3) Amorphous coatings
Dip coating	50-500	1) Cheap 2) Coatings applied quickly 3) Coating on complex substrates	1) Requires high sintering temperatures 2) thermal expansion mismatch
Sol-gel	<1	1) Coating on complex shapes 2) Low processing temperatures 3) Relatively cheap as coatings are very thin	1) Some processes require controlled atmosphere processing 2) Expensive raw materials
Hot isostatic pressing	200-2000	Produces dense coatings	1) Cannot coat complex substrates 2) High temperature required 3) Thermal expansion mismatch 4) Elastic property difference 5) Expensive
Electrophoretic deposition	100-2000	1) Uniform coating thickness 2) Rapid deposition rates 3) Coating on complex substrates	1) Difficult to produce crack-free coatings 2) Requires high sintering temperatures
Pulsed laser deposition	0.05-1	1) Coating with crystalline and amorphous 2) coating with dense and porous	----
Biomimetic coatings	<30	1) Low processing temperatures 2) Can form bonelike apatite 3) Coating on complex shapes 4) Can incorporate bone growth stimulating factors	1) Time consuming 2) Requires replenishment and a constant pH of simulated body fluid
Autocatalytic baths	Investigated in this PhD thesis		Simple, economic and capable of producing uniform coating on complex shape implant

These methods produce calcium phosphate coatings by immersing metal and polymer implants in an aqueous solution containing calcium and phosphate ions at pH and physiological temperatures [Yan et al., 1997; Kokubo, 1998; Barrère et al., 1999]. It has also been proven that the chemical pretreatment in alkaline solution can improve the bonding between titanium substrate and calcium phosphate coatings fabricated by the subsequent biomimetic deposition in SBF [Wang et al., 2004].

### 3.4.1 Calcium phosphates

Calcium phosphates (Ca-P) have been widely used in bone grafts in orthopaedics and dentistry; there is great interest in understanding the chemical structure, dissolution and phase stability. Generally, all calcium orthophosphates consist of three major chemical elements: Calcium (oxidation state  $\text{Ca}^{2+}$ ), phosphorous and oxygen. The orthophosphate group  $\text{PO}_4^{3-}$  is structurally differing from meta-group  $\text{PO}_3^-$ , pyro  $\text{P}_2\text{O}_7^{4-}$  and poly phosphate group  $(\text{PO}_3)_n^{n-}$  [Wang and Nancollas, 2008]. The complete

list of known calcium orthophosphates, including their standard abbreviations and the major properties, is given in **Table 9**. More details on calcium-phosphate phases are given in **Annex 2**.

Table 9. Existing calcium orthophosphates and their major properties [Dorozhkin, 2009].

Ca/P ionic ratio	Compound	Chemical formula	Solubility at 25°C, g/L	pH (*)
0.5	Monocalcium phosphate monohydrate (MCPM)	$\text{Ca}(\text{H}_2\text{PO}_4)_2 \cdot \text{H}_2\text{O}$	~18	0.0-2.0
0.5	Monocalcium phosphate anhydrous (MCPA)	$\text{Ca}(\text{H}_2\text{PO}_4)_2$	~17	[c]
0.6	Canaphite	$\text{CaNa}_2\text{P}_2\text{O}_7 \cdot 4(\text{H}_2\text{O})$		
1.0	Dicalcium phosphate dihydrate (DCPD), mineral (brushite)	$\text{CaHPO}_4 \cdot 2\text{H}_2\text{O}$	~0.088	2.0-6.0
1.0	Dicalcium phosphate anhydrous (DCPA), mineral (monetite)	$\text{CaHPO}_4$	~0.048	[c]
1.33	Octacalcium phosphate (OCP)	$\text{Ca}_8(\text{HPO}_4)_2(\text{PO}_4)_4 \cdot 5\text{H}_2\text{O}$	~0.0081	5.5-7.0
1.5	$\alpha$ -Tricalcium phosphate( $\alpha$ -TCP)	$\alpha\text{-Ca}_3(\text{PO}_4)_2$	~0.0025	[a]
1.5	$\beta$ -Tricalcium phosphate( $\beta$ -TCP)	$\beta\text{-Ca}_3(\text{PO}_4)_2$	~0.0005	[a]
1.2-2.2	Amorphous calcium phosphate (ACP)	$\text{Ca}_x\text{H}_y(\text{PO}_4)_z \cdot n\text{H}_2\text{O}$ $n = 3-4.5; 15-20\% \text{H}_2\text{O}$	[b]	~5-12 [d]
1.5-1.67	Calcium-deficient hydroxyapatite (CDHA) <sup>[e]</sup>	$\text{Ca}_{10-x}(\text{HPO}_4)_x(\text{PO}_4)_{6-x}(\text{OH})_2$ $x$ [f] ( $0 < x < 1$ )	0.0094	6.5-9.5
1.67	Hydroxyapatite (HA)	$\text{Ca}_{10}(\text{PO}_4)_6(\text{OH})_2$	~0.0003	9.5-12
1.67	Fluorapatite (FA)	$\text{Ca}_{10}(\text{PO}_4)_6\text{F}_2$	~0.0002	7-12
2.0	Tetracalcium phosphate (TTCP), mineral hilgenstockite	$\text{Ca}_4(\text{PO}_4)_2\text{O}$	~0.0007	[a]

(\*) stability range in aqueous solutions at 25 °C

[a] These compounds cannot be precipitated from aqueous solutions.

[b] Cannot be measured precisely. However, the following values (g/L) were found:  $25.7 \pm 0.1$  (pH = 7.40),  $29.9 \pm 0.1$  (pH = 6.00),  $32.7 \pm 0.1$  (pH = 5.28).

[c] Stable at temperatures above 100 °C.

[d] Always metastable.

[e] Occasionally, CDHA is named as precipitated HA.

[f] In the case  $x = 1$  (the boundary condition with Ca/P = 1.5), the chemical formula of CDHA looks as follows:  $\text{Ca}_9(\text{HPO}_4)(\text{PO}_4)_5(\text{OH})$ .

Most of these compounds are based on calcium salts of orthophosphoric acid ( $\text{H}_3\text{PO}_4$ ), e.g., amorphous calcium phosphate (ACP,  $\text{Ca}_9(\text{PO}_4)_6$ ), brushite (DCPD,  $\text{CaHPO}_4 \cdot 2\text{H}_2\text{O}$ ), tricalcium phosphate (TCP,  $\text{Ca}_3(\text{PO}_4)_2$ ) or hydroxyapatite (HA,  $\text{Ca}_5(\text{PO}_4)_3\text{OH}$ ). Also orthophosphates, condensed phosphates like pyrophosphate ( $\text{P}_2\text{O}_7$ )<sup>4-</sup> are attractive for bone replacement since these ions are present in serum and are thought to participate in the biomineralization process. Variations in Ca-P composition can lead to different dissolution/precipitation behaviour and may, therefore, also affect the bone response differently.

### 3.4.2. Biomimetic coating and simulated body fluid

Biomimetic coating is a methodology based on the precipitation of Ca-P on titanium surface by immersion in SBF that is imitating the nature. This method involves the heterogeneous nucleation and growth of bone-like crystals on the surface of the implant at physiological temperatures and pH conditions. There are several advantages of this method such as its simplicity and its low investment

cost compared with the plasma spray process which is usually applied. Besides, it can be used to coat substrates with complex geometries or porous substrates, and makes it possible to include organic molecules in the film to induce and accelerate the regeneration of living tissues.

In general, two subsequent steps were used to enhance the heterogeneous nucleation of the CaP. *First*, the implants are treated with an alkaline solution in order to form titanium hydroxyl groups on the titanium surface, to serve as nucleating points [Kokubo et al., 1989]. Others have used high concentrations of calcium and phosphate ions in an increasing pH solution to form a thin layer on the titanium surface. *Second*, to promote nucleation and growth of biomimetic layer, the implants are soaked in Simulated Body Fluid (SBF), a solution with ion concentrations and a pH values similar to those of human blood plasma [Habibovic et al., 2002].

Table 10. The development of simulated body fluid to imitate the extracellular fluid compared to human blood plasma.

	$Na^+$	$K^+$	$Mg^{2+}$	$Ca^{2+}$	$Cl^-$	$HCO_3^-$	$HPO_4^-$	$SO_4^{2-}$	Buffer
Human blood plasma	142.0	5.0	1.5	2.5	103.0	27.0	1.0	0.5	–
Ringer's solution	130	4.0	–	1.4	109.0	–	–	–	–
Hank's solution	142.1	5.33	0.9	1.26	146.8	4.2	0.78	0.41	–
Original SBF	142.0	5.0	1.5	2.5	148.8	4.2	1.0	–	TRIS
c-SBF	142.0	5.0	1.5	2.5	147.8	4.2	1.0	0.5	TRIS
Tas-SBF	142.0	5.0	1.5	2.5	125.0	27.0	1.0	0.5	TRIS
Bigi-SBF	141.5	5.0	1.5	2.5	124.5	27.0	1.0	0.5	HEPES
r-SBF	142.0	5.0	1.5	2.5	103.0	27.0	1.0	0.5	HEPES
m-SBF	142.0	5.0	1.5	2.5	103.0	10.0	1.0	0.5	HEPES
i-SBF	142.0	5.0	1.0	1.6	103.0	27.0	1.0	0.5	HEPES
n-SBF	142.0	5.0	1.5	2.5	103.0	4.2	1.0	0.5	TRIS
SBF×1.5	213	7.5	2.3	3.8	221.7	6.3	1.5	0.8	TRIS
SBF×5	714.8	–	7.5	12.5	723.8	21.0	5.0	–	

The biomimetic method, i.e. a physicochemical method in which a substrate is soaked into a solution that simulates the physiologic conditions, for several periods of time enough to form a desirable layer of calcium phosphate on the substrate surface (**Table 10**) [Kokubo and Takadama, 2006].

The SBF plays a significant role in determining the phase composition, crystallization, growth rate of biomimetic apatite coating, which actually are affected by the composition, concentration, pH, flowing state of simulated body fluid and its additives, such as trace elements, proteins and drugs. Several trials to develop the cellular SBF to mimic the inorganic ion concentration of human blood plasma have been reported [Kokubo and Takadama, 2006; Kokubo, 1990a] (**Table 10**).

In earlier attempts, Ringer's and Hank's (HBSS) solutions were very popular [[Ringer, 1883; Hanks, 1975]. But due to the importance of pH values of the solutions to be similar to human blood plasma, SBF solutions' pH were fixed at 7.4 by using TRIS (tris-hydroxymethyl-aminomethane)-HCl (hydrochloric acid) as a buffer solution to result the original SBF [Kokubo et al., 1990b]. This original SBF lacks the  $SO_4^{2-}$  ions, which is contained in human blood plasma, as shown in **Table 10**. This was corrected in the paper published by Kokubo et al. in 1991. Since then, the c-SBF has been referred to as "SBF" by many researchers. More details are given in **Annex 3**.

### 3.4.3. *Titanium nitride*

Titanium nitride (TiN) coatings are often employed for improving the tribological performance of tools and machine parts in industrial applications due to its mechanical [Leng et al., 2001] and chemical properties including high hardness and a low wear coefficient [Holmberg and Matthews, 1994]. Moreover, TiN possesses anti-corrosion properties [Kao et al., 2002]. It was previously reported that coating a metallic implant with TiN was effective to reduce the wear damage and to improve the corrosion resistance of Ti alloys [Peterson et al, 1988; Maurer et al., 1993]. TiN is commonly used also as a biomaterial [Staia et al., 1995] because of its chemical stability and good mechanical properties. Moreover TiN interlayer plays a role as a diffusion barrier. It is biologically inert and well tolerated by living tissues [Kao et al., 2002]. Moreover, the TiN interlayer generates improvements of calcium phosphate or apatite film mechanical performance, by increasing its bond strength and adherence [Nelea et al., 2002].

# **Chapter 2**

## **Ca-P coating by autocatalytic method:**

### **understanding and optimization of the process**

In this chapter, we are going to present the experimental methods used in this thesis by beginning with a description of the experiments performed. Two different substrates [Ti-6Al-4V (TAV) and laboratory-Ti] with two different buffer layers of different roughnesses were studied. The first buffer layer, sodium titanate, was chemically prepared in several steps which were chemically etching followed by alkaline and heat treatment. The second buffer layer was titanium nitride, deposited by pulsed laser deposition (PLD) on the metal substrate after mechanical polishing and chemical etching (Fig. 11).

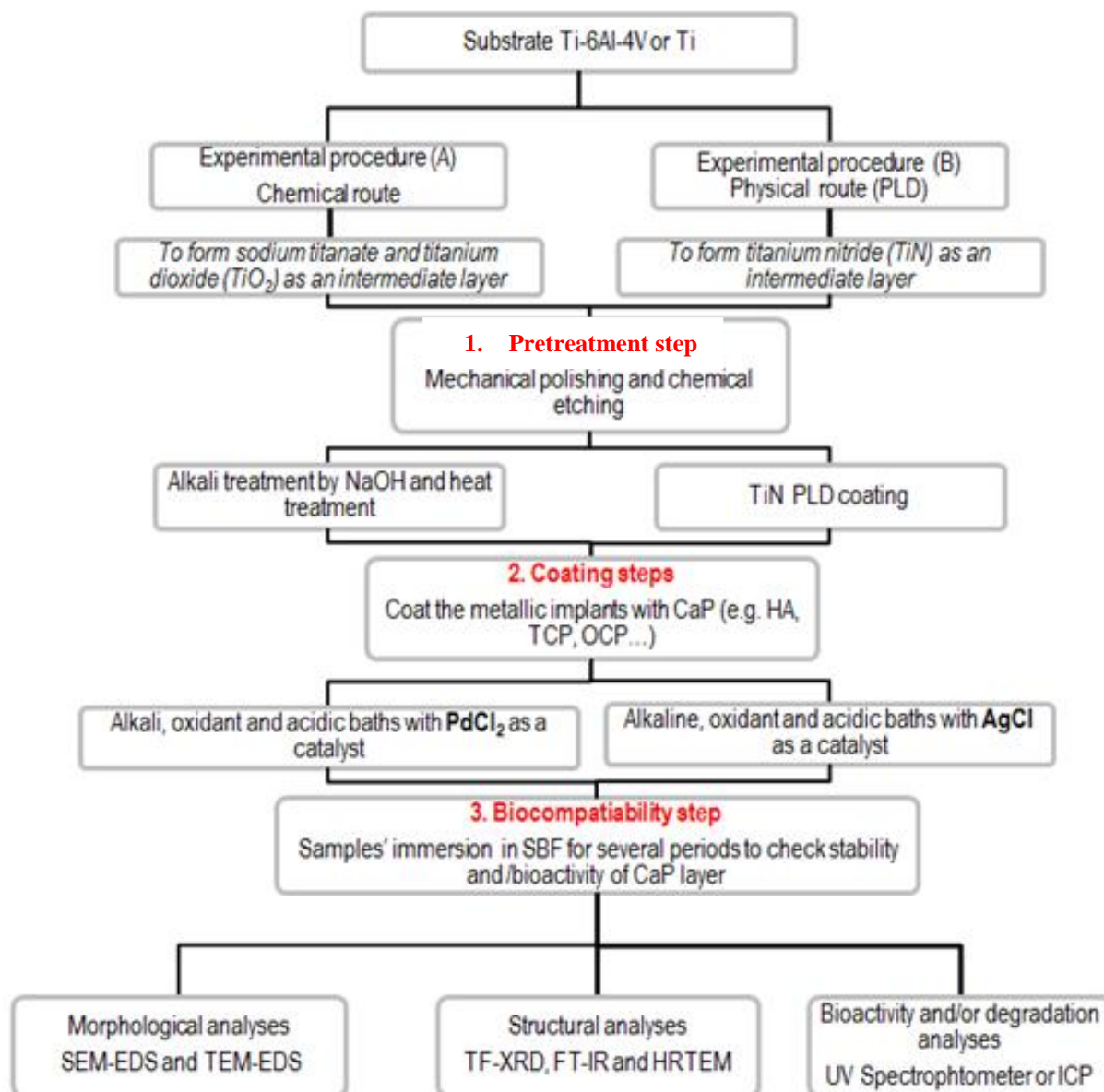


Figure 11. Flow sheet of experimental design

To deposit calcium phosphate layer on these substrates, three autocatalytic baths (acidic, alkaline and oxidant) were performed. These baths were distinguished by their working conditions, compositions, pH and temperatures. The calcium source and catalyst were kept constant.

To check the stability of the formed layer and its bioactivity, samples were immersed in SBF for different periods of time.

To confirm the deposition of Ca-P layer after immersion in each bath or after SBF, structural and morphological analyses were performed. Structural analyses were done by using Fourier Transform Infrared spectroscopy (FT-IR) and X-ray diffraction (XRD). Microstructural characterizations were performed by scanning electron microscope (SEM), transmission electron microscope (TEM) and confocal microscopy. Biochemical analyses were performed by spectrophotometry and ultraviolet-optical emission spectrometers with ICP excitation source. Flow sheet (**Fig. 11**) summarizes the experimental steps used in this thesis.

### **PART I. Substrate pretreatment**

#### **1. State of art: Surface state modification**

The surface properties, such as the surface composition, hydrophilicity and roughness, of titanium implant play an important role on the rate and quality of osteointegration (implant-tissue interaction) [Le Guehennec et al., 2007]. However, metallic surfaces are in general not sufficiently bioactive to chemically bond with the surrounding tissue which may lead to a weak fixation of the implant. Hence, surface treatment based on Ca-P coating is usually needed to enhance the bioactivity so as to improve the osteointegration with bone tissues.

##### *1.1. Surface roughness*

Surface roughness can be classified into three levels according to the scale of the features into the following: macro-, micro- and nano- sized topologies.

(i) Macro-topography, in the range from few mm to 10  $\mu\text{m}$ . Several studies have shown that this range is responsible for early fixation and long-term mechanical stability of the prosthesis compared to smooth surfaces [Buser et al., 1991; Gotfredsen et al., 1995; Wennerberg et al., 1995].

(ii) Micro-topography, ranging between 1 and 10  $\mu\text{m}$ . To maximize the interlocking between mineralized bone and the implant surface, this range of roughness (1–10  $\mu\text{m}$ ) is preferable. A moderate roughness of 1–2  $\mu\text{m}$  can be used to limit the problems detected by using high roughness, such as an increase in peri-implant as well as an increase in ionic leakage [Albrektsson and Wennerberg, 2005]. Several reports introduced by A. Wennerberg et al. (1995, 1998) have shown that a surface roughness in this range resulted in greater bone to implant contact and higher resistance to torque removal than other roughness values.

(iii) The nanotopography plays an important role in the adsorption of proteins, adhesion of osteoblastic cells, and also the rate of osteointegration [Brett et al., 2004]. However, to produce surface roughness in this nanorange is generally quite difficult by using chemical treatments. Therefore, various pretreatments are applied to accelerate the coating process including acid etching, alkaline treatment, and heat treatment. There are several methods used to create a rough surface of titanium implants such as grit blasting, anodizing, and acid etching. One of these methods is etching with strong acids such as HCl, H<sub>2</sub>SO<sub>4</sub>, HNO<sub>3</sub>, and HF for roughening titanium implants.

Etching the alloy in a 0.18 M HF and 1.88 M HNO<sub>3</sub> at 20 °C for up to 10 minutes causes a roughening of the surface due to the material dissolution [Sittig et al., 1999]. Acid etching produces micro pits on titanium surfaces with sizes ranging from 0.5 to 2  $\mu\text{m}$  in diameter [Massaro et al., 2002] which improve the osteointegration .

### 1.2. Pretreatment in alkaline NaOH

Alkaline (NaOH or KOH) treatment of metallic implant is one among several existing methods used to make titanium surfaces bioactive [Adawy et al., 2009; de Jonge et al., 2008; Liu et al., 2004]. The alkali-heat treatment is a simple and practical one, proposed by Kim *et al.* (1996). In this process, the Ti surface is submitted to a chemical treatment by using alkaline solution in which the native surface oxides and (mainly) metallic species are converted to form a hydrogel film. During the alkaline treatment, the surface-passive TiO<sub>2</sub> layer partially dissolves into the alkaline solution because of the corrosive attack of hydroxyl group:



This reaction is assumed to proceed simultaneously with the following hydration of Ti metal:



A further hydroxyl attack to hydrated TiO<sub>2</sub> will produce negatively charged hydrates on the surfaces of the substrates as follows:



These negatively charged species are combined with alkaline ions in the aqueous solution, resulting in the formation of an alkaline titanate hydrogel layer.

### 1.3. Heat treatment

The formed sodium titanate hydrogel layer is dehydrated by heat treatment and transformed into an amorphous sodium titanate from 400 to 500 °C, then fairly densified at 600 °C, and then converted into crystalline sodium titanate and rutile above 700 °C [Kim et al., 1997]. Because of this structural change, the further release of Na<sup>+</sup> ions in the SBF decreases, therefore, the formation of hydrated titania on the surface is not favoured and the time required to form biolayer decreases. Thus, heat treatment at 600 °C is an effective process to promote Ti osteointegration due to the dehydration of hydrogel film, stabilizing it as amorphous sodium titanate containing a small fraction of crystalline phase [Kim et al., 1996, 1997; Liu et al., 2004]. Also, heat treatment for alkali-treated film on Ti alloy is applied to improve the film substrate adhesion and respectively improve the osteointegration, since the formed hydrogel on Ti alloy is mechanically unstable. Nishiguchi et al. (1999; 2001a) evaluated detaching and shear stresses of bones connected to Ti alloys after *in vivo* implantation period. They showed that the implants with surfaces modified by heat treatment presented a higher performance in the mechanical tests compared to the untreated ones and to those which were only alkaline treated. In addition, no fibrous tissue could be observed in the only heat-treated sample during direct implant-bone connection, achieving maximum fixation strength in earlier periods of *in vivo* implantation.

Many attempts have been done to optimize the treatment process for improving the bioactivity. Uchida et al. (2002) used both hot water and heat treatments after alkaline treatment to convert the sodium titanate gel into anatase, which significantly enhances the formation of the biolayer on the

metal surface after immersion in SBF. Another trial developed by Takemoto et al. (2006) used dilute hydrochloric acid (HCl) treatment between alkaline and heat treatments for porous titanium implants. They showed the ability to remove sodium from the alkali-treated porous titanium more effectively than conventional hot water treatment, and the subsequent heat treatment converted titanium oxide into anatase.

One of the coating methodologies is a biomimetic method that is a physicochemical method in which a substrate is soaked into a solution that simulates the physiologic conditions, for several periods of time, enough to form a desirable layer of calcium phosphate on the substrate surface [Kokubo and Takadama, 2006]. There are several advantages of this method such as its simplicity and its low investment cost compared with the plasma spray process which is usually applied. Besides, it can be used to coat substrates with complex geometries or porous substrates, and with the possibility to include organic molecules in the film to induce and to accelerate the regeneration of living tissues [Teixeira et al., 2004].

Kokubo et al. described the interaction of pretreated titanium implant *in vitro* [Kokubo et al., 1996; Kokubo and Yamaguchi, 2010]. An alkaline and heat-treated Ti substrate was soaked in SBF and a dense and uniform layer of the bonelike apatite was formed following the mechanism described in Fig. 12.

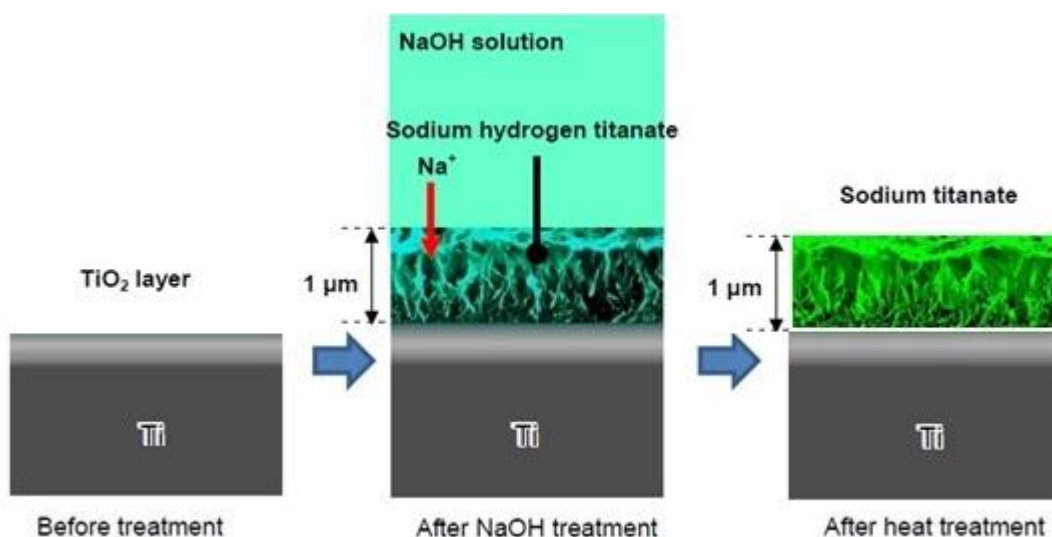


Figure 12. Structural change of titanium surface after NaOH (alkaline) treatment and heat treatment [Kokubo and Yamaguchi, 2010].

H<sub>3</sub>O<sup>+</sup> ions on the surface layer replaced the Na<sup>+</sup> ion in SBF, producing Ti-OH groups on the metal surface. Ionic activity product (multiplications of Ca<sup>2+</sup> and P<sup>3-</sup>) of the apatite in the surrounding fluid is increase by increasing OH ionic concentration because these groups induced the apatite nucleation and accelerated the apatite nucleation [Ajeel et al., 2013]. The apatite nuclei grew spontaneously by consuming the calcium and phosphate ions from SBF [Kim et al., 1996]. The resultant apatite layer was tightly bonded to the substrate, since it is integrated to the Ti substrate through the hydrated titania (Ti-OH) and titanium oxide which are gradually changing in their concentrations, as shown in Fig. 13.

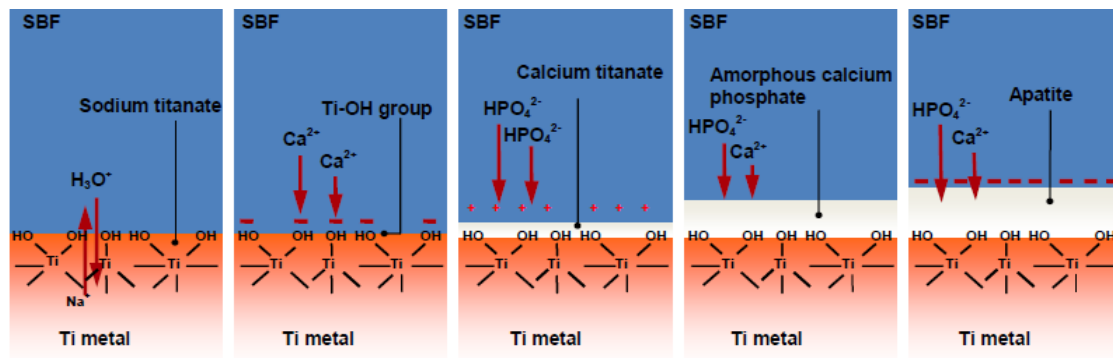


Figure 13. Surface structure changes of Ti metal after alkaline and thermal treatment then soaked in SBF [Kokubo and Yamaguchi, 2010].

*In vivo*, following implantation, metal implants which are coated with layers of calcium phosphates, release ions from these phases into the peri-implant region increases the saturation of body fluids and precipitates a biological apatite onto the surface of the implant [DeGroot et al., 1998]. This layer of biological apatite might contain endogenous proteins and serve as a matrix for osteogenic cell attachment and growth. The bone healing process around the implant, therefore, is enhanced by this biological apatitic layer. The biological fixation of titanium implants to bone tissue is faster with a calcium phosphate coating than without [Morris et al., 2000; Barrere et al., 2003]. It is well-recognized that calcium phosphate coatings have led to better clinical success rates in the long-term than uncoated titanium implants [Morris et al., 2000; Geurs et al., 2002]. These long-term success rates are due to a superior initial rate of osteointegration [Geurs et al., 2002].

The aim of this work is to study the effect of NaOH in alkaline treatment, then of different heating regimes and their influence in the formation of the biomimetic biolayer on titanium alloy substrates.

The chemical-heat treated substrates were dipped for 4 days in SBF to investigate their ability to form a biolayer. The immersion in SBF simulates the initial behaviour after implantation, which is the most critical period concerning the bond at the implant-bone interface. The samples were characterized by FESEM and FT-IR before and after SBF immersion.

## PART II. Coating deposition by autocatalytic baths on pretreated substrates

### 1. State of the art

Autocatalytic baths are chemical baths with different compositions and conditions for each bath. Autocatalytic reactions are chemical reactions in which at least one of the reactants is also a product. Leonor and Reis (2003) reported that new autocatalytic baths were used to produce Ca-P coatings on several polymeric biomaterials.

This method has several advantages, such as:

- 1) Ca-P coating can be produced onto complex-shaped and/or micro porous implants.
- 2) The method is simple and a cost-effective way to produce Ca-P coating.
- 3) The deposition route is totally electroless, but depends on redox chemical reaction.

4) There is no adverse effect of heating.

Here we present three different autocatalytic baths: acidic, alkaline [Leonor and Reis, 2003] and oxidant [Oliveira et al., 2005] ones. Acidic, alkaline and oxidant baths are mainly composed of calcium chloride ( $\text{CaCl}_2$ ) which acts as the source of calcium. On the other hand, sodium hypophosphite ( $\text{NaH}_2\text{PO}_2 \cdot \text{H}_2\text{O}$ ) and sodium pyrophosphate ( $\text{NaP}_2\text{O}_7 \cdot 10\text{H}_2\text{O}$ ) act as a source of phosphorous and reducing agent for alkaline and oxidant ones respectively. Sodium fluoride ( $\text{NaF}$ ) is used as an etching agent, succinic acid ( $\text{C}_4\text{H}_6\text{O}_4$ ) act as an accelerator of the reaction (for acidic bath). Oxygen peroxide ( $\text{H}_2\text{O}_2$ ) is used in oxidant bath as oxidizing agent. Finally palladium chloride ( $\text{PdCl}_2$ ) and silver chloride ( $\text{AgCl}$ ) are, separately, used as the catalysers and worked as an arm of ionic change between the substrate and the solution for all baths.

### ***1.1. Role of palladium ions***

Palladium is a metallic element, which resembles and occurs together with the other platinum group metals and nickel. Palladium chloride acts as catalyser or catalyst in autocatalytic baths. Catalyst is a substance that participates in the chemical reaction to change its rate, without being consumed itself in it.

There are two types of catalysers:

1) positive catalyst, which speeds up the reaction, and 2) inhibitors which are substances used to slow catalyst's effect.

Catalysers generally react with one or more reactants that act as intermediates and subsequently give the final reaction product, in the process regenerating the catalyst. Jing et al. (2010) studied the antibacterial activity of Pd by doping several concentration of Pd with titania nanoparticles, to verify that the 3 mol% Pd-TiO<sub>2</sub> nanoparticles display antibacterial activities superior to pure TiO<sub>2</sub> and the other doped TiO<sub>2</sub> nanoparticles .

### ***1.2. Role of silver ions (catalyser and antibacterial ions)***

Sometimes when bone healings are associated with infection, the healing process becomes more complicated and the implant failure is expected since the implant becomes loosened due to the formation of bacterial colony on the implant surfaces. Ionic silver ( $\text{Ag}^+$ ) incorporation with implants can solve these problems because it possesses anti-infective properties and can effectively reduce the deleterious effects of bacteria.

$\text{Ag}^+$  is considered to be effective against a broad range of micro-organisms, with low concentrations, of  $10^{-9}$  to  $10^{-6}$  M against bacteria, fungi and viral pathogens [Russell and Hugo, 1994]. In recent years silver exhibits good antibacterial properties, especially as nano-particles, which has been widely used in a variety of medical applications such as wound dressings and also to reduce infections in burns treatment, arthroplasty, as well as to prevent bacterial colonization on prostheses, catheters, and human skin [Shiva et al., 2011].

The antibacterial activity of silver is dependent on the balance between the activity of the  $\text{Ag}^+$  ions which kill bacteria and the total amount of silver released from the coatings, which - if too high - results in cytotoxicity.

The activity of silver as an antibacterial agent is mainly dependent on the silver cation ( $\text{Ag}^+$ ), which binds strongly to electron donor groups on biological molecules containing sulphur, oxygen or nitrogen. In order to enhance the antibacterial performance of silver *in vivo* it is often necessary to increase the concentration of  $\text{Ag}^+$  ions released from the coating relative to that of metallic silver. As reported by Betts et al.(2005) that the addition of 1% platinum (Pt) was found to significantly enhance the antibacterial effectiveness of the coating due to higher rates of  $\text{Ag}^+$  release. Recently, Shiva et al., (2011) observed the limited inhibition for bacterial growth at 8.5  $\mu\text{g/ml}$  of  $\text{Ag-SiO}_2$  while 10  $\mu\text{g/ml}$  inhibited the growth of *E. Coli* strain up to 6 h, whereas 100  $\mu\text{g/ml}$  was effective throughout the 24 h incubation and totally prevented growth. Several reports proved the electrostatic attraction between negatively charged bacterial cells and the positively charged nano-particles is crucial for the activity of nano-particles as bactericidal materials [Hamouda and Baker, 2000; Sondi and Salopek-Sondi, 2004]. The mechanism of the bactericidal effect of silver colloid particles against bacteria is not well known. It is possible that Ag nano-particle act similarly to the antimicrobial agents used for the treatment of bacterial infections. These agents show four different mechanisms of actions:

- (1) interface with cell wall synthesis, by attaching the surface of cell membrane and disturb its power function such as permeability and respiration [Murray et al., 1965],
- (2) inhibition of protein synthesis,
- (3) interference with nucleic acid synthesis, by penetrating the bacteria and cause further damage by interacting with sulfur- and phosphorous containing compounds such as DNA [Gibbins & Warner, 2005], and
- (4) inhibition of metabolic pathway [Tenover, 2006].

Antimicrobial susceptibility tests are classified into different methods, based on the applied principle. They include: diffusion (Kirby-Bauer and Stokes), dilution (minimum inhibitory concentration, MIC), and diffusion and dilution (E-test method).

Also silver, as one of precious metal catalyst, emerged as partial oxidation and epoxidation **catalyst** as early as 1900s. It is used industrially in the oxidation of methanol to formaldehyde and in epoxidation of ethylene [Cassandra and Robert, 2011].

## PART III. Experimental part

### 1. Materials and methods

#### Substrates

In present study, we compared the effect of the new autocatalytic baths (each bath with different catalysts) on several kinds of titanium substrates such as Ti, and Ti-6Al-4V (TAV) implants with different roughnesses (**Fig. 14**). The adhesion of the coatings through a micromechanical adhesion mechanism has strong effects on the roughness [Qunyang and Kyung-Suk, 2009]. The substrates were divided into *four different groups* according to their roughness, buffer layer and autocatalytic baths used, as follows:

**Group I** possesses three subgroups:

(a) Commercially available cylindrical bars of titanium alloy - Grade 5 (Ti-6Al-4V), used for dental applications, of 4 mm in diameter and 4 mm in height were used (ASTM 136). The substrates were ground with SiC paper (400 grit) and cleaned by successive ultrasonic treatments in acetone, then in 70% ethanol and in double distilled (dd) water for 15 minutes each, separately (**Fig. 14**).

(b) Laboratory titanium alloy (Ti-6Al-4V) sheet material was processed and delivered from Clausthal University of Technology, Institute of Material Science and Technology. Small samples (10×10×1 mm<sup>3</sup>) were cut out of the sheets. They were polished mechanically using a grinder-polisher with SiC paper (400, 1200 and 4000 grit SiC paper) under 10 and 20 N force with a speed 100 rpm each step for 2 minutes.

(c) Ti - Grade 2 (Ti CP-3) sheet was also prepared and delivered from the same institute, and cut into specimen (10×10×0.5 mm<sup>3</sup>). Size and state of surface are the same of samples cited in (b).

**Group II** represents a commercially available titanium alloys (Ti-6Al-4V). The square specimens of 10×10 mm<sup>2</sup> surface and 1 mm thickness were mechanically polished up to 4000 grit size under the same conditions described for Group I (b and c).

**Group III** corresponds to a commercially titanium (Ti-grade 4; Ti CP-1). The specimens (10×10×2 mm<sup>3</sup>) were mechanically polished under the same conditions as described for Groups I and II followed by polishing with non-crystallizing colloidal silica suspension under 10 N and 300 rpm speed for 3 minutes.

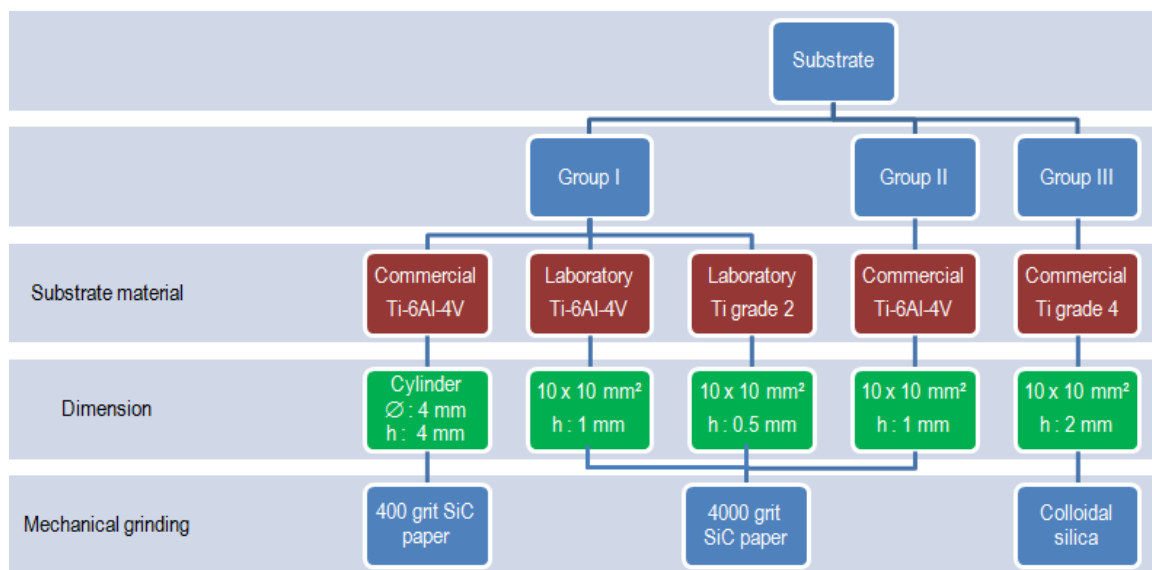


Figure 14. Schematic diagram of the specimens' classifications.

Prior to the coating steps the above substrates were subjected into two steps: "Pretreatment" (**Fig. 15**) to prepare the surface for coating with calcium phosphate ("coating deposition").

### 1.1. Step 1: Substrate pretreatment

*Cleaning step* was performed to decontaminate the surface from embedded particles and machining impurities due to polishing steps (**Fig. 15**). Samples were cleaned in acetone for 15 minutes, then in 70% ethanol for another 15 minutes and finally in dd water for 15 minutes. The cleaning procedure was maintained at room temperature in an ultrasonic cleaner.

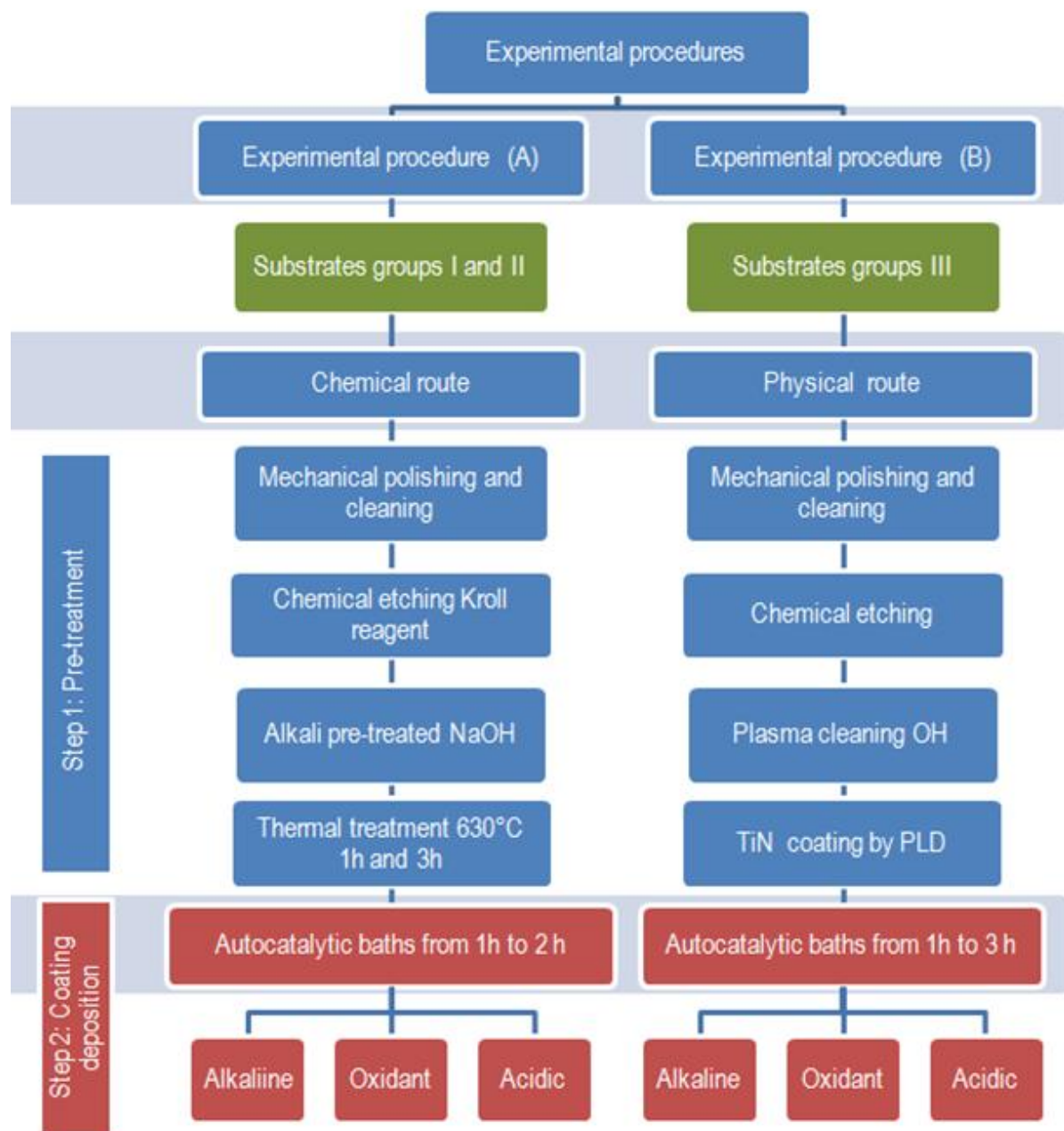


Figure 15. Schematic diagram of the experimental work.

### 1.1.1. Experimental procedure A: chemical route

This treatment leads to the formation of sodium titanate as a buffer layer. This layer was built on the substrates to increase the bond strength and adherence between the substrate and the layer of Ca-P which will be deposited later.

All samples were *chemically etched* to remove native surface oxides and to enhance micro-structural features such as grain size and phase morphologies. Samples were etched for 10 minutes in Kroll's reagent (Table 11), a mixture of 2 ml hydrofluoric acid (HF, 40 %), 4 ml nitric acid (HNO<sub>3</sub>, 66 %) in 1000 ml deionised water and then rinsed with dd water and dried overnight at room temperature [Bigi et al., 2005].

Table 11. Composition of Kroll etching solution.

Etchant	Composition	Concentration	Conditions
Kroll's Reagent	Distilled water	1000 ml	10 minutes
	Nitric acid (HNO <sub>3</sub> , 66 %)	4 ml	
	Hydrofluoric acid (HF, 40 %)	2 ml	

*Etched samples* were immersed in concentrated solution of 10 M NaOH at 60°C for 24 h and then washed in dd water [Horkavcova et al., 2008]. Afterwards, Ti metal was subjected to *alkaline NaOH treatment*, where a sodium titanate hydrogel layer was formed as a buffer layer on its surface. This layer acts as a corrosion product and increases the bond strength and adherence between the metallic substrate and the future Ca-P layer [Kokubo et al., 1999].

Subsequent *thermal treatment* was carried out after alkaline treatment to dehydrate and stabilize the buffer gel layer of the amorphous sodium titanate which was formed during the previous step [Kokubo et al., 1999]. Then the samples were heat-treated up to (600 ± 10) °C. The temperature was raised with a heating rate of 3°C/minutes, (**Groups I and II** sample designated 3 h) or 10°C/minutesute, (**Group I**, sample designated 1 h) followed by a plateau of 1 h, then left to cool down to room temperature inside the furnace. Finally, they were kept in a desiccator for further analyses.

### 1.1.2. Experimental procedure B: physical route

Pulsed laser deposition (PLD) of TiN coatings on controlled titanium surface is favourable for high fatigue resistance [Pelletier et al., 2011]. It shows good mechanical properties, i.e. a very strong adherence to the substrate, and hardness, Young's modulus, stiffness and mechanical wear are similar to those specific to the human bone. To complete this process an autocatalytic route is applied to induce the group of a Ca-P layer in a way similar to the process of natural bone formation on a TiN layer

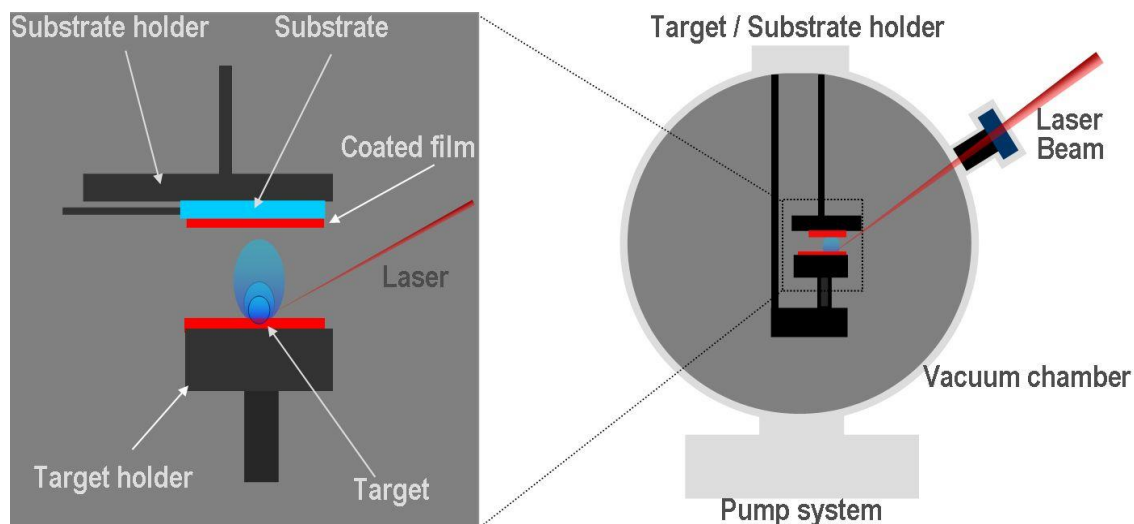


Figure 16. Schematic principle of PLD system.

The samples (group III) were immersed in 1 M NaOH and 0.5 M H<sub>2</sub>O<sub>2</sub> at 75°C for 10 minutes to clean and decontaminate the titanium surface from embedded particles and machining impurities. Then, they were 10 minutes treated in 0.2 M oxalic acid (H<sub>2</sub>C<sub>2</sub>O<sub>4</sub>) at 85°C to produce a microporous surface and finally immersed in nitric acid for final passivation.

After the *etching step*, 300 nm nitrite titanium (TiN) layers were coated on Ti/Ti alloys by PLD (**Fig. 16**) in order to enhance good adhesion properties. All depositions were performed with pulses generated by a YAG Quantel ( $\lambda = 355$  nm). The laser source was placed outside the irradiation chamber. The irradiation spot size was about 2 mm<sup>2</sup> and incident fluence was 1.5 J/cm<sup>2</sup>. The Ti target was mounted in a special holder which could be rotated and/or translated during the application of multi-pulse laser irradiations in order to avoid piercing and to continuously submit a fresh zone to laser exposure. During the deposition, the titanium substrate was kept at approximately 600°C. PLD experimental parameters are listed in **Table 12**.

*Table 12. PLD experimental conditions of TiN films.*

Sample	Temp substrate (°C)	Dynamical pressure (DP) (mbar)	DP during ablation (mbar)	Energy (mJ)	Focalisation (mm)	Laser pulse	Deposition time (minutes)
TiN	600±2	O <sub>2</sub> 1.2×10 <sup>-2</sup>	MW + plasma	10	690	60000	100

### ***1.2. Step 2: Coating deposition: Acidic, alkaline and oxidant baths***

This step acts a key for apatite formation when implanted in the host to accelerate the integration of the implant with the surrounding bone tissue to achieve its stability for long period. Additionally, these coatings prevent the release of some harmful ions such as, Al and V ions, under certain conditions which may lead to ionic accumulation inside the tissues.

For producing electroless Ca-P coatings, during only 2 h, three types of baths were used. These baths are chemical baths which depend mainly on redox-reaction to deposit Ca-P layer under the following compositions and operating conditions shown in **Table 13**. Each bath is prepared by dissolving the specific reagent of each bath in the same order and concentration showed in **Table 13**. Each bath was prepared under the magnetic stirring for the completely dissolving each reagent.

*Table 13. Inorganic composition of chemical baths.*

Bath	Reagents	Concentration [g/L]	pH adjusted	Bath temperature [°C]
Acidic	Calcium chloride (CaCl <sub>2</sub> )	21.0	NaOH: 5.3 ± 0.1	80 ± 2
	Sodium fluoride (NaF)	5.0		
	Succinic acid (C <sub>4</sub> H <sub>6</sub> O <sub>4</sub> )	7.0		
	Sodium hypophosphite (NaH <sub>2</sub> PO <sub>2</sub> ·H <sub>2</sub> O)	24.0		
	Palladium chloride or silver chloride (PdCl <sub>2</sub> or AgCl)	0.885		
Alkaline	Calcium chloride (CaCl <sub>2</sub> )	25.0	NaOH: 9.2 ± 0.1	60±2
	Sodium pyrophosphate (NaP <sub>2</sub> O <sub>7</sub> ·10 H <sub>2</sub> O)	50		
	Sodium hypophosphite (NaH <sub>2</sub> PO <sub>2</sub> H <sub>2</sub> O)	21.0		
	Palladium chloride or silver chloride (PdCl <sub>2</sub> or AgCl)	0.885		
Oxidant	Calcium chloride (CaCl <sub>2</sub> )	5.6	NaOH: 7.0 ± 0.1	70 ± 2
	Sodium pyrophosphate (NaP <sub>2</sub> O <sub>7</sub> ·10 H <sub>2</sub> O)	6.7		
	Oxygen peroxide (H <sub>2</sub> O <sub>2</sub> )	34		
	Palladium chloride or silver chloride (PdCl <sub>2</sub> or AgCl)	0.9		

## Chapter 2: CaP coating by autocatalytic method: understanding and optimization of the process

*Calcium chloride* ( $\text{CaCl}_2$ , SIGMA-ALDRICH, c1016-100G) acts as the source of calcium, while *sodium hypophosphite* ( $\text{NaH}_2\text{PO}_2 \cdot \text{H}_2\text{O}$ , SIGMA-ALDRICH, EC No. 2316699) has a dual function as a source of phosphate in addition to act as a reducing agent.

*Sodium fluoride*, ( $\text{NaF}$ , PROLABO, Lot No.90149) and *succinic acid* ( $\text{C}_4\text{H}_6\text{O}_4$ , SIGMA-ALDRICH, S3674-100G) are present only in acidic bath, which acts as an etching agent and as an accelerator of the reaction respectively [Leonor and Reis, 2003].

*Sodium pyrophosphate* ( $\text{NaP}_2\text{O}_7 \cdot 10\text{H}_2\text{O}$ , SIGMA-ALDRICH, 221368-500G) acts as a source of phosphorous in alkaline and oxidant baths. The presence of *hydrogen peroxide* solution ( $\text{H}_2\text{O}_2$ , SIGMA-ALDRICH, concentration 50% in water, 516813-500 ml) in oxidant bath and in this bath only to act as an oxidizing agent [Oliveira et al., 2005]. As a catalyser *palladium chloride* ( $\text{PdCl}_2$ , SIGMA-ALDRICH) – is acting as an arm of ionic change between the substrate and the baths- in Reis et al. work [Leonor and Reis, 2003] was used. Here, we newly introduced silver chloride ( $\text{AgCl}$ , SIGMA-ALDRICH) as a catalyst too.

### 1.3. Samples' notation

The previously prepared samples (pretreated samples) of each group were immersed in each bath separately for 1 or 2 h (according to the three following group, see **Table 14**) under the operating condition of each bath shown in **Table 13**. During the immersion of each sample, the bath should be under the magnetic stirring because the bath was not a solution but it was a suspension as not all reagents are dissolved completely.

Table 14. Samples' notation.

Group	Sample	Substrate	Mechanical grinding, grit SiC paper	Heat treatment (h)	Bath time (h)	Catalyst
Group I <sub>Pd</sub>	TAV <sub>400</sub> -1h-bath <sub>Pd</sub>	TAV	400	1	2	PdCl <sub>2</sub>
	TAV <sub>400</sub> -3h bath <sub>Pd</sub>	TAV	400	3	2	PdCl <sub>2</sub>
	TAV <sub>4000</sub> - bath <sub>Pd</sub>	TAV	4000	3	2	PdCl <sub>2</sub>
	Ti <sub>4000</sub> -bath <sub>Pd</sub>	Ti	4000	3	2	PdCl <sub>2</sub>
Group II <sub>Ag</sub>	TAV <sub>4000</sub> - bath <sub>Ag</sub>	TAV	4000	3	2	AgCl
Group III	TiN-bath1 <sub>Pd</sub>	Ti	Colloidal silica	—	1	PdCl <sub>2</sub>
	TiN-bath1 <sub>Ag</sub>	Ti	Colloidal silica	—	2	AgCl

### 1.4. Step 3: Biocompatibility step

Bioactivity and biostability of the formed layers during coating steps were evaluated by examining the apatite-forming ability on the substrate during incubation in a simulated body fluid (SBF) with ionic concentrations nearly equal to those of human blood plasma.

Table 15. Ionic concentration (mM) of SBF1 and SBF1.5 in comparison with human blood plasma [Kokubo and Takadama, 2006].

	Ionic concentration (mM)							
	Na <sup>+</sup>	K <sup>+</sup>	Mg <sup>2+</sup>	Ca <sup>2+</sup>	Cl <sup>-</sup>	HCO <sub>3</sub> <sup>-</sup>	HPO <sub>4</sub> <sup>2-</sup>	SO <sub>4</sub> <sup>2-</sup>
Human blood plasma	142.0	5.0	1.5	2.5	103.0	27.0	1.0	0.5
SBF1	142.0	5.0	1.5	2.5	147.8	4.2	1.0	0.5
SBF1.5	213.0	7.5	2.3	3.8	221.7	6.3	1.5	0.8

According to Kokubo's design the SBF solution ISO 23317, buffered at pH 7.4 with trimethanol aminomethane-HCl, is nearly equal to those in human body blood plasma as shown in **Table 15**.

### 1.4.1. Preparation of SBF

To prepare SBF polyethylene beaker (1000 ml) should be used. At the beginning, 700 ml of dd water. was set in the water bath on the magnetic stirrer. The water in the beaker was heated to  $(36.5 \pm 1.5)^\circ\text{C}$  with stirring.

The reagents were dissolved in the following order: sodium chloride (NaCl, SIGMA-ALDRICH, S7653), sodium bicarbonate ( $\text{NaHCO}_3$ , SIGMA-ALDRICH H, S6297), potassium chloride (KCl, SIGMA-ALDRICH, P9333), potassium phosphate dibasic trihydrate ( $\text{K}_2\text{HPO}_4 \cdot 3\text{H}_2\text{O}$ , SIGMA-ALDRICH), magnesium chloride hexahydrate ( $\text{MgCl}_2 \cdot 6\text{H}_2\text{O}$ , SIGMA-ALDRICH, M2670), 39 ml of 1M of HCl, calcium chloride ( $\text{CaCl}_2$ , SIGMA-ALDRICH, c1016-100G) and sodium sulphate ( $\text{Na}_2\text{SO}_4$ , SIGMA-ALDRICH) in water at  $(36.5 \pm 1.5)^\circ\text{C}$  one by one, then a small amount of Tris (tris-hydroxymethyl aminomethane) and HCl were used to adjust the pH at 7.5 at  $37.5^\circ\text{C}$  [Kokubo and Takadama, 2006].

The SBF solution was replenished during the soaking period of 48 h for Groups Ia and III, and each 7 days for the other groups. All samples were immersed simultaneously in freshly prepared SBF solution for several periods according to their group. Alloys in solutions were kept in a water bath at a constant temperature of  $37^\circ\text{C}$ . Each sample was immersed vertically in order to avoid the aggregation of the solution precipitates on its surface. The volume of SBF used is calculated according to the following equation:

$$V_s = \frac{S_a}{10} \quad \text{Eq. 9}$$

where  $V_s$  is the volume of SBF (ml) and  $S_a$  is the apparent surface area of the sample ( $\text{mm}^2$ ) [Kokubo and Takadama, 2006].

## 2. Characterisations of the biolayer

The phosphate, hydroxyl, and carbonate *groups forming* the deposited layers were investigated by Fourier transform infrared in reflection mode (FT-IR, Thermo Nicolet, Madison, WI).

*Crystalline structures* of the deposited coatings were examined by thin film X-ray diffraction (TF-XRD) analysis. The coatings were scanned in the standard  $\theta$ - $2\theta$  geometry from  $5$  to  $50^\circ$  with a  $0.01^\circ$  step sizes and 5 s dwell time.

The coated layers on the metal substrates were scratched, collected on a copper grid and then examined by TEM (TOPCON 002B, 200 kV, CCD camera). Images of different areas of the samples and selected area electron diffraction pattern (SAED) were recorded. The lattice distances were measured and compared to the International Centre for Diffraction Data base (ICDD) for phase's determination.

The *morphologies* of the sample surfaces were examined after coating with carbon films, using a field emission scanning electron microscopy (FESEM, JEOL 6700F) equipped with an energy dispersive spectroscopy (EDS-X) unit at 3 kV accelerating voltage. EDS-X analysis were performed at 7 kV on  $10 \mu\text{m} \times 10 \mu\text{m}$  area and repeated three times at least.

$R_a$  and  $R_q$  corresponding to the mean *roughness* and the root mean square roughness values, respectively were calculated using confocal microscopy. To reach this aim, several scans of  $0.5 \times 0.5 \text{ mm}^2$  were performed over the surface with a  $2 \text{ }\mu\text{m}$  step and a frequency of 300 Hz. The resolution is about 80 nm and the accuracy about  $0.1 \text{ }\mu\text{m}$ .

The *stability of the forming layer* was examined by measuring  $\text{Ca}^{2+}$  and P ions in SBF after immersion of each treated sample. Biochemical analyses of Ca and P ions in SBF solutions left after each soaking periods were performed using biochemical kits (Centronic GmbH, Germany) and spectrophotometer (Jenway LTD, U.K.) or by using *ICP-AES*. The pH changes of SBF solutions due to the soaking of the specimens were measured by pH meter (SCHOTT instrument, Lab 850).

# Chapter 3

## Results and Discussions

The results with their respective discussions are presented into four main parts. **Part I** concerns the pretreated substrates (NaOH treatment followed by heat treatment), while **Part II**, **Part III** and **Part IV** describe the pretreated substrates (Part I) followed by immersion in acidic bath, alkaline bath and oxidant baths, respectively. PdCl<sub>2</sub> or AgCl catalysts (**Table 16**) were employed in the three baths. Moreover, as described in **Fig. 14** different substrates (TAV or Ti) and different surface's states (400 or 4000 grit) were used.

Table 16. Substrate, buffer layer and catalyst used in each group

Group	Substrate	Buffer layer	Catalyst used
Group I	TAV and Ti	Sodium titanate	PdCl <sub>2</sub>
Group II	TAV	Sodium titanate	AgCl
Group III	Ti	TiN	PdCl <sub>2</sub> and AgCl

## PART I. Pretreated metallic substrates

In this part we clarify the pretreatment steps done to create the samples before immersion in different baths. **Table 17** gives the prefixes of each sample used in *Part I* and their corresponding treatments.

Table 17. Sample notation of pretreated substrates. (Duration of SBF is in day: d).

Substrate	Grit of SiC	Pretreatment steps			Biomimetic bath				Sample notation
		Etching	NaOH	Heating rate (°C/minute)	SBF1 (4 d)	SBF1.5 (2 d)	SBF1 (7 d)	SBF1 (14 d)	
Ti-6Al-4V	400	—	—	—	—	—	—	—	TAV <sub>400</sub> -C
		yes	—	—	—	—	—	—	TAV <sub>400</sub> -K
		yes	yes	—	—	—	—	—	TAV <sub>400</sub> -A
		yes	yes	10	—	—	—	—	TAV <sub>400</sub> -1h
		yes	yes	3	—	—	—	—	TAV <sub>400</sub> -3h
		yes	yes	10	yes	—	—	—	TAV <sub>400</sub> -1h-SBF1
		yes	yes		yes	yes	—	—	TAV <sub>400</sub> -1h-SBF1.5
		yes	yes	3	yes	—	—	—	TAV <sub>400</sub> -3h-SBF1
	yes	yes	yes		—	—	—	TAV <sub>400</sub> -3h-SBF1.5	
	4000	—	—	—	—	—	—	—	TAV <sub>4000</sub> -C
		yes	—	—	—	—	—	—	TAV <sub>4000</sub> -K
		yes	yes	—	—	—	—	—	TAV <sub>4000</sub> -A
		yes	yes	3	—	—	—	—	TAV <sub>4000</sub>
		yes	yes	3	—	—	yes	—	TAV <sub>4000</sub> -SBF1*
Ti CP-3	4000	yes	yes	3	—	—	—	—	Ti <sub>4000</sub>
		yes	yes	3	—	—	—	yes	Ti <sub>4000</sub> -SBF2**

SBF1\* indicates the immersion in SBF for 7 days; SBF2 \*\* indicates the immersion in SBF for 14 days

### 1. Morphological analysis of alkaline (NaOH) pretreated substrates

**Figure 17** exhibits the surface morphology of Ti-6Al-4V after the pretreatment steps cleaning (denoted TAV<sub>4000</sub>-C), etching (denoted TAV<sub>4000</sub>-K) and NaOH treatment (denoted TAV<sub>4000</sub>-A) as presented in **Table 17**. **Fig. 17(a)** showed that the grinded surface by SiC 400 had several deep grooves after cleaning. **Fig. 17(b)** (grinded by SiC 4000) had lower roughness and a smoother surface. The chemical composition in **Fig. 17(c)** proved that both samples consist of Ti, Al and V.

Surface morphologies of TAV<sub>400</sub> and TAV<sub>4000</sub> after etching with Kroll's reagent are presented in **Fig. 17(d)** and **Fig. 17(e)**. At a higher magnification (inserted in **Fig. 17(f)**), one can tell that the presence of V structures seems to resist Kroll's etching. EDS-X analysis (**Fig. 17(f)**) shows the background (in red) composed principally of Ti, Al and V ions and the grains (in blue) with a higher amount of V.

After NaOH treatment (**Fig. 17(g)**), both substrates had similar surface morphology, very dissimilar to the one observed after etching (**Fig. 17(d)** and **Fig. 17(e)**). **Fig. 17(g)** shows that a hydrogel layer of porous network structures was formed on the surfaces due to the alkaline treatment (with a porosity less than 200 nm) as shown in inserted image in **Fig. 17(h)**. Such treatment produced a layer of approximately few  $\mu\text{m}$  thick containing  $\text{Na}^+$  and  $\text{Ti}^{4+}$  ions, made of  $\text{TiO}_2$  and sodium titanate with some rose-like structure growing out of the porous background (**Fig. 17(i)**). This morphology was similar to that reported by Jonášová et al. (2004). This formed layer was mainly composed of sodium titanate as shown in **Fig. 17(h)**. We can conclude from EDS-X analysis that the hydrogel layer was thick enough due to the absence of Al and V elements, which were previously detected in the last step on the substrate.

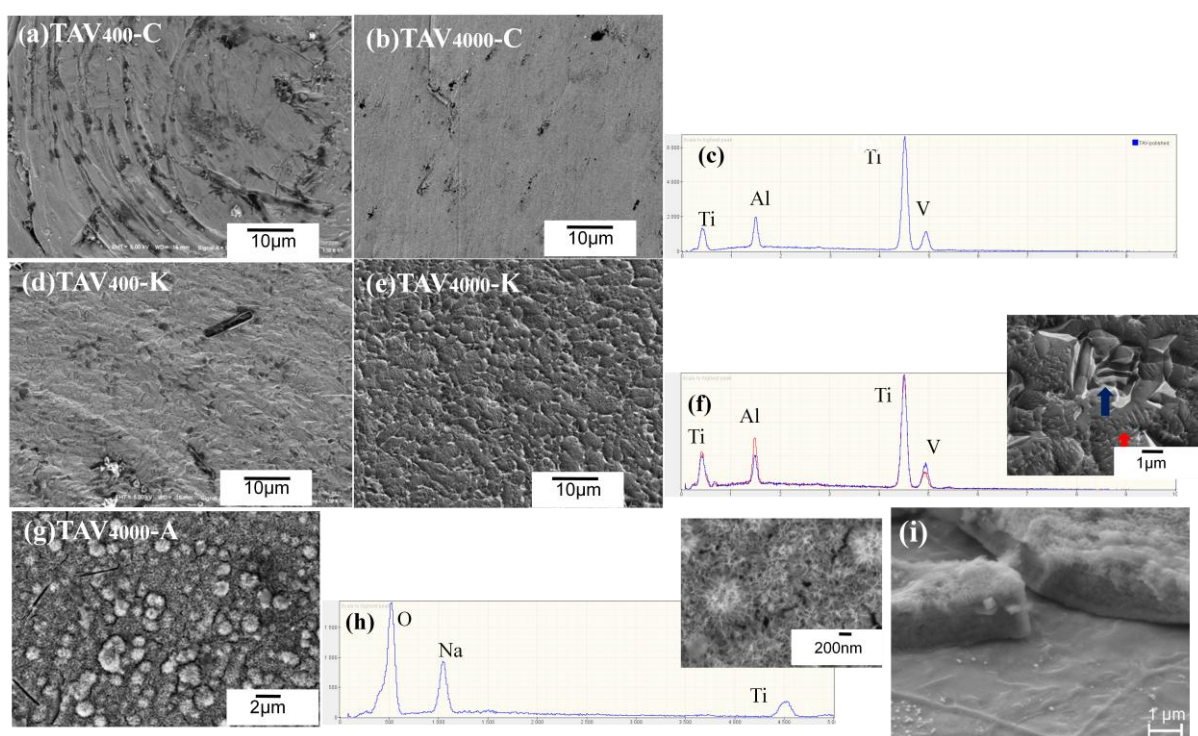


*Figure 17. FESEM images of TAV polished and cleaned; after chemical etching and NaOH treated and their corresponding EDS-X analyses. Sample's notation is given in **Table 17**.*

After the alkaline treatment, each sample was heat treated as a last step of the pretreatment steps before immersing in the autocatalytic baths. Heat treated samples were used as *control samples*.

Heat treated substrates - subjected to heating rate of  $10^\circ\text{C}/\text{minute}$  (denoted TAV<sub>400</sub>-1h in **Table 17**) and  $3^\circ\text{C}/\text{minute}$  (denoted TAV<sub>400</sub>-3h) - were showed in **Fig. 18(a,b)** and **Fig. 18(d,e)** respectively. A porous network was clearly observed in both figures similar to the one observed before in **Fig. 17(g)** with some rose-like structure growing out of the porous background but with a clear and larger porosity of ca. 200 nm.

Numerous cracks were observed (**Fig. 18(b,e)**). They were located in the reticulated structure with a uniform shape and size for both heating regimes. Lee et al. (2002) reported that the formation of this porous structure on the surfaces of alkali-treated titanium alloys could be because of the local corrosion of Ti-6Al-4V surface by the  $\text{OH}^-$  radical. It was also reported [Lee et al., 2002] that titanium alloy exhibits superior corrosion resistance in a strong corroding environment like acids and alkalis because of an excellent passivation film [Fontana, 1987]. However, corrosion resistance tends to deteriorate rapidly as the temperature and concentration of the corroding solution increases. So titanium alloys showed poor corrosion resistance when maintained in a strong alkaline solution with high concentration at 60 °C and a lot of reacted hydrogen gases were observed on the surface of polished titanium alloy specimens when they were soaked in the alkaline solution.

As shown in **Fig. 18(g,h)**, similar porous hydrogel layer with some rose-like morphology was proved by reducing the roughness (increasing the used SiC grit 4000) in addition to the presence of some platy structure growing out of the porous background. EDS-X analysis (**Fig. 18(i)**) proved that both background and plates are composed of sodium titanate, however, the plates had higher amount of  $\text{Na}^+$  ions.

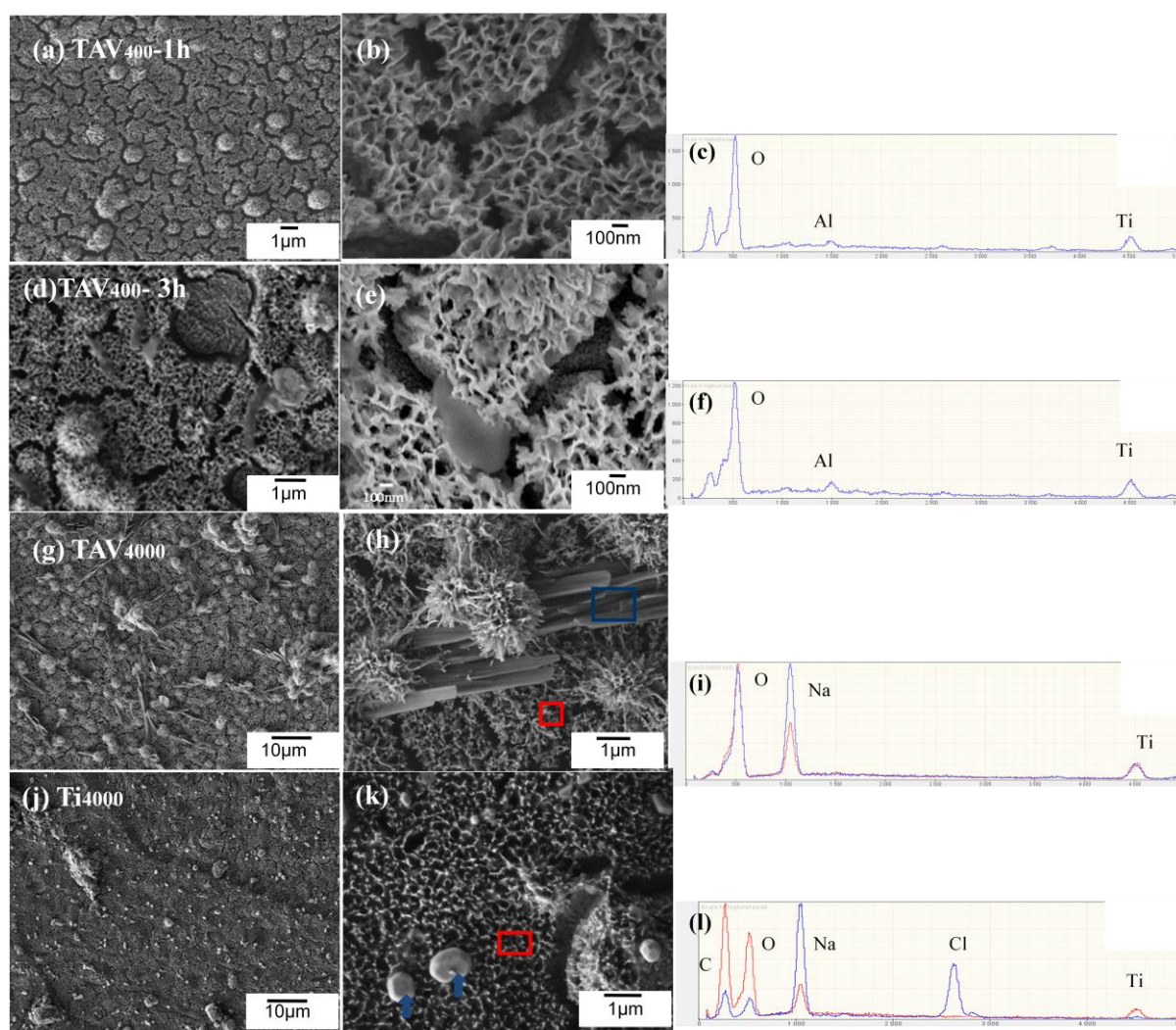


Figure 18. FESEM images of TAV<sub>400</sub> and TAV<sub>4000</sub> with two heating rate (10 and 3°C/minute) and their corresponding EDS-X analyses. Sample's notation is given in Table 17.

The surface of Ti substrate after NaOH and heat treatments (denoted Ti<sub>4000</sub>, **Table 17**) presented in **Fig. 18(j)** was completely covered with a homogenous layer. At higher magnification (**Fig. 18(k)**), this layer seems to be porous with fused layer filling these pores (red), in addition to presence of some cubes of NaCl (blue) spreaded on the surface. EDS-X analyses clarify that the homogenous layer was sodium titanate layer while the other one, which fills the pores, is suggested to be sodium carbonate (**Fig. 18(l)**).

From the above results, we can conclude that alkaline treatment followed by heat treatment lead to the formation of sodium titanate layer, as shown in **Fig. 18**. This kind of morphology can help the integration of the implants due to its porous nanostructured surface which imitates the natural structures of cortical bone. It, therefore, allows designing titanium implants having reduced risks of failure [Hulander et al. 2011].

For biocompatibility testing, each sample was immersed in SBF for different periods for the biomimetic coating method as reported [Kokubo and Takadama, 2006].

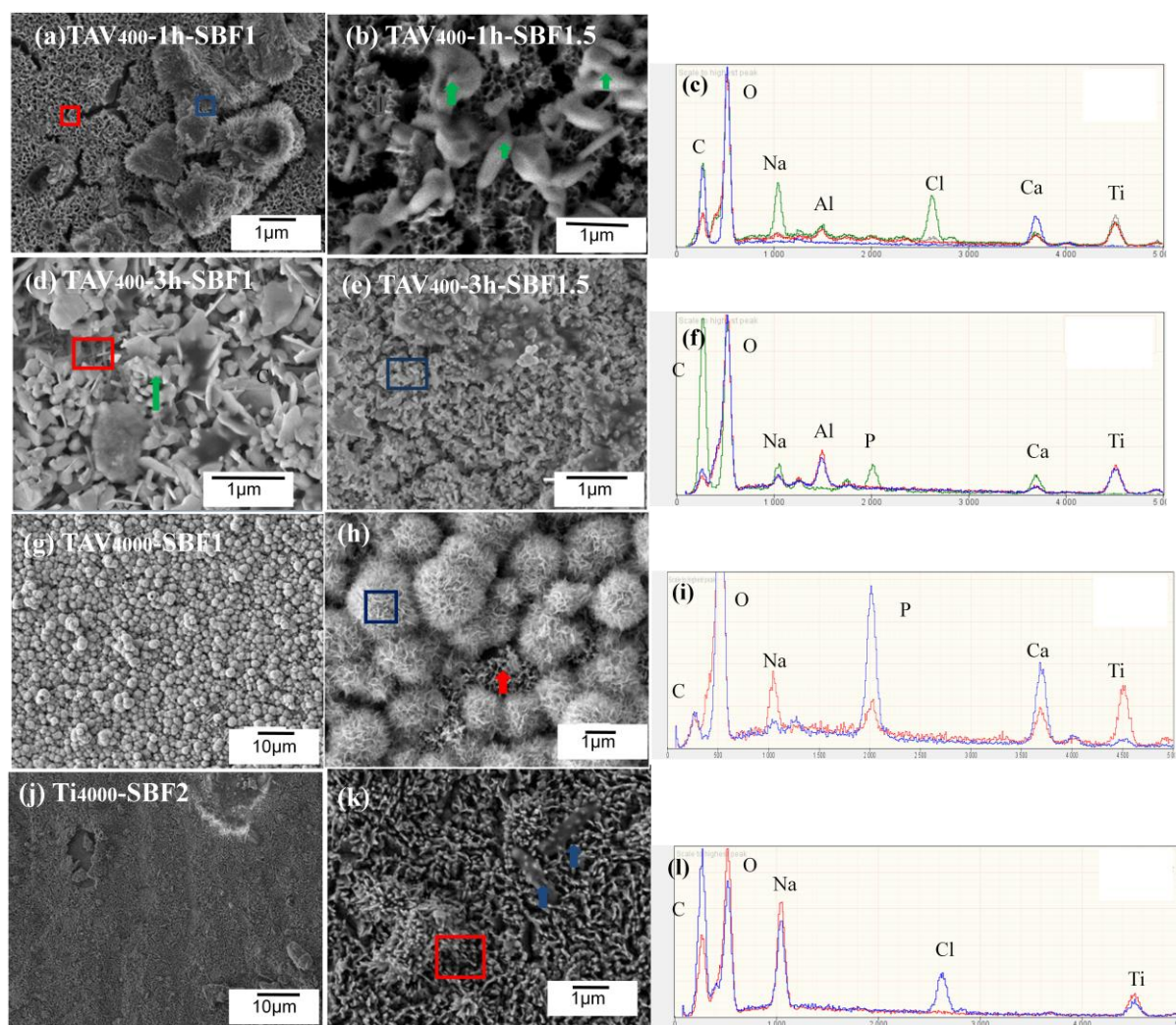


Figure 19. FESEM images of (a) TAV<sub>400</sub>-1h after immersion 4 d in SBF1, (b) TAV<sub>400</sub>-1h-SBF1 after immersion another 2 d in SBF1.5, (d) TAV<sub>400</sub>-3h after immersion 4 d in SBF1, (e) TAV<sub>400</sub>-3h-SBF1 after immersion additional 2 d in SBF1.5, (g,h) TAV<sub>4000</sub> immersed in SBF for 7 d, (j,k), Ti<sub>4000</sub> immersed in SBF for 14 d and (c,f,i,l) their corresponding EDS-X analyses.

After immersing the sample TAV<sub>400</sub>-1h in SBF1 for 4 days, **Fig. 19(a)** proves that the surface still had the same morphology as it was observed before the immersion (**Fig. 18(a,b)**), with a similar porous network, while compact agglomerates were recorded (**Fig. 19(a)**, blue) lying on the surface. This structure was mainly composed of CaCO<sub>3</sub> as confirmed by EDS-X analysis (**Fig. 19(c)**, blue). The porous background is principally composed of Ti and O elements with small amounts of Ca. After immersion of TAV<sub>400</sub>-1h-SBF1 for another 2 days in SBF1.5, **Fig. 19(b)** showed that the surface still had similar morphology and chemical composition as before immersion. Nevertheless, some individual and fused NaCl crystals were also observed as shown in **Fig. 19(b,c)** green).

The morphology of TAV<sub>400</sub>-3h after immersion in SBF1 for 4 days (**Fig. 19(d)**) was completely different compared to the reference sample (**Fig. 18(d,e)**). At this time, it was not clear which SBF's mechanism was responsible of the morphological transformation from heat-treated surface to the one observed after SBF immersion.

The surface of the sample TAV<sub>400</sub>-3h-SBF1 presented some Ca-P aggregates (**Fig. 19(d)**, green) dispersed in a network of tabular crystals containing Na, Ti and O (**Fig. 19(d)**, red). Finally, the sample TAV<sub>400</sub>-3h-SBF1 immersed for additional 2 days in SBF1.5 (**Fig. 19(e)**) looked more compact compared to TAV<sub>400</sub>-3h-SBF1. It seems that there was dissolution of the Ca-P aggregates and a reduction of tabular crystals. This is accompanied by reduction of P and Ca elements as detected by SEM-EDS-X (**Fig. 19(f)**, blue).

Another morphology was observed after immersion of TAV<sub>4000</sub> in SBF1 for 7 days, **Fig. 19(g,h)** showing that sodium titanate hydrogel layer, formed in **Fig. 18(g,h)**, was able to induce island-like precipitations consisting of needle-like crystallites as reported in other research as Kim et al.(1999) and Kokubo et al. (2010). It was confirmed from EDS-X that these islands (blue) were Ca, Na and P precipitations while the background was sodium titanate (red, **Fig. 19(i)**).

Relatively to the substrate Ti<sub>4000</sub> - being immersed in SBF for 14 days - **Fig. 19(j,k)** showed a similar morphology and composition as observed in **Fig. 18(j,k)**. Here sodium titanate layer failed to induce any phosphate precipitations and this could be explained due to the pores were filled preventing, therefore, ionic exchange.

It can be concluded from the above results that modification of titanium implant surfaces by alkaline and heat treatments were able to induce porous nanostructured morphology which could help the integration of the implants, according to the following mechanism:

During SBF soaking, the Na<sup>+</sup> ions released from the hydrogel layer via exchange with H<sub>3</sub>O<sup>+</sup> or H<sup>+</sup> ions produced in the surrounding fluid resulted in Ti-OH layer formation [Fatehi et al., 2008]. This was ascribed to induce apatite nucleation via incorporation of Ca<sup>2+</sup> or increasing the OH<sup>-</sup> concentration. The consumption of H<sub>3</sub>O<sup>+</sup> causes an increase in the pH concentration and an increase in apatite formation. The positively charged Ca<sup>2+</sup> may act as nucleation sites for carbonate-hydroxyapatite formation by attaching themselves to the negatively charged (PO<sub>4</sub><sup>3-</sup>) and (CO<sub>2</sub><sup>3-</sup>) to form Ca-P enriched surface layer which crystallizes into bone-like apatite (carbonate hydroxyapatite) [Jonásová et al., 2004].

## 2. Topological analysis of alkaline (NaOH) pretreated substrates

To complete the interpretation of the effects produced by the mechanical polishing and chemical treatment on the surface of the substrates, topographical studies to provide evidences of the surface roughness of the coatings were undertaken. **Figure 20** shows the relevant changes in surface

topography over areas of  $0.5 \times 0.5 \text{ mm}^2$ . It is clear that upon using 400 SiC grit, the  $R_a$  and  $R_q$  are higher than the values with 4000 grit. The  $R_a$  roughness values (**Fig. 20(a)**) are 10 times that in **Fig. 20(b)**. After etching step (kroll reagent), the roughness of TAV<sub>400-K</sub> (**Fig. 20(c)**) decreased due to the formation of a layer which seems to fill the grooves observed after polishing as shown in its SEM (**Fig. 17(d)**). While in case of TAV<sub>4000</sub> (**Fig. 20(d)**) the roughness increased due to the presence of some structures resisting etching as shown in its SEM (**Fig. 17(e)**). The roughness of TAV<sub>400</sub> and TAV<sub>4000</sub> is shown in **Fig. 20(e,f)**. After alkaline treatment and consequently, the formation of the hydrogel layer had similar values (**Fig. 17(g)**).

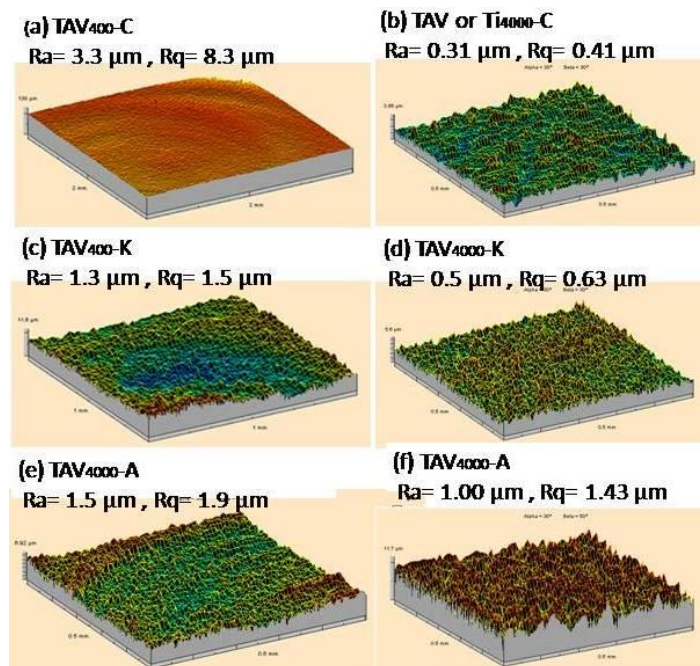


Figure 20. Confocal 3D images of roughness TAV polished and cleaned (a and b), after chemical etching (c, d) and after alkaline treatment (e, f).

The value recorded for the mean roughness  $R_a$  of the sample treated for one hour (**Fig. 21(a)**) is slightly higher than the values of mean roughness  $R_a$  obtained for samples treated for 3 h (**Fig. 21 (d,g)**). A reduction of both  $R_a$  and  $R_q$  values was detected after immersion in SBF (**Fig. 21(b,e)**) because of a transformation of the porous morphology into a more compact one due to deposition as proved by their SEM (**Fig. 18(j)**). Similarly, TAV<sub>4000</sub> treated for 3 h attained nearly half their values upon SBF immersion (**Fig. 21(e,f)**). The situation is nearly the same after immersion in SBF (**Fig. 21(c, f)**). Roughness values on Ti<sub>4000</sub> surface are of the same order of magnitude before and after SBF (**Fig. 21(i,j)**). Its detailed SEM morphology proves that it is completely covered with a homogenous layer (**Fig. 18(j)**).

It was reported that roughness values ranging between 1-10  $\mu\text{m}$ , maximize the interlocking between mineralized bone and the implant surface and this range of roughness (1-10  $\mu\text{m}$ ) is preferable. Several studies supported by some clinical evidences suggested that the micron-level surface topography leads to greater accretion of bone at the implant surface [Junker et al., 2009, Shalabi et al., 2006]. Other reports suggested that a moderate roughness of 1-2  $\mu\text{m}$  can be used to limit the problems detected by using high roughness, such as an increase in peri-implant as well as an increase in ionic leakage [Albrektsson and Wennerberg, 2005]. Other reports introduced by Wennerberg et al. (1995; 1998) have shown that a surface roughness in this range resulted in greater bone to- implant contact and higher resistance to torque removal than other roughness values.

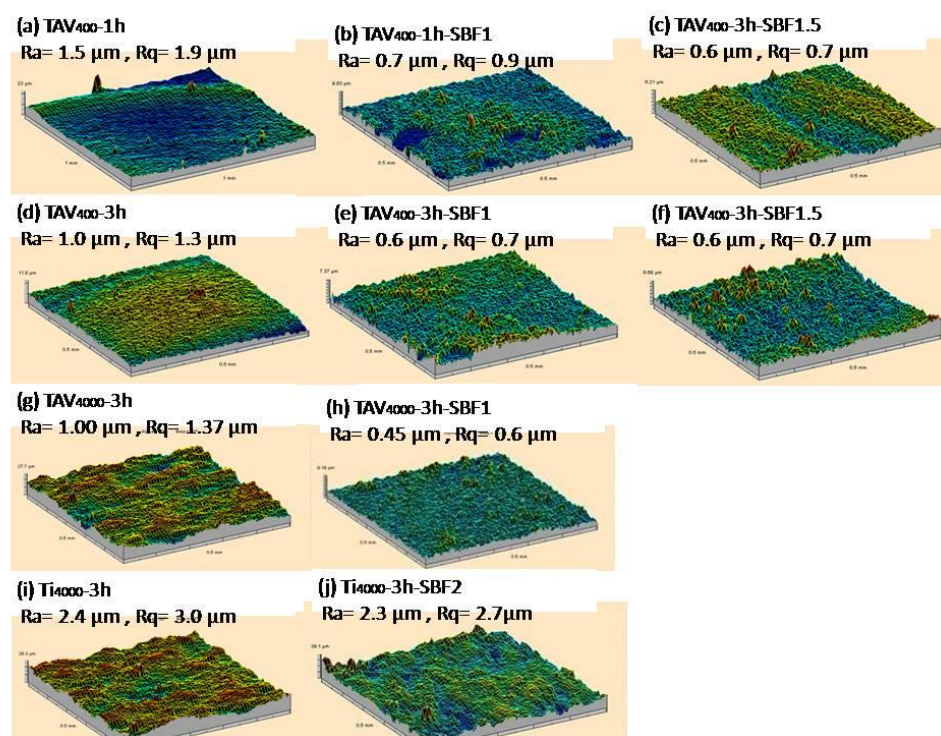


Figure 21. Confocal 3D images of roughness  $TAV_{400}$  subjected to a heating rate  $10^{\circ}\text{C}/\text{minute}$  (a), and its immersion in SBF1 and SBF1.5 (b,c),  $TAV_{400}$  subjected to heating rate  $3^{\circ}\text{C}/\text{minute}$  (d), its immersion in SBF1 and SBF1.5 (e,f);  $TAV_{4000}$  subjected to a heating rate of  $3^{\circ}\text{C}/\text{minute}$  (g), its immersion in SBF (h),  $Ti_{4000}$  subjected to a heating rate  $3^{\circ}\text{C}/\text{minute}$  (i) and its immersion in SBF (j).

### 3. Structural analysis of pretreated samples

The formed layer was subjected to FT-IR study, after the bath and SBF, in order to confirm the presence of phosphate, carbonate and hydroxyl groups. **Fig. 22** showed FT-IR spectra of all substrates after immersion in SBF only since before SBF (after heat treatment only), no significant bands could be detected.

**Fig. 22(a)** showed FT-IR spectra of  $TAV_{400-1h}$  after immersion in SBF1 and SBF1.5. Two bands at  $546$  and  $589\text{ cm}^{-1}$  were identified in both spectra; these two bands are originating from  $\nu_4$  bending vibration of  $\text{PO}_4^{3-}$ . This last one becomes sharper after immersion for 1 h in SBF1.5. Moreover, the  $\nu_3$  stretching vibration of  $\text{PO}_4^{3-}$  ( $1042\text{ cm}^{-1}$ ) was observed only after immersion in SBF1.5. The  $\text{HPO}_4^{2-}$  group was represented by two small peaks at  $719$  and  $758\text{ cm}^{-1}$  in 1h-SBF1, and also detected at  $778\text{ cm}^{-1}$  in 1h-SBF1.5 [Abdel-Fattah et al., 2011]. The two tiny peaks at  $1458$  and  $1513\text{--}1554\text{ cm}^{-1}$  corresponded to  $\nu_3$  vibrational mode of carbonate group ( $\text{CO}_3^{2-}$ ) in  $TAV_{400-1h}\text{--SBF1}$ . These are also detected for sample  $TAV_{400-1h}\text{--SBF1.5}$  with an increasing sharp peak at  $1591\text{ cm}^{-1}$ . Additionally, the existence of  $\nu_2$  vibrational mode  $\text{CO}_3^{2-}$  after SBF1.5 were proven by Barinov et al. (2006) to be an indicator of the biolayer formation. The  $\text{OH}^-$  group after immersion in SBF1.5 bands at  $3700$  and  $3665\text{ cm}^{-1}$  were detected. This  $\text{OH}^-$  group could stimulate the growth of phosphate groups on the treated surface.

After changing heating rate, **Fig. 22(b)** shows the presence of  $\nu_4$  bending vibration of  $\text{PO}_4^{3-}$  at  $527$  and  $577\text{ cm}^{-1}$  which were a bit reduced and shifted after immersion in SBF1.5. Furthermore,  $\nu_3$  stretching

vibration  $\text{PO}_4^{3-}$  was detected both in  $\text{TAV}_{400}\text{-3h-SBF1}$  and  $\text{TAV}_{400}\text{-3h-SBF1.5}$  samples with a difference: the tiny peak at  $1175\text{ cm}^{-1}$  was splitted into two peaks at  $1069$  and  $1218\text{ cm}^{-1}$  after immersion in SBF1.5.

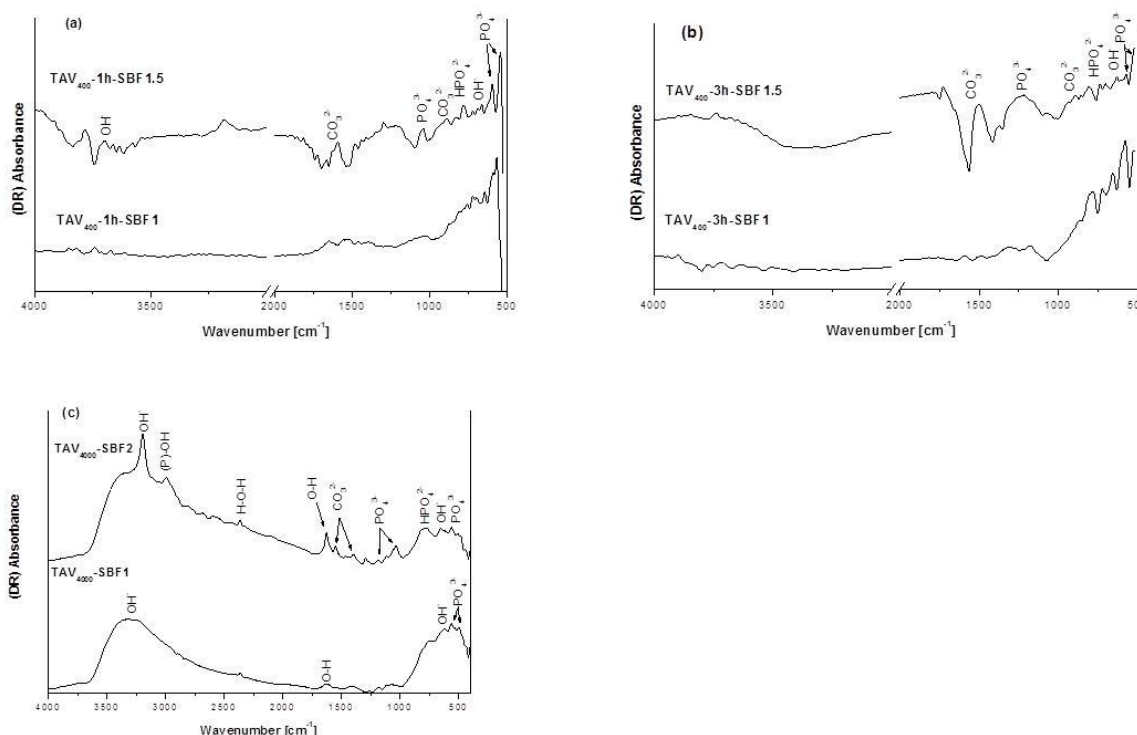


Figure 22. FT-IR Spectra of (a)  $\text{TAV}_{400}$  subjected to heating rate  $10^\circ\text{C}/\text{minute}$ , (b)  $3^\circ\text{C}/\text{minute}$  after immersing in SBF1 followed by SBF1.5 for 4 and 2 d and (c)  $\text{TAV}_{4000}$  after immersing in SBF1 for 7 and 14 d.

The growth of a broad band around  $1218\text{ cm}^{-1}$  could be linked to the P–O asymmetric  $\nu_3$  stretching mode of  $\text{PO}_4^{3-}$  group which may indicate a deviation of the ideal tetrahedral structure of the phosphate group. The presence of  $\text{HPO}_4^{2-}$  peaks at  $724$  and  $781\text{ cm}^{-1}$  after SBF1 were shifted to  $700$  and  $738\text{ cm}^{-1}$  after SBF1.5. The  $\text{TAV}_{400}\text{-3h-SBF1}$  sample presented two tiny peaks also at  $1489$  and  $1590\text{ cm}^{-1}$ , corresponding to the  $\nu_3$  vibrational mode of  $\text{CO}_3^{2-}$ . After immersion in SBF1.5, they appear as a unique peak at  $1504\text{ cm}^{-1}$  with an increased intensity.

Fig. 22(c) showed FT-IR spectra of  $\text{TAV}_{4000}$  after immersion in SBF for one and two weeks. The presence of  $\nu_4$  bending vibration of  $\text{PO}_4^{3-}$  was identified in the region of  $500\text{-}560\text{ cm}^{-1}$  in both spectra. Furthermore, several bands of brushite, dicalcium phosphate dihydrate (DCPD;  $\text{CaHPO}_4\cdot 2\text{H}_2\text{O}$ ) were detected but only after immersion for two weeks in SBF ( $\text{TAV}_{4000}\text{-SBF2}$ ) [Kwon et al., 2003; Kumta et al., 2005]. Brushite bands were detected at  $560\text{ cm}^{-1}$  for O–P–O  $\nu_4$  bending mode and  $1170\text{ cm}^{-1}$  for P–O  $\nu_3$  stretching mode of  $\text{PO}_4^{3-}$  beside a band at  $790\text{ cm}^{-1}$  originating from P–O–H bending of  $\text{HPO}_4^{2-}$  in addition to another new band at  $2950\text{ cm}^{-1}$  which represents the (P)O–H stretching. A broad OH band was detected at  $3100\text{-}3480\text{ cm}^{-1}$ , while the band at  $2355\text{ cm}^{-1}$  was assigned to the combination of H–O–H.

In biological apatites, some of  $\text{PO}_4^{3-}$  ions are replaced by  $\text{CO}_3^{2-}$  ions. The peak position of  $\nu_3$  vibrational mode depends on whether the  $\text{CO}_3^{2-}$  ions substitute for  $\text{OH}^-$  or  $\text{PO}_4^{3-}$  in the hydroxyapatite lattice [Stoch et al., 2003]. In fact, a slight increase of phosphate group vibration was observed in

**Fig. 22(a)**, whereas it was not detected by SEM-EDS-X analysis. FT-IR studies allowed us to conclude that after SBF1.5, the quantity of  $CO_3^{2-}$  groups has strongly increased and this was confirmed by EDS-X analysis on TAV<sub>400</sub>-1h-SBF1.5 in **Fig. 19(c)**.

One could conclude that, heat treated samples (3°C/minute) was successful to form Ca-P precipitation on TAV<sub>400</sub> after 7 days, but this forming layer has not completely covering the pretreated surface. In order to enhance Ca-P coating after only 2 h, autocatalytic baths have been tested and presented in next sections..

### Conclusion of Part I

To create bioactivity on titanium alloy, the state of the metallic surface changed by mechanical chemical and thermal treatments. After grinding, the surface of Ti and its alloys were immersed in alkaline NaOH solution followed by different regimes of heat treatment. The obtained surface morphology was optimized by the growth of porous sodium titanate layer. In particular, it was observed that the present specific NaOH treatment and a subsequent heat treatment (1 and 3 h) allowed formation of a layer with high specific surface which permits the formation of Ca-P and compact CaCO<sub>3</sub> agglomerates once immersed in SBF. Moreover, the formation of Ca-P after 4 days in SBF1 was observed only for the 3 h heat-treated samples, while the formation of Ca-P appeared after the SBF1.5 immersion for the 1 h heat-treated sample. Finally, the results suggest that a temperature rise of 3°C/minute allows a successful build-up of sodium titanate network, more favourable to a stable growth of Ca-P and CaCO<sub>3</sub> biolayer compared to the other one (10°C/minute).

## Part II: Sample treated by acidic bath

The aim of this part is to deposit Ca-P layer by an autocatalytic *acidic bath* on metallic implant in order to form in a way that is similar to the process of natural bone formation. The inorganic composition of this chemical bath is given in **Table 13**. After the metallic surface pretreatment (Part I), substrates from Groups I, II and III were immersed in acidic bath, and continuously agitated by a magnetic stirrer for 2 h. Then the samples were washed with bi-distilled water and dried at room temperature over night and kept in the desiccator for analyses. A complete list of the treated specimens is given in **Table 18**.

### 1. Structural analysis of samples after treatment with acidic bath

To examine the structural analysis of the phases forming the coating, substrates were analysed by thin film X-ray diffractometry (TF-XRD) and TEM and SAED analyses after the scratching of the coatings with a diamond pen.

#### 1.1. Group I

**Figure 23** shows FT-IR spectra of TAV<sub>400</sub> with different heating rates for 1 and 3 h, TAV<sub>4000</sub> and Ti<sub>4000</sub> (for heating rate 3h) after 2 h in acidic bath, then followed by different immersion in SBF (**Table 18**).

In **Fig. 23(a)**, the band at 541 cm<sup>-1</sup> originating from  $\nu_4$  *bending vibration* of PO<sub>4</sub><sup>3-</sup> group was detected, with additional two bands of HPO<sub>4</sub><sup>2-</sup> at 700 and 770 cm<sup>-1</sup>, are identified in TAV<sub>400-1h-AcPd</sub>. The presence of *carbonate group* was assigned by the detection of  $\nu_2$  *vibrational mode* of CO<sub>3</sub><sup>2-</sup> group at 866 cm<sup>-1</sup> after the acidic bath (TAV<sub>400-1h-AcPd</sub>).

After immersion in SBF for 4 days (**Fig. 23(a)**, TAV<sub>400-1h-AcPd-SBF1</sub>), the peak of  $\nu_4$  *bending vibration* for PO<sub>4</sub><sup>3-</sup> group shifted at 580 cm<sup>-1</sup> and only one band of HPO<sub>4</sub><sup>2-</sup> group was detected. Finally, after additional 2 days in SBF1.5 (**Fig. 23(a)**, TAV<sub>400-1h-AcPd-SBF1.5</sub>),  $\nu_4$  *bending vibration* of PO<sub>4</sub><sup>3-</sup> group was still present, with the presence of  $\nu_3$  *stretching vibration* for PO<sub>4</sub><sup>3-</sup> at 1050 cm<sup>-1</sup>. A new peak begins to grow at 729 cm<sup>-1</sup> characteristic for HPO<sub>4</sub><sup>2-</sup>.

**Figure 23(b)** demonstrates the presence of  $\nu_4$  *bending vibration* of PO<sub>4</sub><sup>3-</sup>-derived bands recorded at 520, 588 cm<sup>-1</sup> in TAV<sub>400-3h-AcPd</sub>. Also a new band of  $\nu_3$  *stretching vibration* of PO<sub>4</sub><sup>3-</sup> was also identified at 1028 and 1066 cm<sup>-1</sup>. These last bands were shifted and increased after immersion in SBF1 for 4 days. Moreover, four peaks at 700, 737, 758, and 795 cm<sup>-1</sup> represent HPO<sub>4</sub><sup>2-</sup> group. It was observed that the peak at 758 cm<sup>-1</sup> disappeared after immersion in SBF1 (TAV<sub>400-3h-AcPd-SBF1</sub>) [Mohammed et al., 2012b; Abdel-Fattah et al., 2011].

Table 18. Complete series of sample (Group I, II and III) treated with acidic autocatalytic bath.

Group	Substrate	Grit of SiC	Pretreatment steps		Acidic Ac bath (h)	Biomimetic bath				Sample notation	
			Intermediate layer	Heating rate (°C/minute)		SBF1 (4 d)	SBF1.5 (2 d)	SBF1 (7 d)	SBF1 (14 d)		
Group I PdCl <sub>2</sub>	Ti-6Al-4V	400	Na <sub>x</sub> Ti <sub>y</sub> O <sub>z</sub> H <sub>t</sub>	10	2	—	—	—	—	TAV <sub>400</sub> -1h-AcPd	
				3		—	—	—	—	TAV <sub>400</sub> -3h-AcPd	
				10		yes	—	—	—	TAV <sub>400</sub> -1h-AcPd-SBF1	
				3		yes	—	—	—	TAV <sub>400</sub> -3h-AcPd-SBF1	
				10		yes	yes	—	—	TAV <sub>400</sub> -1h-AcPd-SBF1.5	
				3		yes	yes	—	—	TAV <sub>400</sub> -3h-AcPd-SBF1.5	
		4000	Na <sub>x</sub> Ti <sub>y</sub> O <sub>z</sub> H <sub>t</sub>	3	2	—	—	—	—	TAV <sub>4000</sub> -AcPd	
						—	—	yes	—	TAV <sub>4000</sub> -AcPd-SBF1*	
						—	—	yes	yes	TAV <sub>4000</sub> -AcPd-SBF2**	
		Group I PdCl <sub>2</sub>	Ti CP-3	4000	Na <sub>x</sub> Ti <sub>y</sub> O <sub>z</sub> H <sub>t</sub>	3	2	—	—	—	—
—	—							yes	—	Ti <sub>4000</sub> -AcPd-SBF1*	
—	—							yes	yes	Ti <sub>4000</sub> -AcPd-SBF2**	
Group III PdCl <sub>2</sub>	Ti CP-1	Colloidal silicas	TiN	—	1	—	—	—	—	TiN-Ac1Pd	
					2	—	—	—	—	TiN-Ac2Pd	
					1	yes	—	—	—	TiN-Ac1Pd-SBF1	
					2	yes	—	—	—	TiN-Ac2Pd-SBF1	
					1	yes	yes	—	—	TiN-Ac1Pd-SBF1.5	
					2	yes	yes	—	—	TiN-Ac2Pd-SBF1.5	
							<b>SBF (3 d)</b>	<b>SBF (7d)</b>	<b>SBF (14 d)</b>		
Group II AgCl	Ti-6Al-4V	4000	Na <sub>x</sub> Ti <sub>y</sub> O <sub>z</sub> H <sub>t</sub>	3	2	—	—	—	—	TAV <sub>4000</sub> -AcAg	
							yes	—	—	—	TAV <sub>4000</sub> -AcAg-SBF
							yes	yes	—	—	TAV <sub>4000</sub> -AcAg-SBF1*
Group III AgCl	Ti CP-1	Colloidal silicas	TiN	—	2	—	—	—	—	TiN-AcAg	
					2		—	yes	—	TiN-AcAg-SBF1*	
					2		—	yes	yes	TiN-AcAg-SBF2**	

SBF1\* indicates the immersion in SBF for 7 days; SBF2\*\* indicates the immersion in SBF for 14 days

After the immersion in SBF1.5 for 2 days, the  $\text{PO}_4^{3-}$  group presented the  $\nu_4$  bending vibration,  $\nu_2$  bending vibration and  $\nu_3$  stretching vibration for the same group were detected, with the presence of two bands characteristic for  $\text{HPO}_4^{2-}$  after SBF1.5 (TAV<sub>400</sub>-3h-Ac<sub>Pd</sub>-SBF1.5). These vibrational modes of  $\text{CO}_3^{2-}$  group are identified after immersion in SBF 4 days according to the growth of the peak at  $1500\text{ cm}^{-1}$ , which is also validated by the detection of  $\nu_2$  vibrational mode at  $891\text{ cm}^{-1}$  (TAV<sub>400</sub>-3h-Ac<sub>Pd</sub>-SBF1.5). The formation of biolayer is proved by the presence of  $\nu_2$  vibrational mode  $\text{CO}_3^{2-}$  [Mohammed et al., 2012b; Barinov et al., 2006].

The stretching and bending vibrations of hydroxyl  $\text{OH}^-$  group were distinguished before and after immersion in SBF (stretching bands at  $3404$  and  $3744\text{ cm}^{-1}$ ), respectively and bending band at  $645\text{ cm}^{-1}$ . The  $\text{OH}^-$  group could stimulate the growth of the phosphate groups onto the surface; this band is shifted and grew broad post immersion in SBF1.

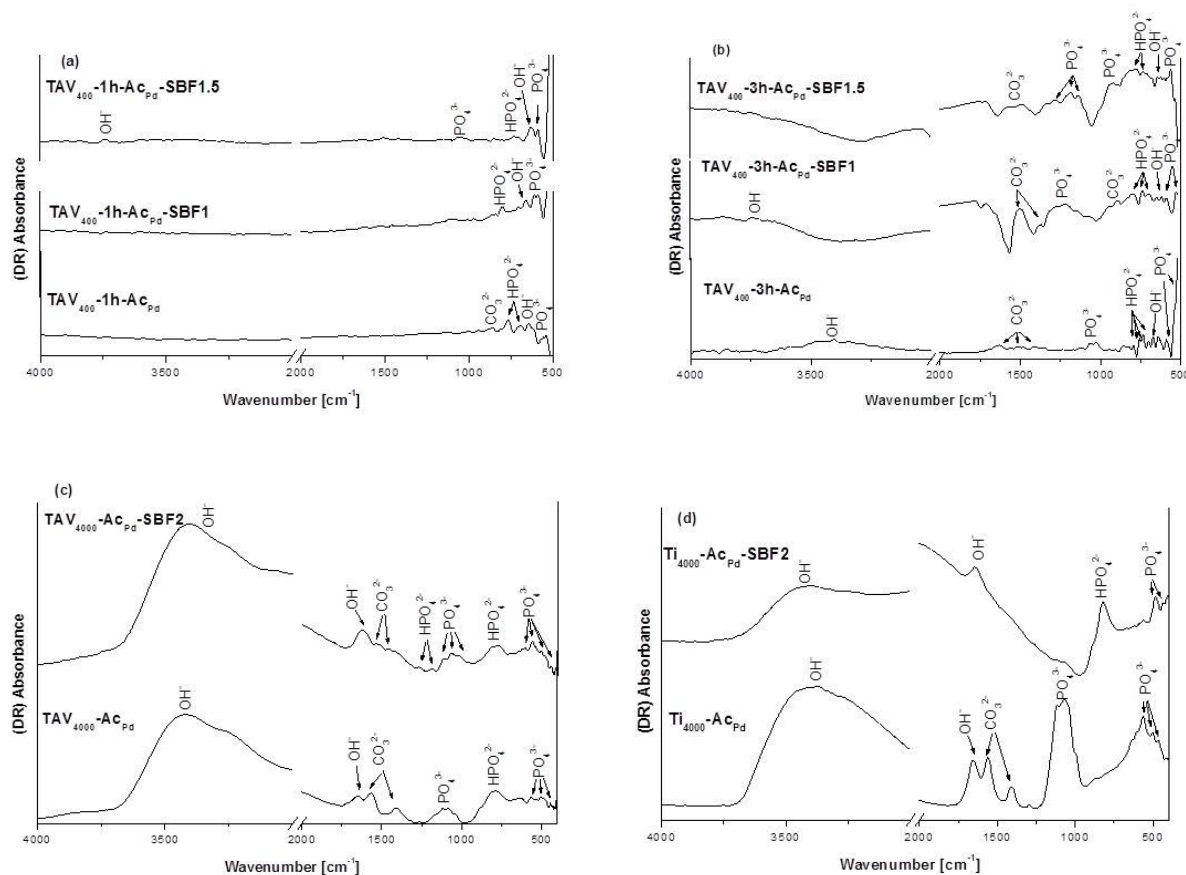


Figure 23. FT-IR spectra after immersing 2 h in acidic bath followed by immersion in SBF (a) TAV<sub>400</sub> subjected to 1h heat treatment. (b) TAV<sub>400</sub>, (c) TAV<sub>4000</sub> and (d) Ti<sub>4000</sub> were subjected to 3 h heat treatment.

The presence of the bands assigned to the asymmetric  $\nu_3$  stretching modes  $\text{P-O}$ , detected between  $1030\text{--}1120\text{ cm}^{-1}$  before (TAV<sub>4000</sub>-Ac<sub>Pd</sub>) and after SBF (TAV<sub>4000</sub>-Ac<sub>Pd</sub>-SBF1) in Fig. 23(c). These recorded bands were overlapped in TAV<sub>4000</sub>-Ac<sub>Pd</sub> and triply degenerated to small bands at  $1020$ ,  $1060$ , and  $1111\text{ cm}^{-1}$  in TAV<sub>4000</sub>-Ac<sub>Pd</sub>-SBF1. They correspond to Octa Calcium Phosphate (OCP) as suggested by Leeuwenburgh et al. (2006). The bands assigned to  $\nu_2$  and  $\nu_4$  bending modes of  $\text{P-O-P}$  were recorded within range of  $430\text{--}500\text{ cm}^{-1}$  and  $560\text{--}620\text{ cm}^{-1}$ , respectively. Moreover,  $\delta_{\text{OH}}$  mode of hydrogen bonded  $\text{HPO}_4^{2-}$  of OCP were identified at  $1196$  and  $1236\text{ cm}^{-1}$  [Leeuwenburgh et al., 2006;

Abdel-Fattah and Elkhooly, 2010]. The  $\text{CO}_3^{2-}$  was recorded in the range of  $1400\text{-}1560\text{ cm}^{-1}$ , but decreased after SBF1 due to dissolution. Additionally, in  $\text{TAV}_{4000}\text{-Ac}_{\text{Pd}}\text{-SBF1}$ , structural hydroxyl group band was observed at  $3400\text{-}3500\text{ cm}^{-1}$  and also at  $1630\text{ cm}^{-1}$ . The last one increased after immersing in SBF1.

In **Fig. 23(d)**  $\text{Ti}_{4000}$ , the asymmetric  $\nu_3$  stretching modes of P–O were detected at  $1030\text{-}1120\text{ cm}^{-1}$  in  $\text{Ti}_{4000}\text{-Ac}_{\text{Pd}}$ . These bands are characteristic of the OCP. The  $\nu_4$  bending mode P–O–P located at  $556\text{ cm}^{-1}$  and observed in  $\text{Ti}_{4000}\text{-Ac}_{\text{Pd}}$  but they disappeared after immersion in SBF ( $\text{Ti}_{4000}\text{-Ac}_{\text{Pd}}\text{-SBF2}$ ) [Wang et al., 2004]. In addition, the bands allocated to  $\nu_2$  bending mode were recorded within range of  $430\text{-}500\text{ cm}^{-1}$  before and after SBF. The presence of  $\text{CO}_3^{2-}$  bands at  $1414$  and  $1560\text{ cm}^{-1}$  are characteristic of B- and A- type of bone like carbonate apatite which may be due to substitute of  $\text{PO}_4^{3-}$  groups. Hydroxyl  $\text{OH}^-$  group was identified as a broad peak between  $3400\text{-}3500\text{ cm}^{-1}$  and also at  $1635\text{ cm}^{-1}$  ( $\text{Ti}_{4000}\text{-Ac}_{\text{Pd}}$ ). After the SBF,  $\text{HPO}_4^{2-}$  group grew into sharp peak at  $815\text{ cm}^{-1}$ .

TF-XRD recorded in the same conditions (scan range:  $2\theta = 10$  to  $50^\circ$ ) (**Fig. 24**) shows after acidic bath (red) and after immersion in SBF for 14 days (blue). **Fig. 24(a)** presents peaks at  $2\theta = 35.0, 38.7$  and  $40.2^\circ$  which come from the substrate as  $\alpha$  and  $\beta$ –Ti (ASTM-89-5009 and 89-4913). After immersion in SBF, no noticeable peaks for Ca-P layer could be detected.

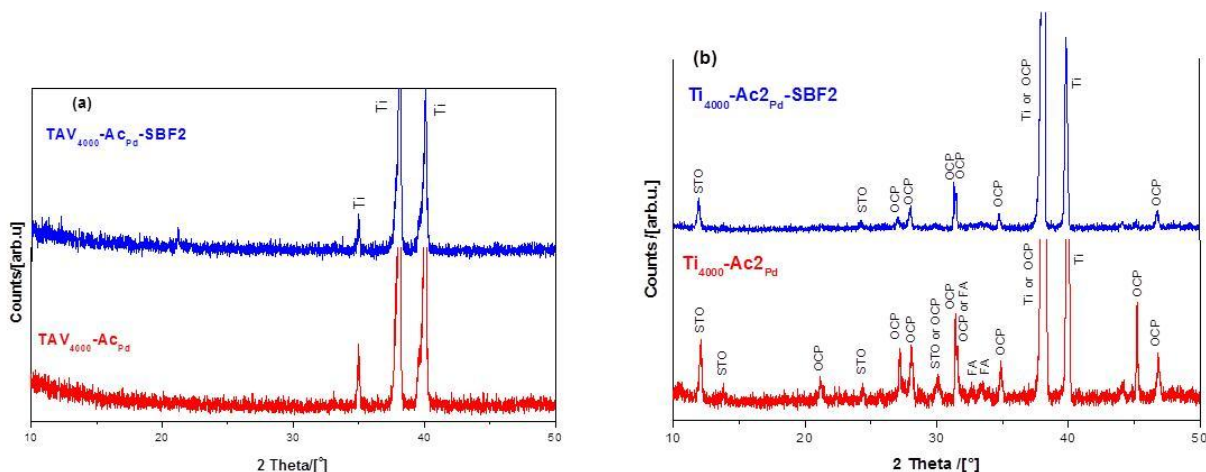


Figure 24. TF-XRD patterns for (a)  $\text{TAV}_{4000}$  and (b)  $\text{Ti}_{4000}$  after treatment in acidic bath for 2 h (red) and after immersion in SBF for 14 d (blue).

In the case of  $\text{Ti}_{4000}$  (**Fig. 24(b)**), the Ti substrate peaks were detected at  $2\theta = 40.1$  and  $38.3^\circ$  (ASTM-89-5009), in addition to some sodium titanium oxide peaks, (buffer interlayer, experimental procedure A) were noticed at  $2\theta = 12.05, 13.8, 30.9$  and  $24.5^\circ$  ( $\text{Na}_2\text{Ti}_7\text{O}_{15}$ , STO ASTM-76-1648). Finally, well crystalline OCP ( $\text{Ca}_8(\text{HPO}_4)_2(\text{PO}_4)_4\cdot 5\text{H}_2\text{O}$ ) ASTM-44-0778) peaks were found mixed with the ones of fluoroapatite (FA, ASTM-15-0876). After SBF, only STO and OCP patterns were detected.

Typical TEM examinations and EDS-X analyses of the scratched coatings are presented in **Fig. 25(a,c)** after 2 h in acidic bath, and after SBF for 14 days **Fig. 25(d,f)** respectively. Collected particles after acidic coating (**Fig. 25(a,d)**) appeared to be of micro sizes and selected area electron diffraction (SAED) patterns corresponded to a large amount of OCP particle as demonstrated in **Fig. 25(b,e)**. Planes of OCP being (232), (111) and (312) are recorded in (b) while those of (323) and (323) are recorded in **Fig. 25(c)** respectively.

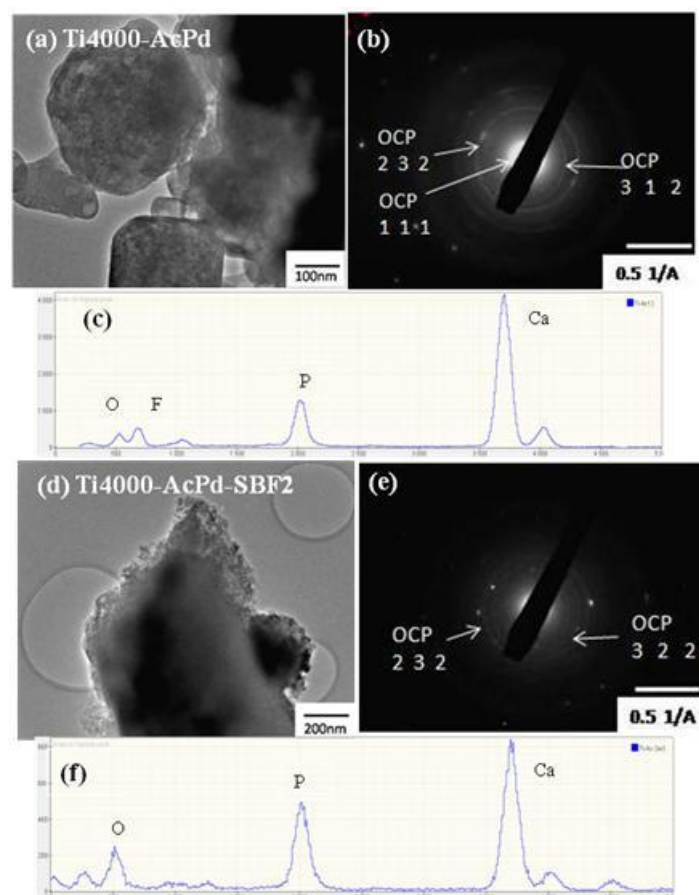


Figure 25. TEM images of the scratched coating  $Ti_{4000}\text{-AcPd}$  (a) and after SBF for 14 d (d), the corresponding SAED patterns (b,e) and their corresponding EDS-X analyses (c,f).

## 1.2 Group II

TF-XRD patterns of  $TAV_{4000}$  treated in acidic bath with AgCl as catalyst is denoted  $TAV_{4000}\text{-Ac}_{Ag}$  (Fig. 26). Diffraction peaks detected, after the bath, only identified the  $\alpha$  and  $\beta$ -Ti at  $2\theta = 35.0, 38.7$  and  $40.2^\circ$  (ASTM-89-5009 and 89-4913). Moreover, the existence of rutile (R,  $TiO_2$ ; ASTM-77-0446) can be validated by the presence of  $27.2$  and  $35.7^\circ$  peaks. They can come from the buffer interlayer. While, after immersing in SBF for 7 days ( $TAV_{4000}\text{-Ac}_{Ag}\text{-SBF1}$ ), some peaks recorded at  $2\theta = 32^\circ$  ( $31.8, 32.1$  and  $33^\circ$  overlapped peaks) and  $25^\circ$  can be attributed to hydroxyapatite (HA,  $Ca_{10}(PO_4)_6(OH)_2$ ; ASTM-89-7834).

TEM observation of the  $TAV_{4000}\text{-Ac}_{Ag}$  scratched coating; Fig. 27(a) rounded particles appear to be ranging between 100-400 nm in diameter. The asterisks in Fig. 27(a) indicate the centers of SAED (Fig. 27(b)) and their EDS-X analysis areas (Fig. 27(c)). EDS-X analysis (Fig. 27(c)) detected Ca, P, O and F elements (from the coating) and Na and Ti from the sodium titanate interlayer. Nevertheless, in SAED no phases of Ca-P was recorded and only the pattern of poly-crystalline coating composed of  $CaF_2$  crystal (ASTM-040864) could be observed.

TEM image (Fig. 27(d)) of the scratched layer of  $TAV_{4000}\text{-Ac}_{Ag}\text{-SBF1}$  showed oval coating within nano-metric range. The EDS-X of these coatings (Fig. 27(f)) identified similar elements which are Ca, P and O. SAED Fig. 27(e) proves the  $TAV_{4000}\text{-Ac}_{Ag}\text{-SBF1}$  layer is carbonated hydroxyapatite ( $Ca_{10}(PO_4)_3(CO_3)_3(OH)_2$ , ASTM-190272).

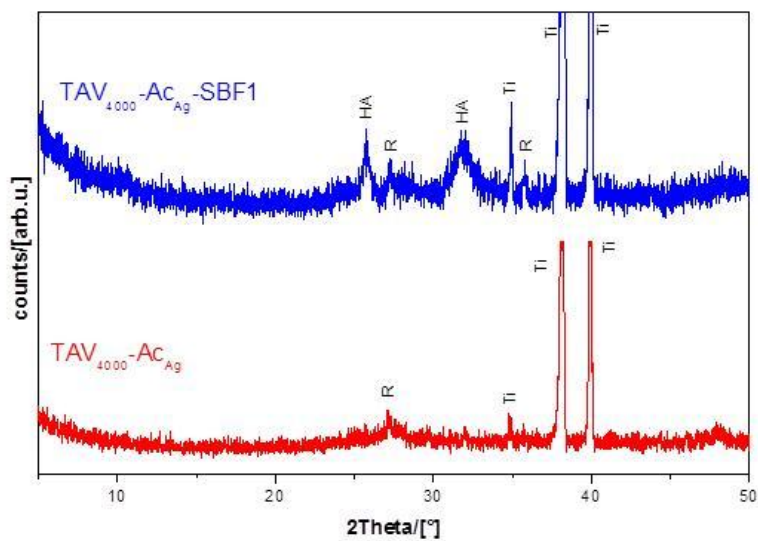


Figure 26. TF-XRD patterns for TAV<sub>4000</sub> after treatment in acidic bath with AgCl for 2 h (red) and after immersion in SBF for 7 d (blue).

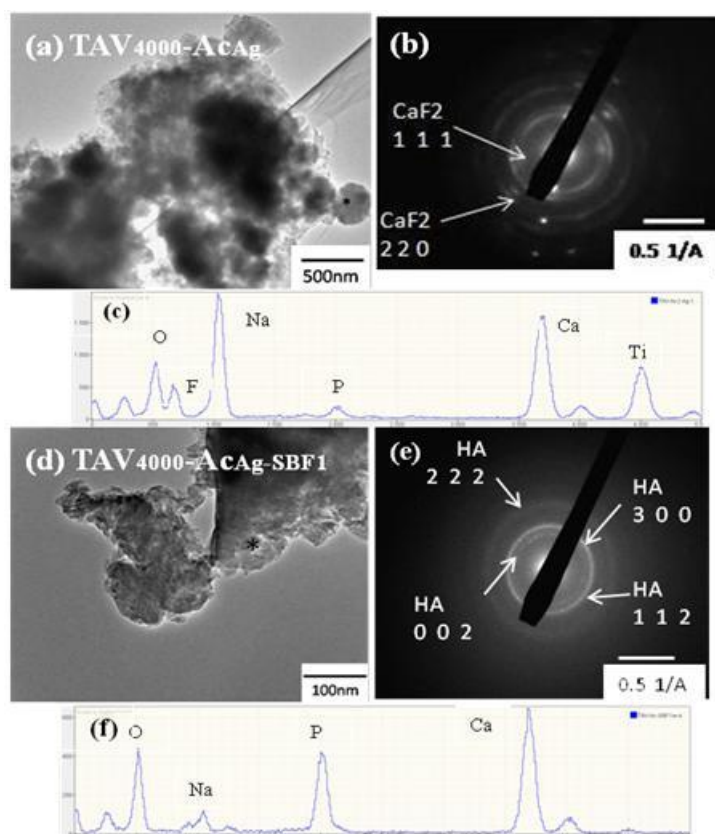


Figure 27. TEM images of Ca-P coatings (a) after 2 h in acidic bath with AgCl and d) after SBF1 for 7 d, (b,e) diffraction pattern and (c,f) corresponding EDS-X analyses.

### 1.3. Group III

The FT-IR spectrum (**Fig. 28(a)**) shows the formed layer on TiN (buffer layer) after immersion 1 h in acidic bath. The  $\nu_4$  bending vibration  $\text{PO}_4^{3-}$  at 557 and 600  $\text{cm}^{-1}$  after immersion in acidic bath were observed. These bands shifted after immersing in SBF1 to 521 and 575  $\text{cm}^{-1}$  then splitted into 4 sharp peaks post SBF1.5. While the  $\nu_3$  stretching vibration of  $\text{PO}_4^{3-}$  was observed growing as a broad band at 1134 and 1186  $\text{cm}^{-1}$  after immersion in SBF1.5. Concerning  $\nu_1$  stretching vibration of  $\text{PO}_4^{3-}$  cannot be observed in TiN-Ac1<sub>Pd</sub>-SBF1 but was detected as small peaks in TiN-Ac1<sub>Pd</sub> and begins to appear again as a broad shoulder in TiN-Ac1<sub>Pd</sub>-SBF1.5. Also the presence of  $\text{HPO}_4^{2-}$  peaks at 760 and 796  $\text{cm}^{-1}$  for TiN-Ac1<sub>Pd</sub> and at 734  $\text{cm}^{-1}$  in TiN-Ac1<sub>Pd</sub>-SBF1 while the presence at 734 and 767  $\text{cm}^{-1}$  is recorded after SBF1.5.

The occurrence of a broad band at 1480  $\text{cm}^{-1}$  in TiN-Ac1<sub>Pd</sub>-SBF1 was originating from  $\nu_3$  vibrational mode of  $\text{CO}_3^{2-}$  which decreased and divided into 2 peaks at 1481 and 1584  $\text{cm}^{-1}$  after immersion in SBF1.5 beside the band of  $\nu_2$  vibrational mode of  $\text{CO}_3^{2-}$  in the last sample. The detection of a peak at 670  $\text{cm}^{-1}$  was characteristic to the presence of Ti-N from the intermediate layer [Mark et al., 2006].

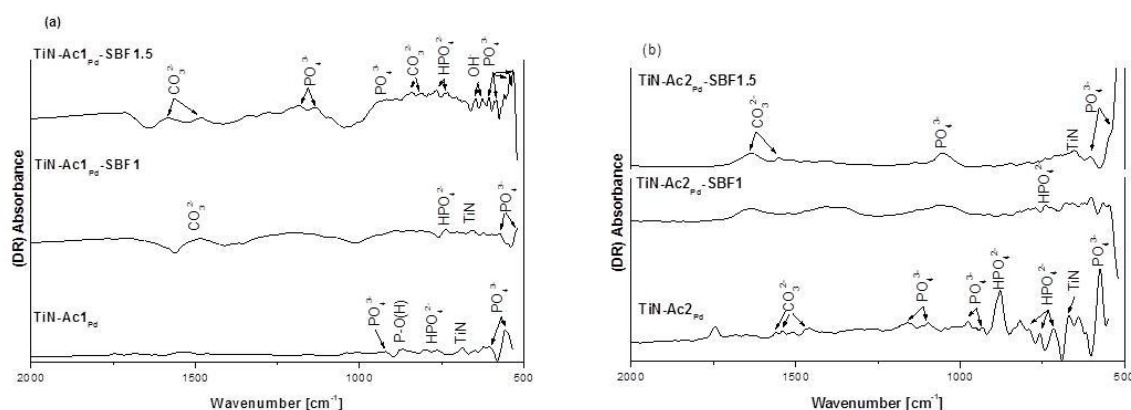


Figure 28. FT-IR spectra of TiN (a) after 1 h, (d) after 2 h in acidic bath followed to immersion in SBF1 and SBF1.5.

The presence of  $\nu_4$  bending vibration for  $\text{PO}_4^{3-}$  group at 570  $\text{cm}^{-1}$  after immersion for 2 h in acidic bath (TiN-Ac2<sub>Pd</sub>) **Fig. 28(b)**. After immersion in SBF1 (TiN-Ac2<sub>Pd</sub>-SBF1) this peak was divided into three faint peaks and after SBF1.5 (TiN-Ac2<sub>Pd</sub>-SBF1.5) in two other ones.

Furthermore,  $\nu_3$  stretching vibration of  $\text{PO}_4^{3-}$  was observed after bath treatment (TiN-Ac2<sub>Pd</sub>) as small peaks at 1048, 1096 and 1156  $\text{cm}^{-1}$ ; they became sharp peaks after immersion in SBF1 (TiN-Ac2<sub>Pd</sub>-SBF1) and SBF1.5 (TiN-Ac2<sub>Pd</sub>-SBF1.5) at 1064 and 1055  $\text{cm}^{-1}$  respectively.

Concerning  $\nu_1$  stretching vibration of  $\text{PO}_4^{3-}$ , a sharp peak was observed (TiN-Ac2<sub>Pd</sub>) and then it was distinguished as small peaks in TiN-Ac2<sub>Pd</sub>-SBF1 and TiN-Ac2<sub>Pd</sub>-SBF1.5. It means that this band begin to disappear after SBF.  $\text{HPO}_4^{2-}$  peaks at 716, 759, 789 and 817  $\text{cm}^{-1}$  were detected (TiN-Ac2<sub>Pd</sub>) while they slightly decreased after immersion in SBF1 at 738 and 769  $\text{cm}^{-1}$  and after SBF1.5 they disappeared.

$\text{CO}_3^{2-}$  group – originating from  $\nu_3$  vibrational mode – was identified by small peaks at 1460, 1506 and 1541  $\text{cm}^{-1}$  (TiN-Ac2<sub>Pd</sub>). They became a broad band at 1345-1405  $\text{cm}^{-1}$  and a sharp peak at 1633  $\text{cm}^{-1}$

after immersion in SBF1 (TiN-Ac<sub>2</sub>Pd-SBF1), then tiny peaks at 1396, 1466, 1551 and one sharp at 1631 cm<sup>-1</sup> after immersion in SBF1.5 (TiN-Ac<sub>2</sub>Pd-SBF1.5).

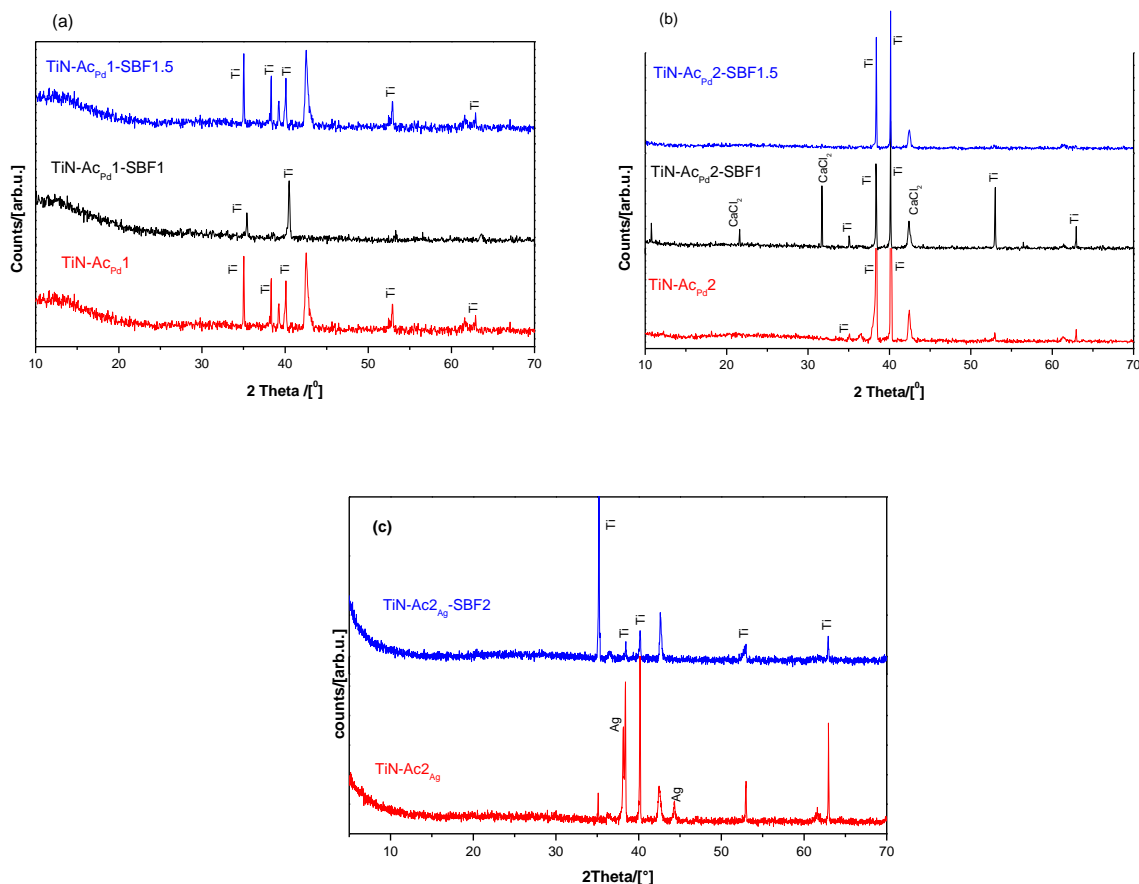


Figure 29. TF-XRD patterns for TiN after treatment in acidic bath (a) with PdCl<sub>2</sub> for 1 h (red), (b) with PdCl<sub>2</sub> for 2 h (red) followed by immersing in SBF1 for 4 d (black), then another 2 d in SBF1.5 (blue) and (c) with AgCl for 2 h (red) followed by immersion for 14 d in SBF1 (blue).

In **Fig. 29(a)**, XRD peaks at  $2\theta = 35.1, 38.4, 40.2, 53.0$  and  $63.0^\circ$  identified the Ti substrate (ASTM 89-4893). Ca-P layer was not noticed before or post SBF immersion. Same conclusions can be given for **Fig. 29(b)**. Nevertheless, some new peaks could be seen after immersion for 4 days in SBF1; they are characteristic for calcium chloride (CaCl<sub>2</sub>, ASTM-49-1092). No presences of Ca-P precipitations can be detected.

By changing the catalyst, **Fig. 29(c)**, similar peaks of crystal structure of Ti and TiN were recorded. After the acidic bath, new peaks were observed at  $38.1$  and  $44.3^\circ$  which were characterising the face centred Ag (ASTM-89-3722), these peaks of Ag disappeared after two weeks immersion in SBF proving released Ag.

**Figure 30** shows TEM image and EDS-X analysis of the Ti surfaces after soaking in acidic bath with AgCl for 2 h. **Fig. 30(a)**, (red arrow) illustrates several round particles with diameter of approximately 300-400 nm and squared shape particles (blue arrow). EDS-X analysis in **Fig. 30(b)** proved that they are mainly composed of Ag element mixed with minor amount of CaF (blue arrow). Then, after two weeks of SBF soaking no Ca-P was detected proving their dissolution.

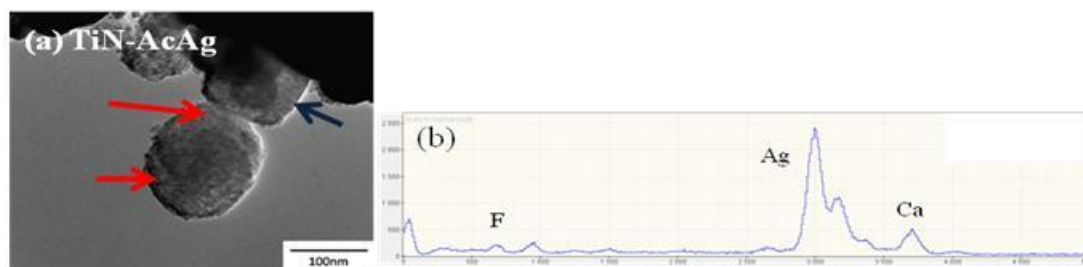


Figure 30. TEM image of scratch layer after 2h in Ac bath with AgCl (a) and its corresponding EDS-X analysis.

## 2. Morphological analysis of samples after treatment with acidic bath

### 2.1. Surface morphology of Group I

Surface morphology of TAV<sub>400</sub>-1h after immersion for 2 h in acidic bath is shown in **Fig. 31(a)**. TAV<sub>400</sub>-1h-Ac<sub>Pd</sub> proved that the surface was partially covered with compact nanometric spherules (**Fig. 31(b)**), which are mainly CaCO<sub>3</sub> as shown in EDS-X analysis (blue, **Fig. 31(c)**). These spherules contain high amount of Ca, C and O elements in this region, while the uncovered area (red, **Fig. 31(c)**) is mainly composed of Ti and Al from the substrate and tiny amount of Na and P elements.

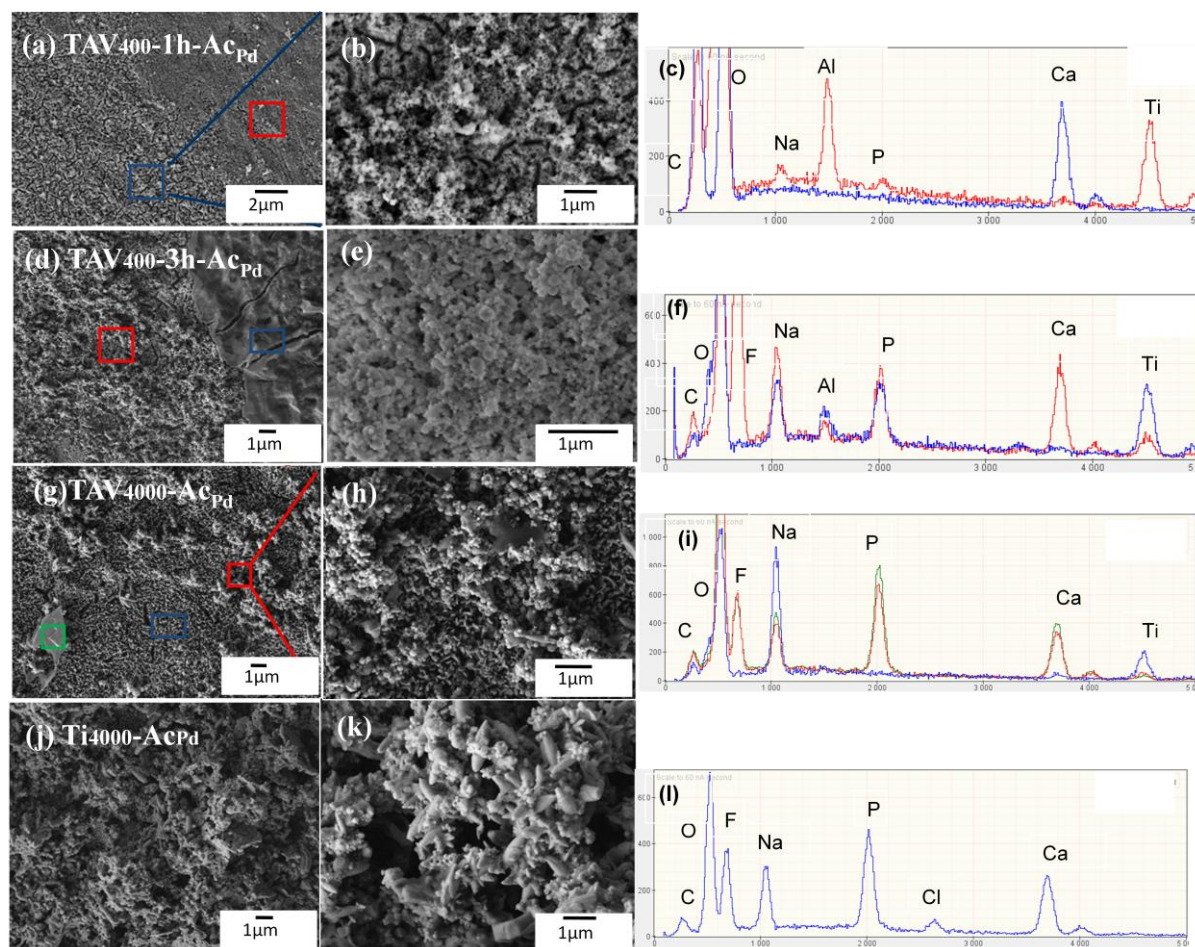


Figure 31. FESEM images of different substrates after immersion for 2 h in acidic bath: (a,b) TAV<sub>400</sub>-1h, (d,e) TAV<sub>400</sub>-3h, (g,h) TAV<sub>4000</sub>, (j, k) Ti<sub>4000</sub> and (c,f,i,l) their corresponding EDS-X analyses.

TAV<sub>400</sub>-3h (3°C/minute, **Fig. 31(d,e)**) presented a similar structure with nanometric compact spherules as observed in **Fig. 29(a,b)**. Moreover, a thin compact film covered the background. These spherules were a mixture of Na, Ca, F and P elements (red, **Fig. 31(f)**) while the film was composed of Na, P and O elements (blue, **Fig. 31(f)**). In both regions, Ti and Al are detected which means that this produced layer is thin.

**Fig. 31(g)** exhibits the surface morphology of TAV<sub>4000</sub> after immersion in acidic bath for 2 h (TAV<sub>4000</sub>-Ac<sub>Pd</sub>). Its surface was completely covered with a dense and uniform layer of sodium titanate (Al was not detected) arranged in vertical plates (blue, **Fig. 31(g, h)**). At higher magnification, one can note that these agglomerates are a mixture of CaF (cube with hole, **Fig. 31(h)**) with Na, Ca, F, P elements spindle shape and small spherules with the detection of another plate shape of similar composition (green, **Fig. 31(g)**) as shown in EDS-X analyses (**Fig. 31(i)**). Ca-P layer was observed on Ti<sub>4000</sub> after immersion for 2 h in acidic bath (**Fig. 31(j)**). This layer is uniform and dense as proved by the absence of Ti element by EDS-X analysis (**Fig. 29(i)**). At higher magnification (**Fig. 31(k)**), it was confirmed that this layer is made of spindle shape and small spherules similar to those observed in **Fig. 31(h)**. Moreover, TAV<sub>4000</sub> and Ti<sub>4000</sub> had similar coating morphology and compositions but with different distribution.

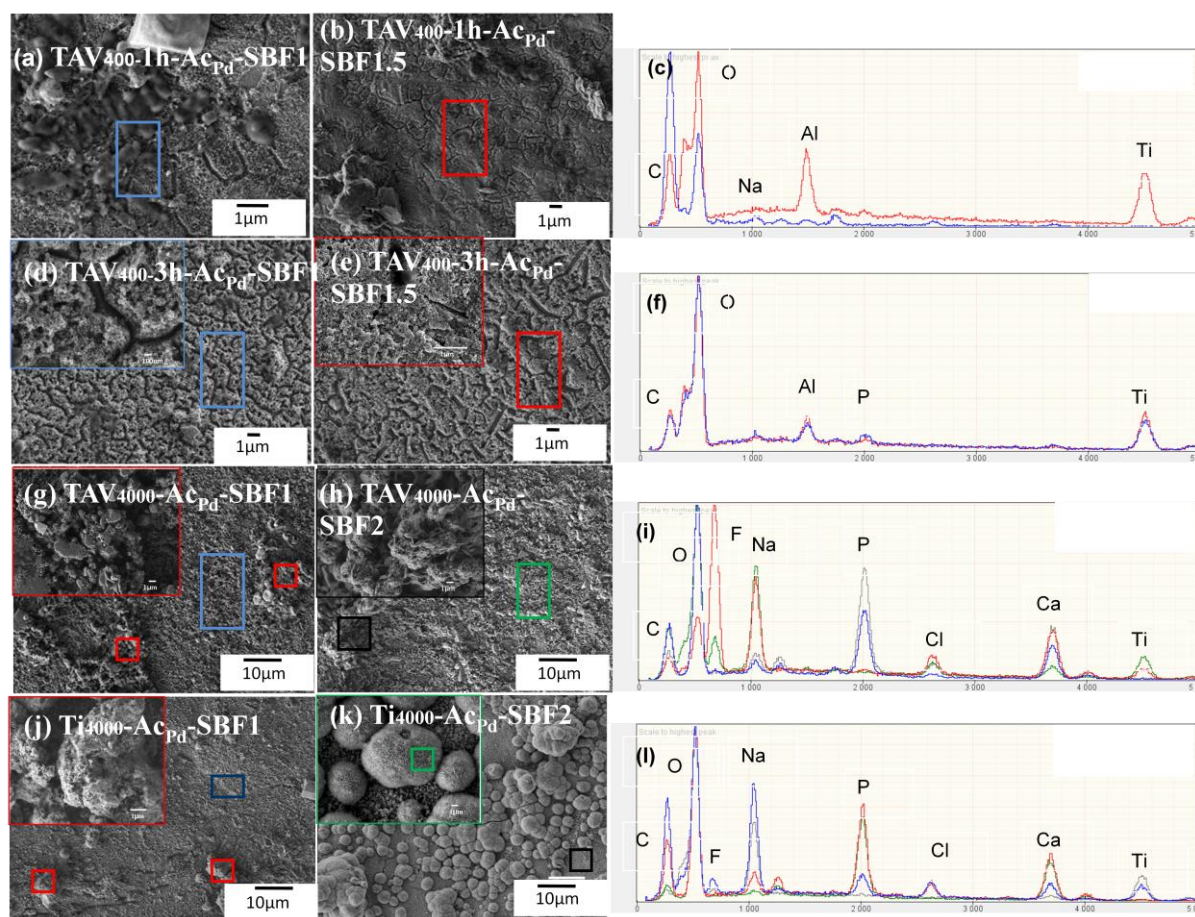


Figure 32. FESEM images of Group I after immersion for 2h in acidic bath followed by immersion in SBF1 for 4 d followed by another 2 d in SBF1.5 and their corresponding EDS-X analyses.

To check the stability of the formed layer, after immersion in acidic bath, each sample presented in **Fig. 31** was immersed in SBF for different periods as shown in the **Fig. 32**.

FESEM observations proved that all compact spherules observed in TAV<sub>400</sub>-1h-AcPd were dissolved. Ca or P elements (**Fig. 32(a)** and **(c, blue)**) after 4 days in SBF1 (TAV<sub>400</sub>-1h-AcPd-SBF1) were not detected. Compared to TAV<sub>400</sub>-3h-AcPd after immersion in SBF1 for the same period, the presence of a tiny amount P element was identified on the background (**Fig. 32(d, f)**).

By increasing the immersion time of both samples (TAV<sub>400</sub>-1h-AcPd-SBF1 and TAV<sub>400</sub>-3h-AcPd-SBF1) for another 2 days in SBF1.5, the surface of TAV<sub>400</sub>-1h-AcPd-SBF1.5 became bare as proved in **Fig. 32(b)** and **(c, red)**. However, TAV<sub>400</sub>-3h-AcPd-SBF1.5 still had a similar morphology and composition recorded in **Fig. 32(d, f)**; one can conclude that the immersion time (4 days in SBF1 followed by another 2 days in SBF1.5) is not enough to preserve or rebuild Ca-P layer. To avoid this drawback, the immersion time in SBF was increased up to two weeks in the following samples.

After immersion of TAV<sub>4000</sub>-AcPd in SBF for 7 days (**Fig. 32(g)**), the background still had the same morphology observed in **Fig. 31(g)**. It is mainly composed of sodium titanate (**Fig. 32(i)**, red) with a network of Ca, P and O elements (**Fig. 32(g)** inserted, and **(i)** blue) and some plates dipped in this network. Raising the immersion time for another 1 week (**Fig. 32(h)**), the background is still composed of sodium titanate with decreasing Ca elements when compared with previous one in addition to the existence of similar network of Ca-P (**Fig. 32(h)** inserted, grey). It seems that there is dissolution of the Ca-P aggregates. A reduction of P and Ca in backgrounds was identified by EDS-X analysis (**Fig. 32(i)**, green), but this reduction was observed only in the background, but both samples had similar network.

Ti<sub>4000</sub>-AcPd after immersion in SBF for 7 days (**Fig. 32(j)**) showed only a sodium titanate background (EDS-X, **Fig. 32(i)**, blue), clearly proving that the homogenous Ca-P layer recorded in **Fig. 31(ik)** were completely dissolved. Furthermore, the presence of some aggregates spread on the surface was observed. They are mainly composed of Ca, P, O and C (**Fig. 32(j)**, red). While after another week in SBF, islands like spherules were spread on the surface (**Fig. 32(k, green)**). The formation of Ca-P layer with a similar morphology was reported for Ti and its alloys [Kim *et al.*, 1999]. These islands failed to cover the entire surface due to the detection of sodium titanate from the background as shown in its EDS-X analysis (**Fig. 32(l)**, grey).

### 2.2. Surface morphology of Group II

To enhance Ca-P formation especially on TAV substrates, changing the catalyst was a constructive idea, by using AgCl instead of PdCl<sub>2</sub>. Ag<sup>+</sup>, one of the precious metal catalyst (like Pd<sup>2+</sup>), has a dual function to act as a catalyst in addition to its antibacterial activity. In this work, this bath was followed under the same conditions used in Group I (**Table 18**).

**Figure 33(a,b)** showed that a homogeneous coating was formed and it is composed of nanometric sphere-like structure grew inside the network having different sizes ca 100-400 nm in diameter. According to their EDS-X analyses, the structure observed is mainly composed of Ca-P mixed with CaF and NaCl (blue) growing on the sodium titanate background (**Fig. 33(c)**, red). After immersion of the treated samples in SBF for 7 days, hemispherical-like coatings completely covered the network of sodium titanate layer as observed before (**Fig. 33(d)**). At higher magnification (**Fig. 33(e)**), one can observe some holes in these hemisphere aggregates which is suggested to be due to the release of CaF particles after deposition of Ca-P layer. EDS-X analyses (**Fig. 33(f)**) proved that the layer is mainly composed of Ca and P without detection of Ti from the background proving the thickness of the formed layer. The formation of Ca-P layer with a similar morphology was reported for Ti and its

alloys [Kim *et al.*, 1999; Lee *et al.*, 2002; Kim *et al.*, 1996] after 10 and 30 days proving, therefore, the role of Ag in enhancing phosphate deposition.

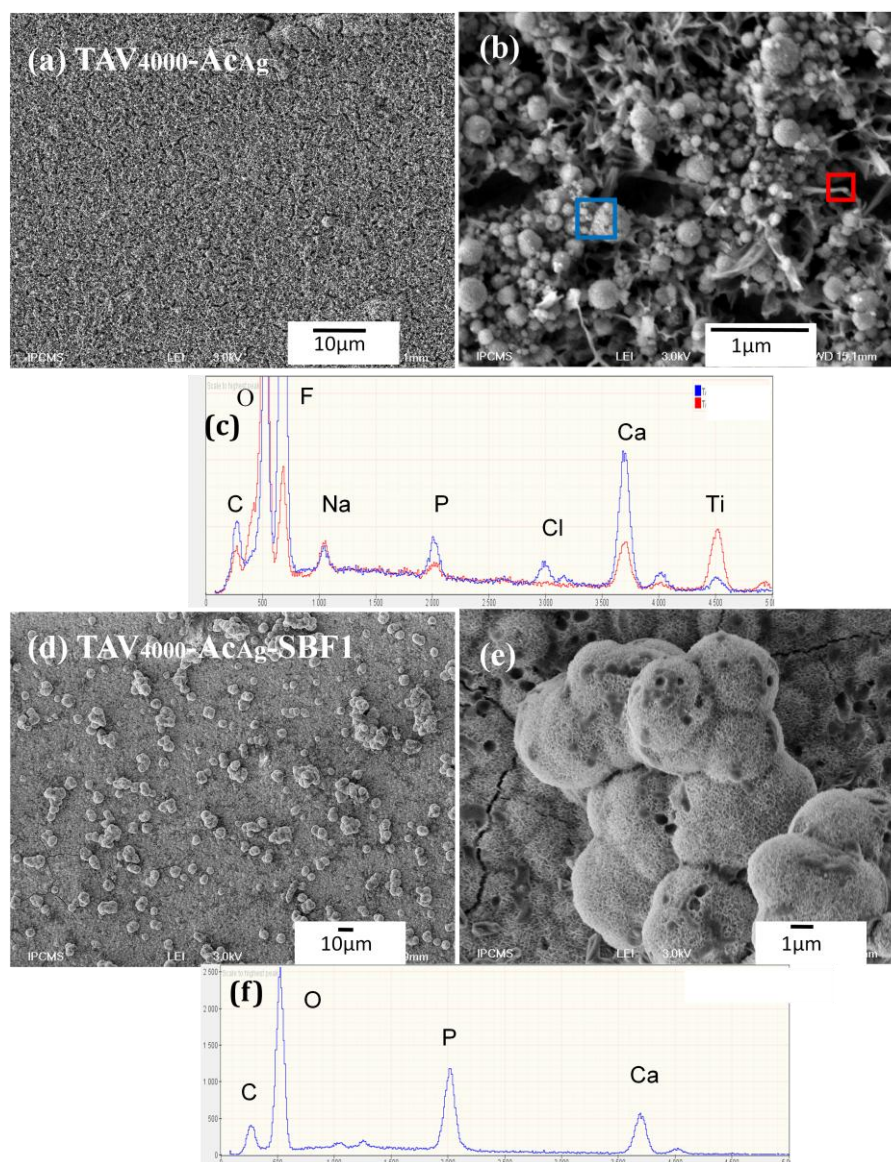


Figure 33. FESEM images of TAV<sub>4000</sub> (a,b) after immersion in acidic bath for 2 h, (d,e) after immersion TAV<sub>4000</sub>-AcAg in SBF for 7d and (c,f) corresponding EDS-X analyses.

### 2.3. Surface morphology of Group III

In this group, we will study the behaviour of TiN interlayer - coated by pulsed laser deposition - in acidic bath using two catalysts (Table 19).

Surface morphology of TiN-Ac<sub>1</sub>Pd (Fig. 34(a,b)) and TiN-Ac<sub>2</sub>Pd (Fig. 34(d,e)) showed that both surfaces were not completely covered; the agglomeration seems to be more dense in case of TiN-Ac<sub>1</sub>Pd. EDS-X analyses (Fig. 34(c)) confirmed that the agglomerates were mainly composed of CaF cubes with holes; NaP (red) and Ca-P some plates (blue). Otherwise, TiN-Ac<sub>2</sub>Pd surface (Fig. 34(e)) presents very small aggregates, spread on the surface with the same composition as TiN-Ac<sub>1</sub>Pd (red) and some massive parts composed of Na, Ca, P and F, as demonstrated in EDS-X analyses (Fig. 34(f)).

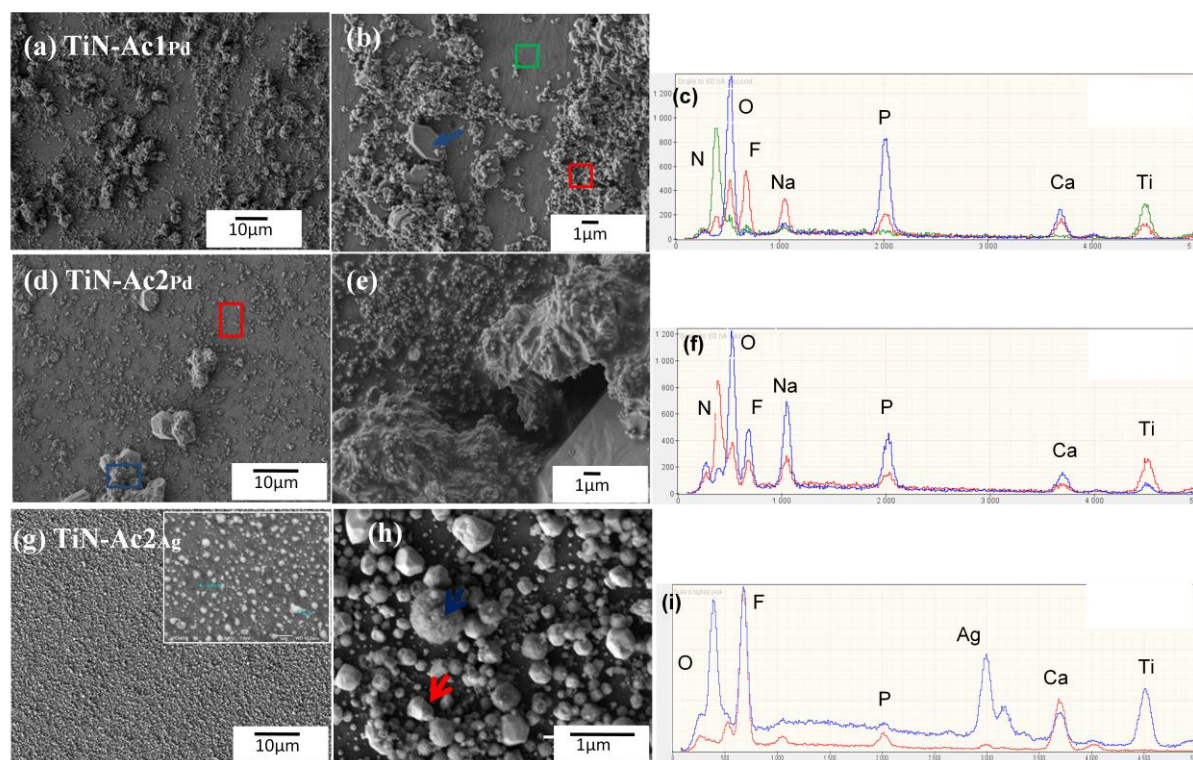


Figure 34. FESEM images of TiN after immersion in acidic bath (a,b) with  $\text{PdCl}_2$  for 1 h, (d,e) with  $\text{PdCl}_2$  for 2 h, (g,h) with  $\text{AgCl}$  for 2 h and (f,i) corresponding EDS-X analyses.

The acidic bath with  $\text{AgCl}$  produces a surface partially covered (**Fig. 34(g)**). **Fig. 34(h)** exhibits different morphologies on the layer: spheres, cubes and tetragonal shapes. By EDS-X analyses, the spheres are mainly composed of metallic  $\text{Ag}$  (**Fig. 34(i)**, blue), cubes and tetragonal shapes are done by  $\text{CaF}_2$  (**Fig. 34(i)**, red). A small amount of P could be detected in the background.

The stability of deposited layer was followed by immersing the samples in SBF (see **Table 18**). After immersion of  $\text{TiN-Ac1}_{\text{Pd}}$  sample in SBF for 4 days (**Fig. 33(a)**), some aggregates were observed mainly composed of  $\text{CaF}$  cubes (**Fig. 33(c)**). No P element was detected in  $\text{TiN-Ac1}_{\text{Pd}}$ . The film was completely dissolved, losing the P elements and keeping  $\text{CaF}_2$  ( $\text{CaF}_2$  is not easily dissolved). The additional immersion for 2 days in SBF1.5, affected the layer (**Fig. 33(b)**) to have massive precipitations spread over the surface (TiN, red). These precipitations are a mixture of Ca-P with  $\text{CaF}_2$  as identified in **Fig. 33(c)** (green). This could be due to the rebuilding of the biolayer supported by the increase of P element.

Regarding  $\text{TiN-Ac2}_{\text{Pd}}$ , after immersion in SBF1 for 4 days, the cubes of  $\text{CaF}_2$  are still observed (**Fig. 35(d)**, blue) without any P elements. After additional two days in SBF 1.5 (**Fig. 35(e)**) massive precipitations spread on the surface (TiN, red). These precipitations are mixture of Ca and P with Ca and F as detected in **Fig. 35(c)**, green). This means that P begins to rebuild. The morphology is similar to **Fig. 35(d)** but become denser, this suggested density is due to  $\text{CaF}_2$  mixed with another  $\text{CaCl}_2$  precipitations as proved in EDS-X analyses (**Fig. 35(f)**).

The morphology of  $\text{TiN-Ac2}_{\text{Ag}}$  after immersion in SBF for 7 days was similar to the structure observed in **Fig. 32(g)**, meaning that  $\text{Ag}$  is not dissolved in SBF (**Fig. 35(g)**). While after additional 7 days in SBF there is no detection of  $\text{Ag}$  elements (completely released in SBF). The observed cubes of  $\text{CaF}_2$  became thinner denoting beginning to dissolution without detection of P elements meaning this need for more time immersion in SBF.

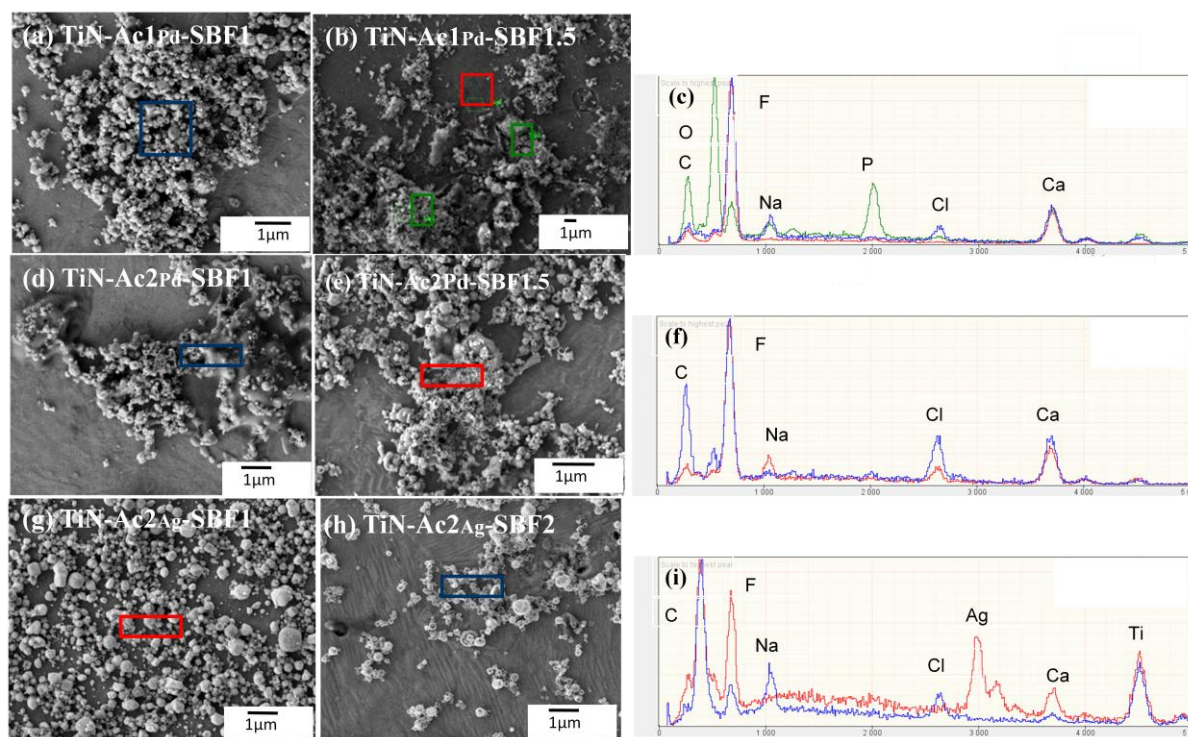


Figure 35. FESEM images of TiN-Ac after immersion in SBF (a) SBF1 for 4 d, (b) SBF1.5 for another 2 d, (d) SBF1 for 4 d, (e) SBF1.5 for another 2 d, (g) SBF1 for 7 d, (h) SBF for 14 d and (c,f,i) corresponding EDS-X analyses.

### 3. Biochemical analysis of SBF of Groups I, II and III

It was assumed that any change by decrease/increase in  $\text{Ca}^{2+}$  or phosphorus concentrations, compared to the mother solution SBF, would represent a deposition/release on/from the samples surfaces respectively.  $\text{Ca}^{2+}$  and P variation, uptake onto the samples, is given in **Fig. 36**.

#### 3.1. Group I

**Figure 36(a)** shows the effect of heat treatment with acidic bath of  $\text{TAV}_{400}\text{-1h-AcPd}$  and  $\text{TAV}_{400}\text{-3h-AcPd}$  after immersion in SBF for several periods.

Both samples ( $\text{TAV}_{400}\text{-1h-AcPd-SBF1}$  and  $\text{TAV}_{400}\text{-3h-AcPd-SBF1}$ , **Fig. 36(a)**) showed that  $\text{Ca}^{2+}$  ions release with absorption of P ions from SBF after 4 days. This was observed as a pronounced increase in  $\text{Ca}^{2+}$  ions in SBF with decrease in P ions. After two days immersion in SBF1.5,  $\text{TAV}_{400}\text{-1h-AcPd-SBF1.5}$  preserved a similar level of  $\text{Ca}^{2+}$  ions with absorption of some P ions. On the contrary, the samples  $\text{TAV}_{400}\text{-3h-AcPd-SBF1.5}$  started to release its  $\text{Ca}^{2+}$  and P ions from the layer.

A sharp decrease in the ionic concentration of both  $\text{Ca}^{2+}$  and P ions is recorded in **Fig. 36(b)**. Therefore, the consumption of these ions built up a dense Ca-P layer during the first and second soaking periods. This behaviour was observed in both samples ( $\text{TAV}_{400}\text{-AcPd-SBF1}$  and  $\text{TAV}_{400}\text{-AcPd-SBF2}$ ) with lower roughness regardless the substrate type.

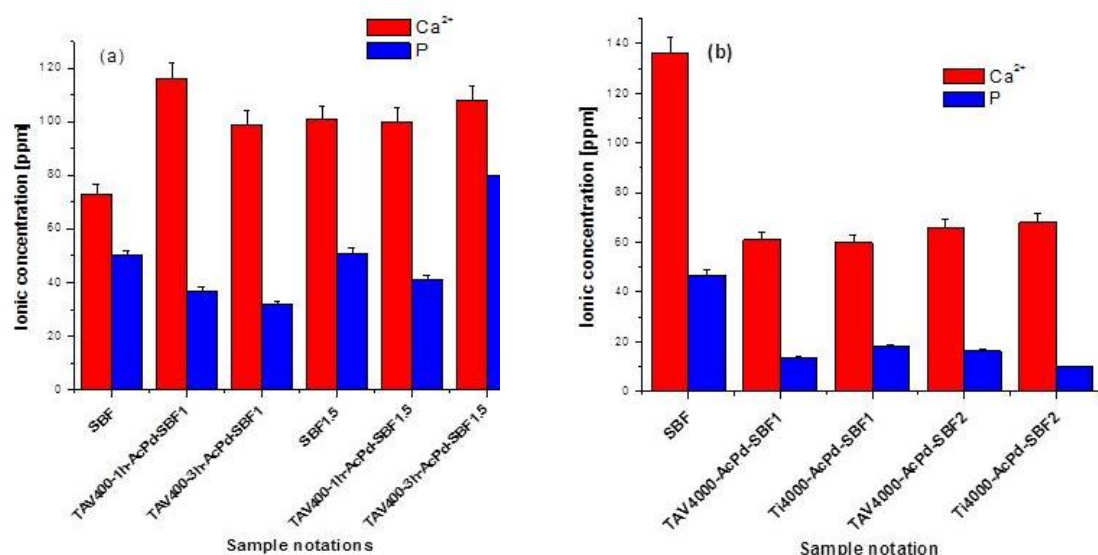


Figure 36. Concentrations of  $\text{Ca}^{2+}$  and  $\text{P}$  ions (a) TAV<sub>400</sub> in SBF1 (4 d) followed by another 2 d in SBF1.5, (b) TAV<sub>4000</sub> and Ti<sub>4000</sub> in SBF for 7 and 14 d

### 3.2. Group II

After the immersion of TAV<sub>4000</sub>-AcAg for three days in SBF, the solution (Fig. 37, TAV<sub>4000</sub>-AcAg-SBF1) showed a decrease in  $\text{Ca}^{2+}$  without any variation in  $\text{P}$  concentration. Another 3 days soaking in SBF, a pronouncedly decreasing for  $\text{Ca}^{2+}$  and  $\text{P}$  ions was observed (Fig. 37, TAV<sub>4000</sub>-AcAg-SBF2) confirming therefore, that a CaP layer, in particular HA was formed, as also observed in Figs. 26, 27(e) and 33(d, e).

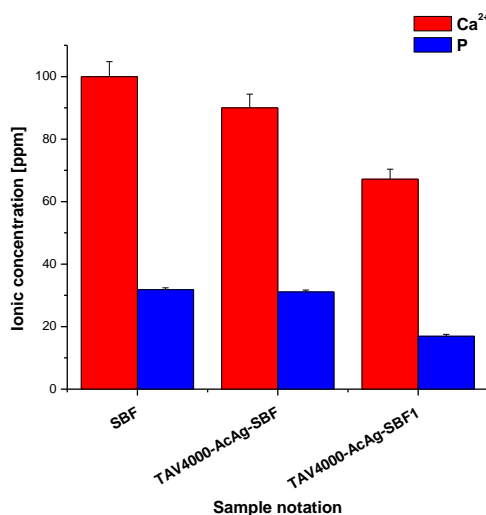


Figure 37. Concentrations of  $\text{Ca}^{2+}$  and  $\text{P}$  ions in SBF after immersion of TAV<sub>4000</sub> immersed in acidic bath with AgCl after 3 and 7 d.

### 3.3. Group III

Figure 38(a) shows that TiN-Ac1<sub>Pd</sub> after 4 days in SBF1 (TiN-Ac1<sub>Pd</sub>-SBF1) and additional 2 days in SBF1.5 (TiN-Ac1<sub>Pd</sub>-SBF1.5). Noticeable decrease in both  $\text{Ca}^{2+}$  and  $\text{P}$  ions concentration is recorded.

However, in case of TiN-Ac<sub>2Pd</sub>, Ca<sup>2+</sup> ions concentrations always decreased after several periods in SBF1 and 1.5. This absorption in Ca<sup>2+</sup> ions is suggested to be consumed in CaF<sub>2</sub> or CaCl<sub>2</sub> structures recorded in EDS as in **Fig. 35(d)**.

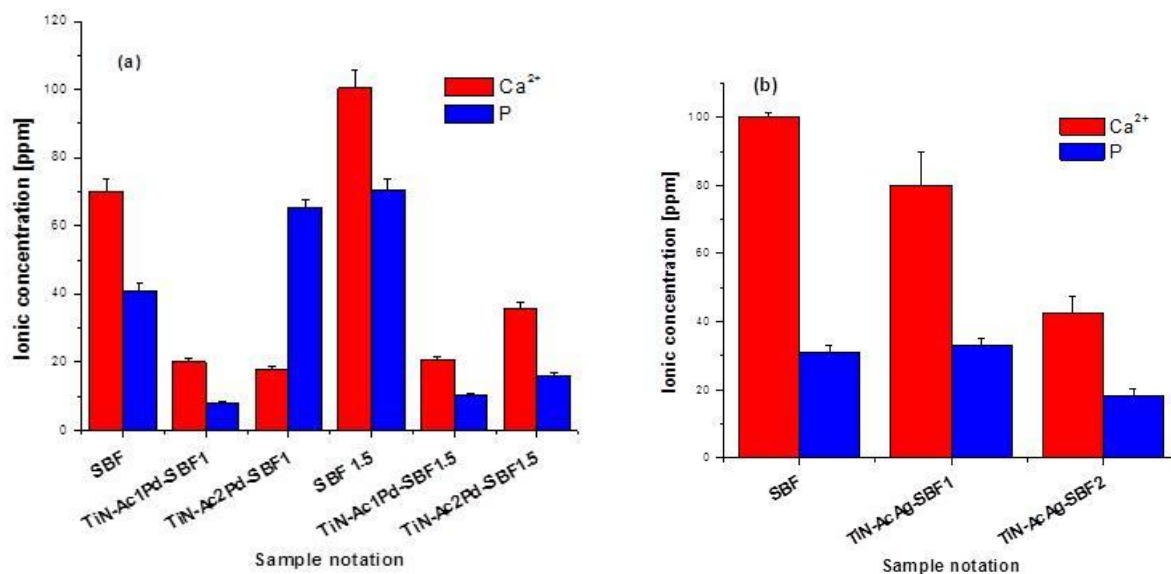


Figure 38. Concentrations of Ca<sup>2+</sup> and P ions (a) TiN after treatment with acidic bath for 1 and 2 h with PdCl<sub>2</sub> in SBF1 (4 d) followed by another 2 d in SBF1.5, (b) TiN after treatment with acidic bath for 2 h with AgCl in SBF for 7 and 14 d.

**Figure 38(b)** showed slight decrease in Ca<sup>2+</sup> ions concentrations, without noticeable reduce in P ions for TiN-Ac<sub>Ag</sub> after 7 days (TiN-Ac<sub>Ag</sub>-SBF1). After 14 days of immersion in SBF, a clear reduction (absorption) in both Ca<sup>2+</sup> and P levels. Moreover, these elements were not observed in EDS-X analysis after 14 days immersion (**Fig. 35(i)**).

It was found that Group III immersed in acidic bath failed to form a homogeneous distribution on metallic surfaces. These areas of Ca-P layer were not stable after 4 days in SBF. As an exception for TiN-Ac<sub>1Pd</sub>: Ca-P precipitations began to rebuild after additional 2 days in SBF1.5. One can suppose that mirror polishing is one of the factors that enhance this dissolution because roughness plays an important role on Ca-P growth or precipitation and anchoring.

## Conclusion of Part II

One can conclude that the surface state of sampleTAV<sub>400</sub> compared to TAV<sub>4000</sub> influences the formed layer in acidic bath:

(i) The formed Ca-P layers on TAV<sub>400</sub>-1h-Ac<sub>Pd</sub> and TAV<sub>400</sub>-3h-Ac<sub>Pd</sub> were not stable after SBF immersion. EDS-X analyses confirmed such degradation of the coatings after immersion in SBF with the detection of tiny amount of Ca and P;

(ii) Pretreated TAV<sub>4000</sub> and Ti<sub>4000</sub> substrates showed build up of Ca-P layers during the autocatalytic process (especially in case of Ti<sub>4000</sub>). This formed layer on Ti<sub>4000</sub> was proved through several morphologic and structural techniques to be OCP using FT-IR (**Fig. 23(d)**), TF-XRD (**Fig. 24(b)**) and SAED (**Fig. 25(b)**) after 2 h immersion in the bath. After immersion in SBF, these films (e.g. Ti<sub>4000</sub>)

were stable and could be due to nuclei for more Ca-P precipitation. The grown of Ca-P layer was observed morphologically by using SEM (**Fig. 32(k)**) and EDS-X analysis (**Fig. 32(l)**). Furthermore, these results were confirmed by using TF-XRD (**Fig. 24(b)**) and SAED (**Fig. 25(e)**). In addition, to confirm these results the biochemical analysis of SBF showed reduction of  $\text{Ca}^{2+}$  and P ions (**Fig. 36(b)**) proving therefore, the deposition process.

The acidic autocatalytic bath is a simple and easy way to induce a rapid formation of Ca-P layers. Since the SBF immersion tests showed that the coating is not stable after 14 days with respect to TAV<sub>4000</sub>. Therefore, a new direction was taken: the autocatalytic baths were modified by changing the catalyst. A comparison between the layers built up by using PdCl<sub>2</sub> and AgCl was performed. A homogenous distribution of Ca-P was morphologically proved using SEM and EDS-X (**Fig. 33 (a,b,c)**) after 2 h immersion in the bath with AgCl. These Ca-P particles stimulated the building of a homogenous layer of HA (**Fig. 26** and **Fig. 27(e)**) after immersion in SBF for 7 days this layer completely covered the TAV substrate, as confirmed (**Fig. 33(d, e)**). The stability and quantification of the stability of the biolayer was also proved.

In TiN a buffer layer, after acidic bath, promoted deposition of some discrete Ca-P precipitation especially after 1h by using PdCl<sub>2</sub> as catalyst. While in case of AgCl, the bath was able to deposit tiny amount of Ca-P in addition to Ag as a metal. SBF was not able to enhance phosphatic deposition. So, one can say that TiN seems to delay precipitation and /or need more time to grow of Ca-P post 14 days soaking of SBF.

## Part III. Alkaline bath

A complete list of treated specimen by alkaline bath is given in **Table 19**.

### 1. Structural analysis of samples after treatment with alkali bath

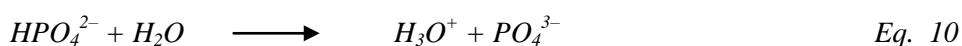
#### 1.1 Structural analysis of Group I

**Figure 39(a)** showed FT-IR spectra of TAV<sub>400</sub>-1h-Al<sub>Pd</sub> after several immersions in SBF. After 2 h in alkaline bath, only one band at 590 cm<sup>-1</sup> from the  $\nu_4$  *bending vibration* of PO<sub>4</sub><sup>3-</sup> group was detected. While after immersion in SBF for 4 and 6 days, this band was splitted into two faint bands in the region of 500-600 cm<sup>-1</sup>. The weak bands of  $\nu_3$  *vibration mode* of CO<sub>3</sub><sup>2-</sup> group only appeared after immersion in SBF1 and then it disappeared. The *bending vibration* for OH<sup>-</sup> group was observed in the region of 650-680 cm<sup>-1</sup> after SBF.

By changing the rate of heating the of the samples (TAV<sub>400</sub>-3h-Al<sub>Pd</sub>), using the same bath duration, **Fig. 39(b)** illustrated the characteristic band of  $\nu_4$  *bending vibration* of PO<sub>4</sub><sup>3-</sup> group at 550-600 cm<sup>-1</sup> in all the three spectra. Furthermore, after SBF this band splitted into two peaks. Only after SBF immersion,  $\nu_1$  *bending* (900-920 cm<sup>-1</sup>) and  $\nu_3$  *stretching vibration* (1050-1200 cm<sup>-1</sup>) bands of PO<sub>4</sub><sup>3-</sup> group were also observed. Additionally, the presence of HPO<sub>4</sub><sup>2-</sup> band was noticed in the region of 750-830 cm<sup>-1</sup>. CO<sub>3</sub><sup>2-</sup> group  $\nu_3$  *vibration mode* at 1500 and 1380 cm<sup>-1</sup> were detected after immersion in SBF. This band is shifted and become broad after immersion in SBF1.5.

The bands of brushite were detected in the spectrum of TAV<sub>4000</sub>-Al<sub>Pd</sub> [Kwon et al., 2003; Kumta et al., 2005]. Brushite bands are detected at 570 and 518 cm<sup>-1</sup> for O-P-O  $\nu_4$  *bending mode* and 1169 cm<sup>-1</sup> for P-O  $\nu_3$  *for stretching* of PO<sub>4</sub><sup>3-</sup> while at 790 cm<sup>-1</sup> P-O-H bending of HPO<sub>4</sub><sup>2-</sup> was recorded. A broad band was detected between 3100-3480 cm<sup>-1</sup>. The band at 2355 cm<sup>-1</sup> was assigned for the combination of H-O-H and another band of HPO<sub>4</sub><sup>2-</sup> at 790 cm<sup>-1</sup> which decreased post SBF immersion. Decreasing the roughness from 3µm of TAV<sub>400</sub> to 0.3 µm lead to a number of spectral details indicating some transformations (**Fig. 39(c)**) accompanying brushite formation. After SBF immersion, some brushite bands were still detected such as band at 2927 cm<sup>-1</sup> which is assigned for (P)O-H stretching while the band at 2355 cm<sup>-1</sup> was assigned for the combination of H- and O-H. The presence of two bands (600-602 cm<sup>-1</sup> and 553-563 cm<sup>-1</sup>) is characteristic of carbonate HA while bands at 885, 1455 and 1540 cm<sup>-1</sup> are typical peaks of the A-type of carbonated HA according to [Barinov et al., 2006]. The peaks of carbonated HA prove substitution for hydroxyl group.

The transformation of brushite to HA can be explained due to the occurrence of an internal hydrolysis reaction which partially transforms HPO<sub>4</sub><sup>2-</sup> into PO<sub>4</sub><sup>3-</sup>.



Eq. 10 explains the decrease in HPO<sub>4</sub><sup>2-</sup> band and increase in PO<sub>4</sub><sup>3-</sup> band after SBF immersion.

Table 19. Complete series of sample (Group I, II and III) treated with alkaline autocatalytic bath

Group	Substrate	Grit of SiC	Pretreatment steps		Alkaline Al bath (h)	Biomimetic bath				Sample notation	
			Intermediate layer	Heating rate (°C/minute)		SBF1 (4 d)	SBF1.5 (2 d)	SBF1 (7 d)	SBF1 (14 d)		
Group I PdCl <sub>2</sub>	Ti-6Al-4V	400	Na <sub>x</sub> Ti <sub>y</sub> O <sub>z</sub> H <sub>t</sub>	10	2	—	—	—	—	TAV <sub>400</sub> -1h-Al <sub>Pd</sub>	
				3		—	—	—	—	TAV <sub>400</sub> -3h-Al <sub>Pd</sub>	
				10		yes	—	—	—	TAV <sub>400</sub> -1h-Al <sub>Pd</sub> -SBF1	
				3		yes	—	—	—	TAV <sub>400</sub> -3h-Al <sub>Pd</sub> -SBF1	
				10		yes	yes	—	—	TAV <sub>400</sub> -1h-Al <sub>Pd</sub> -SBF1.5	
				3		yes	yes	—	—	TAV <sub>400</sub> -3h-Al <sub>Pd</sub> -SBF1.5	
		4000	Na <sub>x</sub> Ti <sub>y</sub> O <sub>z</sub> H <sub>t</sub>	3	2	—	—	—	—	TAV <sub>4000</sub> -Al <sub>Pd</sub>	
						—	—	yes	—	TAV <sub>4000</sub> -Al <sub>Pd</sub> -SBF1*	
						—	—	yes	yes	TAV <sub>4000</sub> -Al <sub>Pd</sub> -SBF2**	
		Group I PdCl <sub>2</sub>	Ti CP-3	4000	Na <sub>x</sub> Ti <sub>y</sub> O <sub>z</sub> H <sub>t</sub>	3	2	—	—	—	—
—	—							yes	—	Ti <sub>4000</sub> -Al <sub>Pd</sub> -SBF1*	
—	—							yes	yes	Ti <sub>4000</sub> -Al <sub>Pd</sub> -SBF2**	
Group III PdCl <sub>2</sub>	Ti CP-1	Colloidal silicas	TiN	—	1	—	—	—	—	TiN-Al <sub>Pd</sub>	
					1	yes	—	—	—	TiN-Al <sub>Pd</sub> -SBF1	
					1	yes	yes	—	—	TiN-Al <sub>Pd</sub> -SBF1.5	
Group II AgCl	Ti-6Al-4V	4000	Na <sub>x</sub> Ti <sub>y</sub> O <sub>z</sub> H <sub>t</sub>	3	2	—	—	—	—	—	TAV <sub>4000</sub> -Al <sub>Ag</sub>
							yes	—	—	—	TAV <sub>4000</sub> -Al <sub>Ag</sub> -SBF
							yes	yes	—	—	TAV <sub>4000</sub> -Al <sub>Ag</sub> -SBF1*
Group III AgCl	Ti CP-1	Colloidal silicas	TiN	—	2	—	—	—	—	TiN-Al <sub>Ag</sub>	
					2	—	yes	—	—	TiN-Al <sub>Ag</sub> -SBF1*	
					2	—	yes	yes	—	TiN-Al <sub>Ag</sub> -SBF2**	

SBF1\* indicates the immersion in SBF for 7 days; SBF2\*\* indicates the immersion in SBF for 14 days

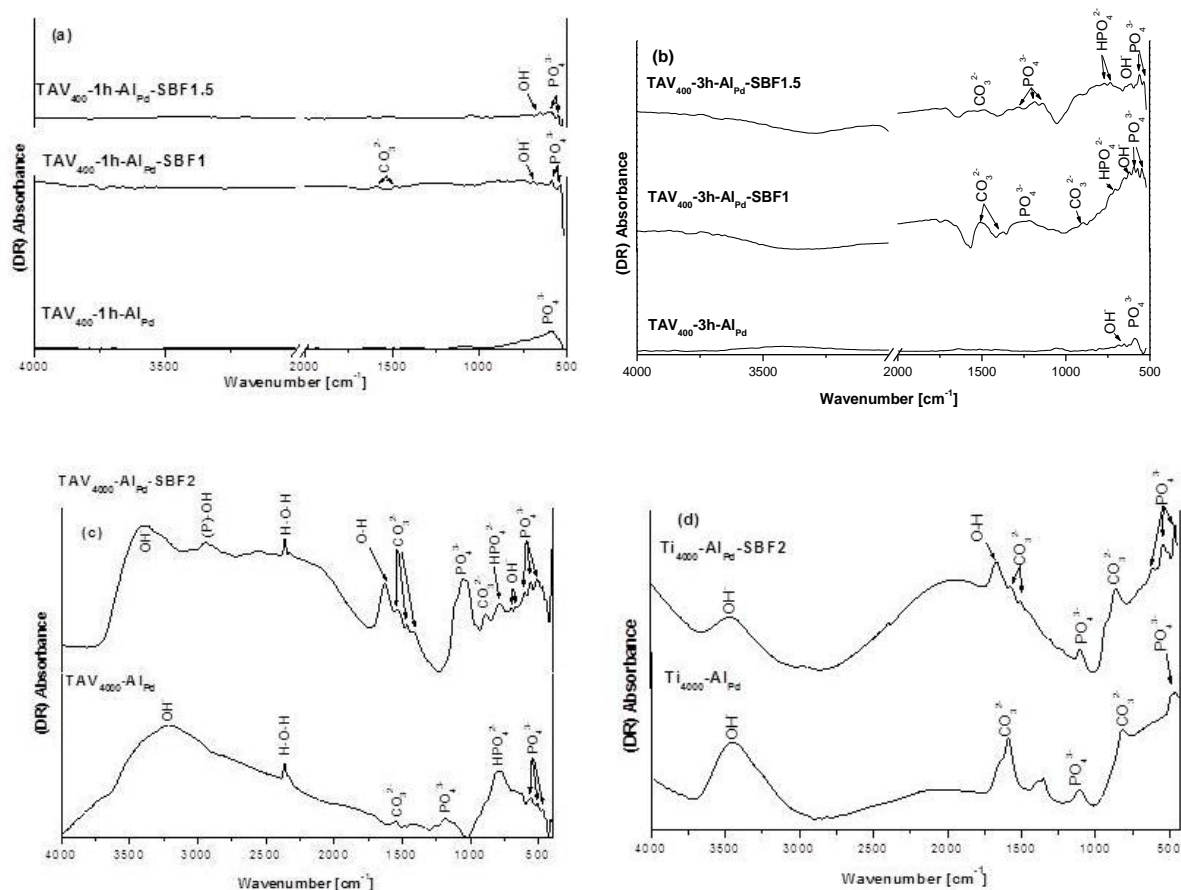


Figure 39. FT-IR spectra after immersing 2 h in alkaline bath followed by immersion in SBF (a)  $TAV_{400}$  subjected to heating rate  $10^{\circ}\text{C}/\text{minute}$ , (b)  $TAV_{400}$ , (c)  $TAV_{4000}$  and (d)  $Ti_{4000}$  subjected to heating rate  $3^{\circ}\text{C}/\text{minute}$ .

**Figure 39(d)** illustrated FT-IR spectra of the  $Ti_{4000}$  substrate after alkaline bath ( $Ti_{4000}\text{-AlPd}$ ) followed by the SBF ( $Ti_{4000}\text{-AlPd-SBF2}$ ). The  $\beta$ -TCP bands were observed on  $Ti_{4000}\text{-AlPd-SBF2}$  at  $1120\text{ cm}^{-1}$  (P–O stretching modes) and at  $560\text{ cm}^{-1}$  (P–O–P  $\nu_4$  bending mode) [Spataru et al., 2008]. In addition, the presence of  $\text{CO}_3^{2-}$  bands ( $885, 1455$  and  $1540\text{ cm}^{-1}$ ) the band of  $\text{PO}_4^{3-}$  group ( $553\text{-}563\text{ cm}^{-1}$ ) indicated the growth of A-type of carbonated HA after immersion 14 days in SBF according to Barinov et al., (2006). Moreover,  $\nu_2$  bending vibration of  $\text{PO}_4^{3-}$  at  $470\text{ cm}^{-1}$  was detected in both spectrums ( $Ti_{4000}\text{-AlPd}$  and  $Ti_{4000}\text{-AlPd-SBF2}$ ). Enhancing phosphate precipitations, after immersion 14 days in SBF, was confirmed by the detection of a new peak at  $560\text{ cm}^{-1}$  of  $\nu_4$  bending mode of P–O–P. This last one began to grow and also it can be observed the splitting of  $\nu_2$  bending vibration to form a sharp peak ( $408$  and  $488\text{ cm}^{-1}$ ). The peaks in the range  $1300$  to  $1600\text{ cm}^{-1}$  are due to  $\nu_3$  vibrational mode for  $\text{CO}_3^{2-}$ , while the peak at  $830\text{ cm}^{-1}$  is due to the carbonate  $\nu_2$  vibrational mode. The hydroxyl groups stretch mode band was observed in the region of  $3000\text{-}3400\text{ cm}^{-1}$  in the both spectrum. After immersion in SBF2, one can note the band attributed to O–H ( $1632\text{ cm}^{-1}$ ) of lattice water molecules of most of the calcium phosphate phases [Jalota et al., 2006].

The XRD peaks ( $2\theta = 35.0, 38.7$  and  $40.2^{\circ}$ ) of the TAV substrate, **Fig. 40(a)** proving  $\alpha$  and  $\beta$  –Ti, respectively (ASTM-89-5009 and 89-4913). After 2 h in the bath, some peaks ascribed to brushite were detected at  $2\theta = 21.33$  and  $33.7$  (B, ASTM-04-0740) to confirm the results obtained by FT-IR (**Fig.39(c)**). These peaks disappeared after immersion in SBF for 14 days due its dissolution.

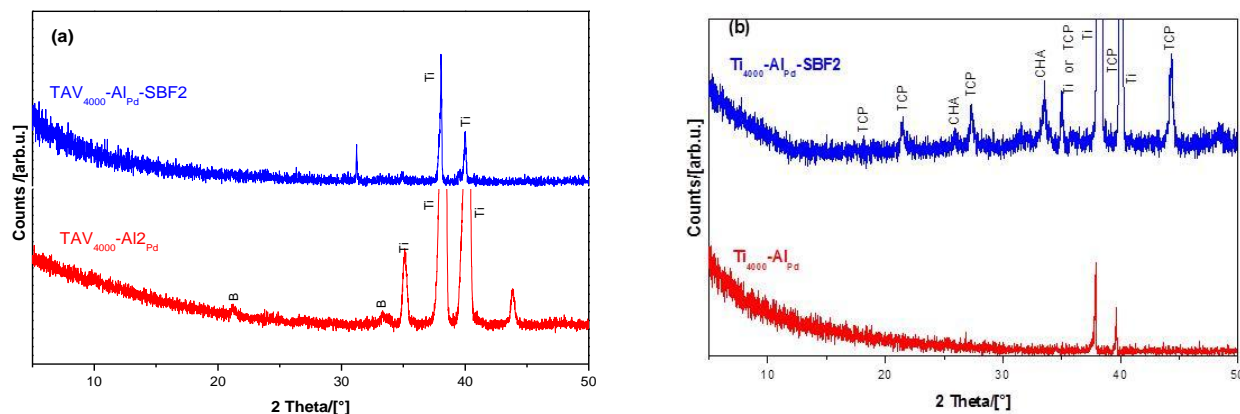


Figure 40. TF-XRD patterns for (a) TAV<sub>4000</sub> and (b) Ti<sub>4000</sub> after treatment in alkaline bath for 2h (red) and after immersion in SBF for 14 d (blue).

Only the peaks  $2\theta = 38.7$  and  $40.2^\circ$  due to the Ti substrate were detected (ASTM-89-4893) (**Fig. 40(b)**). Later on immersing in SBF for 14 days, Ca-P precipitation was detected ( $2\theta = 18.0, 21.4, 35.1, 39.8$  and  $44.3^\circ$ ) corresponding to  $\beta$ -TCP, known as Whitlockite, (TCP, ASTM-03-0713). Additionally, two peaks could be attributed to carbonated HA (CHA, ASTM-19-0272) at  $2\theta = 33$  (overlapped of  $32.19$  and  $33.4^\circ$ ) and  $25.7^\circ$ .

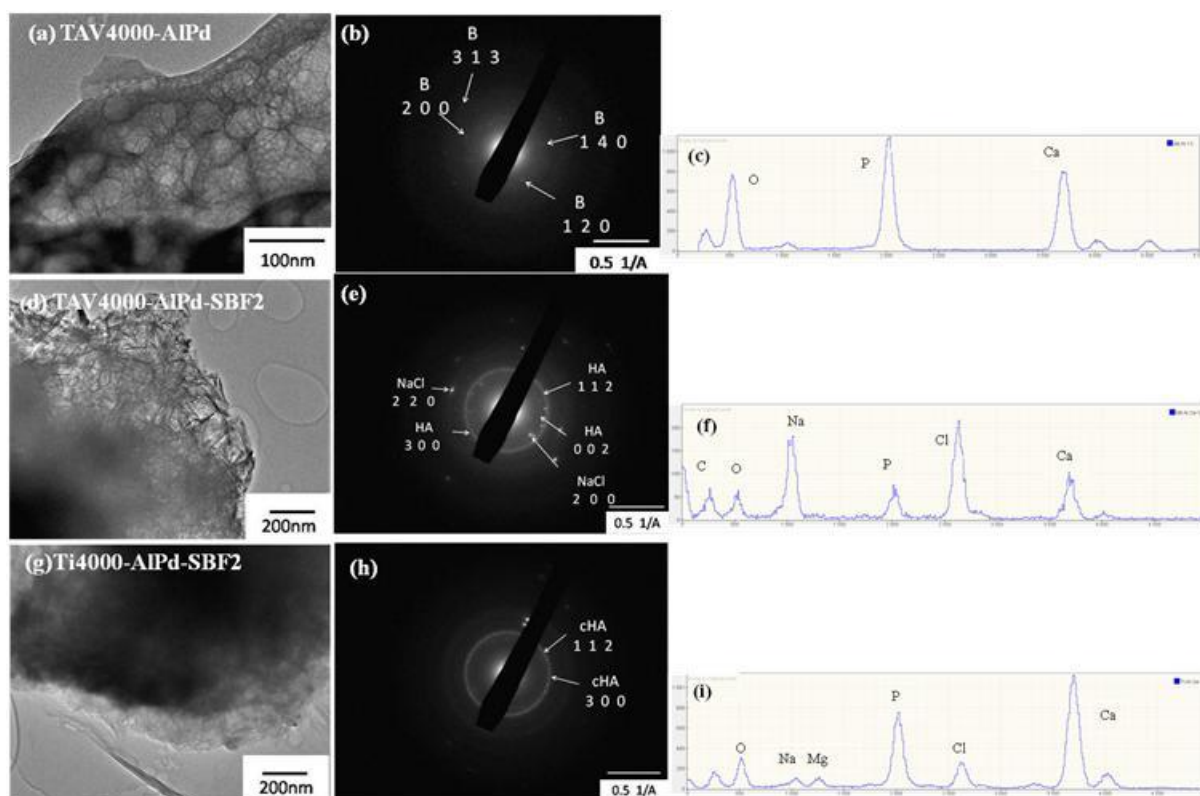


Figure 41. TEM images of calcium phosphate coatings (a) TAV<sub>4000</sub> after 2h in alkaline bath, (d)TAV<sub>4000</sub>-AlPd,(g) Ti<sub>4000</sub>-AlPd after SBF for 14 d, (b,e,h) corresponding SAED and (c,f,i) and their corresponding EDS-X analyses.

**Fig. 41(a)** illustrates TEM images of TAV<sub>4000</sub> after alkaline bath. They were mainly composed of high calcium and phosphorous concentrations as revealed by their EDS-X analysis (**Fig. 41(c)**). **Fig. 41(b)** shows the selected area diffraction rings corresponding to (2 0 0), (1 2 0), (1 4 0) and (3 1 3) planes of

brushite (B, ASTM-04-0740). During the immersion in SBF for 14 days, needle-like crystals were observed (**Fig. 41(d)**), mainly composed of Ca, P mixed with Na and Cl elements (see EDS analysis, **Fig. 41(f)**). As reported by Tsuji et al., (2008) and Kim et al., (2005) these could be made of HA. This was also confirmed by SAED (**Fig. 41(e)**) by the diffraction rings corresponding to carbonated HA (cHA, ASTM-19-0272). The presence of NaCl in cubic face-centred were detected by SAED with the diffraction rings corresponding to (2 0 0) and (2 2 0) planes (ASTM-8802300).

It is interesting to compare the TEM examination results with that of the TF-XRD and FT-IR which confirmed the presence of brushite after immersing TAV<sub>4000</sub> in alkaline bath (**Fig. 39(c)** and **40(a)**) then further the transformation of brushite into HA after immersion of TAV<sub>4000</sub>-Al<sub>Pd</sub> in SBF for 14 days (**Fig. 39(c)** and **Fig. 41(e)**). Nevertheless, TEM images of Ti<sub>4000</sub>-Al<sub>Pd</sub> did not show any Ca-P layer. After immersion in SBF2 (Ti<sub>4000</sub>-Al<sub>Pd</sub>-SBF2, **Fig. 41(g)**) nanometric longitudinal structures were observed and **Fig. 41(i)** indicated that they are composed of Ca, P and small amounts of Na and Mg, similar to bone mineral (Ca,P, Na and Mg) [Takadama et al., 2001]. The SAED of the scratched coatings (**Fig. 41(h)**) illustrated the diffraction rings corresponding to (1 1 2) and (3 0 0) planes of hexagonal carbonated HA (cHA, ASTM-19-0272); without  $\beta$ -TCP detection as proved by TF-XRD patterns.

### 1.2 Structural analysis of Group II

**Figure 42** showed the  $\alpha$  and  $\beta$ -Ti substrate (ASTM-89-5009 and 89-4913). After immersing in SBF for 7 days, peaks ascribed to hydroxyapatite [HA, Ca<sub>10</sub>(PO<sub>4</sub>)<sub>6</sub>(OH)<sub>2</sub>](ASTM-89-7834) were detected at  $2\theta = 25^\circ$  and  $32^\circ$  (overlapping of  $31.8, 32.1$  and  $33^\circ$ ) which is agreement with previously reported Kim et al.(1996 and1997).

**Figure 43(a)** showed TEM images of scratched coating (TAV<sub>4000</sub>-Al<sub>Ag</sub>) consisting of rounded and longitudinal nanometric particles. The asterisk, in **Fig. 43(a)**, indicate the measured spots in SAED (**Fig. 43(b)**) and their EDS-X analyses areas (**Fig. 43(c)**). Chemical analyses indicate the presence of Ca, P and O (from deposited coating) with some Na and Ti (from the sodium titanate background). The diffraction rings corresponding to (0 1 0) and (1 0 0) planes of canaphite (CaNa<sub>2</sub>P<sub>2</sub>O<sub>7</sub>(H<sub>2</sub>O)<sub>4</sub>, ASTM-84-1536) appear by SAED of scratched coatings. This phase is similar to the pyrophosphate but containing sodium.

The formation of canaphite was suggested due to the presence of the pyro-group in the alkaline bath. Kasuga reported that the presence of pyrophosphate was able to enhance of apatite-formation by using through his work on calcium pyrophosphate glass-ceramics [Kasuga, 2005]. This is due to instability of pyrophosphate group which easily hydrolyses into two inorganic hydrogen phosphates:



This inorganic phosphate is one of some groups known as the promising candidates as inducers for the apatite formation [Kokubo et al., 2003].

After immersion in SBF for 7 days, different disintegrated surface morphology was observed (**Fig. 43(d)**) elemental chemical analysis (see the asterisks) suggests that the layer is Ca-P (**Fig. 43(f)**). This was confirmed by SAED which present several diffraction rings of HA [ASTM-89-7834] (**Fig. 43(e)**). The presence of HA post SBF was also confirmed by XRD pattern in **Fig. 42**.

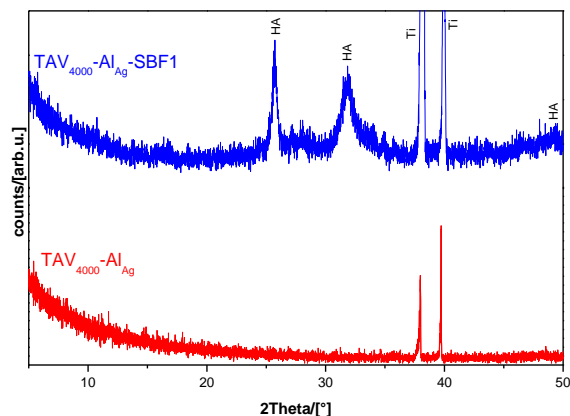


Figure 42. TF-XRD patterns for TAV<sub>4000</sub> after treatment in alkaline bath with AgCl for 2 h (red) and after immersion in SBF for 7 d (blue).

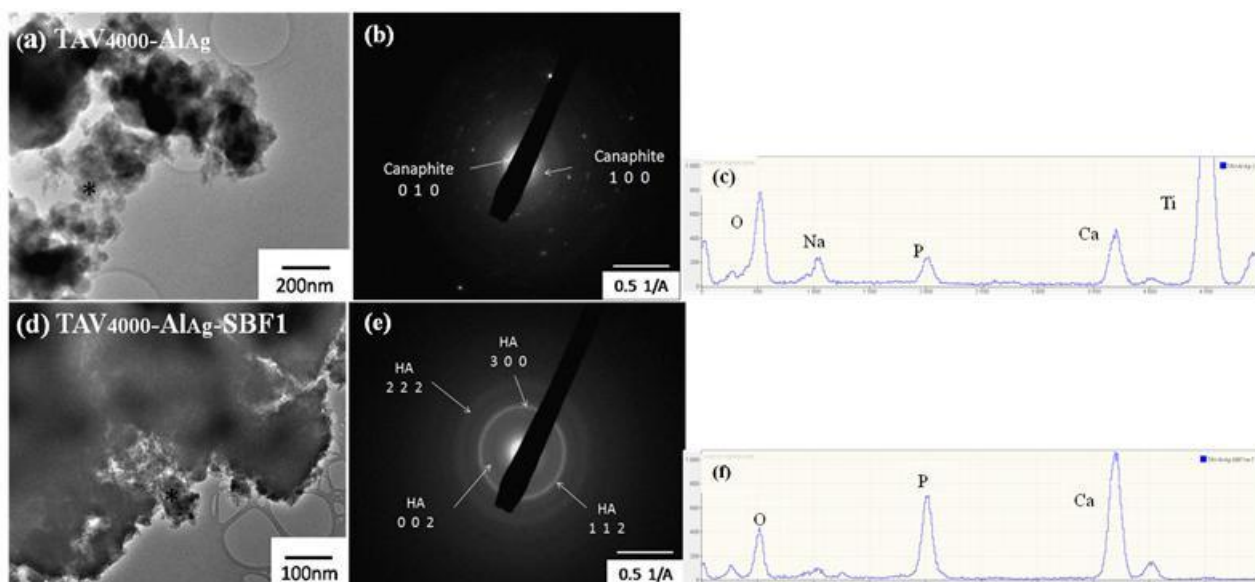


Figure 43. TEM images of calcium phosphate coatings (a) after 2 h in alkaline bath with AgCl and (d) after SBF for 7 d, (b,e) diffraction patterns and (c,f) their corresponding EDS-X analyses.

### 1.3. Structural analysis of Group III

The FT-IR spectrum of TiN post immersion in alkaline bath with PdCl<sub>2</sub> reported the bands assigned to  $\nu_4$  bending mode of P–O–P located inbetween 540-600 cm<sup>-1</sup> in all spectra (**Fig. (44)**). In addition, the band assigned for symmetric  $\nu_1$  stretching modes of P–O was recorded at 948 cm<sup>-1</sup> in both TiN-AlI<sub>Pd</sub> and TiN-AlI<sub>Pd</sub>-SBF1.5 samples while the bands assigned for the double degenerate asymmetric  $\nu_3$  stretching modes of P–O in the range 1100-1170 cm<sup>-1</sup> are recorded only after SBF1.5 immersion (**Fig. (44)**).

A broad band detected in all spectra in the range of 1400-1600 cm<sup>-1</sup> are attributed to  $\nu_3$  vibrational mode of carbonate groups. This peak was grown as a factor due to immersion in SBF. The detection of clear peak at 670 cm<sup>-1</sup>, after the bath and SBF1, was characteristic of Ti-N from the intermediate layer.

The bands of brushite were detected after the bath (as initial precipitation) and after immersion in SBF1.5. Brushite bands are located at 566 and 520  $\text{cm}^{-1}$  for O–P–O(H) *bending mode* while at 650  $\text{cm}^{-1}$  could be related to water *vibrational mode*. The band at 738  $\text{cm}^{-1}$  is characteristic of P–O–H out of plane bending, while that at 976  $\text{cm}^{-1}$  is for P–O stretching. The 2927  $\text{cm}^{-1}$  is assigned for (P)O–H stretching [Kumta et al., 2005].

The crystal structure of Ti-TiN after immersion in alkaline bath with PdCl<sub>2</sub> or AgCl is presented in **Fig. 45**. In case of PdCl<sub>2</sub> as a catalyst (**Fig. 45(a)**), the crystal structure of Ti after 1 h in the alkaline bath followed by immersing in SBF1 for 4 days presented no detection of any Ca-P precipitation. The recorded peaks at  $2\theta = 35.09, 38.7, 40.2, 52.9$  and  $62.2^\circ$  were typical patterns of the Ti substrate (ASTM-89-4893). While after immersing in SBF1.5 for another 2 days, another peaks at  $2\theta = 11, 21.5$  and  $31.5^\circ$  were suggested to be a well crystalline brushite as Ca-P coatings (B, ASTM-09-0077). The presence of brushite after SBF1.5 was confirmed in FT-IR spectrum (**Fig. 44**). One has to note that the peaks of brushite are slightly shifted..

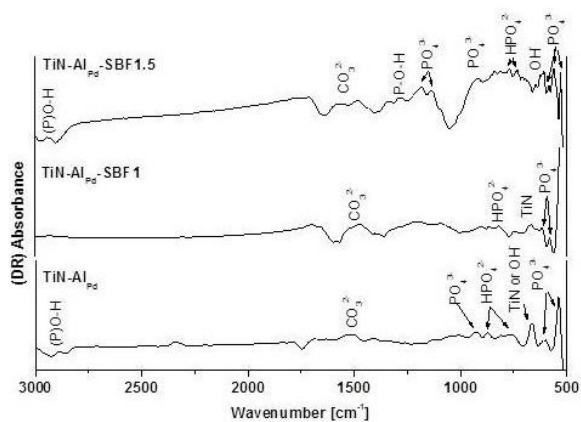


Figure 44. FT-IR spectrum of TiN after treatment in alkaline bath and after immersion in SBF1 for 4 d then another 2 d in SBF1.5.

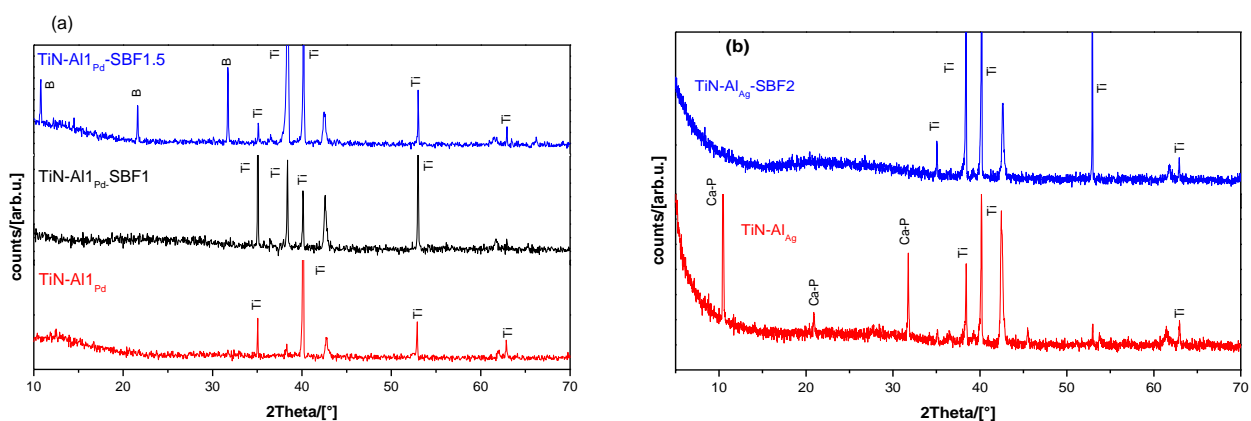


Figure 45. XRD patterns for TiN after treatment in alkaline bath (a) with PdCl<sub>2</sub> and (b) with AgCl (Red) then followed by immersion in SBF (black and blue).

By using the other catalyst AgCl, a reversible behaviour was recorded in **Fig. 45(b)** in comparison to **Fig. 45(a)** using PdCl<sub>2</sub> as a catalyst. The XRD patterns showed that after the bath, beside the presence of Ti peaks (from the substrate), several peaks at  $2\theta = 10.5, 21.2$  and  $31.7^\circ$  indicated the presence of

hexagonal calcium phosphate oxide (Ca-P, ASTM-89-6495). Post immersion in SBF for 14 days, none of Ca-P peaks were observed and only the peaks of the substrate and buffer layer were detected.

TEM image (**Fig. 46(a)**) presented several layers of precipitation with hollow gaps. From EDS-X analyses of these layers (**Fig.46(c)**) the layer is composed of Ca, P, Na and O elements. The SAED for scratched coatings (**Fig. 46(b)**) showed diffraction rings corresponding to (0 1 0), (0 3 1), (1 3 1) and (0 4 1) planes of calcium sodium phosphate hydrate, ( $\alpha$  CaNa<sub>2</sub>P<sub>2</sub>O<sub>7</sub>(H<sub>2</sub>O)<sub>4</sub>, ASTM-74-0395). Moreover, after immersion in SBF for 14 days, nothing is detected and this was confirmed by XRD patterns.

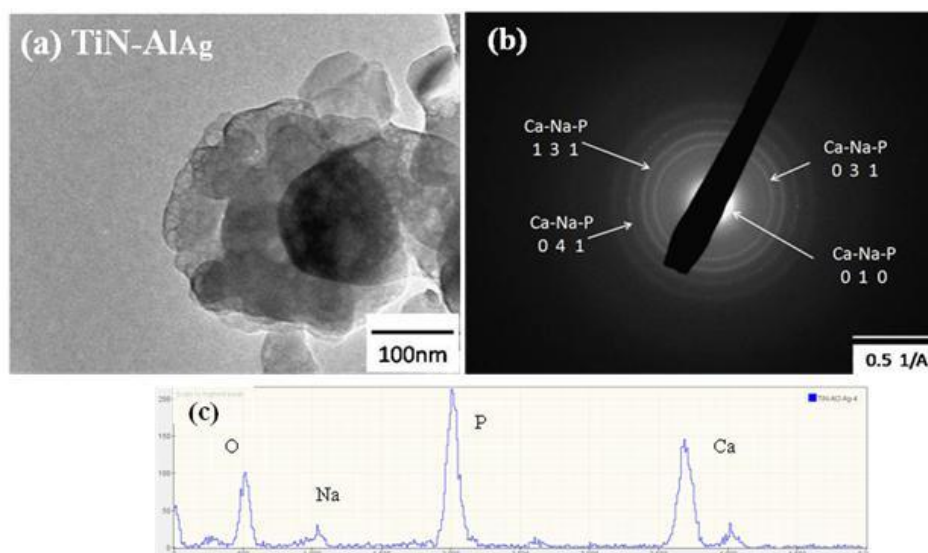


Figure 46. (a) TEM image of calcium phosphate coatings after 2 h in alkaline bath with AgCl, (b) corresponding SAED and (c) corresponding EDS-X analysis.

## 2. Morphological analysis of samples after treatment with alkaline bath

### 2.1. Surface morphology of Group I

The surface morphology of TAV<sub>400</sub>-1h-Al<sub>Pd</sub> (**Fig. 47(a)**) showed that the entire surface was completely covered producing homogenous surface of longitudinal plates arranged randomly but compacted (**Fig. 47(b)**). These plates were mainly composed of Ca, P, Na and Cl ions. Surprisingly, the detection of Si element is due to the alkali released from the glass beaker as shown in its EDS-X analyses (**Fig. 47(c)**).

The treated surface 3 h after immersion in the alkaline bath (**Fig. 47(d)**) had a similar morphology observed in TAV<sub>400</sub>-1h-Al<sub>Pd</sub> (**Fig. 47(a)**). At higher magnification, the plates were fused together without sharp edges (**Fig. 47(e)**). In this sample, there was no detection of P ions elements in EDS-X analysis (**Fig. 47(f)**) meaning that heat treatment with different rates did not affect the morphology of the substrates.

By decreasing the roughness (**Fig. 47(g)**), the surface of TAV<sub>4000</sub> after immersion in alkaline bath for 2 h (TAV<sub>4000</sub>-Al<sub>Pd</sub>) was completely covered with a dense and uniform layer of sodium titanate which appeared as horizontal plates fused together (blue, inserted figure). Some stone like precipitates were spread on the background (**Fig. 47(h)**, red), these stones are mainly composed of Ca-P as shown in their EDS-X analysis (**Fig. 47(i)**, red).

When the same bath was applied for another substrate  $Ti_{4000}$ , (**Fig. 47(j)**) the surface was completely covered with vertically aligned plates of sodium titanate (blue), without detection of Al from the substrate proving that the formed sodium titanate is a thick layer, with the observation of some plates (red) mixed with spindle shape (green, **Fig. 47(k)**) spread on the surface. Both plates and spindles are composed of Na, Ca, P with different amounts as shown in EDS-X analysis (**Fig. 47(i)**). Detection of Si in EDS-X analysis is again suggested being from glass beaker during manipulation.

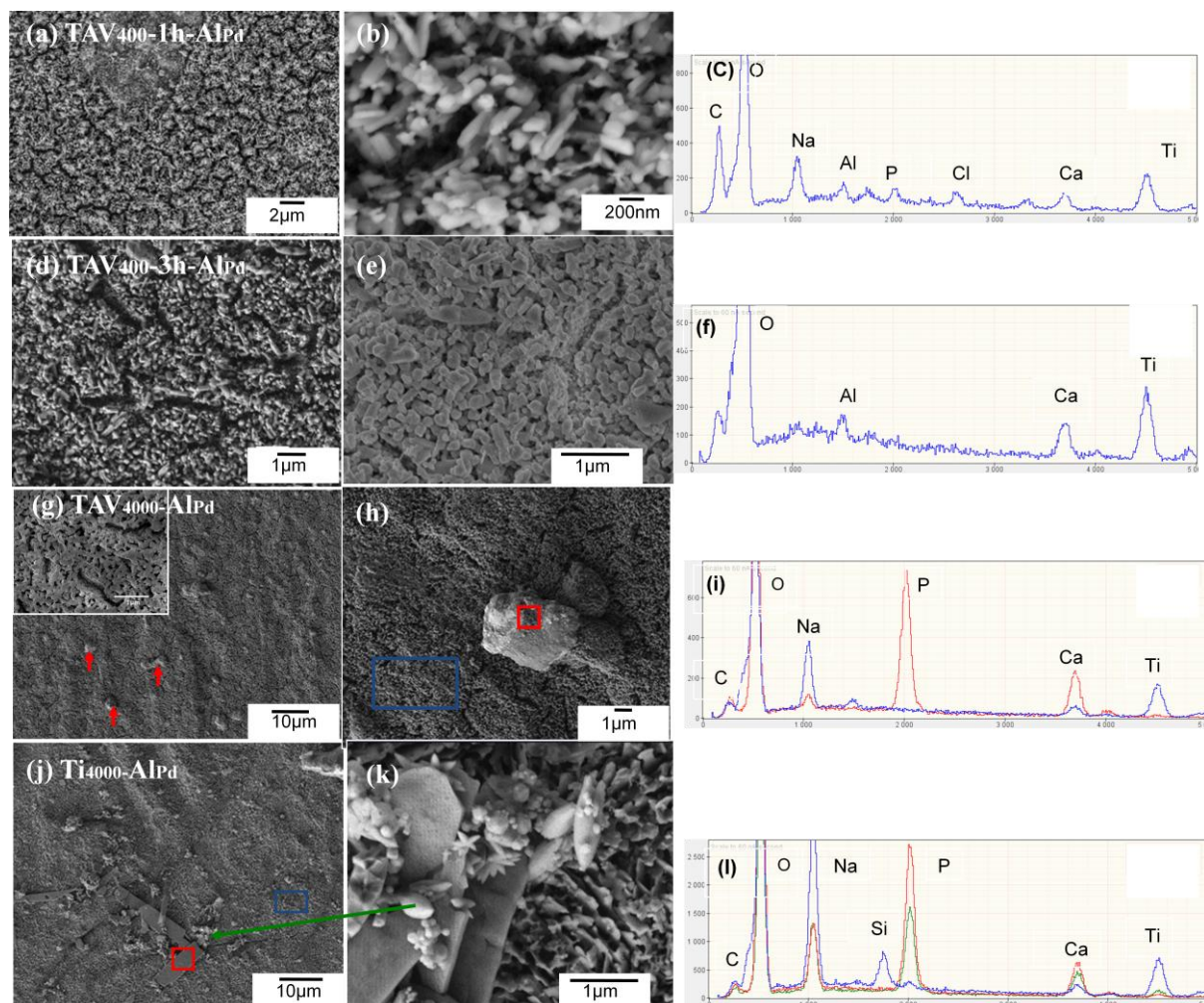


Figure 47. FESEM images of different substrates after immersion for 2 h in alkaline bath: (a,b)  $TAV_{400-1h}$ , (d,e)  $TAV_{400-3h}$ , (g,h)  $TAV_{4000}$ , (j,k)  $Ti_{4000}$  and (c,f,i,l) their corresponding EDS-X analyses.

Similar to group I with acidic bath, the stability of the formed layer after immersion in alkaline bath was validated by immersing each sample shown in **Fig. 47** in SBF for several periods as shown in **Fig. 48**.

After immersion of  $TAV_{400-1h-AlPd}$  in SBF for 4 days (**Fig. 48(a)**), the observed layer was completely different from the other formed layer deposit after immersion in alkaline bath (**Fig. 47(a)**). It seems to be as open network (inserted figure) composed of sodium titanate with small amount of Ca and P as detected in EDS-X analyses (**Fig. 48(c)**, blue). After another 2 days in SBF1.5 (**Fig. 48 (b)**), the surface is still showing the same morphology but with some dissolution of ions. The only detected elements were Ca Ti and O (**Fig. 48(c)**, red). In both samples, the forming layer is thin due to presence of Al from the substrate.

$TAV_{400-3h-AlPd-SBF1}$  presented similar morphology of  $TAV_{400-3h-AlPd}$  (**Fig. 47(d)**). This formed layer looks like longitudinal grains and the surface is mainly composed of titanium oxide with fewer

amounts of Na elements with the absence of P element after immersion (**Fig. 48(f)**, blue). While post immersion in SBF1.5 for additional 2 days (**Fig. 48(e)**), the morphology completely differed from the previous one and converted to be an open network. This layer is composed of titanium oxide and NaCl, with small amount of P elements (**Fig. 48(f)**, red) pointing to the beginning of rebuilt CaP layer. Regarding TAV<sub>4000</sub>-AlPd after immersion in SBF for 7 days (**Fig. 48(g)**), the background still had the same morphology observed in TAV<sub>4000</sub>-AlPd (**Fig. 47(g)**), which was mainly composed of sodium titanate (**Fig. 48(i)**, blue), but there is thin film began to grow over this background which is mainly composed of Ca, Na, P, O and Cl (**Fig. 48(i)**, red). After immersion in SBF for 14 days, sodium titanate with same morphology still appear (inserted figure). Also there are a lot of agglomerates (**Fig. 48(h)**, green) (network like) spread on the surface. These agglomerates had structure similar to that observed after 7 days but with higher amount of Ca-P (**Fig. 48(i)**, green).

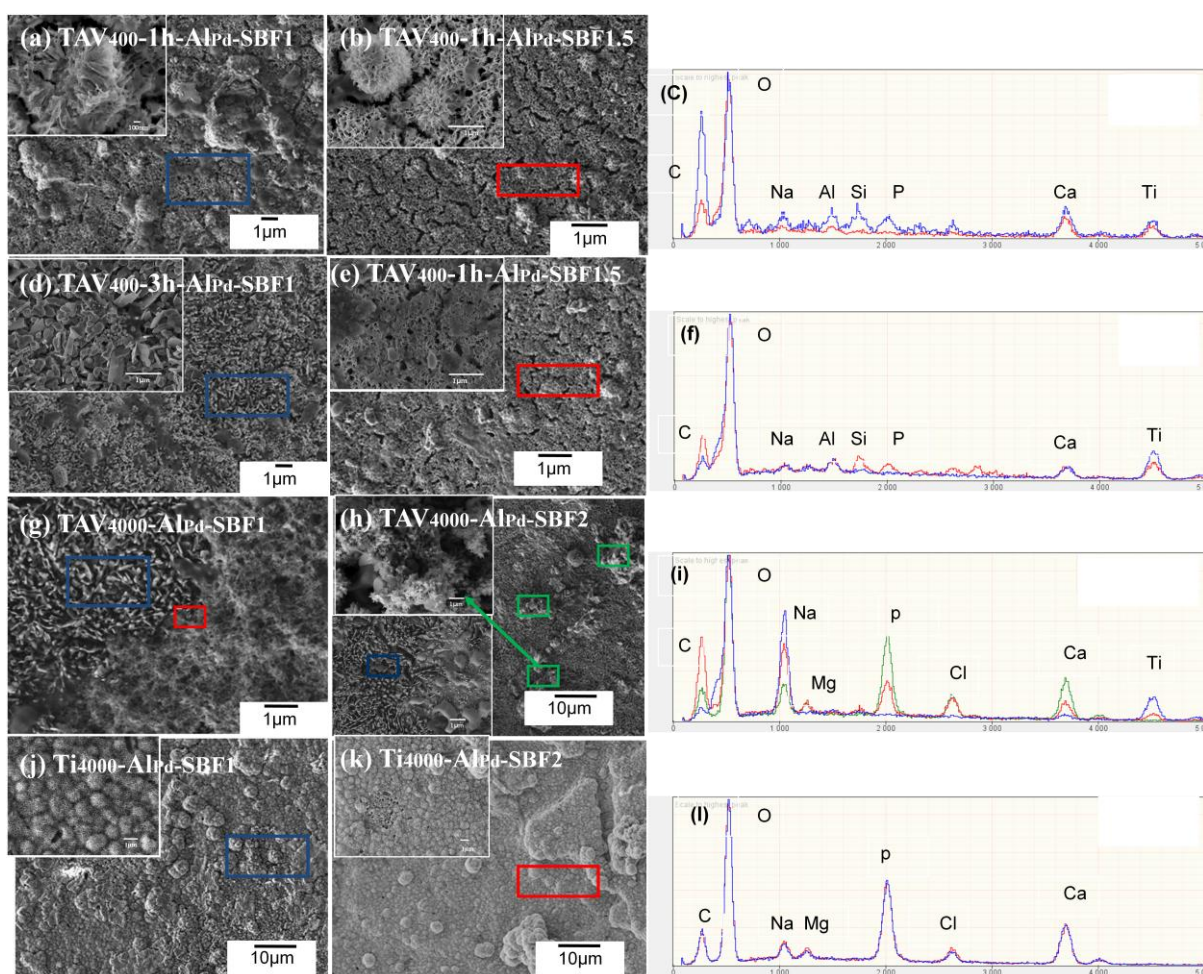


Figure 48. FESEM images of Group I after immersion for 2 h in alkaline bath followed by immersion in SBF: (a,b) TAV<sub>400</sub>-1h-AlPd immersed in SBF1 for 4 d followed by another 2 d in SBF1.5, (d,e) TAV<sub>400</sub>-3h-AlPd immersed in SBF1 for 4 d followed by another 2 d in SBF1.5, (g,h) TAV<sub>4000</sub>-AlPd immersed in SBF for 7 and 14 d, (j,k) Ti<sub>4000</sub>-AlPd immersed in SBF for 7 and 14 d and (c, f, i, l) their corresponding EDS-X analyses.

After immersion of Ti<sub>4000</sub>-AlPd in SBF for 1week (**Fig. 48(j)**), porous network layer completely covered the surface leading to disappearance of sodium titanate coming from background. After additional week in SBF, this porous network layer grew in several layers (**Fig. 48(k)**). EDS-X analyses confirmed that both layers consist of Ca-P with small amounts of Na and Mg (**Fig. 48(l)** blue

and red). The formation of CaP layer with this morphology observed in Ti<sub>4000</sub>-Al<sub>Pd</sub>-SBF1 and Ti<sub>4000</sub>-Al<sub>Pd</sub>-SBF2 was reported for Ti and its alloys [Lee et al., 2002; Kim et al., 1999 and 1996] but after 10 and 30 days immersion in SBF.

## 2.2. Surface morphology of Group II

**Figure 49(a)** showed that after 2 h in alkaline bath, the surface was coated with homogenous layers which completely covered the observed network structure (formed during pretreatment steps, **Fig. 18(g,h)**). Higher magnification revealed that these coatings are fine aggregates with similar size which also grew inside the network. EDS-X analysis, indicates that these aggregates were mainly composed of Na, Ca and P (blue), along with Na and Ti from the background (red) (**Fig. 49(c)**).

After immersion of these treated samples (TAV<sub>4000</sub>-Al<sub>Ag</sub>) in SBF for 7 days, hemispherical-like coatings of Ca-P completely covered the network of sodium titanate layer (**Fig. 49(a,b)**). At higher magnification, these coatings consisted of needle like crystallites (**Fig. 49(e)**). The formed layer was thick enough approximately 5-15 μm as shown in inserted figure. This layer was similar to that layer formed on Ti<sub>4000</sub>-Al<sub>Pd</sub>-SBF1 and Ti<sub>4000</sub>-Al<sub>Pd</sub>-SBF2 (**Fig. 48(j,k)**).

The formation of Ca-P layer with this morphology recorded in TAV<sub>4000</sub>-Al<sub>Pd</sub>-SBF1 was reported for Ti and its alloys [Lee et al., 2002; Kim et al., 1999 and 1996] after 10 and 30 days immersion in SBF.

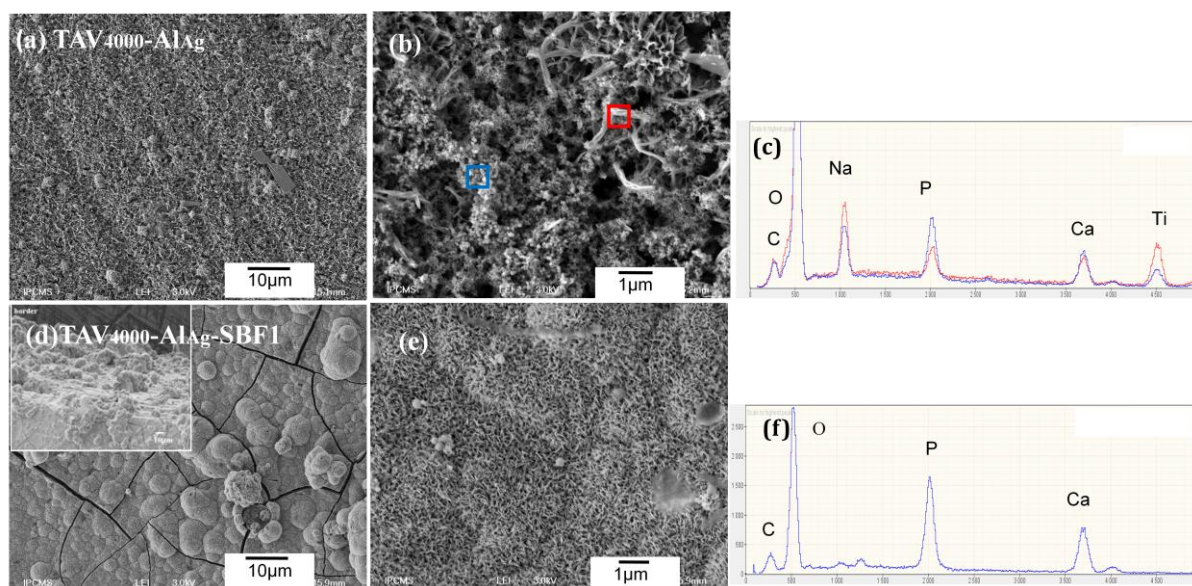


Figure 49. FESEM images of TAV<sub>4000</sub> (a,b) after immersion in alkaline bath for 2 h, (d,e) after immersion TAV<sub>4000</sub>-Al<sub>Ag</sub> in SBF for 7 d and (c,f) corresponding EDS-X analyses.

## 2.3. Surface morphology of Group III

**Figure 50(a)** shows that the background is completely covered with TiN layer with the detection of P ions in this background (**Fig. 50(d)**, blue). Some strips (**Fig. 50(b)**, green) and plates (**Fig. 50(c)**, red) were spread in the background. These plates are mainly composed of Na and P with the presence of some Ca element as shown in EDS-X analyses (**Fig. 50(d)**, red), while the strips are composed of Na, Ca, P elements (**Fig. 50(d)**, green).

By using AgCl as a catalyst instead of PdCl<sub>2</sub>, the surface was completely covered with different shapes of precipitations (blue), **Fig. 50(e)**. At different higher magnification these precipitations were plates beginning to crystallize (**Fig. 50(f)** and inserted figure, red) and needle shapes (red), with the

presence of solid plates semi covered with fine precipitations (**Fig. 50(g)**, green). EDS-X analyses (**Fig. 50(h)**) demonstrated that all shapes of precipitations had the same composition of Ca, P, Na and O elements with different amounts to show that all plates and needles had higher amount of Na instead of Ca which speculate that this ion was responsible to solidify the plates, while the fine aggregates had a higher amount Ca instead of Na.

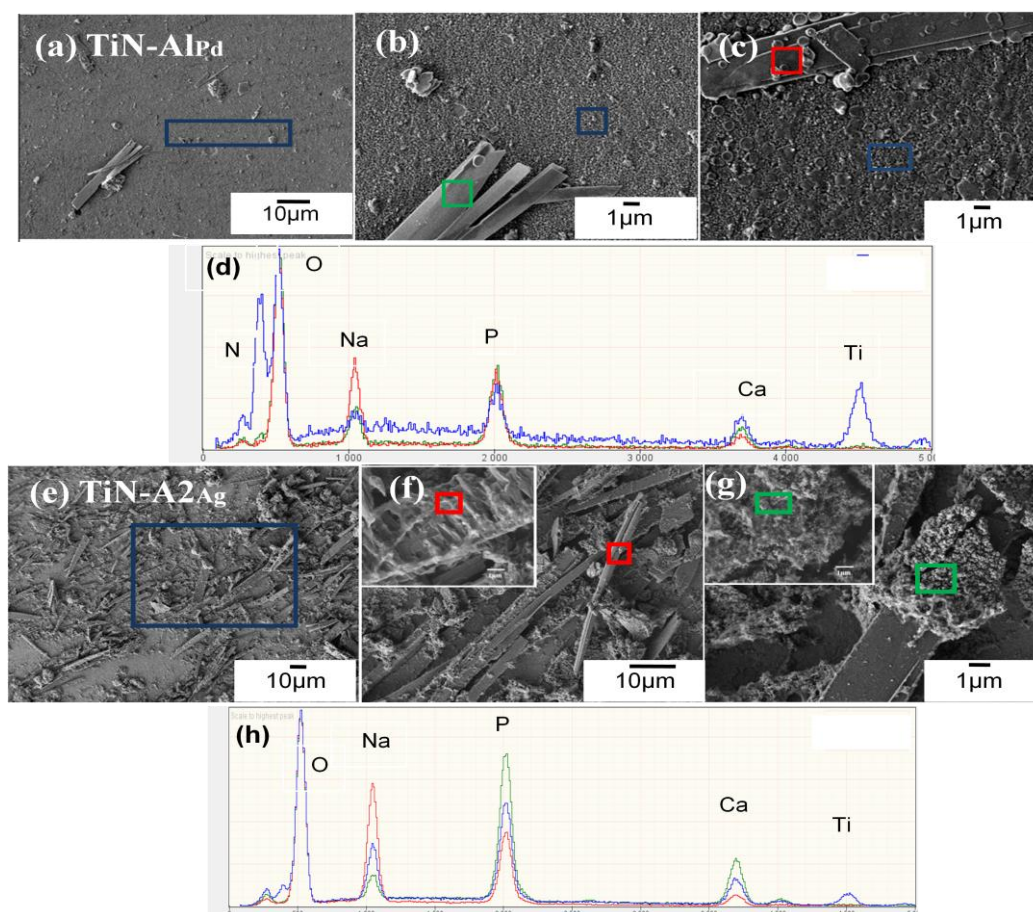


Figure 50. FESEM images of TiN after immersion in alkaline bath (a,b,c) with  $\text{PdCl}_2$  for 1 h, (e,f,g) with  $\text{AgCl}$  for 2 h and (d, h) corresponding EDS-X analyses.

To check the stability of deposited precipitates after the alkaline bath, each sample was immersed in SBF. After immersing TiN- $\text{Al}_{\text{Pd}}$  in SBF1 for 4 days (**Fig. 51(a)**), massive parts were observed (red). At higher magnification, this massive mass is composed of small aggregates with a fused layer around them (**Fig. 51(b)**). From EDS-X analyses (**Fig. 51(c)**), these aggregates are composed of Ca-P mixed with NaCl (red), with the presence of TiN from the background (blue). After another 2 days in SBF1.5 (**Fig. 51(d)**), a growth of a layer (green) with the presence of several massive parts (blue and red) were observed. At higher magnification, these massive were different types of lath like plates. One of them seems to be compact plates (**Fig. 51(f)**, blue) while the other formed porous massive part (**Fig. 51(e)**, red). EDS-X analysis of all precipitations (green, red and blue) nearly had similar quantity of Ca and P elements while the compact one had some Na elements suggested to be the responsible to solidify into compact shape.

Concerning TiN- $\text{Al}_{\text{Ag}}$  after immersion of in SBF for 7 days (**Fig. 51(h)**), all the observed plates shown after the bath were dissolved, however the existence of small dark region spread on the surface (blue). Higher magnifications of these dark region showed that they composed of massive aggregates

(Fig. 51(j), blue) in addition to another structure was observed, seems to be triangle plates with some hemisphere precipitation (Fig. 51(i), red) grown on its surface. EDS-X analyses (Fig. 51(k)) showed that both structures observed composed of Ca, P and O nearly with similar amount with small amount of Mg. By immersing the same sample for another 7 days in SBF (Fig. 51(l)), the surface begins to cover with the grey region as observed in Fig. 51(h). At higher magnification, this grey region seem to be thin film of very fine precipitate begin to spread on the surface with the presence of some cubes (Fig. 51(m)). The composition of this film was mainly Ca, P and O and the cubes were NaCl, with the detection of Ti and N elements from the substrate because the film was thin (Fig. 51(n)).

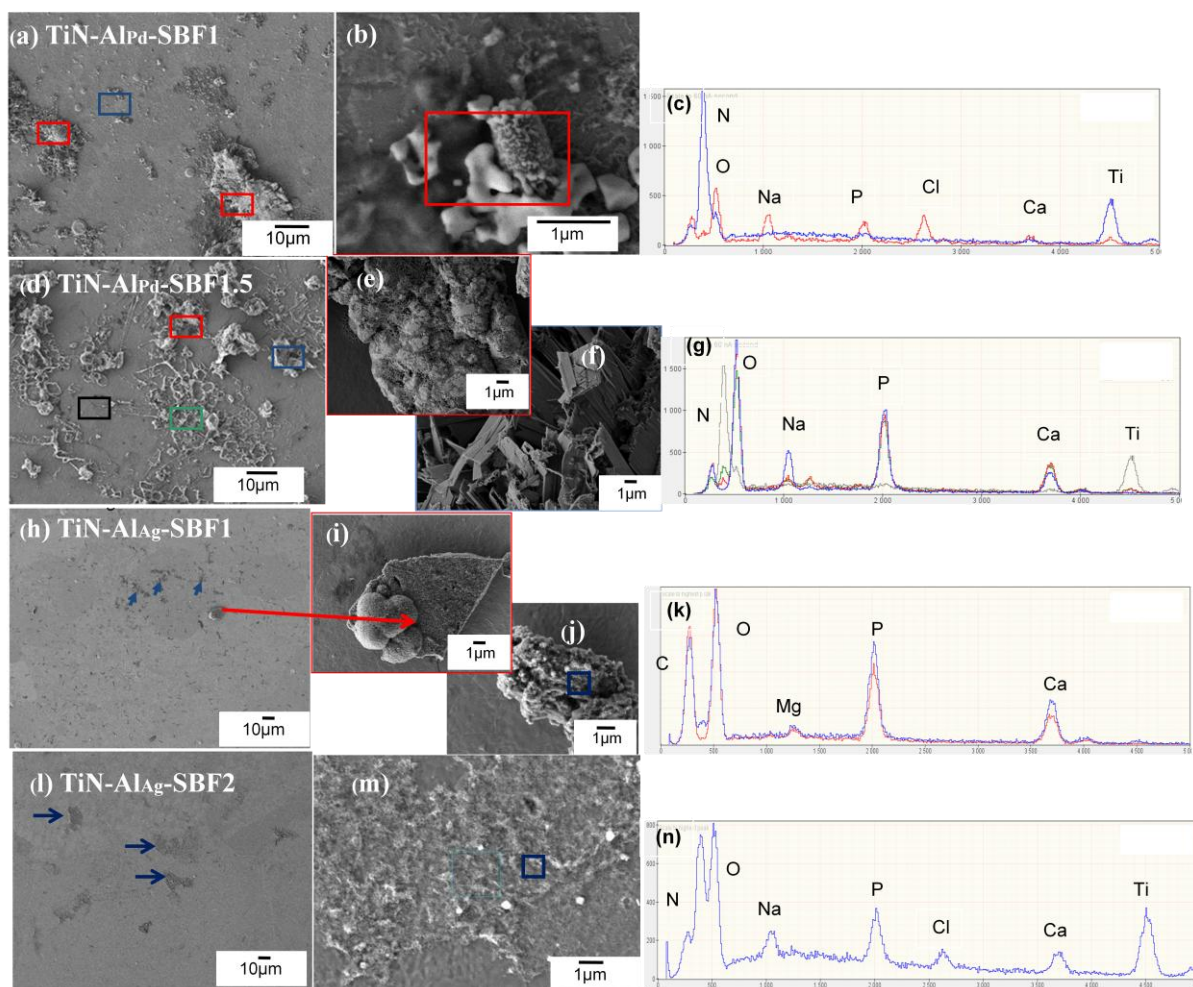


Figure 51. FESEM images of TiN-Al after immersion in (a, b) SBF1 for 4 d, (d,e,f) SBF1.5 for another 2 d, (h,i,j) SBF1 for 7 d, (l,m) SBF for 14 d and (c,g,k,n) corresponding EDS-X analyses.

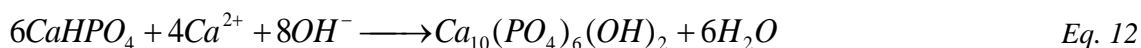
Finally, we found that alkaline bath was able to deposit some Ca-P precipitation on the new buffer layer TiN after 1h by using PdCl<sub>2</sub> while it nearly covered the entire surface with Ca-P deposition on using AgCl. Post SBF, two reversible trends were observed:

- (1) Deposition of Ca-P precipitations were enhanced after 4 days in SBF1 followed with another 2 days in SBF1.5 as proved in Fig. 51(d);
- (2) All depositions observed after the bath (Fig. 51(e)) dissolved after 1week (Fig. 51(h)) then began to rebuild after another week in SBF.

### 3. Biochemical analysis of SBF of Groups I, II and III

Remarkable increase of  $\text{Ca}^{2+}$  and decrease in P elements after 4d for  $\text{TAV}_{400}\text{-1h-AcPd-SBF1}$  and  $\text{TAV}_{400}\text{-3h-AcPd-SBF1}$  (Fig. 52(a)). Post immersion in SBF1.5,  $\text{TAV}_{400}\text{-1h-AcPd-SBF1.5}$  slightly adsorbed  $\text{Ca}^{2+}$  and P elements while on the contrary  $\text{TAV}_{400}\text{-3h-AcPd-SBF1.5}$  released them.

The substrates with lower roughness ( $\text{TAV}_{4000}\text{-AlPd}$  and  $\text{Ti}_{4000}\text{-AlPd}$ ) showed a sharp decrease in the concentrations of both  $\text{Ca}^{2+}$  and P elements (Fig. 52(b)) which prove consuming these ions through transformation of brushite to HA according to the following reaction:



Formation of hydroxyapatite after SBF immersion was confirmed in FT-IR (Fig. 39(c,d)), TF-XRD (Fig. 40(b)) and TEM with SAED (Fig. 41(d-i)).

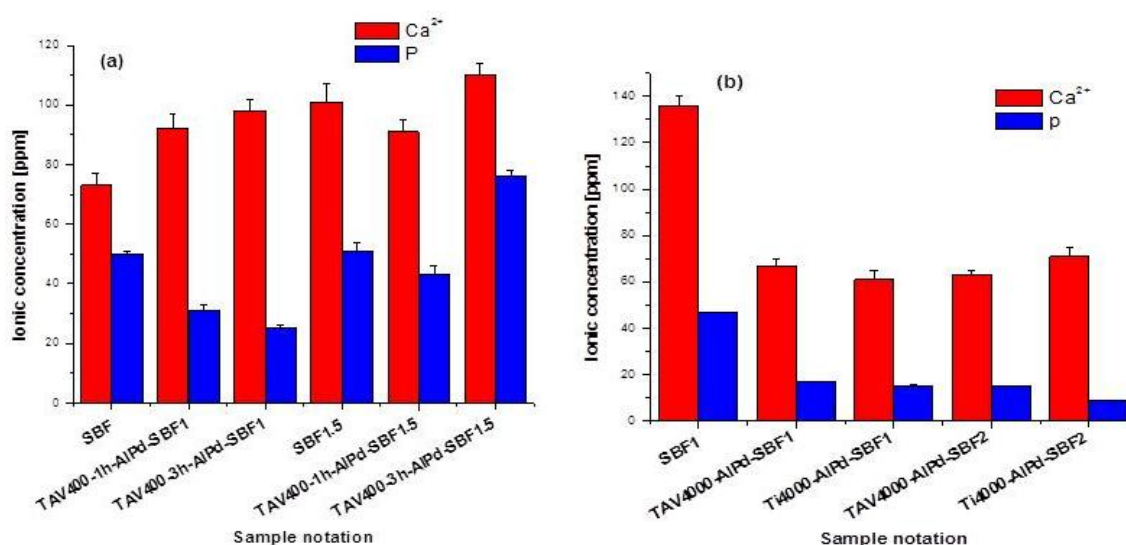


Figure 52. Concentrations of  $\text{Ca}^{2+}$  and P ions (a)  $\text{TAV}_{400}$  in SBF1 (4 d) followed by another 2 d in SBF1.5, (b)  $\text{TAV}_{4000}$  and  $\text{Ti}_{4000}$  in SBF for 7 and 14 d. (Group I)

No observable change in Ca or P elements after 3 or 7 days for  $\text{TAV}_{4000}\text{-AlAg-SBF1}$  or  $\text{TAV}_{4000}\text{-AlAg-SBF2}$  was measured (Fig. 53). However, a thick layer of HA post alkaline bath treatment followed by 7 days in SBF. This result proved that such layer could be formed from Ca and P elements coating the surface after alkaline bath (rich with both  $\text{Ca}^{2+}$  and P ions).

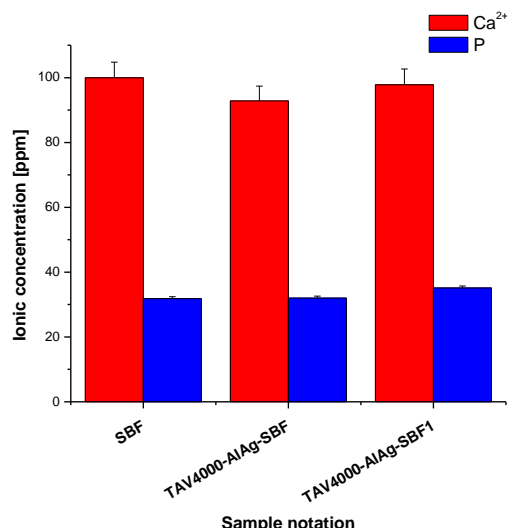


Figure 53. Concentrations of Ca<sup>2+</sup> and P ions in SBF after immersion of TAV<sub>4000</sub> immersed in alkaline bath with AgCl after 3 and 7 d. (Group II).

TiN-Al<sub>Pd</sub>-SBF1 and TiN-Al<sub>Pd</sub>-SBF1.5 showed a remarkable reduction in both Ca<sup>2+</sup> and P ionic concentrations (Fig. 54(a)) after immersion in SBF1 and SBF1.5. Such highly adsorption of both ions was expected after the previous analyses which confirmed the formation of well crystalline brushite after 6 days in SBF (Fig. 45(a)).

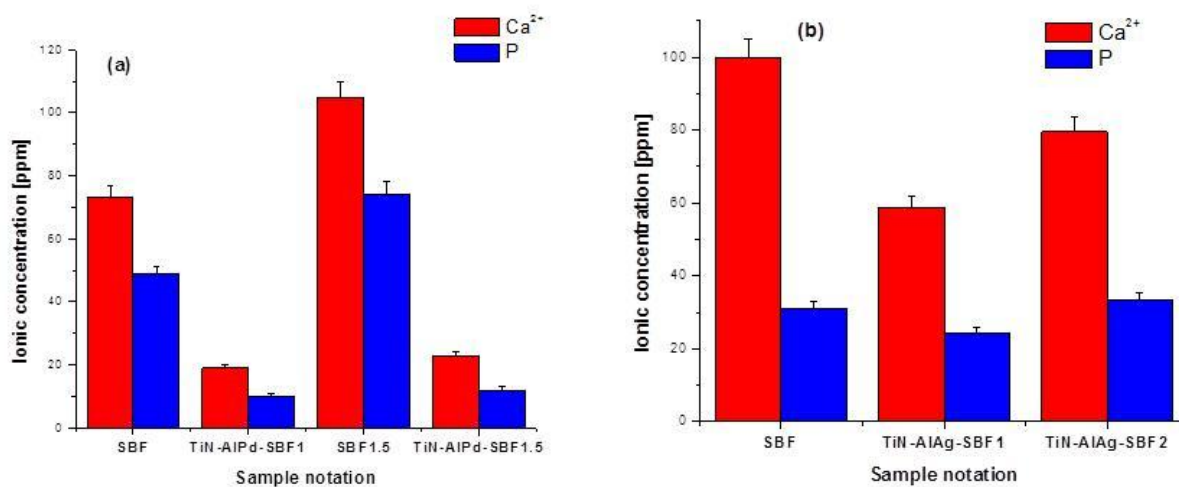


Figure 54. Concentrations of Ca<sup>2+</sup> and P ions (a) TiN after treatment with alkaline bath for 1 and 2 h with PdCl<sub>2</sub> in SBF1 (4 d) followed by another 2 d in SBF1.5, (b) TiN after treatment with alkaline bath for 2 h with AgCl in SBF for 7 and 14 d. (Group III)

Upon changing the catalyst, TiN-Al<sub>Ag</sub>-SBF1 suffered a decrease in both Ca<sup>2+</sup> and P ionic concentrations (Fig. 54(b)). These data were not confirmed in the previous work because it is shown that upon changing the catalyst, TiN-Al<sub>2Ag</sub> was dissolving all Ca-P precipitation. After 14 days in SBF, there are also slightly decrease (absorption) in Ca<sup>2+</sup> ions but without observable decrease in P ions.

### Conclusion of Part III

In this part, we can report that surface roughness and heat treatment and catalyst influenced the formation of biolayer by using alkaline bath:

(i) Similar roughness ( $TAV_{400}$ ) with different heating rates, showed that slow heating rate ( $3^{\circ}\text{C}/\text{minute}$ ), followed by 2 h in alkaline bath ( $TAV_{400}\text{-}3\text{h-Al}_{\text{Pd}}$ ) is better than the other fast heating rate ( $10^{\circ}\text{C}/\text{minute}$ ) especially after immersion for 4 and 6 days in SBF. An enhanced  $\text{PO}_4^{3-}$  groups precipitation as shown by FT-IR (**Fig. 39 (a,b)**) while no noticeable precipitations could be observed by using SEM (**Fig. 48(a,b,d,e)**). However, the detection of tiny amounts of Ca and P elements in EDS-X analysis (**Fig. 48 (c,f)**) proves their presence. Finally, one can conclude that alkaline bath failed to form Ca-P precipitation on TAV having high roughness.

(ii) By decreasing the roughness  $TAV_{4000}$  and  $Ti_{4000}$ , brushite began to be distributed on the substrate after 2 h in the alkaline bath which was transformed to HA after immersion for 14 days in SBF. These result is confirmed by FT-IR (**Fig. 39(c,d)**), TEM (**Fig. 41(d-i)**), EDS-X analyses (**Fig. 48(j,k)**). Moreover, these results were confirmed by the biochemical analysis of SBF showing sharply absorption of Ca and P ions (**Fig. 52(b)**).

As a result, alkaline bath (with  $\text{PdCl}_2$ ) allowed the deposition of Ca-P layer, which acts as nuclei to stimulate the coverage of the surface with bi-phasic precipitations of phosphates ( $\beta$ -TCP and HA). On using the bath with the other catalyst ( $\text{AgCl}$ ), homogenous distribution of Ca-P was formed after 2 h immersion on Group II samples. Furthermore, comparing samples of Group I after SBF immersion of 7 days in, a thick and homogenous layer of HA covered completely the TAV substrate (**Fig. 42, Fig. 43(d,e)** and **Fig. 49(d,e)**).

TiN as a buffer layer – after alkaline baths with both catalysts, facilitated the deposition of Ca-P agglomerates. These last ones enhanced the deposition of Ca-P, in case of  $\text{PdCl}_2$ , after 4 days in SBF1 followed with another 2 days in SBF1.5 as proved in **Fig. 45(a)** and **51(c)**. While, by  $\text{AgCl}$ , the formed precipitations were superficial and they dissolved after 7 days immersion in SBF. Finally, during the other 7 days immersion in SBF, the layer began to be rebuilt.

## Part IV. Oxidant bath

A complete list of treated specimen by oxidant bath is given in **Table 20**.

### 1. Structural analysis of samples after treatment with oxidant bath

#### 1.1. Structural analysis of Group I

**Figure 55(a)** shows FT-IR spectra of TAV<sub>400</sub>-1h-OxPd, after immersion in SBF1 (TAV<sub>400</sub>-1h-OxPd-SBF1) and SBF1.5 (TAV<sub>400</sub>-1h-OxPd-SBF1.5). After the oxidant bath,  $\nu_4$  bending vibration of PO<sub>4</sub><sup>3-</sup> group was observed in the range of 560-600 cm<sup>-1</sup>. Upon immersion in SBF for 4 and 6 days, these bands became sharper and with additional  $\nu_3$  stretching vibration of PO<sub>4</sub><sup>3-</sup> band (1050-1150 cm<sup>-1</sup>). Furthermore, the typical bands of HPO<sub>4</sub><sup>2-</sup> groups were observed after SBF only in the range 700-800 cm<sup>-1</sup>.

**Figure 55(b)** proves the detection of the bands of  $\nu_4$  bending vibration (550-600 cm<sup>-1</sup>) and  $\nu_3$  stretching vibration (1050-1200 cm<sup>-1</sup>) of PO<sub>4</sub><sup>3-</sup> group in all samples (TAV<sub>400</sub>-3h-OxPd, TAV<sub>400</sub>-3h-OxPd-SBF1 and TAV<sub>400</sub>-3h-OxPd-SBF1.5). The bands of HPO<sub>4</sub><sup>2-</sup> group were detected in the region of 750-830 cm<sup>-1</sup> only after SBF1. The presence of CO<sub>3</sub><sup>2-</sup> group was confirmed by detecting a band at 1630 cm<sup>-1</sup> after the bath (TAV<sub>400</sub>-3h-OxPd). This band was enhanced and shifted after SBF1 (TAV<sub>400</sub>-3h-OxPd-SBF1). At the same time,  $\nu_3$  (1380 cm<sup>-1</sup>) and  $\nu_2$  (880 cm<sup>-1</sup>) vibration modes of CO<sub>3</sub><sup>2-</sup> group were detected. These peaks are to characteristic to carbonate, shifted and grew broad after immersion in SBF1.5 (TAV<sub>400</sub>-1h-OxPd-SBF1.5). The OH<sup>-</sup> group (band at 660 cm<sup>-1</sup>) was detected too.

The  $\nu_2$  bending vibration and  $\nu_3$  stretching vibration bands (**Fig. 55(c)**), of PO<sub>4</sub><sup>3-</sup> group at 470 and 1100 cm<sup>-1</sup>, respectively, were present in TAV<sub>4000</sub>-OxPd, TAV<sub>4000</sub>-OxPd-SBF1 and TAV<sub>4000</sub>-OxPd-SBF2. Moreover, one can note the presence of P-O-H out of plane bending (vibrational mode) of HPO<sub>4</sub><sup>2-</sup> at 790 cm<sup>-1</sup>. Finally, the OH<sup>-</sup> band at 661 cm<sup>-1</sup> was recorded to indicate water liberations.

Some brushite bands were detected in TAV<sub>4000</sub>-OxPd such as:

(i) the OH<sup>-</sup> band at 661 cm<sup>-1</sup> indicated the water liberations; (ii) HPO<sub>4</sub><sup>2-</sup> band at 790 cm<sup>-1</sup>; (iii) P-O(H) of HPO<sub>4</sub><sup>2-</sup> band at 880 cm<sup>-1</sup>; (iv) H-O-H band at 2355 cm<sup>-1</sup> and (v) finally the sharp band at 2923 cm<sup>-1</sup> assigned for (P)O-H stretching [Kumta et al., 2005].

In TAV<sub>4000</sub>-OxPd-SBF2, some brushite peaks were replaced with a broad band 3200-3500 cm<sup>-1</sup> indicating stretching of lattice water molecule in addition to small band at 1640cm<sup>-1</sup> assigned to bending lattice of water molecules. In addition, the presence of  $\nu_3$  carbonate band at 1550 cm<sup>-1</sup> is confirmed.

**Figure 55(d)** proved that nearly both spectra had similar bands: the presence of  $\nu_2$  (400-490 cm<sup>-1</sup>) and  $\nu_4$  (550-570 cm<sup>-1</sup>) bending vibration of PO<sub>4</sub><sup>3-</sup>. Besides, the  $\nu_3$  stretching vibration band (1055-1120 cm<sup>-1</sup>) of PO<sub>4</sub><sup>3-</sup> was detected as well as the band characteristic of P-O-H out of plane bending (810 cm<sup>-1</sup>) of HPO<sub>4</sub><sup>2-</sup>.

Table 20. Complete series of sample (Group I, II and III) treated with oxidant autocatalytic bath.

Group	Substrate	Grit of SiC	Pretreatment steps		Oxidant Ox bath (h)	Biomimetic bath				Sample notation	
			Intermediate layer	Heating rate (°C/minute)		SBF1 (4 d)	SBF1.5 (2 d)	SBF1 (7 d)	SBF1 (14 d)		
Group I PdCl <sub>2</sub>	Ti-6Al-4V	400	Na <sub>x</sub> Ti <sub>y</sub> O <sub>z</sub> H <sub>t</sub>	10	2	—	—	—	—	TAV <sub>400</sub> -1h-OxPd	
				3		—	—	—	—	TAV <sub>400</sub> -3h-OxPd	
				10		yes	—	—	—	TAV <sub>400</sub> -1h-OxPd-SBF1	
				3		yes	—	—	—	TAV <sub>400</sub> -3h-OxPd-SBF1	
				10		yes	yes	—	—	TAV <sub>400</sub> -1h-OxPd-SBF1.5	
				3		yes	yes	—	—	TAV <sub>400</sub> -3h-OxPd-SBF1.5	
		4000	Na <sub>x</sub> Ti <sub>y</sub> O <sub>z</sub> H <sub>t</sub>	3	2	—	—	—	—	TAV <sub>4000</sub> -OxPd	
						—	—	yes	—	TAV <sub>4000</sub> -OxPd-SBF*1	
						—	—	yes	yes	TAV <sub>4000</sub> -OxPd-SBF2**	
		Group I PdCl <sub>2</sub>	Ti CP-3	4000	Na <sub>x</sub> Ti <sub>y</sub> O <sub>z</sub> H <sub>t</sub>	3	2	—	—	—	—
—	—							yes	—	Ti <sub>4000</sub> -OxPd-SBF1*	
—	—							yes	yes	Ti <sub>4000</sub> -OxPd-SBF2**	
Group III PdCl <sub>2</sub>	Ti CP-1	Colloidal silicas	TiN	—	1	—	—	—	—	TiN-Ox1Pd	
					1	yes	—	—	—	TiN-Ox1Pd-SBF1	
					1	yes	yes	—	—	TiN-Ox1Pd-SBF1.5	
							<b>SBF (3 d)</b>	<b>SBF (7d)</b>	<b>SBF (14 d)</b>		
Group II AgCl	Ti-6Al-4V	4000	Na <sub>x</sub> Ti <sub>y</sub> O <sub>z</sub> H <sub>t</sub>	3	2	—	—	—	—	TAV <sub>4000</sub> -OxAg	
							yes	—	—	—	TAV <sub>4000</sub> -OxAg-SBF
							yes	yes	—	—	TAV <sub>4000</sub> -OxAg-SBF1*
Group III AgCl	Ti CP-1	Colloidal silicas	TiN	—	2	—	—	—	—	TiN-Ox2Ag	
					2	—	yes	—	—	TiN-Ox2Ag-SBF1*	
					2	—	yes	yes	—	TiN-Ox2Ag-SBF2**	

SBF1\* indicates the immersion in SBF for 7 days; SBF2\*\* indicates the immersion in SBF for 14 days

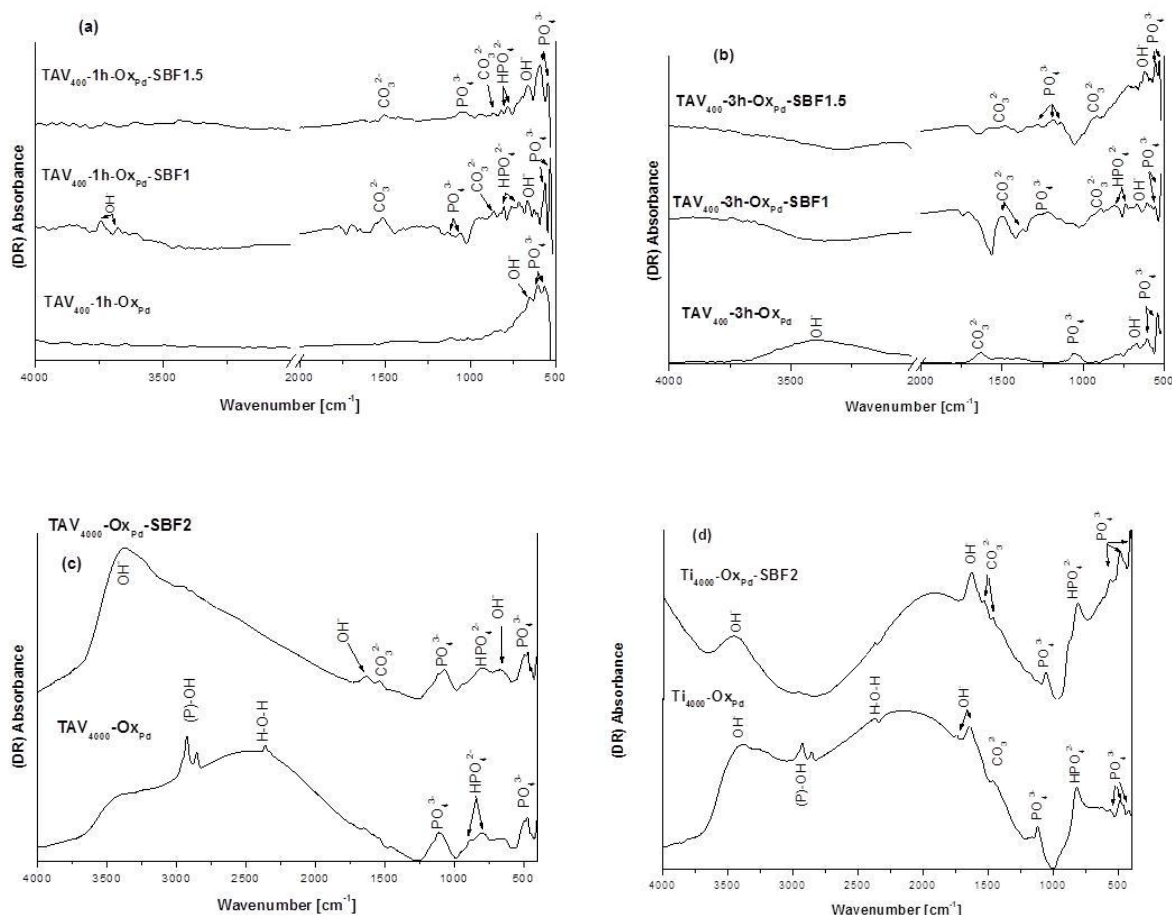


Figure 55. FT-IR spectra after immersing 2 h in oxidant bath followed by immersion in SBF (a)  $TAV_{400}$  subjected to heating rate  $10^{\circ}\text{C}/\text{minute}$ , (b)  $TAV_{400}$  subjected to heating rate  $3^{\circ}\text{C}/\text{minute}$ , (c)  $TAV_{4000}$  subjected to heating rate  $3^{\circ}\text{C}/\text{minute}$  and (d)  $Ti_{4000}$  subjected to heating rate  $3^{\circ}\text{C}/\text{minute}$ .

After the oxidant bath ( $Ti_{4000}\text{-Ox}_{Pd}$ ), some bands characteristic for brushite were detected, such as:

(i) the band at  $810\text{ cm}^{-1}$  originating from  $\text{HPO}_4^{2-}$ ; (ii) the bands at  $1640$  and  $1720\text{ cm}^{-1}$  which indicate the bending and rotation of residual free water (iii) the band at  $2360\text{ cm}^{-1}$  assigned to the combination of H-O-H and (iv) finally the sharp band at  $2923\text{ cm}^{-1}$  assigned for (P)O–H stretching [Kumta et al., 2005]. On immersion in SBF,  $Ti_{4000}\text{-Ox}_{Pd}\text{-SBF2}$  the observed brushite peaks moved out to be replaced by the weak  $\text{CO}_3^{2-}$  bands ( $880$ ,  $1455$  and  $1530\text{ cm}^{-1}$ ). These peaks indicated the growth of A-type carbonated HA, where substitution with hydroxyl group at  $1550\text{ cm}^{-1}$  band [Kumta et al., 2005].

As observed in **Fig. 56(a)** XRD patterns of  $TAV_{4000}\text{-Ox}_{Pd}$  and  $TAV_{4000}\text{-Ox}_{Pd}\text{-SBF2}$  showed only characteristic peaks of the TAV substrate without any noticeable Ca-P. On the contrary, in case of  $Ti_{4000}\text{-Ox}_{Pd}$  (**Fig. 56(b)**), besides the peaks of the Ti substrate other peaks ( $2\theta = 10.9$ ,  $21.4$ ,  $31$  and  $35.07^{\circ}$ ) corresponding to the presence of brushite (B, ASTM-72-0713). On the other hand, after SBF, ( $TAV_{4000}\text{-Ox}_{Pd}\text{-SBF1}$ ) no observable peaks could be detected proving, therefore, dissolution.

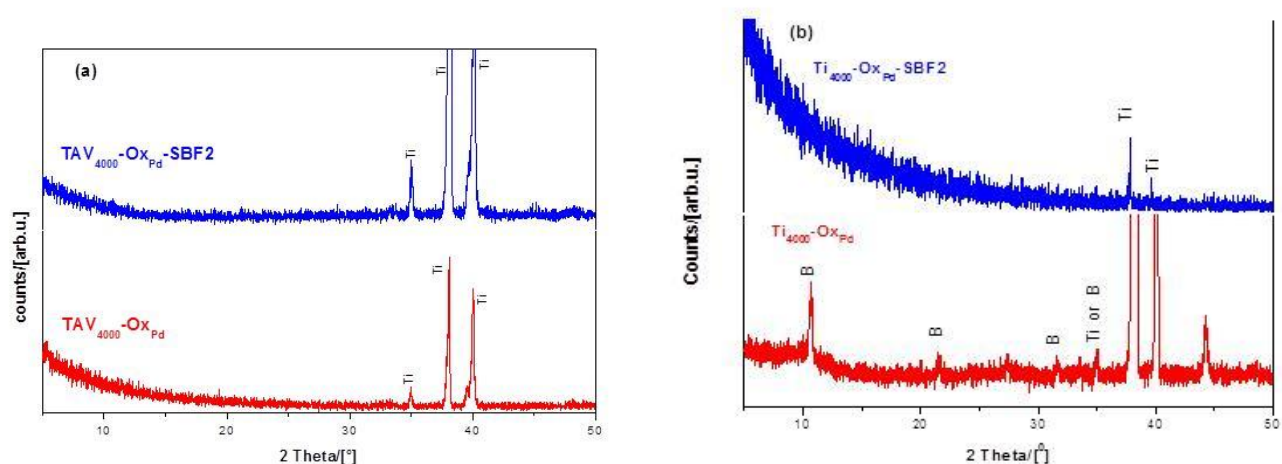


Figure 56. TF-XRD patterns for (a)  $TAV_{4000}$  and (b)  $Ti_{4000}$  after treatment in oxidant bath for 2 h (red) and after immersion in SBF for 14 days (blue).

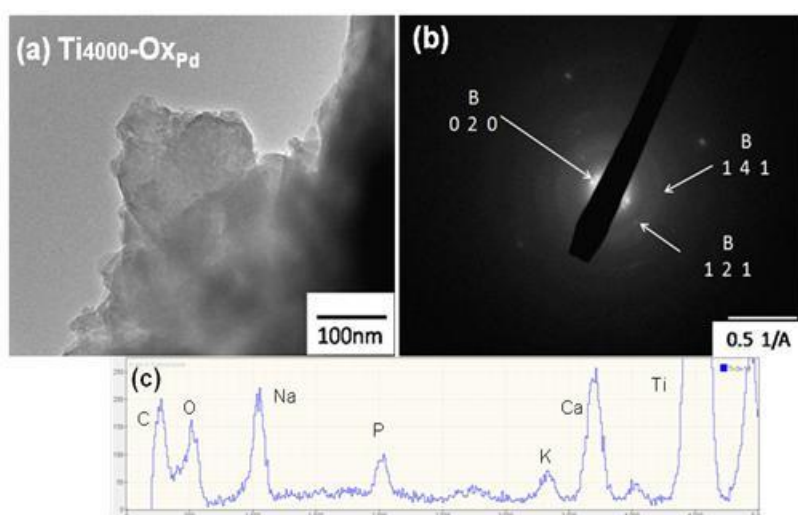


Figure 57. TEM image of calcium phosphate coatings (a)  $Ti_{4000}$  after 2 h in oxidant bath, (b) corresponding SAED and (c) corresponding EDS-X analysis.

**Figure 57(a)** showed TEM images of scratched layer. EDS-X analyses (**Fig. 57(c)**) indicated that this layer is mainly composed of Ca, P with the presence of Na, Ti and O elements. In **Fig. 57(b)**, the presence of brushite was confirmed by SAED analysis of  $Ti_{4000}-Ox_{Pd}$  layer confirming the detection of the brushite (B, ASTM-72-0713) though the diffraction rings corresponding to (0 2 0), (1 2 1) and (1 4 1) planes. No Ca-P coating was observed after the immersing in SBF.

### 1.2. Structural analysis of Group II

**Figure 58** showed XRD patterns of the substrate, which were detected in both graphs. Other peaks were detected at  $2\theta=39.7$  and  $35.5^\circ$  after 2 h in oxidant bath only ( $TAV_{4000}-Ox_{Ag}$ ). These peaks are referred to the presence of whitlockite, one of calcium phosphate phases, (TCP, ASTM-03-0713).

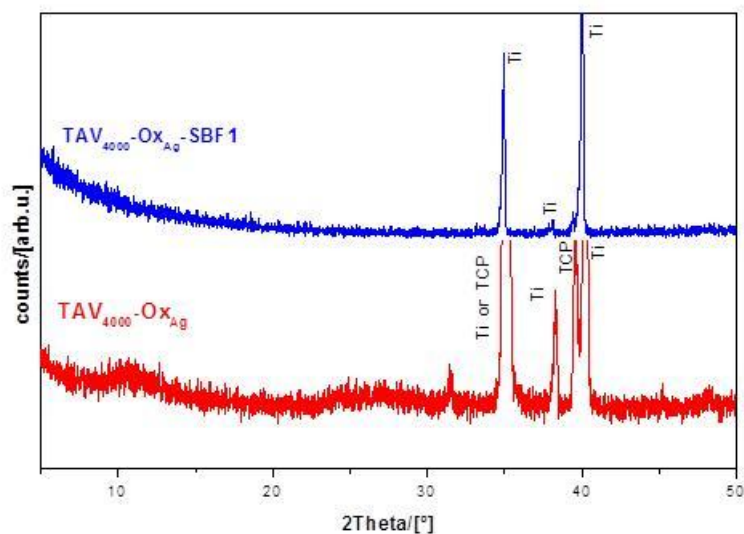


Figure 58. TF-XRD patterns for  $TAV_{4000}$  after treatment in oxidant bath with AgCl for 2 h (red) and after immersion in SBF for 7 days (blue).

TEM image (Fig. 57(a)) indicated the presence of homogenous rounded nanometric precipitations, ranging between 10-20 nm in diameter after 2 h in oxidant bath. EDS-X analyses of this layer proved that it is mainly composed of Ca, Na and P elements (Fig. 57(c)). The SAED of the scratched coatings (Fig. 57(b)) confirms the results obtained in (Fig.56), by detecting diffraction rings characteristic of whitlockite (TCP, ASTM-030713). While after immersion in SBF no characteristic peaks were observed proving their dissolution.

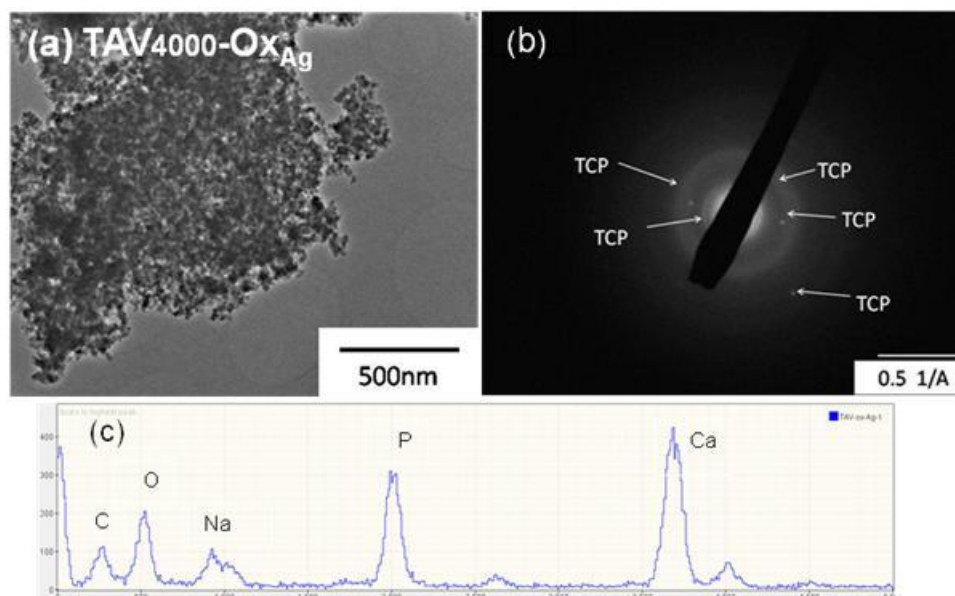


Figure 59. (a) TEM image of calcium phosphate coatings after 2 h in oxidant bath with AgCl, (b) corresponding SAED and (c) corresponding EDS-X analysis.

### 1.3. Structural analysis of Group III

The bands located between  $520\text{-}600\text{ cm}^{-1}$  indicated to  $\nu_4$  bending mode of P–O–P, were detected in all spectra as two peaks after the bath then reduced into only one sharp peak after 4 days in SBF. Afterward these bands were detected as faint ones after SBF1.5. In addition, the band assigned for the symmetric  $\nu_1$  stretching modes of P–O was recorded at  $948\text{ cm}^{-1}$  only in TiN-Ox<sub>Pd</sub>-SBF1.5 samples while the bands assigned for the double degenerate asymmetric  $\nu_3$  stretching modes of P–O between  $1100\text{-}1170\text{ cm}^{-1}$  were recorded only after SBF1 and SBF1.5 (**Fig. 60**). Bands detected in all spectra between around  $1410$  and  $1530\text{ cm}^{-1}$  were attributed to  $\nu_3$  vibrational mode carbonate group. The detection of the clear peak around  $650\text{ cm}^{-1}$ , in all spectra, characterised the presence of Ti-N from the intermediate layer.

The presence of  $\text{HPO}_4^{2-}$  in ACP (Amorphous Calcium Phosphate) was detect as an absorption peak at about  $890\text{ cm}^{-1}$  due to P-O(H) stretching mode of protonated orthophosphate species. Furthermore, there is semi-broad band of a weak intensity near  $2300\text{ cm}^{-1}$  corresponding to H-O(P) stretching in  $\text{HPO}_4^{2-}$  ions [Dorozhkin, 2010].

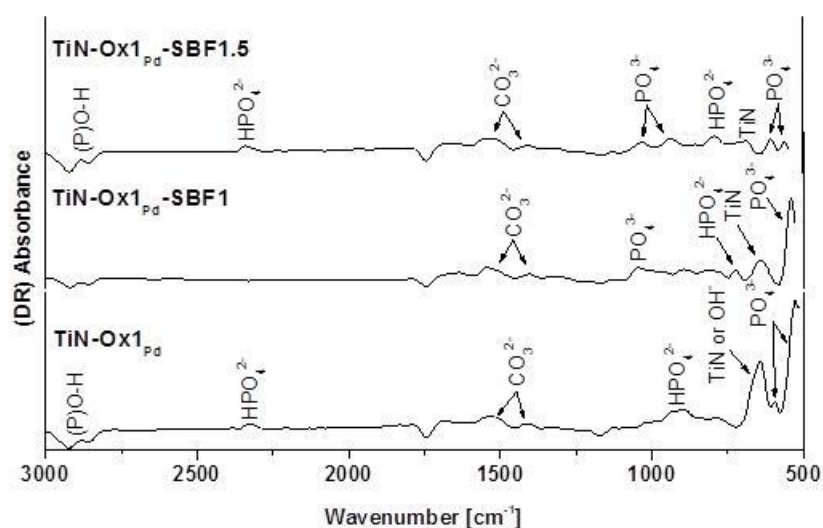


Figure 60. FT-IR spectras of TiN after immersion in oxidant bath with  $\text{PdCl}_2$  followed with immersion in SBF1 for 4 d then another 2 d in SBF1.5.

The peaks detected in **Fig. 61** on using oxidant bath with  $\text{PdCl}_2$  (**a**) or  $\text{AgCl}$  (**b**) were characteristic to Ti substrate at  $2\theta = 35.09$ ,  $38.7$  and  $40.2^\circ$  (ASTM-89-4893) only without any noticeable peaks indicating the absence of Ca-P precipitations.

In spite of the bands recorded by FT-IR analyses characterizing the phosphatic phases, their absence in XRD patterns proved their presence but in amounts below the level of XRD detection.

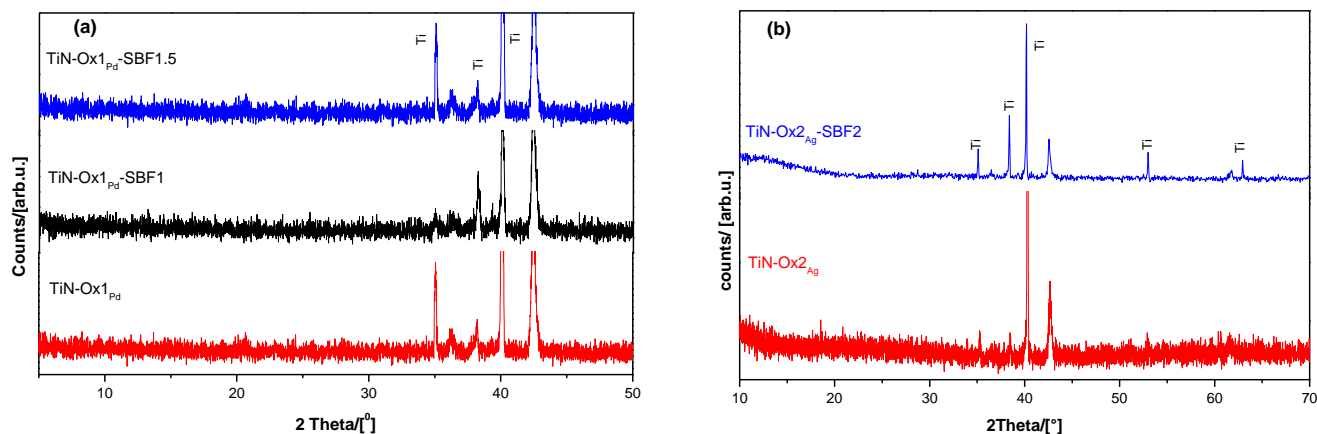


Figure 61. XRD patterns for TiN after treatment in oxidant bath (a) with  $\text{PdCl}_2$  and (b) with  $\text{AgCl}$  (red) then followed with immersion in SBF (black and blue).

## 2. Morphological analysis of samples after treatment with oxidant bath

### 2.1. Surface morphology of Group I

Figure 60(a) showed that the surface of  $\text{TAV}_{400}$ -1h after being immersed in oxidant bath for 2 h; the porous network background, formed after pretreatment, was proved (Fig. 62 (a), blue) in some areas, but the other ones seems to fill the pores of background (Fig. 62(b), green). There were some plates grown on the background (Fig. 62(a), red). It was clear from Fig. 62(c) that the background (blue), composed of sodium titanate layer, was not thick, due to detection of Al element of the substrate. The plates (red) and the fused layer (green) had nearly similar elemental composition (Ca and P elements) with the presence of Pd and Cl (Fig. 62(c), green).

Surface morphology of  $\text{TAV}_{400}$ -3h showed clear porous rosy like background (Fig. 62(d,e), blue) with the presence of some needle or plates (Fig. 62(d), red) spread on the background. EDS-X analyses (Fig. 62(f)) clarified that the background was composed of sodium titanate and the needles or plates were composed of Ca and P elements.

By decreasing the roughness  $\text{TAV}_{4000}$ , Fig. 62(g,h) showed that the surface after immersion in oxidant bath was practically covered with superficial layer. It means that it is spread on the surface and not grown from the background. Horizontal plates with different sizes (blue), were lying on another vertical plates from background (red). From chemical analyses (Fig. 62(i)) the horizontal plates were mainly composed of Ca-P precipitations and the background was a layer of sodium titanate formed during pretreatment step.

Concerning the  $\text{Ti}_{4000}$  substrate after immersing in oxidant bath, its surface (Fig. 62(j,k),  $\text{Ti}_{4000}\text{-Ox}_{\text{Pd}}$ ) was covered with several horizontal plates (red) laying on a background composed of vertical plates (blue). These plates were similar to the ones observed in  $\text{TAV}_{4000}\text{-Ox}_{\text{Pd}}$  (Fig. 62(g,h)). Chemical analyses of these horizontal plates prove that they are composed of Ca and P elements in addition to presence of Na, Ti and O from the background as shown in Fig. 62(l).

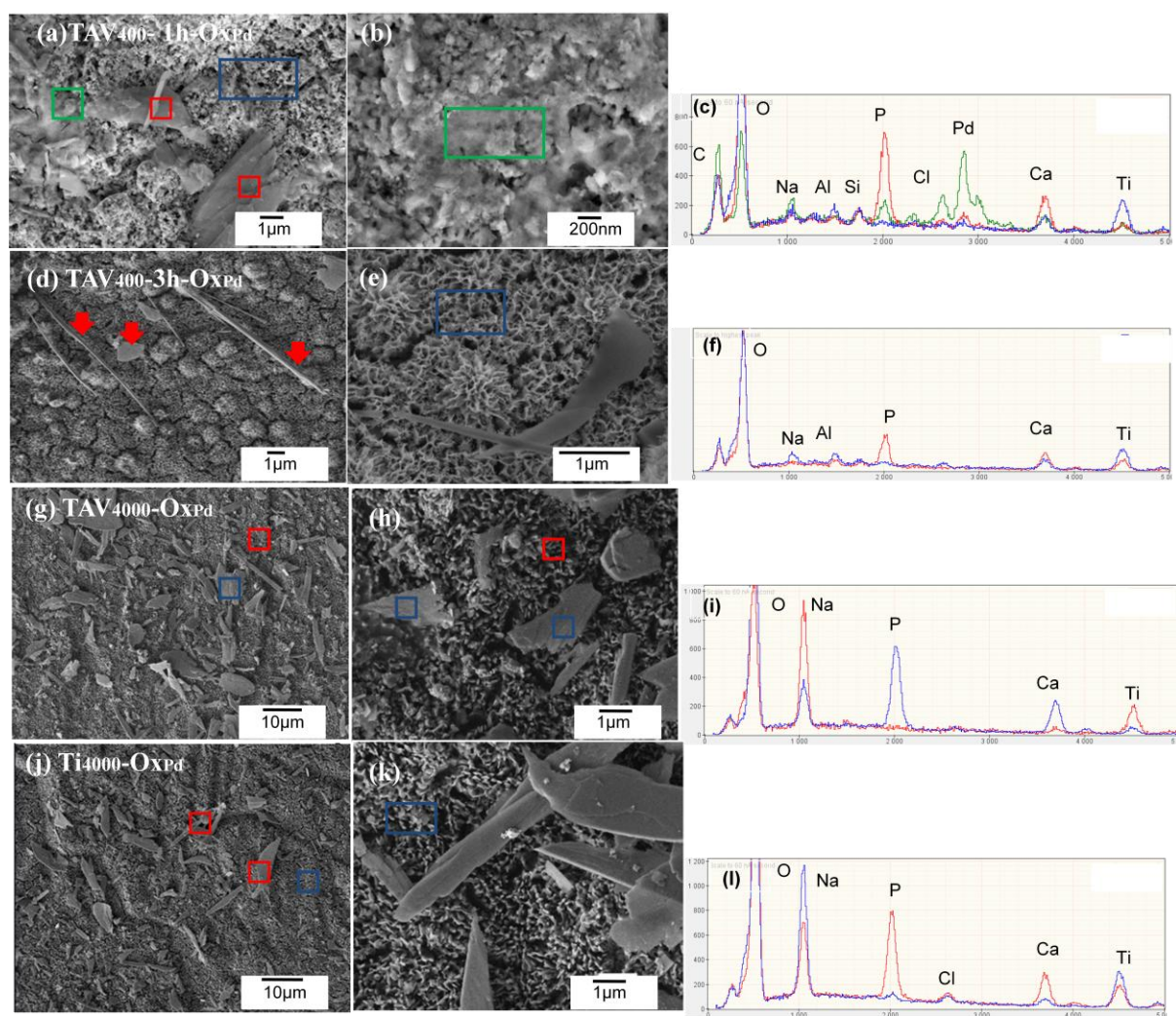


Figure 62. FESEM images of different substrates after immersion for 2 h in oxidant bath: (a,b)  $TAV_{400-1h-OxPd}$ , (d,e)  $TAV_{400-3h-OxPd}$ , (g,h)  $TAV_{4000}$ , (j,k)  $Ti_{4000}$  and (c,f,i,l) their corresponding EDS-X analyses.

Similar to Group I with acidic and alkaline baths, the stability of the formed layer after immersion in each bath was validated by immersing each sample in SBF for different periods as shown in **Fig. 62**.

After immersion of  $TAV_{400-1h-OxPd}$  in SBF for 4 days (**Fig. 63(a)**) all precipitations observed in **Fig. 62(a)** completely dissolved. Only the porous background was observed with some cubes spread on the surface. EDS-X analyses proved that these cubes were NaCl with the presence of Ca elements spreaded on the background (**Fig. 63(c)**, blue). While after immersion for additional 2 days in SBF1.5 (**Fig. 63(b)**), the same morphology was observed but with some precipitations beginning to rebuilt in some areas (red). Chemical analyses clarified that this precipitations were Ca-P lying on background (**Fig. 63(c)**, red).

After immersion of  $TAV_{400-3h-OxPd}$  in SBF for 4 days (**Fig. 63(d)**), the surface had the same morphology of the background observed in  $TAV_{400-3h-OxPd}$  (**Fig. 62(e)**) but without any plates or needle, indicating that they completely dissolved. However, there was no presence of any Ca-P precipitations, but only small elements of Ca and P were detected in EDS-X analysis (**Fig. 63(f)**, blue). And after immersion in SBF1.5 for another 2 days (**Fig. 63(e)**), similar background morphology still observed with similar composition, except Ca element, which dissolved completely, as shown in **Fig. 63(f)**, red.

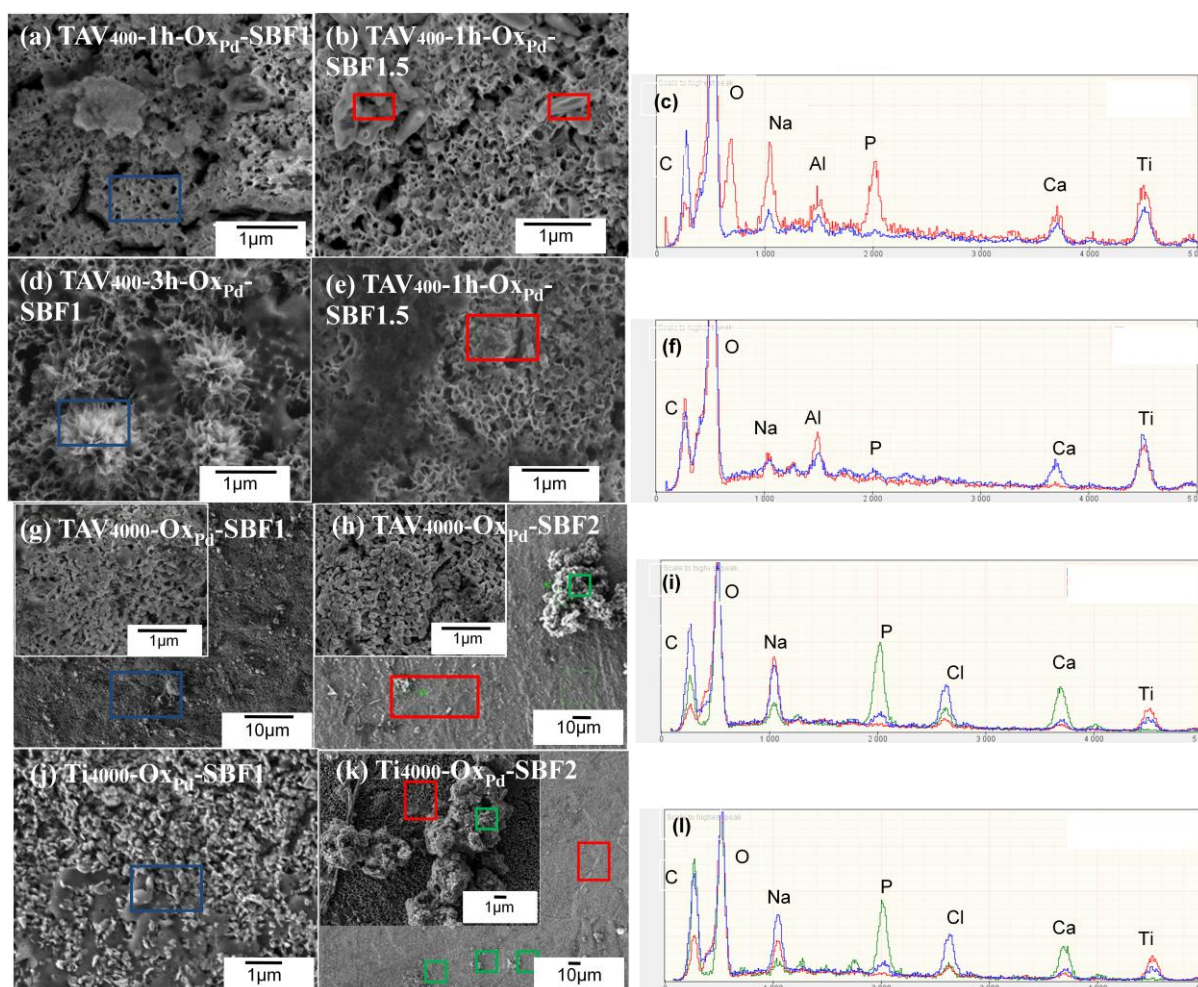


Figure 63. FESEM images of Group I after immersion for 2 h in oxidant bath followed by immersion in SBF: (a,b) TAV<sub>400</sub>-1h-Ox<sub>Pd</sub> immersed in SBF1 for 4 d followed by another 2 d in SBF1.5, (d,e) TAV<sub>400</sub>-3h-Ox<sub>Pd</sub> immersed in SBF1 for 4 d followed by another 2 d in SBF1.5, (g,h) TAV<sub>4000</sub>-Ox<sub>Pd</sub> immersed in SBF for 1 and 14 days, (j,k) Ti<sub>4000</sub>-Ox<sub>Pd</sub> immersed in SBF for 7 and 14 d and (c,f,i,l) their corresponding EDS-X analyses.

The surface of TAV<sub>4000</sub>-Ox<sub>Pd</sub> after immersion in SBF for 7 days (Fig. 63(g)) indicated that the background still had similar morphology observed in Fig. 62(g, h). It is mainly composed of sodium titanate with the presence of some cubes of NaCl distributed on the surface with the detection of small amount of Ca and P elements in EDS-X analyses (Fig 63(i), blue). After another 7 days in SBF (Fig. 63(h)), a similar background was observed as previous figures with the observations of some aggregates beginning to grow on the surface (green). The EDS-X analysis of the background had similar composition (sodium titanate) and the aggregates are composed Ca and P elements in addition to some Na and Cl elements.

Concerning Ti<sub>4000</sub>-Ox<sub>Pd</sub> substrate, after immersion in SBF for 1 and 14 days, similar behaviour to TAV<sub>4000</sub>-Ox<sub>Pd</sub> was observed, e.g. the disappearance of all the horizontal plates after 7 days (Fig. 62(j)). Furthermore, after another 7 days in SBF, the surface seems to be homogenous with the presence of some dots spread on the whole surface (Fig. 62(k), green). At higher magnification, it was found that the homogenous surface (red) of vertical plates (from background) fused together to appear as porous surface. The dots seem to be as some aggregates growing on the surface (green).

EDS-X analyses (**Fig. 62(l)**) proved that the background is composed of Na, Ti and O (red), while the aggregates were composed of Ca and P elements in addition to NaCl grown with Ca-P precipitations.

## 2.2. Surface morphology of Group II

The surface after oxidant bath seems to be completely covered with a homogenous layer (**Fig. 64(a)**). At higher magnification these coatings showed fine grains in nanometric range (**Fig. 64(b)**, blue) in addition to detection of some solid precipitates lying on the fine grains in some areas (inserted figure, red). EDS-X analyses of these fine grains proved that they were mainly composed of Ca, P and O. Na Cl and Ag elements (remaining from the catalyst) were also detected.

After immersing this sample in SBF for 7 days to check its stability (TAV<sub>4000</sub>-Ox<sub>Ag</sub>-SBF1), the surface was homogenous but at higher magnification we observe that all the grains observed in **Fig. 64(a)** disappeared and surface morphology seems to be composed of porous network with some rose-like structures growing on the porous network layer. Such morphology was observed after alkaline and heat treatment too (**Fig. 18(g,h)**). These results were confirmed after EDS-X analyses (**Fig. 64(e)**) proving the presence of elemental Na, Ti and O elements with some Ca distributed on the whole surface without detection of any P.

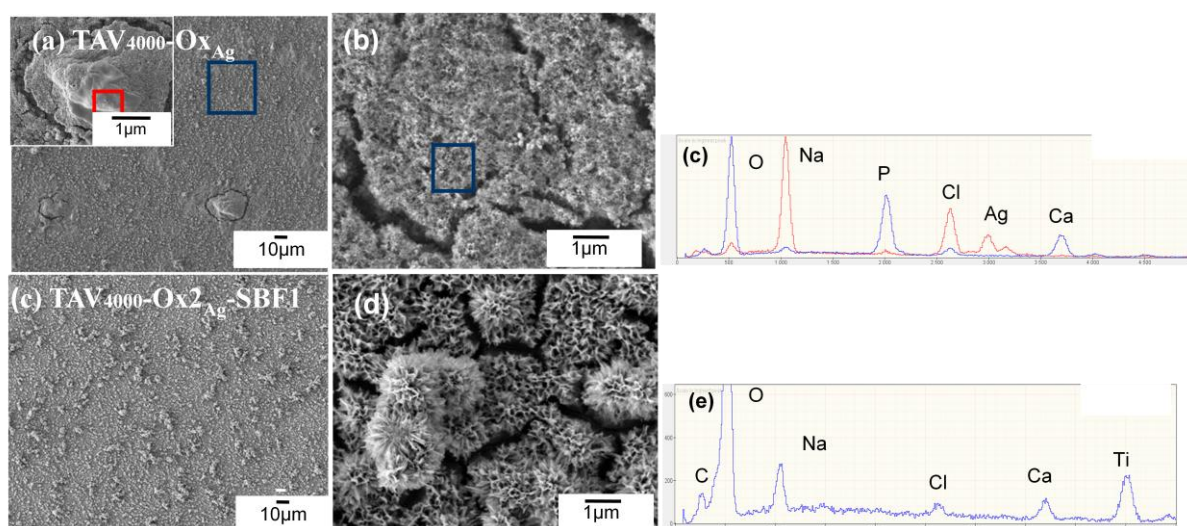


Figure 64. FESEM images of TAV<sub>4000</sub> (a,b) after immersion in oxidant bath for 2 h, (d,e) after immersion TAV<sub>4000</sub>-Ox<sub>Ag</sub> in SBF for 7 days and (c,f) corresponding EDS-X analyses.

## 2.3. Surface morphology of Group III

**Figure 65(a)** illustrated the homogenous coating which covers the substrate after only 1 h immersion in oxidant bath. At higher magnification (**Fig. 65(b)**), the layer appears to have very fine and dense nanometric granules. Moreover, EDS-X analyses (**Fig. 65(c)**) established that Ca, O and P elements along with Pd and Cl elements coming from the catalyst. These coating were thick enough; the TiN was not detected as proved by EDS-X analysis.

With AgCl, **Fig. 65(d)**, the surface had some agglomerates spread on the background, at different and higher magnification some of them were fine nanometric granules (blue, as observed in **Fig. 65(f)**) while the other ones appear as needle shapes (red, **Fig. 65(e)**). EDS-X analyses (**Fig. 65(g)**) demonstrated that the fine granules are Ca, P, Na and O elements, while the needle precipitates were Na, P, O with very few amounts of Ca element.

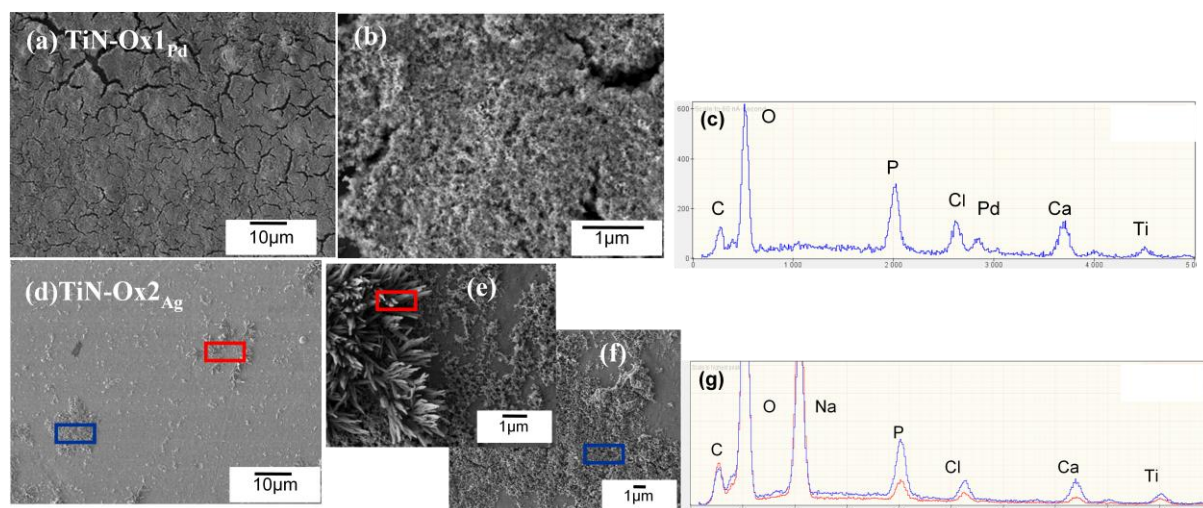


Figure 65. FESEM images of TiN after immersion in oxidant bath (a,b) with  $\text{PdCl}_2$  for 1 h, (d,e,f) with  $\text{AgCl}$  for 2 h and (c,g) corresponding EDS-X analyses.

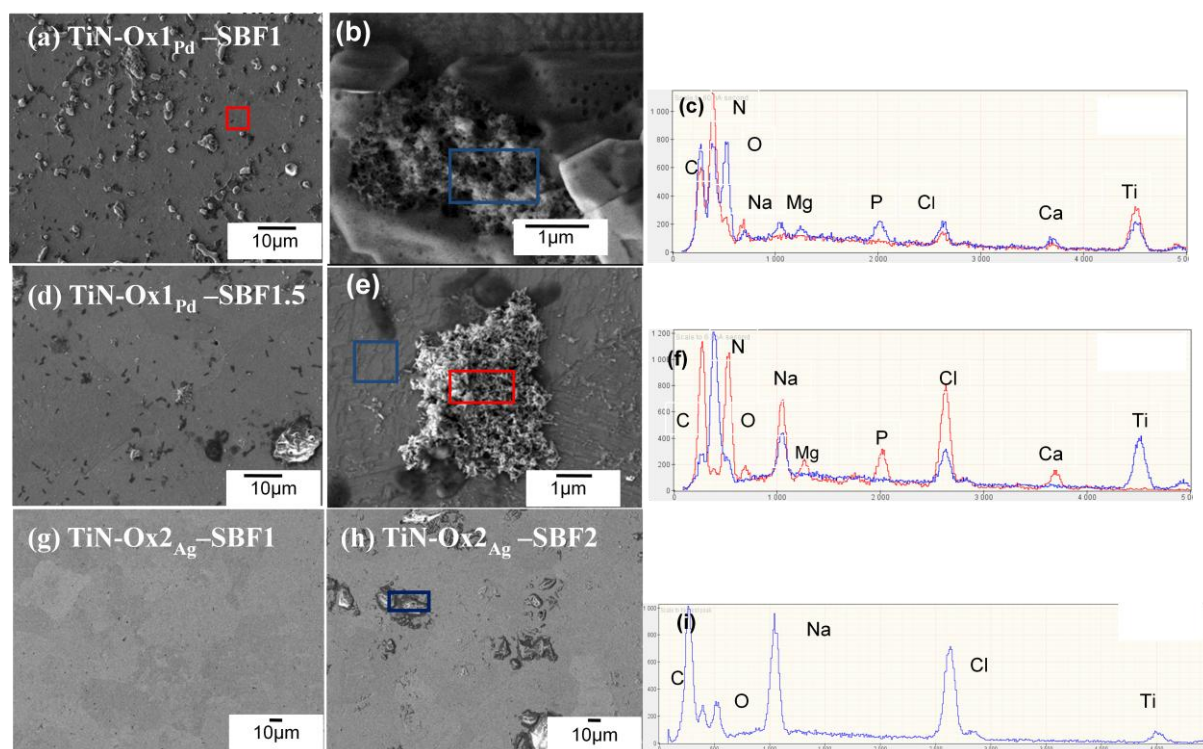


Figure 66. FESEM images of TiN-Ox after immersion in (a,b) SBF1 for 4 d, (d,e) SBF1.5 for another 2 d, (g) SBF1 for 7 days, (h) SBF for 14 days and (c,f,i) corresponding EDS-X analyses.

Upon immersing  $\text{TiN-Ox1}_{\text{Pd}}$  in SBF for 4 days, most of the coatings observed in **Fig. 65(a,b)** dissolved and there are some discrete spots appear on the surface (**Fig. 66(a)**). At higher magnification, these spots had morphology similar to the one observed in **Fig. 65(a,b)** after oxidant bath with presence of solid precipitate surrounding them (**Fig. 66(b)**). From EDS-X analyses it is clear that the splotch (**Fig. 66(c)**, blue) are composed of Ca, Mg and P elements beside Na and Cl (the solid precipitate), these splotch spread on the buffer layer of TiN (**Fig. 66(c)**, red). After another 2 days in SBF1.5, **Fig. 66(d)** showed that splotches decreased, with dissolved Ca-P precipitations gradually. At higher magnification, the remaining splotches, they had the same morphology and similar composition observed in **Fig. 66(d,e)**.

Concerning the other catalyst (AgCl) after immersion in SBF for 7 or 14 days (**Fig. 66 (g,h)**), all the observed precipitations shown after the bath dissolved with the presence of some solid relicts on the surface after 14 days. EDS-X analyses (**Fig. 66(i)**) shown that these solid precipitation was only sodium chloride comes from SBF. That means that all CaP precipitations presented after the bath were completely dissolved.

### 3. Biochemical analysis of Groups I, II and III

An increase in  $\text{Ca}^{2+}$  concentrations with different amounts after immersion in SBF1 (TAV<sub>400</sub>-1h-OxPd-SBF1, TAV<sub>400</sub>-3h-OxPd-SBF1) and SBF1.5 (TAV<sub>400</sub>-1h-OxPd-SBF1.5, TAV<sub>400</sub>-3h-OxPd-SBF1.5) was illustrated in **Fig. 67(a)**. With regard to P elements, a decrease in P concentrations after 4 days (TAV<sub>400</sub>-1h-OxPd-SBF1, TAV<sub>400</sub>-3h-OxPd-SBF1) was recorded. While after immersion in SBF1.5 a slight decrease of P elements for (TAV<sub>400</sub>-1h-OxPd-SBF1.5) in case of TAV<sub>400</sub>-3h-OxPd-SBF1.5, there was an increase in P elements concentration. These results were confirmed with EDS-X analyses, which clarified the presence of some P precipitations in **Fig. 63(c, red)**, **(f, blue)** but with the absence of any P precipitations in **Fig. 63(f, red)**.

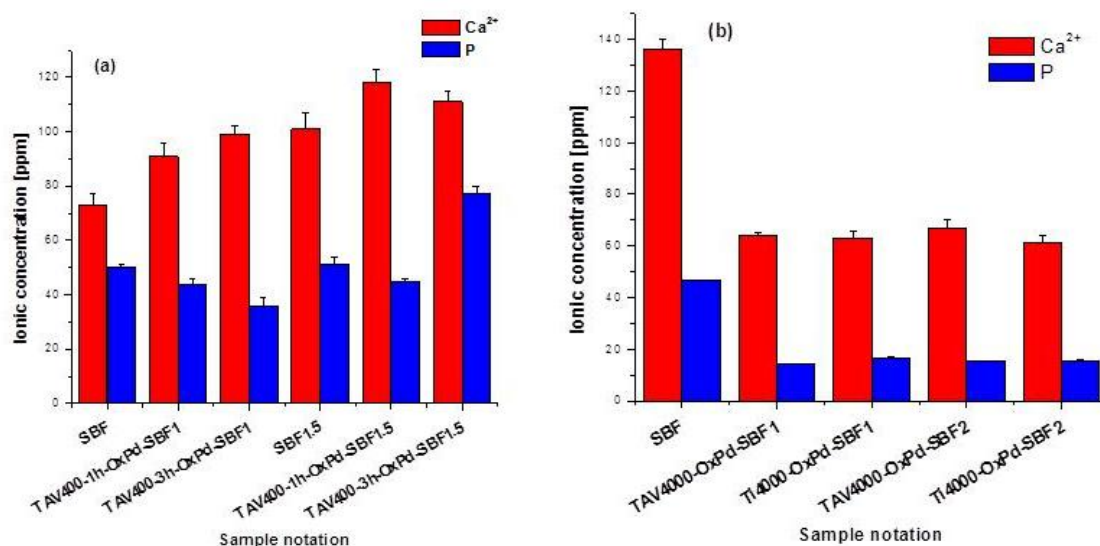


Figure 67. Concentrations of  $\text{Ca}^{2+}$  and P ions (a) TAV<sub>400</sub> in SBF1 (4 d) followed by another 2 d in SBF1.5, (b) TAV<sub>400</sub> and Ti<sub>400</sub> in SBF for 7 and 14 d.

**Fig. 63(b)** recorded a sharp decrease in the ionic concentrations of both  $\text{Ca}^{2+}$  and P ions in -TAV<sub>400</sub>-OxPd-SBF1; Ti<sub>400</sub>-OxPd-SBF1; TAV<sub>400</sub>-OxPd-SBF2 and Ti<sub>400</sub>-OxPd-SBF2-. Such decrease could be due to their consumption to transform Ca-P precipitation observed after 2 h in oxidant bath (**Fig. 60 h,k**) into another Ca-P phase as recorded in **Fig. 63 (h,k)**.

A decrease in  $\text{Ca}^{2+}$  ions after 3 days (**Fig. 68**) is observed, then increased again after 7 days. Regarding P ions slight change after 3 days but an observable release after 7 days could be proved.

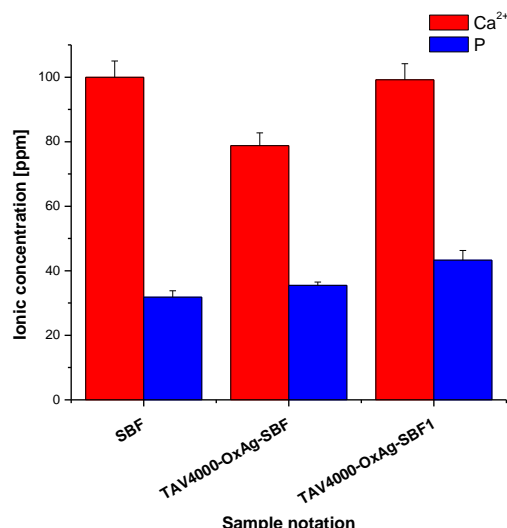


Figure 68. Concentrations of Ca<sup>2+</sup> and P ions in SBF after immersion of TAV<sub>4000</sub> immersed in oxidant bath with AgCl after 3 and 7 d.

A decrease in both Ca<sup>2+</sup> and P ionic concentrations was recorded (**Fig. 69(a)**), after 4 days in SBF1 (TiN-Ox1Pd-SBF1) and another 2 days 1.5 (TiN-Ox1Pd-SBF1.5). Such absorption was unexpected after the previous analyses, which confirm dissolution of Ca-P layer in SBF.

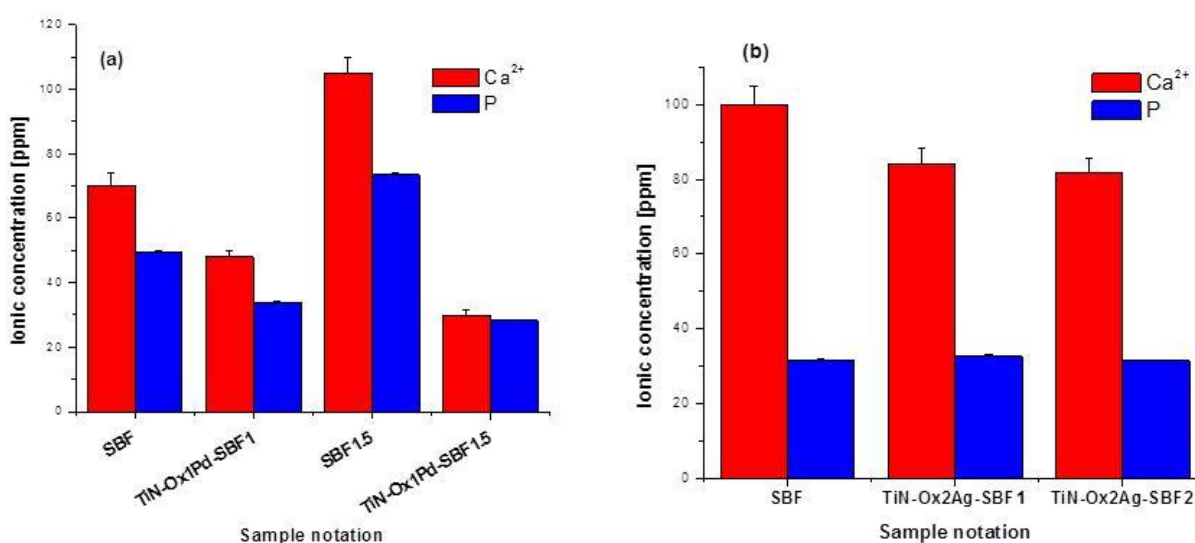


Figure 69. Concentrations of Ca<sup>2+</sup> and P ions (a) TiN after treatment with oxidant bath for 1 and 2 h with PdCl<sub>2</sub> in SBF1 (4 d) followed by another 2 d in SBF1.5, (b)TiN after treatment with oxidant bath for 2 h with AgCl in SBF for 7 and 14 d.

By following the oxidant bath with the other catalyst (AgCl), a slight decrease in Ca<sup>2+</sup> ions concentrations was recorded without any remarkable changes in the P ions concentrations (**Fig. 69(b)**) after 1 and 14 days in SBF.

### Conclusion of Part IV

In this part, it may be concluded that:

- (i) Similar roughness of TAV<sub>400</sub> with heating rate (10°C/minute) followed by 2 h treatment in oxidant bath was better than the other heating rate, while after SBF this bath failed to enhance Ca-P precipitations as shown in **Fig. 61(a-f)**. So, one can conclude that oxidant bath succeeded to form Ca-P precipitation on TAV<sub>400</sub> with high roughness but failed to maintain these precipitations upon SBF immersion.
- (ii) On changing the roughness by using (SiC 4000 grit) TAV<sub>4000</sub> or Ti<sub>4000</sub>, we observe the ability of this bath to cover the surface but with unstable Ca-P plates which easily dissolved after 1 week in immersion in SBF then began to grow another Ca-P precipitation again after another 1 week.

By using a similar bath but with AgCl catalyst, it was found that this bath was able to form a layer with homogenous distribution of Ca and P after 2 h immersion in the bath, however, such coating was unstable in SBF (**Fig. 58, 59 and 64**).

Accordingly, after checking the effect of oxidant bath on Groups I, II and III, two points could be concluded:

**First:** Oxidant bath was a positive way to deposit homogenous layer of Ca-P, only after 1 or 2 h, with both catalysts (AgCl or PdCl<sub>2</sub>) and in both buffer layers, this could be explained due to the presence of H<sub>2</sub>O<sub>2</sub> (one of oxidant bath compositions). Hydrogen peroxide is incompatible with many substances that catalyse its decomposition, including catalysts such as manganese dioxide, silver, and platinum [Petrucci, 2007].



The oxygen/precious metal interaction is one of great complexity and importance, as the oxidative catalyst of precious metals requires binding of oxygen to the surface.

Pt and Pd dioxides dissociates and bind readily, forming well-ordered structure with metal-oxygen bond ca.4.2 eV while for the Au and Ag oxygen is bound less strongly c.a. 3.2 eV. This oxygen will form negative charge on the surface to attract positive ions (Ca<sup>2+</sup> from the bath) to form superficial deposition on the surface and this can be explained, therefore, the speed of Ca-P precipitation. Such superficial precipitation was easily dissolved because it is not a real growth.

**Second:** Nearly all the precipitates were not possible to be recorded by XRD (amorphous phase). This could be explained to be due to the presence of pyrophosphate group in the bath composition which is reported to be a potent inhibitor during the crystallization process of Ca-P precipitation *in vitro* by inhibiting the crystal growth [Russell, 1976; Russell and Fleisch, 1970; Fleisch et al.,1966]. The mechanism of conversion of non-crystalline to crystalline calcium phosphate is thought to involve dissolution of the amorphous salts followed by a crystallization of calcium phosphates from the overlying supersaturated solutions. Once some crystals of calcium phosphate form, in this solution the conversion of the remaining amorphous salts follows rapidly and apparently by an autocatalytic mechanism. If this mechanism is correct, pyrophosphate should retard the conversion of the amorphous salts by inhibiting the crystallisation of calcium phosphate in the overlying solution.

It is interesting to denote how the nucleation of hydroxyapatite crystals is more easily inhibited than the nucleation of brushite. Thus, around  $1 \times 10^{-6}$  M of pyrophosphate caused inhibitory effects on hydroxyapatite crystallite nucleation [Grases et al., 2000].

# Conclusion

## Conclusion

---

To create a bioactive layer on titanium or titanium alloy, a new autocatalytic route was applied. This technique was able to compete the other biomimetic methodology of deposition on metallic implants due to its advantages such as saving time, effective cost in addition to its ability to deposit its layers in complex shapes with different roughness (by using SiC 400 and 4000 grit). The effect of autocatalytic baths having two catalysts for 2 h on different substrates with different buffer interlayer was studied.

One can conclude that:

**Sodium titanate**, as a buffer interlayer, with **PdCl<sub>2</sub>** as catalyst proved that **acidic bath** succeeded to deposit well crystalline bi-phasic Ca-P layer of octa calcium phosphate (OCP) and fluoroapatite (FA). OCP was converted into HA by absorbing some Ca ions from the physiological media especially for titanium substrates with lower roughness (Ti<sub>4000</sub>), while some Ca-P precipitations were deposited on the other substrate with higher roughness. On the other hand, this bath deposited some Ca-P precipitations on TAV<sub>4000</sub> not identified phase as it appears as discrete precipitation.

**Alkaline bath** was able to deposit discrete and different Ca-P precipitations on both substrates TAV<sub>4000</sub> and Ti<sub>4000</sub>. By using FT-IR and SAED, it was found that the precipitations on TAV were brushite (from the Ca-P family) which can be converted into apatite-like Ca-P when being soaked in SBF at the human body temperature and physiologic pH for about one week, or transformed into OCP. These formed precipitations in case of acidic and alkali bath especially on Ti, as a substrate, acted as nuclei to facilitate the formation of a homogenous coverage layer of hydroxyapatite.

**Oxidant bath** was able to form similar plates deposited on both substrates TAV<sub>4000</sub> or Ti<sub>4000</sub>. On the other hand, all morphologies formed after oxidant bath were superficial plates which easily dissolved after 14 days in SBF.

Upon changing the catalyst used in autocatalytic baths by using **AgCl** instead of **PdCl<sub>2</sub>** targeting a dual function, as a catalyst and antibacterial agent, a positive coating methodology was attained due to its ability, with all baths, to induce homogenous distribution of Ca-P of different phases according to their pH on TAV<sub>4000</sub> substrate, after only 2 h immersion in all baths separately. These depositions formed after acidic or alkali bathes acted as nuclei to stimulate the coverage of the surface with thick layers of hydroxyapatite after only 7 days. However, the layer formed after oxidant bath completely dissolved after similar period used with the other bathes.

**Titanium nitride**, as a buffer layer, with **PdCl<sub>2</sub>** as catalyst proved that the **acidic bath** failed to form homogeneous distribution on Ti surface, but it was able to form discrete precipitation of Ca-P after application for 1 or 2 h in acidic bath. These precipitations were not stable post immersion for 4 days in SBF1 but it began to rebuild after additional 2 days in SBF 1.5. The **alkaline bath** was able to deposit some Ca-P precipitation on TiN. These precipitations enhanced the deposition of Ca-P after 4 days immersion in SBF1 followed with another 2 days in SBF1.5. Concerning the **oxidant bath**, similar behaviour was observed with sodium titanate as a buffer layer detected with this buffer layer. It deposited superficial homogeneous layer which is quickly dissolved post short period in immersion in SBF.

By using the other catalyst AgCl, only silver ions were observed after **acidic bath** without the detection of any Ca-P precipitations. While **alkali bath** succeeded to form a homogeneous distribution of superficial Ca-P plates which were dissolved after 7 days in SBF then began to build again after another week. **Oxidant bath** had similar unstable deposition with AgCl.

## Conclusion

---

Finally, it was concluded that acidic and alkali bathes were effective baths with PdCl<sub>2</sub> on Ti substrate while with AgCl on TAV by using sodium titanate as a buffer layer. Oxidant bath failed to deposit a stable layer with both catalysts and on both buffer layer.

Calcium phosphate phases are reported to have several functionalities. Brushite is able to be converted into apatite-like Ca-P when it is soaked in SBF simulated body fluid solutions at the human body temperature and pH for about one week by absorbing Ca<sup>2+</sup> ions from it. On the other hand, OCP and its the transition HA is thermodynamically favored because its structure stacks apatitic layers alternatively with hydrated layer.

The conversion of OCP into HA was investigated in several physiological media which proved that the apatite converted from OCP was Ca-deficient HA, having a chemical composition with a lower Ca/P molar ratio and a higher acid phosphate content as observed in the biological crystals. Several studies reported that OCP enhanced bone formation more than stoichiometric HA or Ca-deficient HA, when they were implanted in murine bone.

Fluorapatite is one of apatites family which had the general formula, Ca<sub>10</sub>(PO<sub>4</sub>)<sub>6</sub>X<sub>2</sub> where X is typically F (Fluorapatite, FA), OH (hydroxyapatite, HA)

In the future work, the efficiency of these coatings at some selected conditions to inhibit bacterial growth will be followed in addition to assessing the cell viability to validate the applications of these coatings.

# References

- Abdel-Fattah, W. I.; El-Sayed, E-S. M.; Talaat, M. S. & Adawy, A. (2011): Comparative study of Sr<sup>+2</sup> and Zn<sup>+2</sup> incorporation in the biomimetic coating of a prosthetic alloy. *The Open Biomaterials Journal* **3**: 4–13.
- Abdel-Fattah, W. I. & Elkhoory, T. A. (2010): Nano-beta-tricalcium phosphates synthesis and biodegradation: 2. Biodegradation and apatite layer formation on nano-β-TCP synthesized via microwave treatment. *Biomedical Materials* **5**: 035015 .
- Abdel-Fattah, W. I.; Sallam, A. M.; Ibrahim, I. H. & Ibrahim, H. (2009): AC Electric Conductivity and Biochemical Analyses of Physiologic Solutions to Follow Biomimetic Coatings on Corals Impregnated with Ag or Zn or Sr Ions. *The Open Biomaterials Journal* **1**: 1-9.
- Abdel-Fattah, W. I.; El-Bassyouni, G.T. & Ibrahim, H. (2008): Biomimetic coating of corals treated with sodium hypochlorite compared to Calcium hypochlorite. *Egyptian Journal of Biomedical Sciences* **27**, (7): 12-36.
- Adawy, A. & Abdel-Fattah, W. I. (2013): An Efficient Biomimetic Coating Methodology for a prosthetic Alloy. *Materials Science and Engineering C* **33**: 1813-1818.
- Adawy, A.; Abd El-Fattah, W. I.; El-Sayed, E. M. & Talaat, M. S. (2009): Biomimetic Coating of Precalcified Ti-6Al-4V Alloy. *The Open Medical Devices Journal* **1**:19-28.
- Ajeel, S. A.; Ali, A. K. A. & Alher, M. A. (2013): Ni Ion Release of TiO<sub>2</sub> and TiO<sub>2</sub>/Hydroxylapatite composite coatings formed on NiTi shape memory alloy produced by powder metallurgy. *International Journal of Mechanical Engineering and Technology* **4** (2): 86-99
- Albrektsson, T. & Wennerberg A. (2005): The impact of oral implants—past and future, 1966–2042. *Journal of Canadian Dental Association* **71** :327-327d.
- Anisimov, S. I.; Bauerle, D. & Luk'yanchuk, B. S. (1993): Gas dynamics and film profiles in pulsed-laser deposition of materials. *Physical Review B* **48**: 12076–12081.
- Anselme, K.; Linez, P.; Bigerelle, M.; Le Maguer, D., Le Maguer, A.; Hardouin, P.; Hildebrand, H.F.; Iost, A. & Leroy, J.M. (2000):The relative influence of the topography and chemistry of TiAl6V4 surfaces on osteoblastic cell behaviour. *Biomaterials* **21**: 1567-1577.
- Bania, P. J. (1993): in D. Eylon, R.R. Boyer, D.A. Koss (Eds.), Titanium Alloys in the 1990's, The Mineral, Metals & Materials Society, Warrendale, PA, 1993: 3–14.
- Barinov, S. M.; Rau, J. V.; Cesaro, S. N.; Dunsin, J.; Fadeeva, I.V.; Ferro, D.; Medvecky, L. & Trionfetti, G.(2006): Carbonate release from carbonated hydroxyapatite in the wide temperature range. *Journal of Materials Science: Materials in Medicine* **17** (7): 597–604.
- Barrère, F.; van der Valk, C.M.; Meijer, G.; Dalmeijer, R.A.; de Groot, K. & Layrolle, P. (2003): Osteointegration of biomimetic apatite coating applied onto dense and porous metal implants in femurs of goats. *Journal of Biomedical Material Research* **67**:655–665.
- Barrère, F.; van Blitterswijk, C.A.; de Groot, K. & Layrolle, P. (2002a): Influence of ionic strength and carbonate on the Ca-P coating formation from SBFx5 solution. *Biomaterials* **23** (9): 1921-1930.
- Barrère, F.; van Blitterswijk, C.A.; de Groot, K. & Layrolle, P. (2002b): Nucleation of biomimetic Ca-P coatings on Ti6Al4V from a SBFx5 solution: influence of magnesium. *Biomaterials* **23** (10): 2211-2220.
- Barrère, F.; Layrolle, P.; van Blitterswijk, C.A. & de Groot K. (1999): Biomimetic calcium phosphate coatings on Ti6Al4V: a crystal growth study of octacalcium phosphate and inhibition by Mg<sup>2+</sup> and HCO<sub>3</sub>. *Bone* **25**: 107S-111S.
- Bauer, T.W.; Geesink, R.C.T.; Zimmerman, R. & McMohan, J.T. (1991): Hydroxyapatite-coated femoral stems: histological analysis of components retrieved at autopsy. *Journal of bone and joint surgery* **73-A**: 1439-1452.
- Belouet, C. (1996): Thin film growth by the pulsed laser assisted deposition technique. *Applied Surface Science* **96–98**: 630–642.

- Betts, A.J.; Dowling, D.P.; McConnell, M. L. & Pope, C. (2005): The influence of platinum on the performance of silver-platinum anti-bacterial coatings. *Materials and Design* **26**: 217-222.
- Bigi, A.; Boanini, E.; Bracci, B.; Facchini, A.; Panzavolta, S.; Segatti, F. & Sturba, L. (2005): Nanocrystalline hydroxyapatite coatings on titanium: a new fast biomimetic method. *Biomaterials* **26**: 4085–4089.
- Bigi, A.; Boanini, E.; Panzavolta, S. & Roveri, N. (2000): Biomimetic growth of hydroxyapatite on gelatin films doped with sodium polyacrylate. *Biomacromolecules* **1**(4): 752-756.
- Bigi, A.; Compostella, L.; Fichera, A.M.; Foresti, E.; Gazzano, M.; Ripamonti, A. & Roveri, N. (1988): Structural and chemical characterization of inorganic deposits in calcified human mitral valve. *Journal of inorganic biochemistry* **34** (2): 75–82.
- Blumenthal, N.C.; Betts, F. & Posner, A.S. (1977): Stabilization of amorphous calcium phosphate by Mg and ATP. *Calcified Tissue Research* **23**:245-250.
- Bonar, L. C.; Grympas, M. D. & Glimcher, M. J. (1984): Failure to detect crystalline burshite in embryonic and bovine chick. *Journal of Ultrastructure Research* **86**: 43-49.
- Boretos, J. W. & Eden, M., eds. (1984): Contemporary Biomaterials, Material and Host Response, Clinical Applications, New Technology and Legal Aspects (pp. 27-88, 128-132, 193-253). Noyes Publications, Park Ridge, NJ
- Boskey, A.L. (1997): Amorphous calcium phosphate: the contention of bone. *J. Dent Res* **76**: 1433-1436.
- Brett, P.M.; Harle, J.; Salih, V.; Mihoc, R.; Olsen, I. & Jones, F.H. (2004): Roughness response genes in osteoblasts. *Bone* **35**:124–33.
- Brown, W. E., Smith, J. P., Lether, J. R. & Frazier, A.W. (1962): Crystallographic and Chemical relation between OCP and HA. *Nature*: 1051-1055.
- Buddy D. R.; Allan S. H.; Fredrick, J. S. & Lemons, J.E. (2004): Biomaterials Science, 2nd ed., Elsevier Academic Press.
- Buser, D.; Schenk, R.; Steinemann, S.; Fiorellini, J.; Fox, C. & Stich, H. (1991): Influence of surface characteristics on bone integration of titanium implants. A histomorphometric study in miniature pigs. *Journal of Biomedical Material Research* **25**:889–902.
- Carllstrom, D. & Engstrom. (1956): Ultrastructure distribution and minor salts in bone tissue G.H. Bourme (ed.). The biochemistry and physiology of bone, Academic Press, New York.
- Carradó A. (2010): Structural, Microstructural, and Residual Stress Investigations of Plasma-Sprayed Hydroxyapatite on Ti-6Al-4V. *ACS Appl. Mater. Interfaces* **2** (2): 561–565.
- Carradó A. & Viart N. (2010). Nanocrystalline spin coated sol-gel hydroxyapatite thin films on Ti substrate: towards potential applications for implants. *Solid State Science* **12** (7): 1047-1050.
- Cassandra, G. F. & Robert J. M. (2011): Precious metal magic: catalytic wizardry. *Materialstoday* **14** (4):134-142.
- Cho, S.A. & Park, K.T. (2003): The removal torque of titanium screw inserted in rabbit tibia treated by dual acid etching. *Biomaterials* **24**:3611–3617.
- Chou, Y., Chiou, W., Xu, Y., Dunn, J., & Wu, B. (2004): The effect of pH on the structural evolution of accelerated biomimetic apatite. *Biomaterials* **25** (22): 5323-5331.
- Clinical Applications of Biomaterials. NIH Consensus Statement 1982 Nov 1-3; **4** (5):1-19, <http://consensus.nih.gov/1982/1982Biomaterials034html.htm>.
- Cochran, D. L.; Schenk, R. K.; Lussi, A.; Higginbottom, F. L. & Buser, D. (1998): Bone response to unloaded and loaded titanium implants with sandblasted and acid-etched surface: a histometric study in the canine mandible. *Journal of Biomedical Material Research* **40**:1-11.
- Collings, E. W. (1984): The physical metallurgy of titanium alloys, in: H.L. Gegel (Ed.), ASM Series in Metal Processing, Edward Arnold Publications, Cleveland, Metals Park, OH.

- Correia, R. N.; Magalhaes, M. C. F.; Marques, P. A. A. P. & Senos, A. M. R. (1996): Wet Synthesis and Characterization of Modified Hydroxyapatite Powders. *J. Mater. Sci., Mater. Med.* **7**: 501-505.
- Cotell, C.M.(1994): Pulsed laser deposition of biocompatible thin films, in: D.B. chrisey, G .K. Hubler (Eds), pulsed laser deposition of thin film, Wiley, New York, 549.
- Daculsi, G. & Bouler, J. M. (2003): Calcium-deficient apatite: a first in vivo study concerning bone ingrowth. *Journal of Biomedical Material Resaerch A* **65** (3), 402–408. Lacefield, W. R. *Implant Dent.* 1998, 7, 315–22, 4.
- De Groot, K.; Wolke, J.G. & Jansen, J.A. (1998): Calcium phosphate coatings for medical implants. *Proc Inst Mech Eng* **212**:137–147.
- De Groot, K. (1991): Medical applications of calciumphosphate bioceramics. *J. Ceram. Soc. Japan* **99**: 943-953.
- De Groot, K.; Geesink, R.; Klein, C.P. & Serekian, P. (1987): Plasma sprayed coatings of hydroxylapatite. *Journal of Biomedical Material Resaerch* **21**(12):1375-81.
- De Jonge, L.T.; Leeuwenburgh, S.C.G.; Wolke, J. G.C. & Jansen, J.A. (2008): Organic inorganic surface modifications for titanium implant surfaces. *Pharm. Res.* **25**: 2357-2369.
- Deng, C.L.; Chen, J.Y.; Fan, H.S. & Zhang, X.D. (2005): Influence of dynamic flow speed on bonelike apatite formation in porous calcium phosphate ceramic in RSBF, *6th Asian Symposium on Biomedical Materials*, **288-289**, pp. 273-276, Emei, China, July 19- 22, 2004.
- Dickens, B.; Schroeder, L. W. & Brown W.E. (1974): Crystallographic studies of the role of Mg as a stabilizing impurity in  $\beta$ - $\text{Ca}_3(\text{PO}_4)_2$ . The crystal structure of pure  $\beta$ - $\text{Ca}_3(\text{PO}_4)_2$ . *J SolidState Chem.* **10**: 232-248.
- Driessens, F.C.M.; Dijk Van, J.W.E. & Borg-greven, J.M.P.M. (1978): Biological calcium phosphates and their role in the physiology of bone and dental tissues I. composition and solubility of calcium phosphates. *Calcified Tissue Research* **26**: 127-137.
- Dorozhkin, S.V. (2010): Amorphous calcium (ortho) phosphates. *Acta Biomaterialia* **6**: 4457-4475
- Dorozhkin, S. V. (2009): Nanodimensional and Nanocrystalline Apatites and Other Calcium Orthophosphates in Biomedical Engineering, Biology and Medicine. *Materials* **2**: 1975-2045.
- Dorozhkin, S.V. & Epple, M. (2002): Biological and Medical Significance of Calcium Phosphates. *Angewandte Chemie International Edition* **41** (17) : 3130-3146.
- Dujovne, A. R.; Bobyn, J. D.; Krygier, J. J.; Miller, J. E. & Brooks, C.E. (1993): Mechanical compatibility of noncemented hip prostheses with the human femur. *Journal of Arthroplasty* **8** (1): 7-22.
- El-Fayoumi, M. A. K.; Abdel-Fattah, W. I. & El-Bassyouni, G. T. (2010): Development of biomimetic coatings on Sm oxide doped ELB (Eu Li Borate) glasses. *J. Mater. Sci, Eng.* **C30**(4):509-517.
- Elliott, J.C. (1994): Structure and Chemistry of the Apatites and Other Calcium Orthophosphates, Elsevier: Amsterdam [The Netherlands]; New York.
- Engh, C. A. & Bobyn, J. D. (1988): The influence of stem size and extent of porous coating on femoral bone resorption after primary cementless hip arthroplasty. *Clin Orthop Relat Res* **231**: 7-28.
- Fatehi, K.; Moztaezadeh, F.; Solati-Hashjin, M.; Tahriri, M.; Rezvannia, M. & Ravarian, R.(2008): In vitro biomimetic deposition of apatite on alkaline and heat treated Ti6Al4V alloy surface. *Bull. Mater. Sci.* **31**, ( 2): 101–108
- Feenstra, T.P. & De Bruyn, P.L. (1979): Formation of Calcium Phosphates in Moderately Supersaturated Solutions. *J Phys Chem* **83**: 475-479.

- Filiaggi, M. J.; Pilliar, R. M. & Coombs, N.A.(1993): Post-plasma-spraying heat treatment of the HA coating/Ti-6Al-4V implant system. *Journal of Biomedical Material Research* **27**: 191-198.
- Fleisch, H.; Russell, R.G. & Straumann, F.(1966): Effect of pyrophosphate on hydroxyapatite and its implications in calcium homeostasis. *Nature* **26**; 212(5065):901–903
- Fontana, M.G. (ed.) (1987): Corrosion Engineering, 3rd edn. McGraw-Hill International Edition, New York, NY.
- Geesink, P.G.T. & Manly, M.T. (1993): Hydroxyapatite coating in orthopaedic surgery, Raven Press, Ltd., New York, USA,1993:10.
- Grases, F.; Ramis, M. & Costa-Bauza, A. (2000): Effects of phytate and pyrophosphate on brushite and hydroxyapatite crystallization. Comparison with the action of other polyphosphates. *Urol Res* **28**, 136–140.
- Geurs, N. C.; Jeffcoat, R. L.; McGlumphy, E. A.; Reddy, M. S. & Jeffcoat, M. K. (2002): Influence of implant geometry and surface characteristics on progressive osseointegration. *Int J Oral Maxillo fac Implants***17**: 811–815.
- Gibson, I. R.; Rehman, I.; Best, S. M. & Bonfield, W. (2000): Characterization of the transformation from calcium deficient apatite to  $\beta$ -tricalcium phosphate. *J. Mater. Sci., Mater. Med.* **12**, 799-804.
- Gittens, R. A.; Olivares-Navarrete, R.; Tannenbaum, R.; Boyan, B.D. & Schwartz, Z., (2011): Electrical Implications of Corrosion for Osseointegration of Titanium Implants. *J Dent Res* **90** (12):1389-1397.
- Gotfredsen, K.; Wennerberg, A.; Johansson, C.; Skovgaard, L.T. & Hjorting-Hansen E. (1995): Anchorage of TiO<sub>2</sub>-blasted, HA-coated, and machined implants: an experimental study with rabbits. *Journal of Biomedical Material Research* **29**: 1223–1231
- Grynepas, M. D.; Bonar, L. C. & Glimcher, M. J. (1984): X-ray diffraction radial distribution function studies on bone mineral and synthetic calcium phosphate. *J. Mater. Sci.***19**: 723-736.
- Habibovic, P.; Barr`ere, F.; van Blitterswijk, C.A.; de Groot, K. & Layrolle, P. (2002): Biomimetic hydroxyapatite coating on metal implants. *J Am Ceram Soc* **85**: 517–522.
- Hamouda, T. & Baker, Jr JR (2000): Antimicrobial mechanism of action of surfactant lipid preparations in enteric gram-negative bacilli. *J Appl Microbiol* **89**: 397-403.
- Han, Y.; Fu, T.; Lu, J. & Xu, K.W. (2001): Characterization and stability of hydroxyapatite coatings prepared by electrodeposition and alkaline-treatment process. *Journal of Biomedical Material Research* **54**, 96-101.
- Hanks, J.H. (1975): Hanks' balanced salt solution and pH control. *Methods in Cell Science* **1** (1): 3-4.
- Hansson, S. & Norton, M. (1999): The relation between surface roughness and interfacial shear strength for bone-anchored implants. A mathematical model. *J Biomech* **32**: 829–836.
- Hench, L. L. & Wilson J. (1993): Introduction. In An Introduction to Bioceramics; Hench, L. L., Wilson, J., Eds.; Advanced Series in Ceramics; World Scientific: Singapore, 1993; **1**: 1-24.
- Holmberg, K. & Matthews, A. (1994): Coatings-tribology:Properties, Techniques and Applications in Surface Engineering. Amsterdam: Elsevier.
- Horkavcova, D.; Plesingerova, B.; Helebrant, A.; Vojtko, M. & Prochazka, V. (2008): Adhesion of the bioactive layer on titanium alloy substrate by tape-test. *Ceramics-Silikaty* **52** (3), 130-138.
- Howell, D.S. (1985): Diseases due to the deposition of calcium pyrophosphate and hydroxyapatite. In Textbook of Rheumatology (2nd edition). Kelley, W.N., Harris, E.D., Ruddy, S. & Sledge, C.B. eds., Saunders ;Philadelphia: 1398-1416.
- Huang, Y.H.; Xiropaidis, A.V.; Sorensen, R.G.; Albandar, J.M.; Hall, J. & Wikesjo, U.M. (2005): Bone formation at titanium porous oxide (TiUnite) oral implants in type IV bone. *Clin Oral Implants Res***16**:105–111.

- Hulander, M.; Lundgren, A.; Berglin, M. *et al.* (2011): Immune complement activation is attenuated by surface nanotopography. *International Journal of Nanomedicine* **6**: 2653–2666.
- Ian, W. B. (1996): Thin Film Growth by Pulsed Laser Deposition. *Ceramics International* **22** (5): 429-434.
- Ige, O.O.; Umoru, L.E.; Adeoye, M.O.; Adetunji, A.R.; Olorunniwo, O.E. & Akomolafe, I.I.(2009): Monitoring, Control and Prevention Practices of Biomaterials Corrosion –An Overview. *Trends Biomater. Artif. Organs***23** (2): 93-104.
- Ivanoff, C. J.; Hallgren, C.; Widmark, G.; Sennerby, L. & Wennerberg, A. (2001): Histologic evaluation of the bone integration of TiO(2) blasted and turned titanium microimplants in humans. *Clin Oral Implants Res***12**:128–134.
- Jalota, S.; Bhaduri, S. B. & Cuneyt Tas A. (2006): *In vitro* testing of calcium phosphate (HA, TCP, and biphasic HA-TCP) whiskers . *J Biomed Mater Res***78A**: 481–490.
- Jonasova, L.; Muller, F.A.; Helebrant, A.; Strnad, J. & Greil, P. (2004): Biomimetic apatite formation on chemically treated titanium. *Biomaterials* **25**, 1187-1194.
- Jing, Z.; Wang, C.; Wang, G.; Li, W. & Lu, D. (2010): Preparation and antibacterial activities of undoped and palladium doped titania nanoparticles. *J Sol-Gel Sci Technol***56**:121-127.
- John, A.; Abiraman, S.; Varma, H. K.; Kumari, T. V. & Umasankar, P. R. (2002): Bone growth response with porous hydroxyapatite granules in artificial sized lapine tibial-defect model. *Bull Mater Sci***25** (2): 141-154.
- Johnsson, M.S. & Nancollas, G.H. (1992): The Role of Brushite and Octacalcium phosphate in Apatite Formation. *Critical Reviews in Oral Biology and Medicine* **3**(1/2):61-82.
- Junker, R.; Dimakis, A.; Thoneick, M. & Jansen, J.A. (2009): Effects of implant surface coatings and composition on bone integration: a systematic review. *Clinical oral implants research***20** Suppl 4, 185-206.
- Kamakura, S.; Sasano, Y.; Shimizu, T.; Hatori, K.; Suzuki, O.; Kagayama, M. & Motegi, K. (2002): Implanted octacalcium phosphate is more resorbable than beta-tricalcium phosphate and hydroxyapatite. *J Biomed Mater Res***59**, 29-34.
- Kasemo, B. & Lausmaa, J. (1986): Surface science aspects on inorganic biomaterials. *CRC Crit. Rev. Clin. Neurobiol***4**: 335-30.
- Kasuga, T. (2005): Bioactive calcium pyrophosphate glasses and glass-ceramics. *Acta Biomaterialia***1**: 55–64.
- Kay, M. I.; Young, R. A. & Posner, A. S. (1964): Crystal Structure of Hydroxyapatite. *Nature* **204**:1050-1052.
- Kao, C.T.; Ding, S.J.; Chen, Y.C. & Huang, T.H.J.(2002): The anticorrosion ability of titanium nitride (TiN) plating on an orthodontic metal bracket and its biocompatibility. *Biomed Mater Res.* **63**(6):786-92.
- Kim, S.; Ryu, H.S.; Shin, H.; Jung, H.S. & Hong, K.S. (2005): In situ observation of hydroxyapatite nanocrystal formation from amorphous calcium phosphate in calcium-rich solutions. *Mater Chem Phys***91**: 500–506.
- Kim, H.M.; Miyaji, F.; Kokubo, T.; Nishiguchi, S. & Nakamura, T. (1999): Graded surface structure of bioactive titanium prepared by chemical treatment. *J Biomed Mater Res.***45**: 100-107.
- Kim, H. M.; Miyaji, F.; Kokubo, T. & Nakamura, T. (1997): Effect of heat treatment on apatite-forming ability of Ti metal induced by alkali treatment. *J. Material Science Material in Medicine***8**: 341-347.
- Kim, H.M.; Miyaji, F.; Kokubo, T. & Nakamura, T.(1996): Preparation of bioactive Ti and its alloys via simple chemical surface treatment. *Journal of Biomedical Materials Research***32**: 409-417.

- Kitsugi, T.; Yamamuro, T.; Nakamura, T.; Kotani, S.; Kokubo, T. & Takeuchi, H. (1993): Four calcium phosphate ceramics as bone substitutes for non-weight-bearing. *Biomaterials* **14** (3): 216-224.
- Kivrak, N. & Tas, A. C. (1998): Synthesis of calcium hydroxyapatite-Tricalcium phosphate (HA-TCP) composite bioceramic powders and their sintering behaviour. *J. Am. Ceram. Soc.* **81** (9): 2245.
- Kokubo, T. & Yamaguchi, S. (2010): Novel Bioactive Titanate Layers Formed on Ti Metal and Its Alloys by Chemical Treatments. *Materials* **3**: 48-63.
- Kokubo, T., & Takadama, H. (2006): How useful is SBF in predicting in vivo bone bioactivity? *Biomaterials* **27** (15): 2907-2915.
- Kokubo, T.; Kim, H. M. & Kawashita, M. (2003): Novel bioactive materials with different mechanical properties. *Biomaterials* **24**: 2161-85.
- Kokubo, T.; Kim, H.-M.; Miyaji, F.; Takadama, H. & Miyazaki, T. (1999): Ceramic-metal and ceramic-polymer composites prepared by biomimetic process. *Composites: part A* **30**: 405-409.
- Kokubo, T. (1998): Apatite formation on surfaces of ceramics, metals and polymers in body environments. *Acta Mater.* **46**: 2519-2527.
- Kokubo, T. (1996): Formation of biologically active bone-like apatite on metals and polymers by a biomimetic process. *Thermochim. Acta* **280/281**: 479-490.
- Kokubo, T.; Miyaji, F.; Kim, H.-M. & Nakamura, T. (1996): Spontaneous formation of bonelike apatite layer on chemically treated titanium metals. *J. Am. Ceram. Soc.* **79**: 1127-1129.
- Kokubo, T. (1991): Bioactive glass ceramics: properties and applications. *Biomaterials* **12**: 155-163.
- Kokubo, T. (1990a): Surface chemistry of bioactive glass-ceramics. *Journal of Non-Crystalline Solids* **120** (1-3): 138-151.
- Kokubo, T.; Kushitani, H.; Sakka, S.; Kitsugi, T. & Yamamuro, T. (1990b): Solutions able to reproduce in vivo surface-structure changes in bioactive glass-ceramic A-W. *Journal of Biomedical Materials Research* **24** (6): 721-734.
- Kokubo, T.; Kushitani, H.; Abe, Y. & Yamamuro, T. (1989): Apatite coating on various substrates in simulated body fluids. *Bioceramics* **2**: 235-242.
- Kumta, P.N.; Sfeir, C.; Lee, D.; Olton, D. & Choi, D. (2005): Nanostructured calcium phosphates for biomedical applications: novel synthesis and characterization. *Acta Biomaterialia* **1**: 65-83.
- Kwon, S-H; Jun, Y-K; Hong, S-H & Kim, H-E. (2003): Synthesis and dissolution behavior of [beta]-TCP and HA/[beta]-TCP composite powders. *J Euro Ceram Soc* **23**: 1039-45.
- Lee, B.H.; Kim, Y.D.; Shin, J. H. & Lee, K. H. (2002): Surface modification by alkali and heat treatments in titanium alloys. *Journal of Biomedical Materials Research* **61**: 466-473.
- Leeuwenburgh, S. C. G.; Wolke, J. G. C.; Siebers, M. C.; Schoonman, J. & Jansen, J. A. (2006): In vitro and in vivo reactivity of porous, electrosprayed calcium phosphate coatings. *Biomaterials* **27**: 3368-3378.
- Leng, Y. X.; Yang, P.; Chen, J. Y.; Sun, H.; Wang, J.; Wang, G. J.; Huang, N.; Tian, X. B. & Chu, P. K. (2001): Fabrication of Ti-O/Ti-N duplex coatings on biomedical titanium alloys by metal plasma immersion ion implantation and reactive plasma nitriding/oxidation. *Surf Coats Tech* **138** : 296-300.
- Lacefield, W. R. (1998): Current status of ceramic coatings for dental implants. *Implant Dent.* **7**(4): 315-22.
- Lenthe, G.H.; Malefijt, M.C.W. & Huiskes, R. (1997): Stress shielding after total knee replacement may cause bone resorption in the distal femur. *J Bone Joint Surg [Br]* **79**: 117-122.

- Leonor, I.B. & Reis, R.L. (2003): An innovative auto-catalytic deposition route to produce calcium-phosphate coatings on polymeric biomaterials. *Journal of Materials Science: Materials in Medicine* **14**: 435-441.
- Le Guehennec, L.; Soueidan, A.; Layrolle, P. & Amouriq, Y. (2007): Surface treatments of titanium dental implants for rapid osseointegration. *Dental materials* **23**: 844-854.
- Li, J.G.; Liao, H.H. & Sjöström, M. (1997): Characterization of calcium phosphates precipitated from simulated body fluid of different buffering capacities. *Biomaterials* **18** (10): 743-747.
- Li, T.T.; Lee, J.H.; Kobaysi, T. & Aoki, H. (1996). Hydroxyapatite coating by dipping method, and bone bonding strength. *Journal of Materials Science: Materials in Medicine* **7** (6): 355-357.
- Li, P.J. & de Groot, K. (1993): Calcium phosphate formation within sol-gel prepared titania in vitro and in vivo. *J. Biomed. Mater. Res.* **27** : 1495-1500.
- Liu, X.; Chu, P.K. & Ding, C. (2004): Surface modification of titanium, titanium alloys, and related materials for biomedical applications. *Mater. Sci. Eng. R* **47**: 49-121.
- Liu, Y.; Hunziker, E.B.; Randall, N.X.; de Groot K. & Layrolle P. (2003): Proteins incorporated into biomimetically prepared calcium phosphate coatings modulate their mechanical strength and dissolution rate. *Biomaterials* **24**: 65-70.
- Liu, D.M.; Troczynski, T. & Seng, W.J. (2001): Water-based sol-gel synthesis of hydroxyapatite: process development. *Biomaterials* **22**: 1721-1730.
- Long, M. & Rack, H. J. (1998): Titanium alloys in total joint replacement-a materials science perspective. *Biomaterials* **19** (18): 1621-1639.
- Makishima, A., Aoki, H. in: T. Yamaguchi, H. Yanagida (1984) (Eds.), *Bioceramics*, Giho-do Pub. Co., Tokyo: 28.
- Manivasagam, G.; Dhinasekaran, D. & Rajamanickam, A. (2010): Biomedical Implants: Corrosion and its Prevention - A Review. *Recent Patents on Corrosion Science* **2**: 40-54.
- Mark, Q. S.; Benjamin, A. M.; Joseph DiCarlo, Carl. P. T. & William J. D. (2006): An infrared study of the surface chemistry of titanium nitride atomic layer deposition on silica from TiCl<sub>4</sub> and NH<sub>3</sub>. *Thin Solid Films* **514**: 97-102.
- Massaro, C.; Rotolo, P.; De Riccardis, F.; Milella, E.; Napoli, A.; Wieland, M.; Textor, M.; Spencer, N. D. & Brunette, D. M. (2002): Comparative investigation of the surface properties of commercial titanium dental implants. Part I: chemical composition. *Journal of Materials Science. Materials in Medicine* **13**: 535-548.
- Maurer, A.M.; Brown, S.A.; Payer, J.H.; Merritt, K. & Kawalec, J.S. (1993): Reduction of fretting corrosion of Ti-6Al-4V by various surface treatments. *J Orthop Res* **11**: 865-873.
- Metsger, D.S.; Rieger, M.R. & Foreman, D.W. (1999): Mechanical properties of sintered hydroxyapatite and tricalcium phosphate ceramic. *Journal of Materials Science: Materials in Medicine* **10**: 9-17.
- Minsky, M. (1988): Memoir on inventing the confocal microscope. *Scanning* **10**, 128-138.
- Mohammed, H. I.; Abdel-Fattah, W. I.; El-Sayed, M.; Talaat, M. S.; Sallam, A. S. M.; Faerber, J.; Pourroy, G.; Roland, T. & Carrado, A. (2012): Influence of heat treatment on Ti6Al4V for biomimetic biolayer. *Bioinspired, Biomimetic and Nanobiomaterials* **1**(3), 173-182.
- Mohammed, H. I.; Abdel-Fattah, W. I.; Sallam, M. A.; El-Sayed, M. E.; Talaat, M. S. H.; Faerber, J.; Pourroy, G.; Roland, T. & Carradò, A. (2012a): Calcium phosphate coating on Ti6Al4V by autocatalytic route. *Bioinspired, Biomimetic and Nanobiomaterials* **1**(4): 221-228.
- Mølhave, K. (2004): Tools for In-situ Manipulation and Characterization of Nanostructures, PhD Thesis, 2004. MIC - Department of Micro and Nanotechnology Technical University of Denmark.

- Morris, H.F.; Ochi, S.; Spray, J.R. & Olson, J.W. (2000): Periodontal-type measurements associated with hydroxyapatite-coated and non-HA-coated implants: uncovering to 36 months. *Ann Periodontol* **5**: 56–67.
- Murray, R.G.E.; Steed, P. & Elson, H. E. (1965): The location of the mucopeptide in sections of the cell wall of Escherichia coli and other gram-negative bacteria. *Can J Microbiol* **11**: 547-560.
- Nagano, M.; Nakamura, T.; Kokubo, T.; Tanahashi, M. & Ogawa, M. (1996): Differences of bone bonding ability and degradation behaviour in vivo between amorphous calcium phosphate and highly crystalline hydroxyapatite coating. *Biomaterials* **17**: 1771-1777.
- Nan, H.; Chen, Y-R.; Luo, J-M.; Jin, Y.; Rong, L.; Jing, X.; Xue, Z-N. & Liu, X-H. (1994): In Vitro Investigation of Blood Compatibility of Ti with Oxide Layers of Rutile Structure. *J. Biomater. Appl.*, **8**: 404–412.
- Nelea, V.; Pelletier, H.; Muller, D.; Broll, N.; Mille, P.; Ristoscu, C. & Mihailescu, I.N. (2002): Mechanical properties improvement of pulsed laser-deposited hydroxyapatite thin films by high energy ion-beam implantation. *Appl. Surf. Sci.* **186**: 483-489.
- Niinomi, M. (2008): Metallic biomaterials. *Journal of Artificial Organs* **11** (3): 105-110.
- Niinomi, M. (1998): Mechanical Properties of Biomedical Titanium Alloys. *Materials Science and Engineering- A*, **243**: 231-236.
- Nishiguchi, S.; Kato, H.; Neo, M.; Oka, M.; Kim, H.M.; Kokubo, T. & Nakamura, T. (2001): Alkali and heat-treated porous titanium for orthopedic implants. *J. Biomed. Mater. Res.* **54** (2): 198-208.
- Nishiguchi, S.; Nakamura, T.; Kobayashi, M.; Kim, H.; Miyaji, F. & Kokubo, T. (1999): The effect of heat treatment on bone-bonding ability of alkali-treated titanium. *Biomaterials* **20**: 491-500.
- Nurse, R.W.; Welch, J.H. & Gutt, W. (1959): High-temperature phase equilibria in the system dicalcium silicate–tricalcium phosphate. *J. Chem. Soc.*: 1077–1083.
- Ogden, H. R. (1961) in: A.H. Clifford (Ed.), Rare Metals Handbook, Rinhdd Publishing Corporation, Chapman & Hall Ltd., London, 1961: pp. 559–579.
- Oliveira, J.M.; Leonor, I.B. & Reis, R.L. (2005): Preparation of Bioactive Coatings on the Surface of Bioinert Polymers through an Innovative Auto-Catalytic Electroless Route. *Key Engineering Material* **284-286**: 203-207.
- Oyane, A.; Kim, H.M.; Furuya, T.; Kokubo, T.; Miyazaki, T. & Nakamura, T. (2003): Preparation and assessment of revised simulated body fluids. *J Biomed Mater Res* **65A**: 188–195.
- Park, J.Y. & Davies, J.E. (2000): Red blood cell and platelet interactions with titanium implant surfaces. *Clin Oral Implants Res* **11**: 530–539.
- Papadopoulou, L.; Kontonasaki, E.; Zorba, T.; Chatzistavrou, X.; Pavlidou, E.; Paraskevopoulos, K.; Sklavounos, S. & Koidis, P. (2003): Dental ceramics coated with bioactive glass: Surface changes after exposure in a simulated body fluid under static and dynamic conditions. *Physica Status Solidi (a)-Applied Research* **198** (1): 65-75.
- Pawley, J.B. (2006): Hand book of biological confocal microscope, Third Edition.
- Peacor, D. R.; Dunn, P.J.; Simmons, W .B. & Wicks, F.J. (1985): Canaphite a new sodium calcium phosphate from the Paterson area, New Jersey. *Mineralogical Record* **16**: 467-468.
- Peltola, T.; Ptsi, M.; Rahiala, H.; Kangasniemi, I. & Yli-Urpo, A. (1998): Calcium phosphate induction by sol-gel-derived titania coatings on titanium substrates in vitro. *Journal of Biomedical Materials Research Part A*, **41** ( 3), 504-510.
- Peterson, C.D.; Hillberry, B.M. & Heck, D.A. (1988): Component wear of total knee prostheses using Ti-6Al-4V, titanium nitride coated Ti-6Al-4V, and cobalt-chromium-molybdenum femoral components. *J Biomed Mater Res* **22**: 887-903.

- Pelletier, H.; Carradò, A.; Faerber, J. & Mihailescu. I.N. (2011): Microstructure and mechanical characteristics of hydroxyapatite coatings on Ti/TiN/Si substrates synthesized by pulsed laser deposition. *Appl Phys A*, **102**(3): 629-640.
- Polmear, J. J. (1981): Titanium alloys, in: Light Alloys, Edward Arnold Publications, London, 1981 (Chapter 6).
- Qunyang, L. & Kyung-Suk, K. (2009): Micromechanics of rough surface adhesion: a homogenized projection method. *Acta Mechanica Solida Sinica***22**: (5), 377-390.
- Radin, S. R. & Ducheine, P. J. (1992): *Mater. Sci. Mater. Med.***3**, 33.
- Rajiv, K. & Singh, J. N. (1990): Pulsed-laser evaporation technique for deposition of thin films: Physics and theoretical model. *Physical Review***B 41**: 8843–8859.
- Rao, C. N. R. (1963): Chemical application of infrared spectroscopy. New York Academic Press.
- Rastogi, S.K.; Rutledge, V.J.; Gibson, C.; Newcombe, D.A.; Branen, J.R. & Branen, A.L. (2011): Ag colloids and Ag clusters over EDAPTMS-coated silica nanoparticles: synthesis, characterization, and antibacterial activity against Escherichia coli. *Nanomedicine: Nanotechnology, Biology, and Medicine* **7**: 305-314.
- Rautray, T. R.; Narayanan, R. & Kim, Kyo-Han (2011): Ion implantation of titanium based biomaterials. *Progress in Materials Science***56**:1137–1177.
- Rejda, B.V.; Peelen, J.G.J. & de Groot, K. (1977): Tri-calcium phosphate as a bone substitute. *J. Bioeng.* **1**: 93–97.
- Ringer, S. (1883): A further contribution regarding the influence of the different constituents of the blood on the contraction of the heart. *Journal of Physiology***4** (1): 29-42.
- Rosu, R.A.; Serban, V.A.; Bucur, A.L. & Dragos, U. (2012): Deposition of titanium nitride and hydroxyapatite-based biocompatible composite by reactive plasma spraying. *Applied Surface Science***258**: 3871– 3876.
- Russell, A. D. & Hugo, W. B. (1994): Antimicrobial activity and action of silver. *Prog MedChem***31**: 351-370.
- Russell, R.G.G. (1976): Metabolism of inorganic pyrophosphate (PP). *Arthritis and Rheumatism* (New York) **19**:465-479.
- Russell, R. G. & Fleisch H. (1970): Pyrophosphate, phosphonates and pyrophosphatases in the regulation of calcification and calcium homeostasis. *Proc R Soc Med.* **63**(9): 876.
- Sadeghian, Z.; Heinrich, J.G. & Moztaradeh, F. (2004): *CFI, Ceram. Forum Int.* **81**, E39.
- Sarver, J. F.; Hoffman, M. V. & Hummel, F.A. (1961): Phase equilibria and tin-activated luminescence in strontium orthophosphate systems. *Journal of The Electrochemical Society* **108** (12) : 1103–1110.
- Schroeder, L.W.; Dickens, B. & Brown, W.E. (1977): Crystallographic studies of the role of Mg as a stabilizing impurity in  $\beta$ -Ca<sub>3</sub>(PO<sub>4</sub>)<sub>2</sub>. *J. Solid State Chem.***22**: 253–262.
- Semwogerere, D. & Weeks, E. R (2005): Confocal Microscopy, Encyclopedia of Biomaterials and Biomedical Engineering DOI: 10.1081/E-EBBE-120024153, 1-10.
- Shalabi, M.M.; Gortemaker, A.; Van't Hof, M.A.; Jansen, J.A. & Creugers, N.H. (2006): Implant surface roughness and bone healing: a systematic review. *Journal of dental research*, **85**, 496-500.
- Shiva, K. R.; Veronica, J. R.; Charlene, G.; David, A. N.; Josh, R. B. & Branen A. L. (2011): Ag colloids and Ag clusters over EDAPTMS-coated silica nanoparticles: synthesis, characterization, and antibacterial activity against Escherichia coli. *Nanomedicine: Nanotechnology, Biology, and Medicine***7**: 305-314.
- Sittig, C.; Textor, M.; Spencer, N.D.; Wieland, M. & Vallotton, P.H. (1999): Surface characterization of implant materials c.p.Ti, Ti-6Al-7Nb and Ti-6Al-4V with different pretreatments. *Journal of material science: Materials in medicine* **10**: 35-46.

- Skoog, D.A.; Holler, F.J. & Crouch, S.R. (2007): Principles of Instrumental Analysis. 6th ed. Thomson Brooks/Cole, 169-173.
- Sondi, I. & Salopek-Sondi, B. (2004): Silver nanoparticles as antimicrobial agent: a case study on *E.Coli* as a model for gram-negative bacteria. *J Colloid InterfaceSci* **275**: 177-182.
- Staia, M.H.; Levis, B.; Cawley, J. & Henderson T. (1995): Chemical vapour deposition of TiN on stainless steel. Surface and Coatings Technology. *Surf. Coat. Technol.* **76-77** : 231-236.
- Stoch, A.; Brożek, A.; Błażewicz, S. *et al.* (2003): FTIR study of electrochemically deposited hydroxyapatite coatings on carbon materials. *Journal of Molecular Structure* **651-653**: 389-396.
- Sul, Y.T.; Johansson, C.; Wennerberg, A.; Cho, L.R.; Chang, B.S. & Albrektsson, T. (2005): Optimum surface properties of oxidized implants for reinforcement of osseointegration: surface chemistry, oxide thickness, porosity, roughness, and crystal structure. *Int J Oral Maxillofac Implants* **20**: 349-59.
- Sul, Y.T.; Johansson, C.B.; Roser, K. & Albrektsson, T. (2002): Qualitative and quantitative observations of bone tissue reactions to anodised implants. *Biomaterials* **23**: 1809-1817.
- Surowska, B. & Bienias, J. (2010): Composite layers on titanium and Ti6Al4V alloy for medical applications. *J Achiev Mater. Manuf. Eng.* **43** (1), 162-169.
- Suzuki, O.; Kamakura, S. & katagiri, T. (2006): surface chemistry and biological responses to synthetic octacalcium phosphate. *J Biomed Mater Res B Appl Biomater* **77** (1): 201-212.
- Suzuki, O.; Yagishita, H.; Yamazaki, M. & Aoba, T. (1995): Adsorption of bovine serum albumin onto octacalcium phosphate and hydrolyzates. *Cells Mater* **5**: 45-54.
- Symietz, C.; Lehmann, E.; Gildenhaar, R.; Krüger, J; Berger, G.(2010): Femtosecond laser induced fixation of calcium alkali phosphate ceramics on titanium alloy bone implant material. *Acta Biomaterialia* **6** (8): 3318-3324.
- Takadama, H.; Hashimoto, M.; Mizuno, M. b. & Kokubo, T. (2004): Round-robin test of SBF for in vitro measurement of apatite-forming ability of synthetic materials. *Phosphorus Research Bulletin***17**: 119-25.
- Takadama, H., Kim, H. M., Kokubo, T. & Nakamura, T. (2001): TEM-EDX study of mechanism of bonelike apatite formation on bioactive titanium metal in simulated body fluid. *Journal of Biomedical Material Research* **57**: 441-448.
- Takemoto, M.; Fujibayashi, S.; Neo, M.; Suzuki, J.; Matsushita, T.; Kokubo, T. & Nakamura, T. (2006): Osteoinductive porous titanium implants: Effect of sodium removal by dilute HCl treatment. *Biomaterials* **27** (13): 2682-2691.
- Takeuchi, M.; Abe, Y.; Yoshida, Y.; Nakayama, Y.; Okazaki, M. & Akagawa, Y. (2003): Acid pretreatment of titanium implants. *Biomaterials* **24**, 1821-1827.
- Tanahashi, M. & Matsuda, T. (1997): Surface functional group dependence on apatite formation on self-assembled monolayers in a simulated body fluid. *Journal of Biomedical Material Research* **34**: 305-315.
- Tas, A.C. (2000): Synthesis of biomimetic Ca-hydroxyapatite powders at 37°C in syntheticbody fluids. *Biomaterials***21** (14): 1429-1438.
- Teixeira, R. L. P.; De Godoy, G. C. D. & de Magalhaes, P. M. (2004): Calcium phosphate formation on alkali-treated titanium alloy and stainless steel. *Materials Research* **7**: 299-303
- Tenover, F.C. (2006): Mechanisms of antimicrobial resistance in bacteria. *American Journal of Medicine* **119**: 3-10.
- Tsuji, T.; Onuma, K.; Yamamoto, A.; Iijima, M. & Shiba, K. (2008): Direct transformation from amorphous to crystalline calcium phosphate facilitated by motif-programmed artificial proteins. *Proceeding of the National Academy of Science PNAS* **105** (44):16866-16870.

- Uchida, M.; Kim, H.M.; Kokubo, T.; Fujibayashi, S. & Nakamura, T. (2002): Effect of water treatment on the apatite-forming ability of NaOH-treated titanium metal. *Journal of Biomedical Materials Research* **63** (5): 522-530.
- Wan, Z. N.; Dorr, L.D.; Woodstone, T. ; Ranawat, A. & Song, M. (1999): Effect of stem stiffness and bone stiffness on bone remodeling in cemented total hip replacement. *Journal of Arthroplasty* **14** (2): 149-158.
- Wang, L. & Nancollas, G.H. (2008): Calcium Orthophosphates: Crystallization and Dissolution. *Chemical Reviews* **108** (11): 4628-4669.
- Wang, C. X.; Zhou, X. & Wang, M. (2004a): Mechanism of apatite formation on pure titanium treated with alkaline solution. *Bio- Medical Materials and Engineering* **14**, 5-11
- Wang, J.; Layrolle, P.; Stigter, M. & de Groot, K. (2004): Biomimetic and electrolytic calcium phosphate coatings on titanium alloy: physicochemical characteristics and cell attachment. *Biomaterials* **25**: 583–592.
- Wen, H.B.; de Wijn, J.R.; Cui, F.Z. & de Groot, K. (1998): Preparation of bioactive Ti6Al4V surfaces by a simple method. *Biomaterials* **19**, 215-221.
- Wen, H. B.; Wolke, J. G. C.; deWijn, J.R.; Liu, Q.; Cui, F.Z. & deGroot, K.(1997): Fast precipitation of calcium phosphate layers on titanium induced by simple chemical treatments. *Biomaterials* **18**, 1471-1478.
- Wennerberg, A.; Hallgren, C.; Johansson, C. & Danelli, S. (1998): A histomorphometric evaluation of screw-shaped implants each prepared with two surface roughness. *Clinical Oral Implants Research* **9**:11-19.
- Wennerberg, A.; Albrektsson, T.; Albrektsson, B. & Krol, J.J. (1995): Histomorphometric and removal torque study of screw-shaped titanium implants with three different surface topographies. *Clinical Oral Implant Research* **6**: 24–30.
- Willard, H. H.; Merrite, L. L.; J. R. & Dean, J. A. (1970): Instrumental methods of analysis 5<sup>th</sup> ed. Vol. 17, 496, New Delhi, Madrid.
- Williams, D. F. (1987): Definitions in Biomaterials, Progress in Biomedical Engineering, 4. Edition, Elsevier, Amsterdam.
- Willmott, P.R. & Huber, J.R. (2000): Pulsed laser vaporization and deposition. *Reviews of Modern Physics* **72**: 315–328.
- Wu, J.-M.; Zhang, S.-C.; Li, Y.-W. ; Zhao, F.-D.; Wang, M. & Osaka, A. (2006): Influence of film thickness on in vitro bioactivity of thin anatase films produced through direct deposition from an aqueous titanium tetrafluoride solution. *Surface Coating Technology* **201/6**: 3181–3187.
- Xiropaidis, A.V.; Qahash, M.; Lim, W.H.; Shanaman, R.H.; Rohrer, M.D.; Wikesjo, U.M.; et al. (2005): Bone-implant contact at calcium phosphate-coated and porous titanium oxide (TiUnite)-modified oral implants. *Clinical Oral Implants Res* **16**: 532–539.
- Xuanyong, L.; Paul, K. C. & Chuanxian, D. (2004): Surface modification of titanium, titanium alloys, and related materials for biomedical applications, *Materials Science and Engineering R* **47**: 49–121.
- Yan, W.Q.; Nakamura, T.; Kawanabe, K.; Nishiguchi, S.; Oka, M. & Kokubo, T. (1997): Apatite layer-coated titanium for use as bone bonding implants. *Biomaterials* **18**, 1185-1190.
- Young, R.A. & Brown W. E. (1982): structures of biological minerals, In Biological Mineralization and Demineralization, 101-141, (G. H. Nancollas,Ed.) Springer-Verlag, Berlin.
- Zollfrank, C.; Muller, L.; Greil, P. & Muller, F.A. (2005): Photoluminescence of annealed biomimetic apatites. *Acta Biomaterialia* **1**: 663–669.

# Arabic Summary

تستخدم المنزروعات الصناعيه في الأونة الأخيرة خاصة المعدنية على نطاق واسع في ترميم الأنسجة الصلبة كمواد طبيه بديلة . وكشرط أساسي لأي منزرع اصطناعي، وخاصة المعدنية، هو أن تكون، ليس فقط متوافقه حيويًا و لكن أيضا تكون نشطه حيويًا مع العظم المضيف لتكوين طبقة لاحمة قوية.

ويعد التيتانيوم وسبائكه من المنزروعات التي تستخدم على نطاق واسع في ترميم وإصلاح العظام أو زراعة الأسنان لما تتمتع به من خصائصهم الميكانيكية العالية وتوافقهم الحيوى. ومع ذلك، ليست نشطه حيويًا كما هو الحال في سيراميك (فوسفات الكالسيوم) حيث انها تشكل فقط تكامل عظمى خلال زرعها بدلا من تكوين روابط مع العظم.

و يعتبر  $Ti-6Al-4V$  من اشهر السبائك المستخدمة في الطب بسبب خصائصه الميكانيكية الجيده بالرغم من بعض التحفظات حوله كتنسرب بعض الايونات مثل الالومنيوم و الفاناديوم في ظل ظروف معينه و التي قد تؤدي الى تراكمها داخل الانسجة بالاضافه الى التكامل البطيء ما بين التيتانيوم و الانسجة العظميه المحيطة به مما يؤدي الى عدم تحقيق الاستقرار الجراحي على المدى الطويل بل قد يحتاج الأمر إلى مراجعة العملية الجراحية وإستبدال المفاصل مما يؤدي الى ازدياد التكلفة بل وتعريض المرضى لأكثر من عملية جراحية مما يسبب أعباءا مادية وسريرية خاصة على كبار السن.

ولدمج الخصائص الميكانيكية العالية للمواد المعدنية بالإضافة إلى تحقيق توافق سريع وطويل الأجل للأسطح النشطة بيولوجيا، ينبغي أن تطلّى أسطح المنزروعات المعدنية بفوسفات الكالسيوم النشط بيولوجيا، و التي تكون بمثابة حاجز لمنع تنسرب الايونات من المنزروعات بالإضافة إلى تدعيمها للمواقع الجراحية.

وهناك عدة طرق منها الفيزيائية والكيميائية لتحسين سطح التيتانيوم. ومن بين هذه الطرق رش البلازما و هي الطريقة الأكثر شيوعا. ويوجد عدة بدائل لطريقة رش البلازما ،منها طريقه المحاكاة البيولوجية للحصول على طبقه من فوسفات الكالسيوم. وهذه الطريقة يتم فيها غمس العينات في سائل محاكي للظروف الفسيولوجية، مثل السائل المحاكى لسوائل الجسم (SBF) ، لفترة من الوقت تكفي لتشكيل طبقة من فوسفات الكالسيوم عليه.

في هذه الرساله تم الطلاء بطريقه بديلة تعتمد على تقنيات بالحفز على سطح المنزرع المعدني لتشكيل طبقة من فوسفات الكالسيوم بطريقه مماثلة لعملية تكوين العظام الطبيعيه. وهذه الطريقه الجديده ذات خصائص متميزة حيث تتم بدون استخدام الكهرباء ولكن تعتمد على تفاعلات الأكسدة والاختزال بالاضافه الى قدره على التحكم في ظروف التشغيل، وتطبيقها على الأشكال المعقدة، دون التأثير السلبي للحراره إضافة إلى كونها فعالة من حيث التكلفة.

في هذا العمل تم استخدام الاحواض الحمضية أو القلوية أو المؤكسده على نوعين من المنزروعات المعدنية هما سبائك التيتانيوم و التيتانيوم Ti. وقد استخدمت هذه الحمامات مع إحتواءها على اثنين من العوامل الحفازه المختلفه و هما كلوريد البلاديوم و كلوريد الفضة ( $AgCl$  و  $PdCl_2$ ) ، ثم تم التحقق من ثبات الطبقة المترسبه باستخدام اختبارات الغمر في السوائل المماثلة لسوائل الجسم SBF لفترات مختلفه.

وقبل عملية الطلاء، كان من المقرر معالجة سطح المنزرع لتنشيطه من خلال تشكيل طبقة عازلة لجعل السطح جاهزا لترسيب فوسفات الكالسيوم في المرحله التاليه . وتم اختبار نوعين من الطبقات العازلة: (1) أكسيد التيتانيوم الصوديومي (معد كيميائيا) و (2) نيتريد التيتانيوم (معد بطريقه فيزيائيه).

تم اختبار التركيب الكيميائي او التركيبي للطبقه المترسبه باستخدام طبقات من الطاقة الطيفيه للنتشت (EDS)، الأغشية الرقيقة (TF-XRD) و مورفولوجيه و الأشعة تحت الحمراء FT-IR. و الشكل الظاهري الميكروني وكذلك خشونة الطبقة المترسبه عن طريق المسح الضوئي المجهرى الالكتروني (FESEM) والمجهر متحد البؤرة و أجريت التحليلات الكيميائية لتقييم نسب الكالسيوم و الفوسفور للسائل المحاكى للبلازما SBF بعد سحب العينات منه.

ويمكننا أن نستنتج أن الأحواض بالحفز تمكنت من ترسيب فوسفات الكالسيوم بدرجات مختلفه على النحو التالي:

باستخدام أكسيد التيتانيوم الصوديوم (كطبقة عازلة):

(1) الحمام الحمضي مع كلوريد البلاديوم  $PdCl_2$  نجح في تغطية المنزرع من التيتانيوم كاملا بطبقة من فوسفات الكالسيوم بينما أثبت كلوريد الفضة  $AgCl$  أنه أفضل من  $PdCl_2$  بالنسبة لسبائك Ti-6Al-4V، وذلك لأن سطحها بعد هذا الحمام كان طلاءه أكثر تجانسا من الملاحظ في حالة  $PdCl_2$ . و أظهر كلا الطلاءين إستقرارا بعد غمسه في SBF.

(2) فشل الحمام القلوي مع  $PdCl_2$  في تغطية السطح تماما في حين أنه كان قادرا على ترسيب بعض المجاميع من فوسفات الكالسيوم موزعة على السطح. هذه المجاميع تساعد في الإسراع بتشكيل هيدروكسي الأباتيت بعد الغمر في SBF بعد أسبوع واحد فقط خاصة على التيتانيوم. بينما كان Ti-6Al-4V أكثر قابلية  $AgCl$  ، والتي تمكنت من تشكيل توزيع متجانس من فوسفات الكالسيوم في جميع أنحاء السطح للإسراع في تشكيل طبقة كثيفة من هيدروكسي الأباتيت بعد أسبوع واحد.

(3) اما بالنسبة للحمام المؤكسد فكان له تأثيرا إيجابيا و الذي تمكن من تشكيل طبقة من فوسفات الكالسيوم خاصة مع  $AgCl$  على Ti-6Al-4V. ولكن هذا الطبقة سطحه لذوبانها تماما بعد أسبوع واحد في SBF.

### استخدام نيتريدالتيتانيوم (كطبقة عازلة):

(1) إن الحمام الحمضي مع  $PdCl_2$  قادر على تشكيل بعض ترسيبات من فوسفات الكالسيوم. إلا ان هذه الطبقة غير مستقرة بعد الغمر SBF. و فيما يتعلق مع  $AgCl$  فقد فشل هذا الحمام في تشكيل أي رواسب سواء بعد الحمام أو ال SBF.

(2) الحمام القلوي خاصة مع  $AgCl$  كان قادرا على ترسيب طبقة سطحه من فوسفات الكالسيوم ولكن يتم ذوبانها بعد الغمر في SBF لمدة أسبوع.

(3) على غرار طبقة العزل من تيتانات الصوديوم مع حمام أكسدة يتم تكوين طبقة موحدة مغطاة السطح بالكامل باستخدام  $PdCl_2$  وشبه مغطاه مع  $AgCl$ . و قد تم ذوبان كلا الطبقتين تماما بعد الغمر في SBF .

# **Annex 1**

## **Pulsed Laser Deposition**

Lasers can be used to ablate a target material and condense it on the surface of a substrate material to form a thin film. Thin film formation due to pulsed laser ablation of a target material is termed as pulsed laser deposition (PLD). PLD technique for producing thin films became increasingly popular in 1970s due to the advent of lasers delivering nanosecond pulses [Belouet, 1996]. Depending on the type of laser and material thermo-physical properties, ablation can take place under quasi-equilibrium conditions, as in laser-induced thermal vaporization, or far from equilibrium, as in pulsed laser ablation [Bauer, 2000]. A typical setup for thin film deposition by PLD technique is schematically shown in **Fig. 70**.

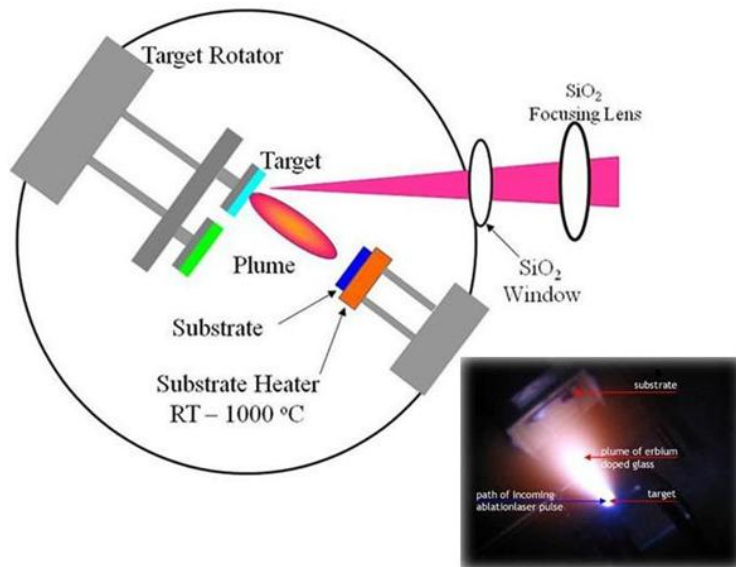


Figure 70. Schematic diagram of PLD, Copyright: <https://rt.grc.nasa.gov/main/rlc/pulsed-laser-deposition-laboratory> and <http://www.nlo.hw.ac.uk/research.html>

It essentially consists of a laser source, reaction chamber, a target, and substrate. Initially an intense laser pulse passes through an optical window of the vacuum chamber and allowed to focus on the bulk target. Above certain power density, significant material removal occurs from the target and a plasma plume is formed. The threshold power density required to produce a plasma plume depends on the thermo-physical properties of the target material, its morphology, laser pulse wavelength, and pulse duration [Belouet, 1996; Willmott & Huber, 2000].

To make the process as efficient as possible, such that energy is not lost due to carrier or thermal diffusion during absorption, short laser pulses should be used at a wavelength strongly absorbed by the target materials. Lasers operable in the Q-switched mode, therefore the Nd:YAG (1.064 nm, 532 nm, 355 nm, 266 nm), ruby (694 nm), and excimers (KrF at 248 nm and ArF at 193 nm) can deposit large amounts of energy efficiently into a thin surface region of the target. With the recent improvement in performance, e.g. reliability, uniformity and stability, the excimer and Nd: YAG lasers have been particularly widely used in PLD [Ian, 1996]. Material from the plume is then allowed to condense on the surface of a substrate to form a thin film. The distance between the target and the substrate is adjusted to match the length of the plasma plume. The substrate is rotated or moved with respect to the plasma plume to form a film of uniform thickness. Assuming an adiabatic expansion of the plasma plume in vacuum the thickness of the film profile obtained by PLD can be calculated as per the following [Anisimov et al., 1993]:

$$h(\theta) = \frac{MK^2}{2\pi\rho_s Z_s^2} (1 + k^2 \tan^2 \theta)^{3/2} \quad \text{Eq. 14}$$

Where  $k$  is a constant which varies with the pulse width of the laser beam,  $M$  is the mass of the plasma plume;  $Z_s$  is the distance at which the substrate is placed Concerning the target and  $\theta$  is the radial angle and  $\rho_s$  is the density of the substrate. For a spherical expansion of the plasma  $h(\theta)$  can be expressed as follows [Rajiv and Singh,1990]:

$$h(\theta) = \frac{M}{2\pi\rho_s Z_s^2} \cos^3 \theta \quad \text{Eq. 15}$$

The knowledge of the film thickness profile can be used to estimate the kinetic energy of the moving species and thereby the temperature of the expanding plasma plume. This in turn may help in predicting the phase transformations that take place for a particular set of laser parameters employed for the deposition process. Also as the high energetic species bombard the surface of the substrate, it may either improve or deteriorate the overall morphology, stoichiometry, and microstructure of the film. Knowing the film thickness profile it is possible to predict the distance between the target and substrate and thereby the energy of the impinging species.

Some advantages associated with PLD process can be listed as follows [Belouet, 1996; Willmott and Huber, 2000; Rajiv and Singh, 1990]:

- 1) The shorter duration of the pulses enables the synthesis of metastable materials which is difficult to be obtained by any other standard technique.
- 2) High intensity of the laser pulse associated with this process allows the possibility to ablate any kind of material for its condensation on a substrate.
- 3) Due to the pulsed nature of the PLD process film growth rate can be controlled to any desired amount.
- 4) Fabrication of composite films consisting of different materials can also be obtained.
- 5) Nanocrystalline films can also be fabricated.

# **Annex 2**

## **Calcium-phosphate phases**

## Amorphous Calcium Phosphate (ACP)

Amorphous calcium phosphate ( $Ca_9(PO_4)_6$ ) is the initial solid phase that precipitates from a highly supersaturated calcium phosphate solution, and can convert readily to stable crystalline phases such as OCP or apatite. Also, during the synthesis of HA crystals through the interaction of calcium and phosphate ions in neutral to basic solution, a precursor amorphous phase is formed which is structurally and chemically distinct from HA.

The chemical composition of ACP is strongly dependent on the solution pH: ACP phases [ACP1 and ACP2] with Ca/P ratios in the range of 1.18 precipitated at pH 6.6, 1.53 at pH 11.7 [Dorozhkin and Epple, 2002] and 1.50-1.67 when adding different amount of carbonates [Feenstra and De Bruyn, 1979]. The transformation mechanism of ACP to apatite at physiological pH has been described as follows:

ACP dissolution, then a transient OCP solid phase reprecipitation through nucleation growth, according to eq. 16, which is hydrolysed into the thermodynamically more stable apatite by a topotactic reaction, which usually takes tens of hours [Nagano et al, 1996].

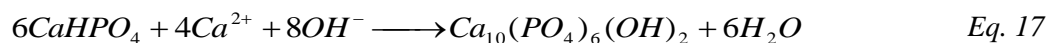


The morphology of synthetic ACP particles, appear as 300-1000 Å spheres in the SEM, consist of a random assembly of ion clusters of 9.5 Å in diameter [Blumenthal et al, 1977]. Aggregated ACP particles readily dissolve and crystallize to form apatite, the thermodynamically stable phase.

ACP has been demonstrated to have better osteoconductivity *in vivo*, better biodegradability than TCP, a good bioactivity [Boskey, 1997].

## Dicalcium Phosphate Dehydrate (DCPD) and Anhydrous (DCPA)

Dicalcium phosphate dehydrate ( $CaHPO_4 \cdot 2H_2O$ ) occurs as the mineral brushite and crystallizes in the monoclinic space group Ia with unit cell parameters  $a = 5.812(2)$  Å,  $b = 15.180(3)$  Å,  $c = 6.239(2)$  Å. DCPD is normally obtained as the primary crystalline product when Ca-P is precipitated at low pH [Rautray et al., 2011]. Its crystal structure consists of chains of  $CaPO_4$  arranged parallel to each other with lattice of water molecules interlayered in between. DCPD is a relatively high solubility Ca-P compound and is known to be converted into apatite-like Ca-P when it is soaked in SBF simulated body fluid solutions at the human body temperature for about one week according to the following reaction,



DCPD can be transformed into OCP according to the following reaction:



Dicalcium phosphate anhydrous ( $CaHPO_4$ ) or monetite is less soluble than DCPD due to the absence of water inclusions and this phase is rarely seen *in vivo* which is suggested that this is due to difficulties of detection as a consequence of its weak X-ray diffraction spectrum [Young and Brown, 1982].

## Tricalcium Phosphate (TCP)

Tricalcium phosphate ( $Ca_3(PO_4)_2$ ) is one of the most important biomaterials [Rejda et al., 1977; Bigi et al., 1988; Nurse et al., 1959] with interesting optical properties [Sarver et al., 1961].

TCP has three polymorphs  $\beta$ ;  $\alpha$ ; and  $\acute{\alpha}$ ; depending on temperature of calcinations [Nurse et al., 1959] but the most common in biomedical field is  $\beta$ -TCP. As reported [Dickens et al., 1974; Schroeder et al., 1977], the  $\beta$ -TCP crystallizes in the rhombohedral space group R3c with unit-cell parameters  $a = b = 10.439(1)$ ;  $c = 37.375(6)$  Å.

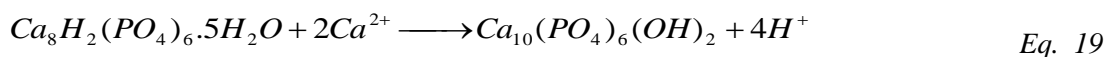
The ideal structure of  $\beta$ -TCP contains calcium ion vacancies that are too small to accommodate Ca ions but allow for the inclusion of Mg ions which thereby stabilize the structure. So it is widely used in the field of biomedical applications such as orthopaedics. It has also been observed to have significant biological affinity, activity and responds very well to the physiological environments [Kivrak and Tas, 1998]. TCP can also be utilized as a precursor for the preparation of apatites [Rejda et al., 1977; Bigi et al., 1988]. The solubility of  $\beta$ -TCP into water is about twice as high as that of HA [Makishima and Aoki, 1984]. These factors give  $\beta$ -TCP an edge over other biomedical materials when it comes to restorability and replacement of the implanted TCP in *in vivo* by the new bone tissue [Gibson et al., 2000]. Its excellent biocompatibility makes it a possible material to act as a scaffold allowing bone regeneration and growth [De Groot, 1991].

$\alpha$ -TCP, however, has received very little interest in the biomedical field due to its quick resorption rate, which limits its usage as biomaterial [Metsger et al., 1999], while  $\beta$ -TCP is essentially a slowly degrading bioresorbable phase [Driessens et al., 1978]. Because of its slow degradation characteristic, the porous  $\beta$ -TCP is regarded as an ideal material for bone substitutes that should degrade by advancing bone growth.

## Octacalcium Phosphate (OCP)

Octacalcium phosphate ( $Ca_8H_2(PO_4)_6$ ) is a more basic Ca-P phase in comparison to brushite. OCP has the lattice  $a = 19.7$  Å,  $b = 9.59$  Å,  $c = 6.87$  Å. OCP has a layered structure involving apatitic and hydrated layers. These apatitic layers have calcium and phosphate ions distributed in a manner similar to that for HA, while the hydrated layer contains lattice water and with less densely packed calcium and phosphate ions.

The water content of OCP crystal is about 1/5 that of DCPD and this is partly responsible for its lower solubility [Johnsson and Nancollas, 1992]. There is general consensus that the OCP structure stacks apatitic layers alternatively with hydrated layer so the transition of OCP to HA is thermodynamically favoured. OCP is unstable relative to HA and tends to hydrolyse according to eq. 19:



The conversion of OCP into HA has been investigated in several physiological media which showed that the apatite converted from OCP was Ca-deficient HA, having a chemical composition with a lower Ca/P molar ratio and a higher acid phosphate content [Suzuki et al., 1995] as observed in biological crystals. Several studies reported that OCP enhanced bone formation more than stoichiometric HA or Ca-deficient HA, when they were implanted in murine bone [Suzuki et al., 2006; Kamakura et al., 2002].

## Canaphite

Canaphite ( $CaNa_2P_2O_7 \cdot 4(H_2O)$ ) one of an orthophosphate group,  $CaNa_2H_2(PO_4)_2 \cdot 3H_2O$ , is shown by crystal-structure analysis to be a natural pyrophosphate identical to synthetic  $\alpha$ - $CaNa_2P_2O_7 \cdot 4H_2O$  [Cheng et al., 1980]. Its structure is, monoclinic, Pc, with  $a = 5.673(4) \text{ \AA}$ ,  $b = 8.48(1) \text{ \AA}$ ,  $c = 10.529(1) \text{ \AA}$ ,  $\beta = 106.13(6)$  and  $Z = 2$  [Peacoer et al., 1985].

In fact, the dipolyphosphate (pyrophosphate) ion,  $(P_2O_7)^{4-}$ , is produced in large quantities in the human body during the synthesis of proteins and other macromolecular substances [Russell, 1976] and is found in low concentrations in blood, saliva, and other body fluids. Moreover, certain crystalline pyrophosphates, namely calcium pyrophosphate dihydrate,  $(Ca_2P_2O_7 \cdot 2H_2O)$ , occur naturally in the cartilage of the joints, and under pathological conditions these crystals may be released into the synovial fluid, causing "calcium pyrophosphate crystal deposition disease" [Howell, 1985]. Pyrophosphate ion is also adsorbed onto the surfaces of calcified tissues in the body and may make up as much as 1% of the total inorganic phosphate in bone and dentin [Russell, 1976].

One of the first reports of sintered dicalcium pyrophosphate as a biomaterial was that of Kitsugi et al. [Kitsugi et al., 1993] who showed that after 10 weeks of implantation the sintered dicalcium pyrophosphate had formed a bond with bone. Other studies have shown that sintered dicalcium pyrophosphate is more rapidly resorbed in vivo than sintered hydroxyapatite. When implanted in rabbit femoral condyles it was shown that sintered  $\beta$ -dicalcium pyrophosphate facilitated complete bone ingrowth after a period of 4 weeks and after 8 weeks was resorbed by a process of dissolution and phagocytosis leaving a newly formed bone structure [Sadeghian et al., 2004].

## Hydroxyapatite (HA)

Apatites have the general formula,  $Ca_{10}(PO_4)_6X_2$  where X is typically F (Fluorapatite, FA), OH (hydroxyapatite, HA,  $Ca_{10}(PO_4)_6(OH)_2$ ), or Cl (Chlorapatite, ClA). The apatite lattice is capable of incorporating of substitute ions, vacancies and solid solutions, for example, X can be replaced by  $\frac{1}{2}CO_3$  or  $\frac{1}{2}O$ ; Ca by Sr, Ba, Pb, Na or vacancies; and  $PO_4$  by  $HPO_4$ ,  $AsO_4$ ,  $VO_4$ ,  $SiO_4$  or  $CO_3$  [Elliott, 1994].

HA is a bioactive ceramic which is widely used as powders or in particulate forms in various bone repairs and as coatings for metallic prostheses to improve their biological performances [Liu et al., 2001]. It is thermodynamically the most stable Ca-P ceramic compound at the pH, temperature and composition of the physiological fluid [Correia et al., 1996]. The hexagonal form of HA, with  $a = b = 9.432 \text{ \AA}$  and  $c = 6.881 \text{ \AA}$  and an exact stoichiometric Ca/P ratio of 1.67 with chemical similarity to mineralized human bone, has a structure consisting of rows of phosphate ions that are found along the a axis with columns of calcium and hydroxide groups located in parallel channels. Ion substitution can readily occur in these channels, and this may account for the high degree of substitution found in natural apatites. In hexagonal HA, the hydroxide ions are disordered within each row, when compared with the monoclinic form, pointing either upward or downward positions in the structure. This induces strains that are compensated for by substitution or ion vacancy [Kay et al., 1964], so the presence of HA is the key to promote osteointegration at the bone-implant interface. Formation of chemical bond with the host tissue offers HA a greater advantage in clinical applications over most other bone substitutes, such as allografts or metallic implants [Bauer et al., 1991]. However, in spite of chemical similarities, mechanical performance of synthetic HA is very poor compared to bone so it is applied as coating on the metallic implant systems (**Table 21**).

Table 21. Comparative composition of inorganic phases of adult human calcified tissues [Dorozhkin and Epple, 2002].

Composition	Enamel [wt%]	Dentin [wt%]	Bone [wt%]	Hydroxyapatite [wt%]
Calcium	36.5	35.1	34.8	39.6
Phosphorus	17.7	16.9	15.2	18.5
Ca/P [molar ratio]	1.63	1.61	1.71	1.67
Sodium	0.5	0.6	0.9	--
Magnesium	0.44	1.23	0.72	--
Potassium	0.08	0.05	0.03	--
Total Inorganic	97	70	65	100
Total Organic	1.5	20	25	--
Water	1.5	10	10	--

## Solubility of calcium phosphate compounds

The stability of Ca-P phases in contact with aqueous solutions are presented in **Fig. 71**. It has shown a typical solubility phase diagram as a relation between solubility isotherms, expressed as plots of  $(\log T_{Ca}T_P)$ , as a function of pH, and  $T_{Ca}$  and  $T_P$  are the total molar concentrations of calcium and phosphate, respectively. **Fig. 71** has been constructed on the assumption that the solution contains equal total molar concentrations of calcium and phosphate ions at an ionic strength of 0.1 M. It can be seen that, at pH above 4.0, HA is the most stable phase, followed by TCP and OCP. At pH values lower than 4.0, DCPD is more stable than HA. The variations in solubility with pH imply that a phase exposed to acidic conditions may be covered by a surface coating consisting of a more acidic calcium phosphate phase. Moreover, in determining the probability of the formation of preferred crystal phases in solutions supersaturated concerning several different phases, kinetic factors are also important.

The formation of HA is much slower than that of either OCP or DCPD, and during simultaneous phase formation, a larger portion of the kinetically favoured phase may be observed, even though it has a much smaller thermodynamic driving force [Johnsson and Nancollas, 1992]. So it is not surprising that under normal physiological conditions of pH 7.2, hydroxyapatite is the stable Ca-P compound. This may drop to as low as pH 5.5 in the region of tissue damage, although this would eventually return to pH 7.2 over a period of time. Even under these conditions hydroxyapatite is still the stable one.

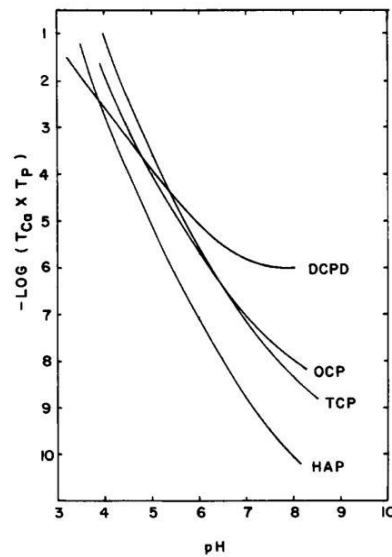


Figure 71. Solubility isotherms of Ca-P phases at 37 °C and  $I = 0.1$  M. Copyright 1992 International and American Association for Dental Research. *Critical Reviews in Oral Biology and Medicine*, 3(1/2). 61-82 (1992).

Now it is recognized that the crystallization of many Ca-P involves the formation of metastable precursors phase that subsequently dissolve as the precipitation reactions proceed.

# **Annex 3**

## **Simulated body fluids**

It can be seen from **Table 22** that corrected SBF is still richer in  $Cl^-$  and poorer in  $HCO_3^-$  ions than the human blood plasma. Therefore, a number of slightly different compositions were proposed. Tas et al. used di-sodium hydrogen phosphate in place of di-potassium hydrogen phosphate to raise the  $HCO_3^-$  concentration to 27 mM in a TRIS-HCl buffered SBF solution (i.e., Tas-SBF) [Tas, 2000]. Bigi et al. increased the content of carbonate ions to 27mM  $HCO_3^-$  by using another buffer HEPES-NaOH buffered SBF solution (i.e., Bigi-SBF) [Bigi et al., 2000]. In 2003, Oyane et al. tried to correct this difference by preparing a revised SBF (r-SBF) in which the concentrations of  $Cl^-$  and  $HCO_3^-$  ions were, decreased and increased respectively, to the levels of the human blood plasma. However, calcium carbonate has a strong tendency to precipitate from this SBF, as it is supersaturated regarding not only apatite, but also to calcite [Oyane et al., 2003]. In 2004, Takadama et al. proposed a newly improved SBF (n-SBF) in which they reduced only the  $Cl^-$  ion concentration to the level of human blood plasma, leaving the  $HCO_3^-$  ions concentration equal to that of the corrected SBF (c-SBF). This improved SBF was compared with the corrected, i.e., conventional, c-SBF in its stability and the reproducibility of apatite formation on synthetic materials. Both SBFs were subjected to round robin testing in ten research institutes. As a result, it was confirmed that the c-SBF does not differ from n-SBF in stability and reproducibility [Takadama et al., 2004].

Table 22. The development of simulated body fluid to imitate the extracellular fluid of the human blood plasma.

	$Na^+$	$K^+$	$Mg^{2+}$	$Ca^{2+}$	$Cl^-$	$HCO_3^-$	$HPO_4^-$	$SO_4^{2-}$	Buffer
Human blood plasma	142.0	5.0	1.5	2.5	103.0	27.0	1.0	0.5	–
Ringer's solution	130	4.0	–	1.4	109.0	–	–	–	–
Hank's solution	142.1	5.33	0.9	1.26	146.8	4.2	0.78	0.41	–
Original SBF	142.0	5.0	1.5	2.5	148.8	4.2	1.0	–	TRIS
c-SBF	142.0	5.0	1.5	2.5	147.8	4.2	1.0	0.5	TRIS
Tas-SBF	142.0	5.0	1.5	2.5	125.0	27.0	1.0	0.5	TRIS
Bigi-SBF	141.5	5.0	1.5	2.5	124.5	27.0	1.0	0.5	HEPES
r-SBF	142.0	5.0	1.5	2.5	103.0	27.0	1.0	0.5	HEPES
m-SBF	142.0	5.0	1.5	2.5	103.0	10.0	1.0	0.5	HEPES
i-SBF	142.0	5.0	1.0	1.6	103.0	27.0	1.0	0.5	HEPES
n-SBF	142.0	5.0	1.5	2.5	103.0	4.2	1.0	0.5	TRIS
SBF×1.5	213	7.5	2.3	3.8	221.7	6.3	1.5	0.8	TRIS
SBF×5	714.8	–	7.5	12.5	723.8	21.0	5.0	–	

In 2003, conventional SBF with the refined recipe was proposed to the Technical Committee ISO/TC150 of International Organization for Standardization as a solution for *in vitro* measurement of apatite-forming ability of implant materials and is being discussed by the committee [Kokubo and Takadama, 2006].

Immersion of pre-treated metal implants in SBF allows the heterogenous nucleation of apatite. However, it would take several days with daily refreshing of SBF solution due to the meta stability of SBF at physiological conditions [Peltola et al., 1998]. There are two approaches to accelerate the coating process: *first*, is to pretreat metal implants with more effective methods to enhance the deposition of apatite as described before and *second*: concentrating the SBF solution.

Several factors are affected on the precipitation of apatite:

1) **Ionic contents** in SBF such as, carbonate or magnesium affects strongly on the formation of biomimetic coating on titanium substrate.

For example: Low ionic content in SBF solution led to the earlier precipitation in the solution resulting in delayed and thinner formation of apatite coating on Ti-6Al-4V while high ionic strength on the other hand delayed precipitation in the solution but favoured apatite heterogeneous nucleation on Ti-6Al-4V [Barrère et al., 2002a].

The presence of  $HCO_3^-$  ions increased the pH value of the solution and influence the rate of dissolved  $CO_2$  also  $HCO_3^-$  favoured the attachment of apatite in Ti-6Al-4V by decreasing apatite crystal size resulting in a better physical attachment of apatite coating on metallic implant [Barrère et al., 2002a]. Furthermore,  $Mg^{2+}$  was strongly related to the formation and attachment of apatite coating because it inhibited precipitation in the solution, with strongly inhibitory effect on apatite crystal growth than  $HCO_3^-$ . Also as reported by Barrère et al., the  $Mg^{2+}$  content in SBF×5 changed the phase composition and crystallinity of the coating [Barrère et al., 2002b].

2) **pH of the solution:** Li et al.,(1997) reported that an apatite with Ca/P molar ratio close to that specific for HA was obtained if the pH of the solution was continuously adjusted to 7.26 during Ca-P precipitation from SBF. Chou et al., investigated the influence of pH of the initial SBF×5 solution on micro-structural evolution and final apatite structure, by immersing the argon plasma etched polystyrene culture dishes into SBF×5 solution with different pH (5.8 or 6.5), then immersed into the identical  $Mg^{2+}$  and  $HCO_3^-$  free SBF×5 (pH = 6.0). The results show that the pH of the initial SBF×5 solutions influenced the final structure of the crystalline apatite. Precursor spheres formed with comparatively high initial pH of SBF×5 (pH 6.5) transformed into larger, single crystals plates, while precursor spheres formed with low initial pH of SBF×5 (pH 5.8) developed minute, polycrystalline plate-like structures over predominantly spherical precursor substrate [Chou et al., 2004].

3) **Flowing state of SBF** effect on biomimetic apatite coatings during the immersion SBF to maintain ions concentration and constant pH for apatite growth. Papadopoulou et al. investigated the surface changes of dental ceramics coated with bioactive glass after the exposure to a SBF under static and dynamic conditions. The carbonated apatite layer formed on the surface of material in static environment was more dense and compact than that formed under dynamic conditions [Papadopoulou et al., 2003]. Deng et al.(2005) investigated the influence of the dynamic flow rate on bone-like apatite formation in porous Ca-P ceramics in revised simulated body fluid (r-SBF). They reported that the crystal shape of bone-like apatite changed with the flow rate .

# **Annex 4**

## **Analyses and Characterizations**

## Structural characterization

Several analyses such as X-Ray Diffractometer (XRD), Fourier Transform Infra-Red Spectroscopy (FT-IR) and Transmission Electron Microscopy (TEM) are used to identify the exact phases of the resultant coatings.

### X-Ray Diffractometer (XRD)

Amorphous substances are distinguished from crystal by their isotropism. Any amorphous structure should crystallize and this process should be exothermic despite the fact that amorphous structures are less stable than crystalline ones. When subjected to X-ray beam, the reflections occur in the form of cones, each of which consists of a large number of diffracted beams, from one particular type of (hkl) planes of the same type of crystals. These diffraction lines can be only measured when they satisfy Bragg's law:

$$d_{hkl} = \frac{\lambda}{2 \sin \theta} \quad \text{Eq. 20}$$

where  $d_{hkl}$  (Å) is the normal distance between (hkl) planes,  $\lambda$  is the wavelength of X-ray beam;  $\theta$  is the angle of diffraction.

ASTM cards contain the pattern of all crystalline substances in the form of their  $d_{hkl}$  (Å) values and relative intensities or reflection. The relative intensity of each line could be measured through dividing the length of an imaginary line from the peak base to its tip over the intensity of the strongest line having as 100% [Rao, 1963]. The  $d_{hkl}$  values and relative intensities of the reflections of unknown specimen should be compared to those of the ASTM card to identify its mineral type. If the three most intensive characteristic peaks identifying the mineral with their relative intensities exactly recorded in the material under investigation, this proves the presence of such phase. The first XRD study of bone was published as early as 1956 [Carllstrom, et al., 1956] in which the identified apatite as the only recognizable mineral phase. He also noted marked broadening of lines bone apatite, which he attributed to its small crystal size. Since then, there have been numerous studies which suggested the existence of other mineral phases in bone, including hydroxyapatite, brushite, octacalcium phosphate and  $\beta$ -TCP [Brown, et al., 1962; Grynpe, et al., 1984 and Bonar, et al., 1984].

*In the present work, the crystalline structures of the deposited coatings were studied by XRD analysis using Siemens D5000 diffractometer using Cu  $K\alpha_1$  (0.154056 nm) radiation equipped with quartz monochromatic at 30 kV and 25 mA. The coatings were scanned in the standard  $\theta$ - $2\theta$  geometry from 5° to 50° with a 0.01° step sizes and 5 s dwell time, or TF-XRD by Smart lab RIGAKU using Cu  $K\alpha_1$  (0.154056 nm) radiation equipped with quartz monochromatic at 45 kV and 200 mA. The coatings were scanned in the standard  $\theta$ - $2\theta$  geometry from 5° to 50° with a 0.01° step sizes and speed duration 0.3s.*

### **Fourier Transform Infra-Red Spectroscopy (FT-IR)**

Infrared spectroscopy, both diffuse reflectance and absorption modes, represents one of the most powerful techniques available today for complementary mineral analysis. Infrared spectrum yields basic information of interatomic bonding. In most cases it can serve as a finger print to give a proof of identification of each group.

*Diffuse reflectance* FT-IR spectroscopy can be used to study the surface structure of any substrates. It has the advantage of being non-invasive technique and thus can be used as a follow up tool. *Transmission* FT-IR spectroscopy, on the other hand, is mainly used to study the powder substrates. A proper amount of the powder set for characterization is mixed with potassium bromide prior to the characterization process.

The FT-IR spectrum could be divided into 3 regions:

*Near-Infrared region* meets the visible region about  $12500\text{ cm}^{-1}$  and extends to about  $4000\text{ cm}^{-1}$ . Many absorption bands resulting from harmonic overtones of O-H, N-H, C-H bonds and deformation of alkyl groups are recorded.

*Med-Infrared region* is divided into regions: *group frequency region*, from  $4000$  to  $1300\text{ cm}^{-1}$  and the *finger print*, from  $1300$  to  $650\text{ cm}^{-1}$ . In the interval from  $4000$  to  $2500\text{ cm}^{-1}$ , the absorption is characteristic of hydrogen stretching vibrations with elements of mass 19 or less. When coupled with heavier masses, the frequencies overlap the triple bond region. The intermediate frequency range,  $2500$  to  $1540\text{ cm}^{-1}$ , is often termed the unsaturated region. Triple bonds, and very little else, appear from  $2500$  to  $2000\text{ cm}^{-1}$ . Double bond frequencies fall in the region from  $2000$  to  $1540\text{ cm}^{-1}$ . By judicious application of accumulated empirical data, it is possible to distinguish among C=O, C=C, C=N. Frequencies of polyatomic systems involve motion of bonds linking a substitute group to the remainder of the molecule. This is the finger print region [Willard, et al., 1970].

*Far-Infrared region* is the region between  $667$  and  $10\text{ cm}^{-1}$  and contains the bending vibration of C, N, O and F with atom heavier than mass 19, and additional bending motions in cyclic or unsaturated systems. The low frequency molecular vibrations found in the far-infrared are particularly sensitive to changes in the overall structure of the molecules.

*In this work, surface chemical analysis of deposited coatings was assessed using diffuse reflectance Fourier transform infra-red spectroscopy (FT-IR 6100 JASCO, DR-81). The samples were examined after autocatalytic baths then after immersion in SBF. The usage of this non-invasive technique gives the ability to follow the progress of coating or its degradation from the substrate.*

### **Transmission Electron microscope (TEM)**

TEM is a microscopy technique whereby a beam of electrons is transmitted through an ultra-thin specimen, interacting with the specimen as it passes through. TEM provides higher resolution, capable of imaging atomic lattice patterns in HRTEM images. Compared to SEM the sample space is very limited and manipulation setups difficult to construct, although commercial systems are available. Electron sources can produce coherent electron beams due to the point-like emitter surface area and small energy spread. The coherent electron beam can be considered as a spherical wave propagating from the emitter and out through the electron optical system, much like a laser beam would propagate through an optical system. The HRTEM (High Resolution-TEM) images are based

on the interference of the electron wave front after it has passed through the sample and reach a CCD detector to give a phase contrast image of the sample [Mølhave, 2004].

*The specimens, in this work, were investigated with a TOPCON transmission electron microscope with an acceleration voltage of 200 kV using a LaB6-cathode. The coating was scratched off the substrates by using diamond pen, and then attached on a copper screen mesh for TEM analysis.*

## **Morphological characterization**

Different methods like FESEM- EDS-X(Field Emission Scanning Electron Microscope and Energy Dispersive Spectroscopy) and confocal microscope were used to observe the morphology of the resultant Ca-P coatings.

### **Scanning Electron Microscope and Energy Dispersive Spectroscopy (SEM-EDS-X)**

SEM can be used to study and analyze the surface morphology of a bulk specimen by displaying the intensity of the low energy secondary electron spectrum and the high energy elastically scattered electrons. In the former case, the surface topography is observed due to changes in the efficiency of emission. The latter one utilizes the increase in cross section or probability scattering with charge on the scattered atoms. Thus, a display is presented of relative distribution of “light” versus “heavy” atoms on the surface. This information is derived from the interaction between the probe electrons and the specimen. The focused electron beam is deflected by scan coils and the probe is scanned across the specimen in a raster mode. Synchronous to this scanning process, the signals generated by the probe beam interaction with the specimen are detected. The recorded intensity modulation gives the contrast in SEM images. The scanning process can be applied to generate a magnified image of the sample.

*In this work, surface morphology of the samples was observed by a JEOL field emission scanning electron microscope (FESEM) at 3 keV accelerating voltage after the surfaces were coated with carbon films. Chemical composition of the layers was followed by an EDS-X analyses (JOEL) at 7 keV in the range of 0-7 keV.*

### **Confocal microscope**

It is an optical imaging technique used to create sharp image of specimen surface, to increase optical resolution and contrast of a micrograph using a point illumination and a spatial pinhole to eliminate out-of-focus light in specimens that are thicker than the focal plane [Pawley, 2006]. This is achieved by excluding most of the light from the specimen that is not from the microscope’s focal plane. Thus, apart from allowing better observation of fine details it is possible to build three-dimensional (3D) reconstructions of a volume of the specimen by assembling a series of thin slices taken along the vertical axis.

Confocal microscopy was pioneered by Marvin Minsky in 1955 [Minsky, 1988]. Nowadays, in modern confocal microscopes, the key elements of Minsky's design have kept: the pinhole apertures and point-by-point illumination of the specimen. Minsky used zirconium arc lamp in his design to avoid building of noisy image from each point to collect accurate measurements. While the modern choice is a laser light source, which has the benefit of being available in a wide range of wavelengths. A laser is used to provide the excitation light (in order to get very high intensities). The laser light reflects off a dichroic mirror. From there, the laser hits two mirrors which are mounted on motors;

these mirrors scan the laser across the sample. Dye in the sample fluoresces, and the emitted light gets descanned by the same mirrors that are used to scan the excitation light from the laser. The emitted light passes through the dichroic and is focused onto the pinhole. The light, passing through the pinhole, is measured by a detector, i.e., a photomultiplier tube [Semwogerere and Weeks, 2005].

*In this work, the mean roughness ( $R_a$ ) and the root square roughness ( $R_q$ ) were measured by using CHR 150N, STILSA. The scan is performed over the surface of  $0.5 \times 0.5 \text{ mm}^2$  with a  $2 \mu\text{m}$  step and a frequency of 300 Hz.*

## Biochemical analysis of SBF

### Inductively coupled plasma - Atomic Emissions Spectroscopy (ICP-AES)

ICP-AES is an emission spectrophotometric technique; depends on the excitation of electrons that emit energy at a given wavelength as they return to ground state. The fundamental characteristic of this process is that each element emits energy at specific wavelengths peculiar to its chemical character. Each element emits energy at multiple wavelengths, so by using the ICP-AES technique is preferable to select a single wavelength (or very few) for a given element. The intensity of the energy emitted at the chosen wavelength is proportional to concentration of under test element in the analyzed sample. Thus, by determining which wavelengths are emitted by a sample and by determining their intensities, the analyst can quantify the elemental composition of the given sample relative to a reference standard. ICP-AES analysis requires a sample in solution. Thus, interstitial waters can be analyzed simply, requiring only dilution in most cases ([www-odp.tamu.edu/publications/tnotes/tn29/technot2.htm](http://www-odp.tamu.edu/publications/tnotes/tn29/technot2.htm)).

### Ultraviolet -visible spectrophotometer

**Ultraviolet-visible spectroscopy** refers to absorption spectroscopy in the ultraviolet-visible spectral region. This means it uses light in the visible and adjacent (near-UV and near-infrared (NIR)) ranges. The absorption in the visible range mainly depends on the perceived color of the chemicals involved. In this region of the electromagnetic spectrum, molecules undergo electronic transitions. [Skoog et al., 2007]. UV-visible spectrophotometer was used to determine the concentration of different ions that are present in SBF using the following reagents and steps:

#### Estimation of $\text{Ca}^{2+}$ concentration:

**Reagent 1 (R1):** 50 ml of KCl [0.2M] + 12ml NaOH [0.2M].

**Reagent 2 (R2):** 52 mg of methylthymol blue sodium salt [ $\text{C}_{37}\text{H}_{40}\text{N}_2\text{Na}_4\text{O}_{13}\text{S}$ ] + 0.75g of 8-hydroxyquinoline [ $\text{C}_9\text{H}_7\text{NO}$ ] 99% dissolve in 500ml of bi-distilled water (**Table 23**).

From a standard solution, calcium realizes a range of 7 tubes numbered from 0 to 6. Then prepare different dilution of calcium salt such as  $\text{CaCO}_3$  or  $\text{CaCl}_2$  for constructing the calibration curve as follows as follows (**Table 23**):

Table 23. Analysis of  $\text{Ca}^{2+}$  concentrations

	0	1	2	3	4	5	6	7
Concentration of solution (mg/l)	0	10	25	50	75	100	125	250
Volume of standard solution of calcium (ml)	0	0.8	2	4	6	8	10	20
Volume of distilled water (ml)	20	19.2	18	16	14	12	10	0
Total volume (ml)	20	20	20	20	20	20	20	20

\*to prepare 250 mg/l by dissolving 0.250g in 1000ml of bi distilled water

For measuring the concentration of  $\text{Ca}^{2+}$  ions two samples (control and unknown sample) are measured at  $\lambda=600\text{nm}$  according to the following **Table 24**:

*Table 24. Preparation of Control and unknown samples.*

	Control	Unknown sample
Volume of $\text{H}_2\text{O}$ ( $\mu\text{l}$ )	50	-
Volume of unknown sample ( $\mu\text{l}$ )	-	50
R1 (ml)	2.5	2.5
R2 (ml)	2.5	2.5

### Analysis of P ions Concentrations

**Reagent 1 (R1):** By dissolve 50 gm of molybdate reagent in 1000 ml  $\text{H}_2\text{O}$ .

**Reagent 2 (R2):** By dissolve 10 gm of hydroquinone in 1000 ml  $\text{H}_2\text{O}$ .

**Reagent 3 (R3):** By dissolve 200 gm of sodium sulfate in 1000 ml of  $\text{H}_2\text{O}$ .

From a standard solution at 1 mmol/l phosphate realize a range of 6 tubes numbered from 0 to 5 as shown in **Table 25**:

*Table 25. Analysis of P concentrations.*

	0	1	2	3	4	5
Concentration of solution (mg/l)	0	0.2	0.4	0.6	0.8	1
Volume of standard solution (ml)	0	0.2	0.4	0.6	0.8	1
Volume of distilled water (ml)	1	0.8	0.6	0.4	0.2	0
Total volume (ml)	1	1	1	1	1	1

For measuring the concentration of P ions two samples (control and unknown sample) are measured at  $\lambda = 700 \text{ nm}$  according to the following **Table 26**:

*Table 26. Preparation of control and unknown samples.*

	control	Unknown sample
Volume of $\text{H}_2\text{O}$ ( $\mu\text{l}$ )		-
Volume of unknown sample ( $\mu\text{l}$ )	-	
R1 (ml)	1	1
R2 (ml)	1	1
R3 (ml)	1	1



جامعة عين شمس-القاهرة- مصر  
كلية العلوم  
قسم الفيزياء



جامعة استراسبورج-  
فرنسا

## تغليف مزدوج من فوسفات الكالسيوم و التيتانات على المنزروعات المعدنية للتطبيقات الطبية

رساله مقدمه من

هدير ابراهيم محمد ابراهيم

للحصول على درجه دكتوراه الفلسفه فى العلوم (الفيزياء الحيويه)

قسم الفيزياء- كلية العلوم- جامعه عين شمس

تحت اشراف:

ا.د. عبد الستار محمد سلام:

استاذ الفيزياء الحيويه- كلية العلوم- جامعه عين شمس- القاهرة- مصر

ا.د. السيد محمود السيد:

استاذ الفيزياء الحيويه- كلية العلوم- جامعه عين شمس- القاهرة- مصر

ا.د. منى صلاح الدين حسن طلعت:

استاذ الفيزياء الحيويه- كلية العلوم- جامعه عين شمس- القاهرة- مصر

ا.د. وفاء اسماعيل عبد الفتاح :

استاذ السيراميك و السيراميك الحيويه- المركز القومى للبحوث- القاهرة- مصر

د. اديل كرادو:

المشرف الاجنبى- استراسبورج- فرنسا

العنوان: تغليف مزدوج من فوسفات الكالسيوم و التيتانات على  
المنزروعات المعدنية للتطبيقات الطبيه

اسم الطالبه: هدير ابراهيم محمد ابراهيم

الدرجه العلميه: دكتوراه الفلسفه فى العلوم (الفيزياء الحيويه)

القسم التابع له: الفيزياء

اسم الكليه: العلوم

الجامعه: عين شمس

سنة التخرج: 2001

سنة المنح: